

Ultrafast dynamics of electronic structure and domain nucleation during photo-induced phase transition in FeRh

Dissertation

for Doctoral Degree

at the Faculty of Mathematics, Computer Science and Natural Sciences

Department of Physics

University of Hamburg

Submitted by

Naman Agarwal

Hamburg

2021



Ultrafast dynamics of electronic structure and domain nucleation during photo-induced phase transition in FeRh

Dissertation

for Doctoral Degree

at the Faculty of Mathematics, Computer Science and Natural Sciences

Department of Physics

University of Hamburg

Submitted by

Naman Agarwal

Hamburg
2021



Reviewers of the dissertation:

Dr. Andreas Scherz
Prof. Dr. Alexander Lichtenstein

Composition of the examination committee:

Prof. Dr. Dieter Horns
Prof. Dr. Gerhard Grübel
Prof. Dr. rer. nat. Christian Back
Dr. Andreas Scherz
Prof. Dr. Alexander Lichtenstein

Chair of examination committee:

Prof. Dr. Dieter Horns

Date of the Disputation:

19 January 2022

Chair of physics subject doctoral committee:

Prof. Dr. Wolfgang Hansen

Head of physics department:

Prof. Dr. Günter H. W. Sigl

Dean of MIN faculty:

Prof. Dr. Heinrich Graener

Ultrafast dynamics of electronic structure and domain nucleation during photo-induced phase transition in FeRh

Dissertation

zur Erlangung des Doktorgrades

an der Fakultät für Mathematik, Informatik und Naturwissenschaften

Fachbereich Physik
der Universität Hamburg

vorgelegt von
Naman Agarwal

Hamburg
2021



Gutachter/innen der Dissertation:

Dr. Andreas Scherz
Prof. Dr. Alexander Lichtenstein

Zusammensetzung der Prüfungskommission:

Prof. Dr. Dieter Horns
Prof. Dr. Gerhard Grübel
Prof. Dr. rer. nat. Christian Back
Dr. Andreas Scherz
Prof. Dr. Alexander Lichtenstein

Vorsitzende/r der Prüfungskommission:

Prof. Dr. Dieter Horns

Datum der Disputation:

19 Januar 2022

Vorsitzender Fach-Promotionsausschusses PHYSIK:

Prof. Dr. Wolfgang Hansen

Leiter des Fachbereichs PHYSIK:

Prof. Dr. Günter H. W. Sigl

Dekan der Fakultät MIN:

Prof. Dr. Heinrich Graener



Declaration on Oath

I hereby affirm, in lieu of an oath, that I have written the present dissertation myself and not to have used any aids or sources other than those specified.

Hamburg, 17.12.2021

Naman Agarwal



Eidesstattliche Versicherung

Hiermit versichere ich an Eides statt, die vorliegende Dissertationsschrift selbst verfasst und keine anderen als die angegebenen Hilfsmittel und Quellen benutzt zu haben.

Hamburg, 17.12.2021

Naman Agarwal

“Nothing in life is to be feared, it is only to be understood.
Now is the time to understand more, so that we may fear less.”
— Marie Curie

Dedicated to
My sister, parents and teachers...

Acknowledgements

This work would not have been possible without significant contributions from colleagues and collaborators from whom I have learnt a lot during the discussions.

My primary supervisor Dr. Andreas Scherz. He, at many a times, was more optimistic about the experiments and my thesis than myself. He has been wonderful supervisor all these years and I really enjoyed having long discussions with him every now and then.

My secondary supervisor Prof. Dr. Alexander Lichtenstein for theoretical support and discussion on simulations which were very integral to understanding of physics described in the thesis.

My colleague Dr. Loïc Le Guyader for being an integral part of the project, for our regular discussions and very useful suggestions for the absorption spectral simulations, FeRh experiments and data analysis. His implementation of the zone-plate-based scheme for absorption spectroscopy was an essential part of the thesis.

My colleagues Dr. Robert Carley, Dr. Alexander Yaroslavtsev (Sasha) for their support in THz emission and FeRh experiments. Their previous experience with LCLS beamtime and data analysis for FeRh phase transition was quite handy in planning FeRh experiments at SCS instrument. I particularly enjoyed working with Robert in laser lab and our instrumentation and off-topic discussions.

My SCS colleagues Giuseppe, Martin, Alex, Jan Torben, Carsten, Rafael, Justine, Natalia, Laurent and Ben who were integral part of planning the beam-times at SCS instrument and constantly supported me.

My colleagues at XFEL and DESY particularly in detector group, controls group, data analysis group and X-ray operations at DESY, without whom beamtimes would not have been successful.

Our collaborators Dr. Jon Ander Arregi and Dr. Vojtěch Uhlíř for fabricating excellent FeRh samples and providing characterization data, without which there will be no beam-time.

Our collaborator Dr. Christian Stamm for providing static heating data for FeRh and experimental data on thermally induced changes in 3d transition metals.

Our collaborators: Dr. Ruslan Kurta, Dr. Viktor Valmispild for the discussions in FeRh project. Dr. Jia Liu, Prof. Tobias Kampfrath, Prof. Michael Gensch, Dr. Igor Ilyakov, Dr. Sergey Kovalev and Dr. Jan-Christoph Deinert for taking part in planning THz emission beamtime at FERMI and in data analysis. Dr. Manuel Izquierdo, Prof. Christian Back, Prof. Hermann Dürr, Dr. Igor Vaskivskiy and Diego Turenne for the discussions during FeRh beamtime.

Finally, to my family and friends for their constant support in the good and bad times and specially during COVID times.

Hamburg, 17 December 2021

Naman

Abstract

Key words: Ultrafast dynamics, Electronic band structure changes, Phase transitions and kinetics, Nucleation and growth, FM domains, 3d metals, FeRh, X-ray free-electron lasers, THz tomography of FEL pulses, Density functional theory (DFT), Elk, X-ray Absorption Spectroscopy (XAS), Small Angle X-ray Scattering (SAXS)

In this thesis, electronic band structure changes in 3d transition metals (Ti, Cr, Co, Cu) and technologically relevant alloy FeRh are investigated under the influence of external excitation (thermal or optical excitation). X-ray absorption spectroscopy simulations based on density functional theory calculations are employed to have a deeper insight into how different factors (temperature, lattice and magnetic ordering) contribute to changes in the electronic structure and to what extent.

Simulations for electronic structure changes due to thermal heating (in equilibrium) in 3d transition metals are compared with the measurements done by collaborators at SLS synchrotron light source. Limits of the simulations, assumptions and further possible improvements to calculations are discussed.

Epitaxial FeRh, which goes through a magnetic (antiferromagnetic to ferromagnetic) and structural (volume expansion) phase transition when heated statically (in equilibrium) or optically (ultrafast, in non-equilibrium), is of great technological importance for magnetic data storage devices based on heat assisted magnetic recording (HAMR). Ultrafast laser induced phase transition in FeRh gives the possibility to disentangle the microscopic mechanisms and their time scales which is otherwise not possible (in case of static heating) due to coupled electronic, lattice and spin degrees of freedom.

Benefiting from the advent of X-ray free electron lasers (XFEL), time-resolved element-specific resonant X-ray absorption spectroscopy (tr-XAS) and small angle X-ray scattering (tr-SAXS) techniques are employed as the investigative tools to probe the laser-induced phase transition in FeRh near Fe L_3 edge. DFT-based X-ray spectral simulations are used to relate the electronic band structure changes measured by tr-XAS to temporal evolution of magnetic dynamics and exchange interactions during the phase transition at sub-picosecond to 100 picoseconds time scale, giving the inherent time scales of different interactions in FeRh.

Time-resolved SAXS measurements provide the insight into microscopic picture of nucleation and growth dynamics of ferromagnetic domains at picosecond time scales. Different aspects of the transition such as bottlenecks in the speed of the transition, the nucleation and growth of FM domains, the evolution of correlations, power law scaling, dynamical slowing down and the statistically-similar nature of phase transition, are discussed.

Further, relevant to future developments at X-ray free electron laser providing attosecond and sub-femtosecond temporal resolution, novel single-shot THz-detection-based technique is presented for single shot timing-jitter correction and measurements of pulse properties (such as pulse shape, pulse duration and relative intensity). Shortcomings and further developments of the method are presented.

Kurzfassung

Schlüsselwörter: Ultraschnelle Dynamik, Änderungen der elektronischen Bandstruktur, Phasenübergänge und -kinetik, Nukleation und Wachstum, FM-Domänen, 3d-Metalle, FeRh, Freie-Elektronen-Röntgenlaser, THz-Tomographie von FEL-Pulsen, Dichtefunktionaltheorie (DFT), Elk, Röntgenabsorptionsspektroskopie (XAS), Röntgenkleinwinkelstreuung (SAXS)

In dieser Arbeit werden elektronische Bandstrukturänderungen in 3d-Übergangsmetallen (Ti, Cr, Co, Cu) und der technologisch relevanten FeRh-Legierung unter dem Einfluss externer Anregung (thermische oder optische Anregung) untersucht. Röntgenabsorptionsspektroskopie-Simulationen basierend auf Dichtefunktionaltheorie-Rechnungen werden verwendet, um einen tieferen Einblick zu erhalten, wie verschiedene Faktoren (Temperatur, Gitter und magnetische Ordnung) zu Veränderungen der elektronischen Struktur und in welchem Ausmaß beitragen.

Simulationen für elektronische Strukturänderungen bei Erwärmung im thermodynamischen Gleichgewicht in 3D-Übergangsmetallen werden mit Messungen verglichen, die von Mitarbeitern am SLS-Synchrotron durchgeführt wurden. Grenzen der Simulationen, Annahmen und weitere mögliche Verbesserungen der Berechnungen werden diskutiert.

Epitaktisches FeRh, das einen magnetischen (antiferromagnetisch zu ferromagnetisch) und strukturellen (Volumenausdehnung) Phasenübergang bei Erwärmung im thermodynamischen Gleichgewicht oder laserinduziert im Nichtgleichgewicht durchläuft, ist von großer technologischer Bedeutung für die magnetische Datenspeicherung, die auf wärmeunterstützter magnetischer Aufzeichnung (HAMR) basieren. Der ultraschnelle laserinduzierte Phasenübergang in FeRh bietet die Möglichkeit, die mikroskopischen Mechanismen und ihre Zeitskalen aufzulösen, was sonst im thermodynamischen Gleichgewicht aufgrund der gekoppelten Elektronik-, Gitter- und Spin-Freiheitsgrade nicht möglich ist.

Die zeitaufgelöste elementspezifische resonante Röntgenabsorptionsspektroskopie (tr-XAS) und die Kleinwinkel-Röntgenstreuung (tr-SAXS) werden als Untersuchungsmethode des laserinduzierten Phasenübergangs in FeRh an der Fe L_3 -Kante eingesetzt. DFT-basierte Berechnungen von Röntgenabsorptionsspektren werden verwendet, um die gemessenen, zeitaufgelösten Änderungen der elektronischen Bandstruktur mit der zeitlichen Entwicklung der Magnetisierungsdynamik und der Austauschwechselwirkungen während des Phasenübergangs auf einer Zeitskala von Femtosekunden bis hundert Pikosekunden in Beziehung zu setzen und dadurch die inhärenten Zeitskalen

der unterschiedlichen Wechselwirkungen in FeRh zu bestimmen.

Zeitaufgelöste SAXS-Messungen liefern Einblicke in das mikroskopische Bild der Nukleation und Wachstumsdynamik ferromagnetischer Domänen auf Pikosekunden-Zeitskalen. Verschiedene Aspekte des Übergangs wie die maximale Geschwindigkeit des Übergangs, die Nukleation und das Wachstum von FM-Domänen, die Entwicklung von Korrelationen, Skalengesetze, und dynamische Verlangsamung sowie die statistisch ähnliche Natur des Phasenübergangs werden diskutiert.

Für zukünftige Entwicklungen bei Röntgenlasern, die ultrakurze Pulse und Zeitauflösungen von Attosekunden und Sub-Femtosekunden bieten, wird des Weiteren eine neuartige auf THz-Detektion-basierende Methode zur Einzelschuss-Timing-Jitter-Korrektur und zur Messung von Pulseigenschaften (wie Puls Form, Pulsdauer und relative Intensität) dargestellt. Grenzen und denkbare Weiterentwicklungen der Methode werden vorgestellt.

Contents

Acknowledgements	ix
Abstract (English/Deutsch)	xi
List of figures	xix
1 Introduction	1
1.1 Phase transitions in condensed matter systems	1
1.2 Phase transitions and dynamics at ultrafast timescales	1
1.3 Phase transition in FeRh at ultrafast time scales and generation of ferromagnetic order	2
1.4 X-rays as the probe for electronic structure at ultrafast time scales	3
1.5 Single shot femtosecond timing correction at FEL facilities	4
1.6 Scope of the thesis	5
2 Theory & simulations	7
2.1 Ultrafast spin dynamics in metallic systems	7
2.1.1 Demagnetization and spin relaxation at ultrafast time-scales	7
2.1.2 Inverse spin Hall effect and THz emission	9
2.2 First order phase transition kinetics, nucleation and domain growth	10
2.3 Density functional theory (DFT)	12
2.3.1 Exchange-correlation functionals	13
2.3.2 Linearized augmented plane wave (LAPW) method & Elk code	14
2.4 X-ray absorption spectroscopy	15
2.5 X-ray absorption spectral calculations including exchange splitting in core levels . .	18
2.6 Electronic structure of FeRh	20
2.6.1 Diatomic molecule picture of antiferromagnetism	20
2.6.2 Hybridization between Fe and Rh	22
2.7 X-ray absorption spectral changes during FeRh phase transition	23
2.8 Resonant small angle X-ray scattering (SAXS)	27
2.9 Small angle X-ray scattering changes during FeRh phase transition	29
3 Experimental techniques	33
3.1 X-ray free-electron lasing process	33
3.2 European XFEL & current state of art instruments	35
3.3 Spectroscopy and Coherent Scattering (SCS) instrument	36
3.3.1 X-ray beam transport and monochromator	36
3.3.2 ALAS	36
3.3.3 X-ray gas monitor (XGM/HAMP)	37

3.3.4	DPS system	38
3.3.5	Kirkpatrick-Baez (KB) focusing mirrors	38
3.3.6	Laser in-coupling(LIN)	39
3.3.7	Optical laser	39
3.3.8	Experimental station: forward scattering fixed target (FFT)	40
3.3.9	Detectors	41
3.4	Soft X-ray experimental techniques at SCS instrument	43
3.4.1	X-ray absorption spectroscopy with transmission intensity monitor	43
3.4.2	X-ray absorption spectroscopy with transmission zone-plate grating scheme	43
3.4.3	Small angle X-ray scattering (SAXS)	45
3.4.4	Time-resolved X-ray imaging & holography	45
3.5	Timing synchronization of XFEL: active timing correction	47
3.6	Timing jitter measurements using the pulse arrival monitor (PAM): passive timing correction	47
3.7	Spectral-encoding-based electro-optic sampling setup for THz detection	48
4	THz-wave decoding of XUV/FEL pulses	49
4.1	Calibration of spectral encoding setup and single-shot THz pulse extraction	51
4.2	Application as the pulse arrival monitor	53
4.3	Application as relative pulse intensity monitor	54
4.4	Discussion and outlook	55
5	X-ray absorption spectral changes in thermally excited 3d transition metals	57
5.1	Pt/Co	60
5.2	Pt/Cr	64
5.3	Pt/Ti	67
5.4	Pt/Cu	70
5.5	Discussion and outlook	73
6	Time resolved X-ray absorption spectroscopy of optically excited FeRh	75
6.1	Energy scans across Fe L_3 edge at fixed time delays	78
6.2	Time delay scans at fixed energies around Fe L_3 edge	81
6.3	Discussion	84
7	Time-resolved small angle X-ray scattering of optically excited FeRh	87
7.1	Time- and momentum-resolved magnetic scattering	87
7.1.1	q-integrated scattering	87
7.1.2	q-resolved magnetic scattering at fixed time delays	89
7.1.3	Time-resolved magnetic scattering in fixed q ranges	90
7.1.4	Fitting of q-resolved scattering distribution	91
7.2	Time evolution of domain size and distribution	92
7.3	Correlation length evolution and dynamical power-law scaling	93
7.4	Statistically-similar behaviour of phase transition	96
7.5	Final remarks on photo-induced phase transtion in FeRh	97
7.6	Discussion and outlook	98

CONTENTS

8 Summary	99
A Appendix	103
A.1 Two-temperature model	103
A.2 Two temperature model for phase transitions	106
A.3 Temperature and magnetic order parameter profiles from 2TM model	111
A.4 Synthesis and characterization of FeRh thin films	113
A.4.1 Epitaxial growth of FeRh on SiC	113
A.4.2 Lattice parameter and thickness determination	115
A.4.3 Phase transition characterization with magneto-optical Kerr effect	118
A.5 Input file for calculation of density of states using Elk	119
Bibliography	125
Curriculum Vitae	147

List of Figures

2.1	Illustration for LAPW method.	15
2.2	Illustration of the effect of spin-orbit and exchange splitting on XAS spectra.	19
2.3	Illustration of AFM and FM state in FeRh.	21
2.4	Hybridization of Fe and Rh in AFM and FM states of FeRh.	22
2.5	Partial density of states in FeRh.	23
2.6	Simulated XAS spectra and spectral changes for AFM and FM state FeRh.	25
2.7	Various types of contributions to the transient scattering signal during FeRh phase transition.	30
3.1	Lasing process for SASE Free-Electron lasers.	34
3.2	Schematic of current operational status of European XFEL.	35
3.3	X-ray beam transport	37
3.4	Schematic of SCS instrument in the experimental hutch for forward scattering geometry [247]	37
3.5	Schematic for the X-ray beam diagnostics using X-ray gas monitor (XGM) and Huge Aperture Multiplier (HAMP). Taken from [248]	38
3.6	Schematic for X-ray focusing system in SCS hutch using KB mirrors	38
3.7	Schematic for optical laser delivery from instrument laser hutch to experiment hutch	39
3.8	Schematic of inside of FFT experimental station for forward scattering experiments.	40
3.9	Left: Schematic for modular structure of DSSC. Right: Working specifications for FCCD and DSSC detectors [247].	42
3.10	Schematic for X-ray fluorescence-based transmission intensity monitor	42
3.11	Schematic for time-resolved X-ray absorption spectroscopy based on transmission zone plate grating (TZPG) and 2D detector	44
3.12	Schematic for time-resolved small angle x-ray scattering (SAXS) measurements.	45
3.13	Experimental setup for single-shot spectral-encoding-based detection of THz pulses.	48
4.1	Spectral calibration	51
4.2	Averaged THz pulse generated by spintronic emitter excited by XUV pulses in time (a) and frequency (b) domain.	52
4.3	Arrival time jitter measured using THz pulses.	53
4.4	THz-detection-based FEL pulse arrival monitor.	53
4.5	THz-based FEL pulse energy monitor.	54
5.1	Schematic for the second harmonic lock-in measurements to measure temperature induced spectral changes	58
5.2	Spin-resolved partial density of states in 3d band for Co around Fermi energy (0 eV)	60

5.3	Electronic changes in Pt/Co.	61
5.4	Effect of core level exchange splitting on XAS spectral changes in Co.	62
5.5	Estimated DC and AC heating components in the temperature change from resistivity measurements and simulations.	63
5.6	Partial density of states in 3d band for non-magnetic (NM) bcc Cr around Fermi energy (0 eV)	64
5.7	Electronic changes in Pt/Cr.	66
5.8	Partial density of states in 3d band for non-magnetic hcp Ti around Fermi energy (0 eV)	67
5.9	Electronic changes in Pt/Ti.	69
5.10	Partial density of states in 3d band for nonmagnetic (NM) fcc Cu around Fermi energy (0 eV)	70
5.11	Electronic changes in Pt/Cu.	72
6.1	X-ray and optical pulse sequence within one train. Attenuation depth of X-rays in FeRh across Fe L_3 edge.	76
6.2	X-ray magnetic circular dichroism (XMCD) versus optical laser fluence measurement.	77
6.3	X-ray absorption spectroscopy near Fe L_3 edge at fixed time delays.	79
6.4	Integrated transient XAS (%) to calculate change in the number of 3d electrons at Fe sublattice	80
6.5	Time delay scans measuring % change in absorption	81
6.6	Illustration of shift in spectral weights during phase transition in FeRh	83
6.7	TDDFT simulations performed by Dr. Vikor Valmispild for the time evolution of optically excited AFM state	85
7.1	SAXS colomaps	88
7.2	q-integrated magnetic scattering and sample structure	89
7.3	q-resolved SAXS	89
7.4	q-resolved and time-resolved line cut waterfall plots of SAXS	91
7.5	Domain size evolution obtained from fitting the q-resolved scattering line cuts.	92
7.6	Correlation function and correlation length	93
7.7	Power law scaling of correlation length.	94
7.8	Statistical similarity in FeRh phase transition.	96
A.1	Illustration of Two Temperature Model	104
A.2	Temperature dependence of physical properties for two temperature model for FeRh.	108
A.3	Parabolic 2TM model for FeRh phase transition.	109
A.4	Coupled temperature evolution during FeRh phase transition.	110
A.5	Temperature (in K) and normalized order parameter (-ve: AFM, 0: PM, +ve: FM) profiles: Time evolution and depth profiles of electronic temperature (a) lattice temperature (b) difference(electronic-lattice) (c) and magnetic order parameter (short (d) & long time (e)). The FM order parameter is formed in the middle of the film according to the 2TM model. Initial 30 nm of the film is already magnetized within 20 ps while the remaining part takes longer time upto several 100 ps.	112
A.6	Epitaxy of FeRh on SiC.	113

LIST OF FIGURES

A.7 X-ray diffraction characterization of crystalline FeRh by out of plane symmetric (a) and in-plane azimuthal(b) scans	114
A.8 Geometry for reciprocal space mapping in XRD measurements for out of plane(a) and in plane lattice paramter(a and b) determination.	115
A.9 FeRh lattice parameters determination.	115
A.10 Estimated FeRh lattice parameters.	116
A.11 FeRh thickness measurements.	117
A.12 Characterization of magnetic phase transition in FeRh using static MOKE microscopy.	118

1 Introduction

This chapter emphasizes on the importance of the phase transitions, ultrafast dynamics, development of free-electron lasers and X-rays as the probe of ultrafast dynamics. At the end, scope of this thesis with short description of following chapters, is provided.

1.1 Phase transitions in condensed matter systems

With ever-increasing demand for advanced data storage devices, researchers are looking for new materials and novel ways for energy efficient, smaller, faster and cheaper data storage and processing [1–34]. Any potential material for data storage device contains different stable/meta-stable states which can be controlled by external parameters such as temperature, pressure, magnetic field, electric field, current etc. These external stimuli lead the material system of interest from one stable/meta-stable state to another. Such a change in the order parameter is termed as phase transition which can be electronic, structural, magnetic in origin or combinations of them. Different states of material can be used as different bit of data. Thus, phase transitions in condensed matter systems are of great technological relevance and need to be understood in details for optimization of these devices.

1.2 Phase transitions and dynamics at ultrafast timescales

It was discovered, first time in 1996, that order parameter (magnetization) in the Ni can be manipulated at ultrafast time scales, when excited by femtosecond laser [35]. Since then, with the goal that potential data storage devices could be operated and controlled at faster (picosecond, sub-picosecond) time scales using pulsed stimuli, there have been various studies showing ultrafast manipulation of order parameters (magnetic, structural etc.) in different materials [36–51]: Stanciu et al. [37] showed that magnetization in $\text{Gd}_{22}\text{Fe}_{74.6}\text{Co}_{3.4}$ can be reversed by femtosecond optical laser. It was shown by Kampfrath et al. [38] that the antiferromagnetic spin waves can be coherently controlled by single cycle THz pulses. Cavalleri et al. [52] discussed the metal to insulator transition in Vanadium oxide at picosecond timescales. It was shown by Fausti et al. [53] that the optical excitation of stripe-ordered cuprate can induce the transient superconductivity at picosecond timescales.

Apart from the technologically driven goal, studying the dynamics of phase transitions at

ultrafast time scales offers the possibility to disentangle the underlying microscopic mechanisms of such dynamics as the time scales of interactions between different degrees of freedom are different by orders of magnitude [54]. This would not be possible in case of equilibrium phase transitions because of coupled degrees of freedom. In particular, related to magnetism, subsystems can be categorized as electronic, lattice/phononic and spin/magnonic subsystems. When excited with femtosecond lasers, these subsystems go out of equilibrium with each other and then relax at different time scales depending on coupling strengths and energy transfer mechanisms between them. By studying the relaxation dynamics of these subsystems, one can get information how these subsystems are coupled to each other [55–64]. By tuning the material parameters, these interactions can be tuned to manufacture more efficient data storage devices. It has been shown [37, 39–41, 43–45] that it is possible to flip/ reorient the magnetization just by using optical excitation at pico-second time scales. This process has been termed as All optical switching (AOS). All optical switching leads the way to fabricating devices capable of ultrafast recording and reading of the data.

1.3 Phase transition in FeRh at ultrafast time scales and generation of ferromagnetic order

FeRh shows a magneto-structural phase transition upon heating [65–73]: when heated from room temperature (300 K) to around 380 K, FeRh goes from an initial antiferromagnetic (AFM) phase to a final ferromagnetic (FM) phase while also expanding by $\sim 0.5\%$ in volume. This transition has been characterized as a first-order phase transition [74], based on sudden onset of magnetization [66], discontinuity in heat capacities [75] and nucleation and growth mechanism [69, 72, 76] as shown by typical first order phase transitions [77–82]. The generation of ferromagnetic order in FeRh makes it a promising candidate for heat-assisted magnetic recording (HAMR) in future device applications. For increasing the data storage density, new devices are required to have smaller grain sizes of storage media. Due to the superparamagnetic limit, smaller grain sizes make the grain thermodynamically unstable which means that it cannot preserve its magnetization direction. Proposed HAMR devices such as exchange coupled FePt/FeRh layers [83] reduce this superparamagnetic limit to lower grain size while maintaining the high stability. Upon heating, the AFM-FM transition in FeRh helps to write the particular state in FePt with lower magnetic field, which is retained after cooling back to AFM state of FeRh. The AFM state ensures the robustness of such devices being unaffected by external stray fields and thermal fluctuations. Further, a higher exchange field and an antiferromagnetic resonance (AFMR) in the THz region makes it a promising candidate for antiferromagnetic spintronics applications [32, 34, 36, 84]. Also, it has been shown that such magneto-structural transition can be achieved at picosecond time scales using femtosecond optical laser heating [85–95]. For optimized, efficient and tunable device fabrication, it is important to understand the underlying microscopic mechanisms responsible for the ultrafast manipulation of different degrees of freedom in FeRh. Even after a number of theoretical and experimental investigations using optical as well as X-ray probes, there has not been any common consensus about the time scales of competing interactions, evolution of microscopic mechanisms, speed limits of the phase transition and role of Rh in the phase transition. [85, 86, 88, 89, 91]. A review on the different studies and interpretation for the underlying mechanism can be found

in [96]. This warrants another approach which directly looks at time-resolved evolution of the electronic structure of FeRh and relates it to subtle features of the phase transition.

The phase transition in FeRh involves the change of local exchange interactions where initially, AFM (antiparallel or negative) type exchange interaction changes to FM (parallel or positive) type exchange interaction. Exchange interactions (between identical particles), which don't have any classical analogue and are purely electronic in nature (Pauli exclusion principle), govern the magnetic order in the material [97–99]. Also, modification of the exchange interaction (magnitude or sign) may lead to a change in atomic distances (or vice-versa) [100, 101]. Since the exchange interaction is electronic in origin, any perturbation to the electronic structure will also lead to a change in exchange interactions (either in magnitude or sign). Thus, the electronic structure of the material lies at the heart of any external perturbations. This gives the idea that the microscopic magnetic interactions and the state of FeRh can be manipulated (traced) by perturbing (probing) the electronic structure of FeRh [102]. A very recently published study using photo-emission technique [95], investigating primarily surface (~ 1 nm depth) dynamics of FeRh phase transition, attempts to relate the band structure changes of occupied states to the generation of ferromagnetic order. It was suggested that the electronic structure can be modified with FM like transients appearing at ~ 350 fs time scale. Also, supported by the time-dependent DFT calculations, it was suggested that charge transfer from Rh to Fe could be a pre-cursor to this transition. Since inherent symmetry breaking at surface can potentially lead to different dynamics compared to bulk, electronic structure within the bulk of thin films needs to be probed to understand the phase transition within bulk.

1.4 X-rays as the probe for electronic structure at ultrafast time scales

There are a number of techniques which have been developed over the years to study the ultrafast dynamics, depending on the material and type of transition being studied [103]. A recent review summarizes some of the ultrafast techniques used in condensed matter [104]. To study ultrafast dynamics, one needs a femtosecond pulsed source which is not yet possible for neutrons. This leaves neutron-based sources out of the equation for now. Further, any electronics-based probe (e.g. electric current pulses generated by oscillator) works up to few 100 GHz and cannot measure femtosecond dynamics occurring in the 1THz to 100 THz frequency domain. This means we have to rely on optical techniques to probe the ultrafast dynamics. Optical techniques are mostly based on pump-probe-type of measurements where the time evolution of the dynamics is measured by varying the time delay between the femtosecond pump and probe pulses. Dynamical changes in the material properties modulate the optical probe which can be measured as a function of the time delay. The pump-probe techniques can be combined with microscopy techniques to further study the microscopic evolution. With the advent of X-ray free electron lasers [105–121], pump-probe optical techniques have been extended to the X-ray region [50, 122–131]. Optical pump and X-ray probe measurements have the advantage of element specificity (absorption edges in the X-ray region are element specific), the spatial resolution (smaller the wavelength better is the resolution) and a higher penetration depth over longer optical wavelengths. X-ray free-electron lasers (XFEL) have provided new ways to look at the evolution of local electronic and atomic

structures with unprecedented temporal and spatial resolutions. Compared to time-resolved electron microscopy and time-resolved atomic force microscopy, X-ray-based techniques provide non-invasive measurements with larger penetration depth. Thus XFEL-based techniques, in the future, will pave the way to technological innovations.

1.5 Single shot femtosecond timing correction at FEL facilities

For achieving femtosecond time resolution at free-electron laser facilities, the optical laser pump pulse needs to be synchronized with the X-ray probe pulse with better than a femtosecond accuracy. Long path traversed by the X-ray pulses contributes to timing fluctuations. Self Amplified Spontaneous Emission (SASE) process itself contributes to timing fluctuations. All the electrons do not follow same path and there is finite divergence in phase space trajectory. Electron bunch generation from the source also contains the fluctuations in time and space. These factors contribute to relative jitter of the arrival times of the optical and the X-ray pulses at the sample even after sophisticated synchronization schemes. Still the femtosecond resolution can be achieved if this pulse-to-pulse timing jitter can be measured and corrected in the post analysis. There have been a number of pulse arrival measurement techniques (such as optical cross-correlation, THz streaking) already developed but they need further improvements in terms of timing sensitivity, required X-ray fluence levels, non-invasiveness and simplicity of implementation and analysis.

1.6 Scope of the thesis

The thesis contains three topics distributed among the chapters.

- THz-detection-based novel single shot timing jitter correction and diagnostics of FEL pulses
- Electronic structure changes in 3d transition metals due to thermal excitation in equilibrium
- Temporal evolution of electronic structure in FeRh and its relation to subtle features in phase transition when excited thermally or optically and microscopic evolution of ferromagnetic order in FeRh

Chapter 2 introduces the relevant topics such as the ultrafast dynamics in magnetic systems, phase transition kinetics, inverse spin Hall effect, THz emission, density functional theory, X-ray absorption spectroscopy (XAS) and small angle X-ray scattering (SAXS). Further, simulations for X-ray absorption spectral modifications, due to change in the electronic band structure, are presented and their relation to magnetic properties in phase transition are discussed.

Chapter 3 describes the single-shot spectral-encoding-based electro-optic sampling technique for THz detection and X-ray free electron lasing process. Further, it describes the status of European XFEL and in particular the SCS instrument where the time-resolved XAS and SAXS measurements on FeRh were performed. It also discusses the timing and synchronization between optical pump and X-ray probe at FEL facilities and the possibility to correct for the pulse-to-pulse timing jitter.

Chapter 4 describes a novel approach which uses THz pulses generated by FEL pulses, using spintronic emitter, to probe the relative timing jitter between optical and FEL pulses. Further, possibility to probe the properties of FEL pulses such as pulse shape, intensity and pulse duration is also described.

Chapter 5 describes the simulations for changes in XAS spectra of 3d transition metals upon thermal excitation, assuming the electron equilibration based on a Fermi-Dirac distribution. The simulations are then compared to experimental data taken by collaborators at the SLS light source.

Chapter 6 describes the time-resolved XAS measurements at FeRh, performed at Spectroscopy and Coherent Scattering (SCS) instrument of European XFEL. The X-ray spectral changes are compared to spectral simulations. Timescales of electronic structure changes and its link to the evolution of exchange interactions and lattice expansion across the phase transition is discussed. The nucleation and coarsening dynamics of FeRh phase transition and slowing down of transition is described as measured by tr-SAXS.

Chapter 7 describes the time- and momentum-resolved SAXS measurements at FeRh, carried out at Spectroscopy and Coherent Scattering (SCS) instrument of European XFEL. Nucleation and coarsening dynamics during FeRh phase transition and slowing down of transition is described as measured by tr-SAXS.

2 Theory & simulations

This chapter introduces concepts relevant to the ultrafast dynamics in magnetic metallic systems and phase transition kinetics. Further, the theoretical concepts related to X-ray absorption spectroscopy (XAS) simulations and small angle X-ray scattering (SAXS) are discussed.

2.1 Ultrafast spin dynamics in metallic systems

The spin of an electron, which is its intrinsic property (angular momentum) and has no classical analogue, interacts with spins of other electrons via the exchange mechanism which is again purely quantum mechanical effect. This additional interaction is responsible for many novel quantum mechanical phenomena, one of them being spontaneous magnetic ordering at finite temperatures. The magnetic ordering in such systems tends to reduce the total energy by preferentially orienting themselves in a particular order. Different kind of magnetic orderings have been observed, depending on material systems and external conditions (temperature, pressure, magnetic and electric field etc). Even, simple elemental systems such as 3d transition metals (Fe, Co, Ni, Cr, Mn) and 4f rare earth metals (e.g. Gd, Tb) show rich magnetic properties because of the unpaired electrons in the 3d and 4f orbitals which can interact strongly with other electrons via the exchange or with the lattice via spin-orbit coupling. Most common spin ordering types are parallel and anti-parallel spin orientation, termed as ferromagnetic ordering or anti-ferromagnetic ordering respectively. Since the spin ordering is stabilized via different types of competing interactions under certain external conditions, it is possible to manipulate the spins by controlling the external conditions such as the magnetic field, temperature and/or pressure.

2.1.1 Demagnetization and spin relaxation at ultrafast time-scales

As shown for the first time in 1996 [35], it is also possible to manipulate spins at very short time scales using femtosecond optical pulses. There have been various theoretical and experimental studies [46, 55–57, 59–61, 86, 87, 132–164] to understand the possible mechanisms of interaction of light/photons with the electron, spin and lattice subsystems which are coupled via different interaction mechanisms. The manipulation of spin system (spin angular momentum) by any mechanism should conserve the total angular momentum. Thus, different mechanisms try to explain how the angular momentum can be transferred from one subsystem to another (so that total angular momentum remains conserved) and on what timescales. The timescale for angular

momentum transfer is the bottleneck for timescale of spin dynamics. In this section, some of the important channels for angular momentum transfer and spin dynamics, which are most relevant to 3d metallic systems, will be described.

Elliott-Yafet type spin-flip scattering

One of the possible channels for angular momentum transfer is the interaction of spin and lattice subsystems via spin-orbit coupling. In this case, due to the spin-orbit coupling, the spin is not a good quantum number which means that it is mixture of spin polarizations (up and down). The spin of one polarization can flip by interacting with the lattice and transferring the angular momentum [60, 134] to the lattice. The Elliott-Yafet type scattering depends on spin orbit coupling. Thus, stronger spin-orbit coupling will lead to higher spin scattering events leading to more demagnetization. Also, spin-flip scattering increases with temperature and is proportional to the spin imbalance. Thus, after the laser excitation and subsequent band structure collapse, due to the sudden increase in temperature of the electronic subsystem, spin-flip rates can be particularly high which lead to spin relaxation and thus demagnetization at ultrafast time scales. The spin-mixing parameter and the temporal evolution of demagnetization due to spin-flips can be calculated theoretically. Apart from phonon/lattice-mediated spin-flip scattering, the electron-electron and the electron-magnon scatterings [55, 141, 144, 157] also play a role in spin relaxation and demagnetization. The quantitative contributions to demagnetization, due to the individual scattering channels, is material-dependent and is still in debate. The electron-phonon scattering (spin-flip or non-spin-flip type) also leads to the thermalization of electron and lattice subsystems at picosecond time scales.

Spin transport

Apart from spin-flip scattering, where angular momentum can be transferred locally between the interacting lattice, magnons or electrons, there is also the possibility of non-local angular momentum transfer through the spin polarized current across metals which leads to various kinds of spin dynamics. [59, 145, 148, 160, 161, 165]. The spin transport can result in the demagnetization of metals [59]. Spin transport across the interfaces or the multilayers can also induce the transient magnetization enhancement in metals [148]. This does not require strong coupling with the lattice, but it depends on the electron velocities in the material. Optical excitation in metals leads to electron transport due to temperature gradient. Such electron transport can be categorized as ballistic, super-diffusive or diffusive electron transport depending on the material properties and also leads to thermalization of different subsystems at picosecond time scales. This electron transport can be spin polarized due to the different mobility of majority and minority carriers in magnetic materials. The different mobility comes from exchange splitting which leads to population difference of majority and minority carriers near the Fermi energy. This spin transport can also lead to demagnetization of magnetic materials at sub-picosecond time scales. Even though, there is spin transport, there may not be net charge current due to effective screening in metals.

Optically Induced Inter-Site Spin Transfer (OISTR)

Due to the difference in the population of electronic density of states of spin sub-bands (of the same character, up or down) of two atomic species at different lattice sites, there is local spin potential. In this scenario, electrons from spin sub-band of one atom can be transported locally to spin sub-band of another atom at another lattice site without spin flip. Net spin transfer character (up or down) will depend on the available number of unoccupied states at the receiving atom. For example, in case of optical excitation of Ni₅₀Fe₅₀ permalloy, electrons from minority spin band of Ni can be transferred to minority spin band of Fe [166]. During optical excitation of the antiferromagnetically coupled atoms, electrons from majority spin band of one atom can be transferred to minority spin band of another atom [167] (brown arrows in Fig. 6.6 c)). This electron transport is done via the coupling of electrons to the electric field generated by the femtosecond laser pulse. This process has been termed as optically induced inter-site spin transfer (OISTR) [135, 139, 168–170]. Since OISTR induced spin relaxation eliminates the need for coupling between the electron, lattice and spin subsystems (as the spin transport is directly mediated by the coherent ultrafast optical field), this can lead to the fastest possible mechanism for demagnetization. Further, such coherent-optical-field-dependent spin transfer is promising for all optical control of future data storage devices at ultrafast time scales. The OISTR effect is revisited to discuss the laser-induced dynamics in FeRh at the early timescales in the chapter 6.

2.1.2 Inverse spin Hall effect and THz emission

Inverse spin Hall effect and spin to charge current conversion

In analogy to the classical Hall effect, the spin Hall effect is the spin accumulation of opposite spins on opposite boundaries of the surface in an electric current carrying sample which does not need to be magnetic. It was first predicted in 1971 [171]. This spin-only-based phenomenon can be explained intrinsically by spin-orbit interaction in the material which leads to a spin-polarized deflection of the charge current [9]. The inverse spin Hall effect, as an inverse effect, leads to the generation of charge current in a sample carrying a spin current [171, 172]. In materials, with strong spin-orbit coupling such as heavy metals W or Pt, inverse spin Hall effect is particularly strong [173]. The inverse spin Hall effect in metals can be modified by alloying which modifies the spin-orbit interactions or spin-dependent scattering [174, 175]. The spin Hall effect and the inverse Hall effect have their technological importance in future spintronic device applications like spin-orbit-torque or spin-transfer-torque-based devices [176–178], magnetic tunnel junctions [179], domain wall dynamics [180] or for measuring spin fluctuations [181]. Though, they still have to overcome some limitations such as short diffusion lengths in non-magnetic materials [9]. It has been also shown that a ultrafast spin current generated in a ferromagnet via optical excitation can be converted to an ultrafast charge current at the interface of ferromagnetic/nonmagnetic metals [182].

THz emission from spintronic emitter

Broadband THz emission from optical rectification in spintronic emitters (Pt (2 nm)/Co₂₀Fe₆₀B₂₀ (1.8 nm)/W (2 nm)) has already been demonstrated in the visible range using femtosecond laser

pulses [182]. Laser-induced super-diffusive spin current in non-magnetic layers (W and Pt) is generated due to spin-polarized electron transport from ferromagnetic layer. Spin current is converted to transverse charge current near FM/NM interface due to the inverse spin hall effect in non-magnetic layers. This charge current gives rise to THz emission perpendicular to magnetization and charge current direction (normal to sample surface for in-plane charge current and magnetization). The high spin-Hall efficiency of Pt and W [173] gives rise to higher charge current and so higher THz emission. Spin Hall angles of W and Pt are opposite to each other. Optimization of the thickness of Pt, W and CoFeB layers leads to constructive interference of the THz emission emitted from both interfaces (W/CoFeB and Pt/CoFeB). The THz emission from the optical excitation is a coherent process so that the THz emission directly captures the properties of excitation pulse such as the bandwidth, pulse duration, pulse shape and pulse energy. The THz electric field increases with the excitation pulse intensity. It has been observed that the THz emission is independent of the wavelength over a broad range and is directly proportional to the absorbed energy density at FM/NM interface [183]. This THz emission process is revisited in the context of time-arrival monitor for FEL pulses in the chapter 4.

2.2 First order phase transition kinetics, nucleation and domain growth

A change in external environment such as the temperature, pressure, magnetic field can make the current order parameter of the material metastable or unstable. In this case, the material tends to undergo transformation to another preferred, thermodynamically-stable state via the minimum energy reaction pathway. It may also involve different intermediate metastable states. Such phase transitions, as discussed in chapter 1 have great technological importance. It has also been demonstrated [39, 40, 43] that some phase transitions can be induced using femtosecond optical pulses at considerably shorter time scales than with electronic or thermal excitations [184]. Few examples of such phase transitions include metal-to-insulator transitions [52, 185–188], optically induced superconductivity [53, 189–192] and AFM to FM phase transition in FeRh [85, 86]. Here, we discuss the kinetics of first order phase transitions, relevant to problem at hand i.e. phase transition in FeRh. First order phase transitions, such as the magneto-structural transition in FeRh, are characterized by a discontinuity in the order parameter and by its sudden onset at the phase boundary.

Nucleation:

Microscopically, phase transitions take place via the nucleation of domains (either spontaneous or at pinning sites) of new phase within the previous metastable or unstable state. The nucleation of domains, which can occur only after nucleation barrier energy is overcome by thermal fluctuations, leads to an effective decrease in the energy of the system, making the system thermodynamically stable.

Coarsening:

Transition proceeds via coarsening dynamics with the growth of already nucleated domains

into bigger domains. Already nucleated domains grow in size by movement of domain walls which leads to bigger domains. Here, new phase expands at the expense of old phase. During this time, the order parameter does not remain conserved.

Coalescence:

At some stage during the phase transition, the expansion of the new phase at the expense of the old phase is not energetically favourable. Though, it may still be energetically favourable that smaller domains merge to form the large domains of new phase. During this time, order parameter remains conserved as total volume of new phase remains constant.

In particular case of thermally-induced FeRh phase transition, it has been shown, using XMCD-PEEM (photo-emission electron microscopy) measurements [69, 72], that the transition proceeds via phase coexistence where the FM domains nucleate and grow within the AFM phase matrix. The growth of FM domains at later stage is by coalescence where small domains merge to form large FM domains. Detailed description of classical nucleation and growth model can be found in [78–81, 193–197] and references therein.

Scaling laws:

Different stages of the magnetic phase transition evolve at different growth rates and can be characterized by calculating the correlation function and the correlation length [194].

Even in the case of first order/abrupt phase transitions like in FeRh, it has been deduced theoretically (in analogy with continuous phase transition) that coarsening dynamics may follow certain scaling laws over time where the scaling length/correlation length has power law dependence with time. For Ising like systems, the power law exponents turn out to be $1/2$ or $1/3$, for a conserved or non-conserved order parameter respectively [194, 197]. This power law scaling is independent of the dimensions. If surface diffusion becomes dominant over bulk diffusion, due to geometrical constraints such as thickness, then power law exponent for conserved order parameter changes to $1/4$ [197]. In practice, this universality in scaling laws may not be true. The coarsening dynamics (and hence scaling laws) in crystals depend on anisotropy and mobility. Thus, the scaling dependence in phase transitions in crystals may not be universal [197, 198]. Another point to note is that the theoretical simulations concerning scaling law and coarsening dynamics have been performed for quasi-equilibrium conditions. Such laws, though assumed to be valid, may not be applicable to non-equilibrium photo-induced phase transitions in their entirety.

In chapter 7, the microscopic evolution of the FM domains and the correlations during optically induced FeRh phase transition measured with tr-SAXS will be discussed.

2.3 Density functional theory (DFT)

First principle ground state calculations can be used to calculate the electronic structure of the systems. Further, the electronic structure of system evaluated in different configurations (temperature, volume, magnetic state etc.), can be used to calculate the changes in measurable observables such as absorption, scattering, reflectivity, diffraction dielectric response, susceptibility etc. in optical or X-ray regime.

Density-Functional-Theory (DFT)-based first principle predictions of material properties and observables have revolutionized our fundamental understanding of many experiments and contributed in devising new experiments. A good illustration on density functional theory and exchange correlation functionals can be found in [199–207]. Here, the basic concepts of density functional theory and exchange-correlation functionals will be summarized.

Formulation of density functional theory goes back to Thomson-Fermi model which approximates the electron distribution/density and potential field using statistical considerations of electron motion in multi-dimensional phase space. Though, it was not until the derivation of two Hohenberg-Kohn (HK) theorems, which led to its use in computational settings.

The two Hohenberg-Kohn theorems are described as the following:

- The external electronic potential $v(r)$ is determined within a trivial additive constant by the electron density $\rho(r)$ of the ground state. Thus, using the electron density, a many-body extended phase space problem can be formulated as a 3-dimensional problem.
- The ground state electron density describes a minimum energy functional. In other words, one can find the ground state electron density by minimizing such energy functional.

Further, the HK formalism for interacting systems is reduced to a solvable non-interacting problem by the Kohn-Sham (KS) equations. The Kohn-Sham equations in canonical form can be written as:

$$\left[-\frac{1}{2}\nabla^2 + v_{eff} \right] \phi_i = \varepsilon_i \phi_i, \quad (2.1)$$

where

$$v_{eff} = v(r) + \frac{\partial J[\rho]}{\partial \rho(r)} + \frac{\partial E_{xc}[\rho]}{\partial \rho(r)} = v(r) + \int \frac{\rho(r')}{|r-r'|} dr' + v_{xc}(r) \quad (2.2)$$

is the local one-electron operator for the Kohn-Sham effective potential, $-\frac{1}{2}\nabla^2$ is the kinetic energy operator, $J[\rho]$ is the classical Coulomb repulsion, $E_{xc}[\rho]$ is the exchange-correlation energy and $\varepsilon_i \phi_i$ are eigenvalues and eigenstates. The exchange correlation energy contains the difference between kinetic energies of the interacting and the non-interacting systems, and also the non-classical component of the electron-electron interactions (i.e. leaving out coulomb repulsion). The electron density $\rho(r)$ can be written as:

$$\rho(r) = \sum_i^N \sum_s |\phi_i(r, s)|^2. \quad (2.3)$$

Total energy is obtained from energy functional:

$$E = \sum_i^N \varepsilon_i - \frac{1}{2} \int \frac{\rho(r)\rho(r')}{|r-r'|} dr dr' + E_{xc}[\rho] - \int v_{xc}(r)\rho(r)dr, \quad (2.4)$$

where eigenvalues ε_i are given as:

$$\sum_i^N \varepsilon_i = \sum_i^N \langle \phi_i | -\frac{1}{2}\nabla^2 + v_{eff} | \phi_i \rangle. \quad (2.5)$$

2.3.1 Exchange-correlation functionals

The exchange-correlation functionals try to find the best approximation to the exchange-correlation energy. All the approximations can be written, in general, as:

$$E_{xc}[\rho(r)] = \int \rho(r)\varepsilon_{xc}(r)dr, \quad (2.6)$$

where $\varepsilon_{xc}(r)$ is energy density. The different functionals have various ways of sampling this energy density around the electron. A particular exchange-correlation functional can more successfully describe some systems while failing to describe others. Thus, the choice of the functional depends on the type of systems to be studied. Here, two important exchange correlation approximations, namely local spin density approximation (LSDA) and generalized gradient approximation (GGA) [201, 207], will be described. These approximations have quite well described vast majority of systems and have been used to describe the systems studied in this thesis.

Local spin density approximation (LSDA)

LDA approximates the exchange-correlation energy at each point of the system by exchange-correlation energy of homogeneous electron gas corresponding to the local electron density. The exchange-correlation energy of homogeneous electron gas is known precisely:

$$E_{xc}^{LDA}[\rho(r)] = \int \rho(r)\varepsilon_{xc}^{hom}[\rho(r)]dr, \quad (2.7)$$

where $E_{xc}^{LDA}[\rho(r)]$ can be separated into the exchange energy $E_x[\rho(r)]$ given by Dirac and the correlation energy $E_c^{LDA}[\rho(r)]$ which is estimated from perturbation and interpolation between low and high electron density limits [199].

For spin polarized calculations, the correlation energy $E_c^{LDA}[\rho(r)]$ can be approximated further depending on the relative spin polarization.

Generalized gradient approximation (GGA)

To better estimate the exchange-correlation energy, as an extension to LDA, the Generalized Gradient Approximation (GGA) was developed by Hohenberg, Kohn and Perdew. It considers the series

expansion of higher order density gradients, which is terminated in real space using delta functions to maintain the validity of positivity and the sum-rule conditions of exchange-correlation. It can be written as an extension to LDA, in term of enhancement factor $F_{xc}[\rho(r), \nabla\rho(r)]$:

$$E_{xc}^{GGA}[\rho(r)] = \int \rho(r) \varepsilon_{xc}^{hom}[\rho(r)] F_{xc}[\rho(r), \nabla\rho(r)] dr. \quad (2.8)$$

$F_{xc}[\rho(r), \nabla\rho(r)]$ can be determined, non-empirically, by sophisticated quantum-mechanical calculations, as done by Perdew and Wang [199, 201–203].

2.3.2 Linearized augmented plane wave (LAPW) method & Elk code

To solve Kohn-Sham equations using variational principle, a proper choice of basis-sets has to be made. Considering the crystalline solids which can be represented as a periodic lattice, movement of free electrons can be described by linear combinations of plane-waves which are solutions of the Bloch equation. Since electrons near the Fermi-energy can be approximated as free electrons, Kohn-Sham calculations in the interstitial region (where electrons are loosely bound) can be solved by assuming combinations of a plane-wave basis. Now, for the bound electrons, we need to consider different basis sets as a plane-wave basis sets don't give good approximation. To define this bound region, either pseudo-potentials or all electron-full potentials can be used. In pseudo-potential-based methods, the real crystal potential is replaced by a smooth approximate potential which could be represented by combinations of plane-waves as well. Also core states are assumed to be fixed (frozen core approximation) as valence electron motion hardly effects the core states. The only complexity lies in finding correct set of plane wave-functions to construct the pseudo-potential [199].

For systems with extended/loosely bound core states (such as containing d or f bands or hybridization with d or f bands), this pseudo-potential type methods fail to give accurate descriptions. For such cases, one needs to refer to more sophisticated methods to describe the core states.

One of the ways to get to an accurate description is to use all-electron full-potential methods in combination with plane-waves. Linearized Augmented Plane Wave (LAPW) method [208–211] consists of a linear combination of plane waves in the interstitial region. Linear combinations of radial wavefunctions and their derivatives, obtained by solving Schrodinger equation or more generalized spin polarized Dirac equation, are chosen as the basis for core states/semi-core states inside muffin-tin radii (Fig. 2.1). Both plane wave and radial wavefunction basis sets and their gradients satisfy continuity and asymptotic conditions at the boundaries. These conditions require higher plain wave cut-offs compared to other methods, thus increasing the computational time but providing more accurate self-consistent solutions.

All the DFT-based simulations in this thesis have been performed with the Elk code. Elk is all electron full potential linearized augmented plane wave (FP-LAPW) code for performing first principle density functional theory-based spin-polarized electronic structure calculations. More detailed features of the Elk code can be found in [212].

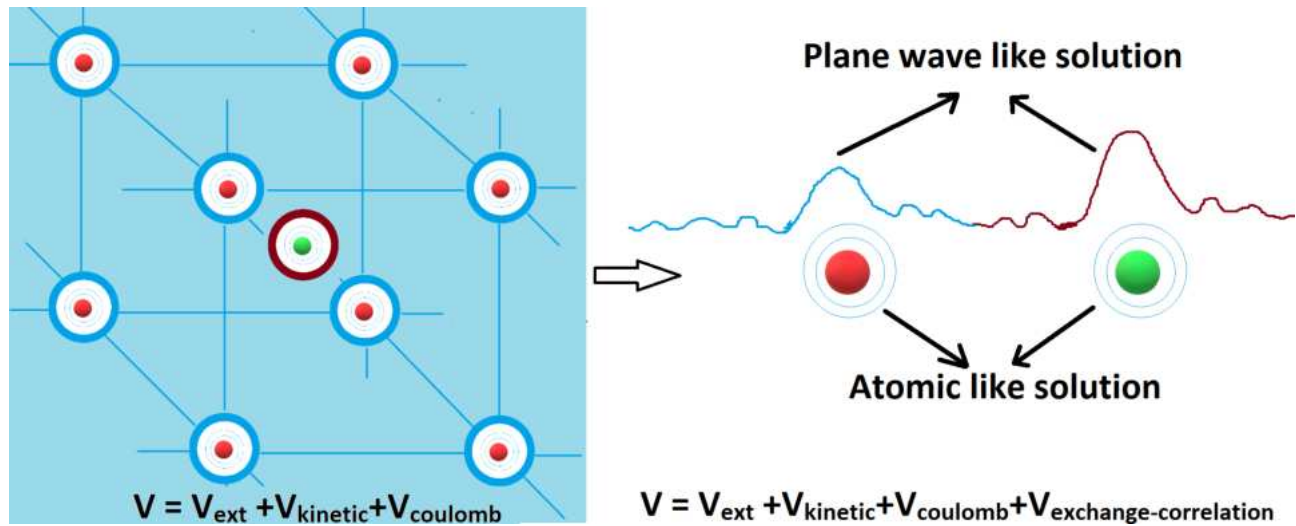


Figure 2.1: Illustration for LAPW method. Solution to complex structures can be divided in two parts in DFT calculations. Core (more localized) part of atom is solved as atom-like Dirac equation. Valence orbitals are expanded as plane waves.

2.4 X-ray absorption spectroscopy

X-ray absorption spectroscopy (XAS) has been developed as versatile element-specific probe of the local chemical environment, electronic and magnetic structure of atoms, molecules and condensed matter. X-ray absorption measurements can be performed in various different ways namely by measuring direct transmitted intensity, total electron yield (TEY), X-ray Fluorescence. The choice of the type of measurement depends on the X-ray energy, sample thickness and the need for the bulk or the surface sensitivity. In this thesis, all the X-ray absorption measurements have been performed in the transmission geometry owing to the need for the bulk sensitivity and the sample thickness closer to the X-ray penetration depth at the L edges of 3d transition metals. Here, I will describe how the transmission intensity measurements give the information about X-ray absorption. X-ray interaction with matter and its attenuation over sample thickness z , can be described by Beer-Lambert's law:

$$I_{\text{out}}(E, z) = I_{\text{in}} e^{-\mu(E)z}, \quad (2.9)$$

where I_{out} is transmitted intensity, I_{in} is incident intensity on sample and μ is attenuation coefficient comprising of all the absorption and scattering events. Though for soft X-ray energies, only absorption is the main contributing factor to the attenuation coefficient. The X-ray absorption process involves the excitation of a core level electron to an unoccupied valence state by absorption of a photon. There are different methods possible to simulate the X-ray absorption spectra such as semi-empirical multiplet methods and first principle methods. A comprehensive review of such methods can be found in [213]. Here the partial density of states-based method to calculate X-ray spectra will be described. The transition can be approximated using the one-electron approximation (electron under effective potential of other electrons/nuclei). Under Born-Oppenheimer approximation (nuclear motion can be neglected), the transition is assumed to be vertical. Further, we assume that major contribution to XAS is coming from the electric dipole (type) transitions (electric dipole approximation). Using the Wigner-Eckart theorem, the transition matrix element can be

decomposed as a product of the reduced matrix element and the Clebsch-Gordan (CG) coefficient. The reduced matrix element only depends on the geometry/physical nature of transition operator and transition states, and is independent of magnetic quantum numbers (m, m') and polarization (q) [214].

$$\langle \alpha l m | T_q^Q | \alpha' l' m' \rangle = \langle l' m' Q q | l m \rangle \frac{\langle \alpha l || T_q^Q || \alpha' l' \rangle}{\sqrt{2l+1}} \quad (2.10)$$

Here, T_q^Q is the spherical tensor of rank Q with components $q = -Q$ to $+Q$, describing the q -polarized electric multipole transition of 2^Q -pole nature from initial core state $|\alpha' l' m' \rangle$ (radial quantum number α' , orbital quantum number l' , magnetic quantum number m') to the final valence state $|\alpha l m \rangle$ (radial quantum number α , orbital quantum number l , magnetic quantum number m). The first term ($\langle l' m' Q q | l m \rangle$) is the Clebsch-Gordan (CG) coefficient while the second term is the reduced matrix element. Following the properties of CG coefficients and spin conservation, the selection rules for the electric dipole transitions can be written as:

$$\begin{aligned} \Delta S &= 0 \\ \Delta l &= 0, \pm 1 (0 \not\rightarrow 0) \\ \Delta m &= 0, \pm 1 \end{aligned} \quad (2.11)$$

Using Fermi-Golden rule for the transition probability and second quantization formalism, the absorption coefficient $\mu(E)$ can be written as follows in terms of the dipole transition matrix elements [215, 216]:

$$\mu(\omega) \propto \sum_{m, m', \sigma} |\langle \phi_{f_{lm\sigma}} | T_{qm\sigma} | \phi_{i_{l'm'\sigma}} \rangle|^2 \delta(E_f(l, m, \sigma) - E_i(l', m', \sigma) - \omega), \quad (2.12)$$

where $|\phi_{i_{l'm'\sigma}} \rangle$ and $|\phi_{f_{lm\sigma}} \rangle$ are initial core state and final valence state wavefunctions respectively.

Further, depending on the core-hole and valence electrons interaction/screening, there are different possible scenarios. Depending on different material systems, metals or insulators, the core hole can be fully or partially screened. The corresponding change, in final state wavefunctions, also affects the X-ray absorption spectra. In most of the 3d metallic systems, the core hole is strongly screened and thus we can consider the final state as composed of the ground state density of states [213]. Thus, absorption coefficient can be written as:

$$I_{XAS}(\omega) \propto \mu(\omega) \propto \sum_{m, m', \sigma} |\langle l m \sigma | T_{qm\sigma} | l' m' \sigma \rangle|^2 \rho(E_f(l, m, \sigma)) \delta(E_f(l, m, \sigma) - E_i(l', m', \sigma) - \omega), \quad (2.13)$$

where $\rho(E_f(l, m, \sigma))$ is the ground state unoccupied density of states of valence levels.

From equation 2.13, we can see that X-ray absorption, from core level to valence level,

depends on excitation energies and unoccupied density of states. The excitation energies for core to valence excitation of electron are element-specific. Unoccupied density of states near Fermi energy are specific to local chemical environment of the element. Thus, X-ray absorption spectroscopy captures the element-specific local electronic structure. The simulated X-ray spectra is convoluted with a Voigt broadening function (consisting of Gaussian broadening for the instrument and Lorentzian broadening for the core-hole lifetime of the transition) to simulate the experimental spectra [217, 218].

2.5 X-ray absorption spectral calculations including exchange splitting in core levels

In the last section, in the equations for the absorption coefficient, we assume that the core state and valence state wavefunctions are orthogonal (independent) eigenfunctions representing the states. For spin polarized materials systems, there exists exchange interaction in core level because of effective spin polarized potential of valence levels. Thus, spin-orbit split core levels are further split due to exchange splitting. For example, 2p core levels ($2p_{3/2}$ and $2p_{1/2}$) are further split into 6 energy levels [219], value of which depends on strength of exchange field. Because of exchange splitting and spin orbit splitting, quantum numbers J, l, m are not good quantum numbers (they don't commute) and so we need to find the new eigenfunctions to represent the new core levels [220, 221]. Here, the splitting due to the exchange coupling is very similar to the Zeeman splitting except that it is because of internal spin-polarized field of atoms compared to external magnetic field in the case of Zeeman splitting. Exchange splitting increases with increase in local magnetic moment of the atom [221]

Hamiltonian for the exchange and spin orbit interaction can be written as:

$$H = H_{s-o} + H_{ex} = \frac{\tau}{2} L \cdot S + E_s m_s. \quad (2.14)$$

$L.S$ term is written in (j,m) basis(eigen-basis for only spin-orbit split levels) as:

$$L.S = \langle J^2 \rangle - \langle L^2 \rangle - \langle S^2 \rangle = j(j+1) - l(l+1) - s(s+1), \quad (2.15)$$

which can be converted to (l,m) basis (eigen basis for uncoupled states) by multiplying with Clebsch-Gordan coefficients. Thus, the new eigen-basis for coupling core states ($|l, s, ml_1, ms_1 \rangle$ and $|l, s, ml_2, ms_2 \rangle$) can be found by finding the eigenvectors of matrix described by matrix element as follows:

$$H_{l,s,ml_1,ml_2,ms_1,ms_2,\tau,E_s} = \sum_{j=|l-s|,m_j=-j}^{j=|l+s|,m_j=j} \left(E_s \times ms_1 + \frac{\tau}{2} \times (j(j+1) - l(l+1) - s(s+1)) \right) \times cg1 \times cg2, \quad (2.16)$$

where $cg1 = \langle l, ml_1, s, ms_1 | j, m_j \rangle$, $cg2 = \langle l, ml_2, s, ms_2 | j, m_j \rangle$ are Clebsch-Gordan coefficients.

Thus, the X-ray absorption intensity (up to a multiplicative constant and without edge jump normalization) for electric dipole transition from l_i (with coupled core level $|c \rangle$) to l_f (with projected valence levels $|m_{l_f}, m_s \rangle$), using q-polarized radiation, can be written as:

$$\mu(q, c, \omega) \propto \sum_{m_{l_f}, m_s, m_{l_i}} |(-1)^{l_f - \max(l_i, l_f)} \sqrt{\frac{\max(l_i, l_f)}{2l_f + 1}} * (l_f - l_i) V_{l_i, m_{l_i}, m_s, c} \langle l_i, m_{l_i}, 1, q | l_f, m_{l_f} \rangle|^2, \quad (2.17)$$

$$\delta(E_f(l_f, m_{l_f}, m_s) - \lambda_c - \omega) \rho(E_f(l_f, m_{l_f}, m_s))$$

where $|c \rangle$ is the coupled core level, (m_{l_i}, m_s) is uncoupled core levels, λ_c are eigenvalues(energies) for coupled core levels and $V_{l_i, m_{l_i}, m_s, c}$ is the vector element of eigenvector representing the coupled

core level $|c\rangle$. In section 2.7, this formalism will be used to calculate the XAS spectra and spectral changes during FeRh phase transition.

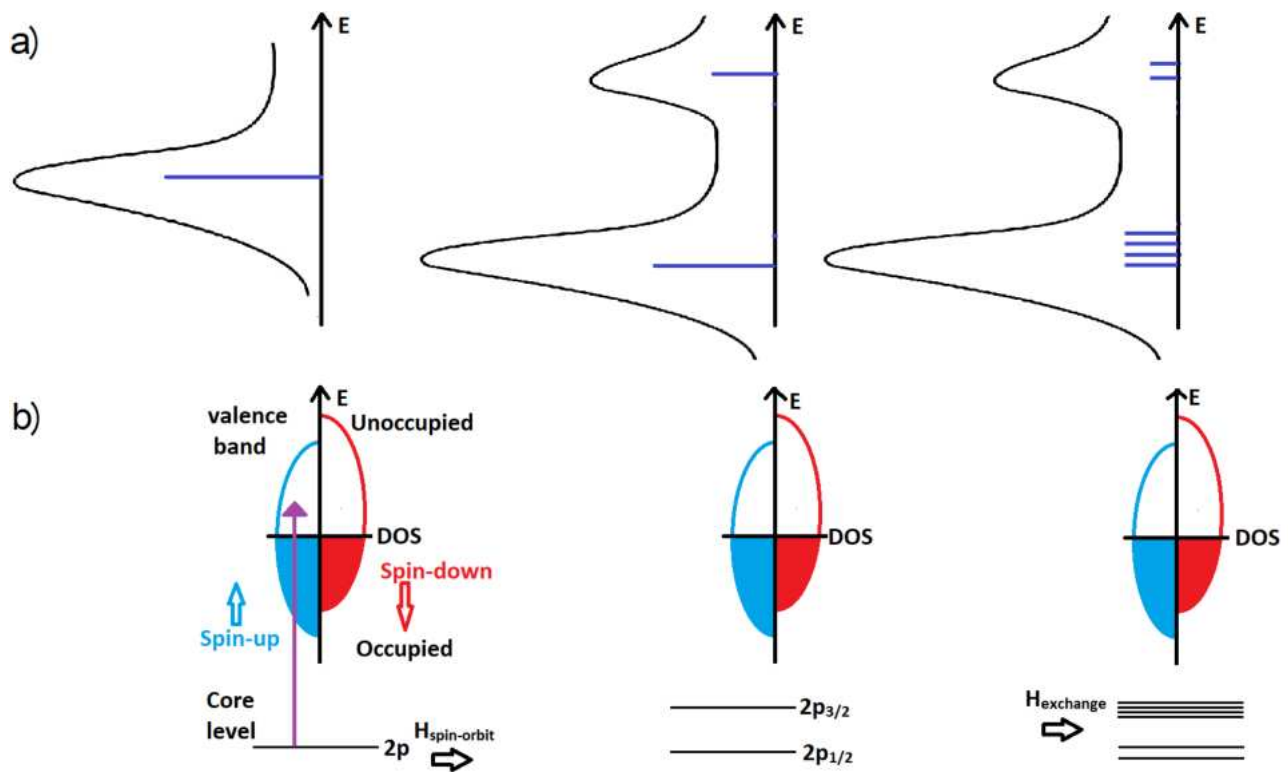


Figure 2.2: Illustration of the effect of spin-orbit and exchange splitting on XAS spectra. The large spin-orbit splitting (bottom-middle) clearly splits the XAS spectra (top-left) into two distinguishable peaks (top-middle). The exchange splitting in the core level (bottom-right) does not show visible effects directly in XAS spectra directly (top-right). It broadens the spectra a little bit but the effects are not directly visible due to the already large lifetime line-width broadening.

2.6 Electronic structure of FeRh

2.6.1 Diatomic molecule picture of antiferromagnetism

Following the simple model from Kübler [222], the appearance of antiferromagnetism in metallic system can be represented as the ionic bonding in a diatomic molecule. Here, the antiferromagnetic exchange interaction can be compared to ionic bonding. The ionic bonding favours a positive charge on one atom while a negative charge on another. This preferential distribution of charge minimizes the energy of bonding orbitals making the ionic bonding/diatomic state favourable while making the whole molecule still neutral. Reverse preferential distribution (opposite of bonding orbitals) takes place for anti-bonding orbitals. In same way, AFM type exchange interaction favours the accumulation of opposite spin polarization on different lattice sites and this also redistributes the spectral weights, as shown in Fig. 2.3(b). Nearly half-filled 3d bands (around 6 3d electrons in Fe) are important for the stability of the AFM state in metals. Half-filled 3d shell ensures that antibonding orbitals remain unoccupied or minimally occupied which maximizes the energy gain from the AFM state. In the AFM state, the two lattice sites, having different spin polarization, are in-equivalent. This can also be seen from the spin-resolved density of states of the exchange-split 3d bands of Fe as shown in Fig. 2.4 a). In FM state, the FM type exchange interaction does not favour any preferential spin accumulation on different lattice sites and thus making both lattice sites equivalent, as shown in Fig. 2.3(c).

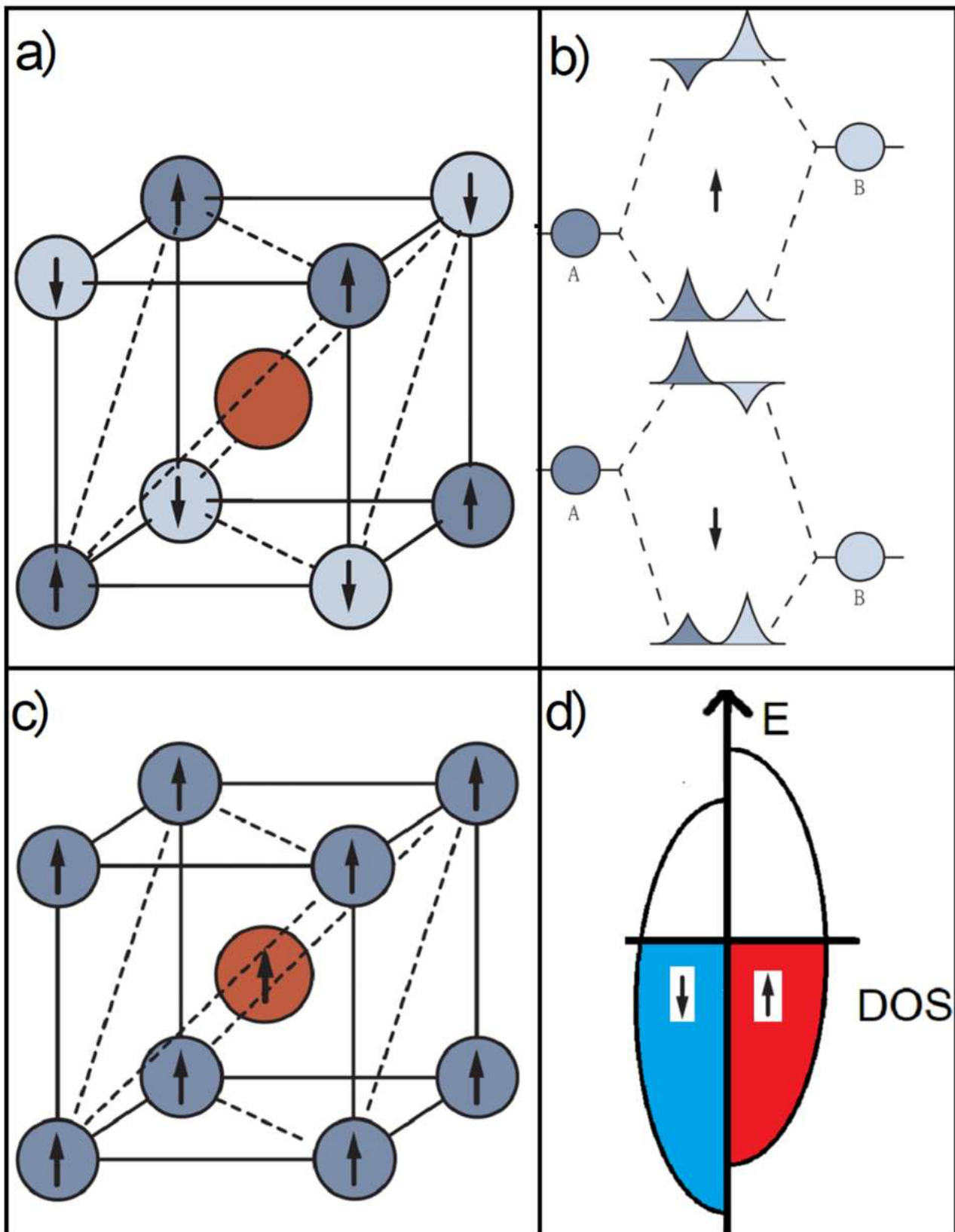


Figure 2.3: Illustration of AFM and FM state in FeRh. a) AFM-II type structure of FeRh with two in-equivalent Fe sublattices. b) Illustration of AFM state (spin up and spin down bands) using covalent bonding picture of neutral diatomic molecule (adapted from [222]). A and B represent two Fe sublattices. Lower symmetric sites are bonding orbitals while upper anti-symmetric sites are anti-bonding orbitals. c) FM structure of FeRh. d) Band structure picture of exchange splitting in FM state where both Fe sub-lattices are equivalent.

2.6.2 Hybridization between Fe and Rh

As done in previous studies [73, 101, 223–226], the atomic-site- and d-band-resolved electronic band structure for FeRh can be calculated in AFM and FM states. As can be seen from Fig. 2.4 as well as previous studies [101, 227], the density of states of Fe and Rh have quite similar features across entire energy range. This suggests a strong overlap between orbitals of Fe and Rh. Strong hybridization between Fe and Rh and implicit FM exchange interaction between Fe and Rh has been suggested to play an important role in the phase transition of FeRh. For instance, it has been predicted, theoretically, that there is anisotropic spin-polarization on Rh atoms within the atomic volume (zero net magnetic moment on Rh) even in case of AFM state [101].

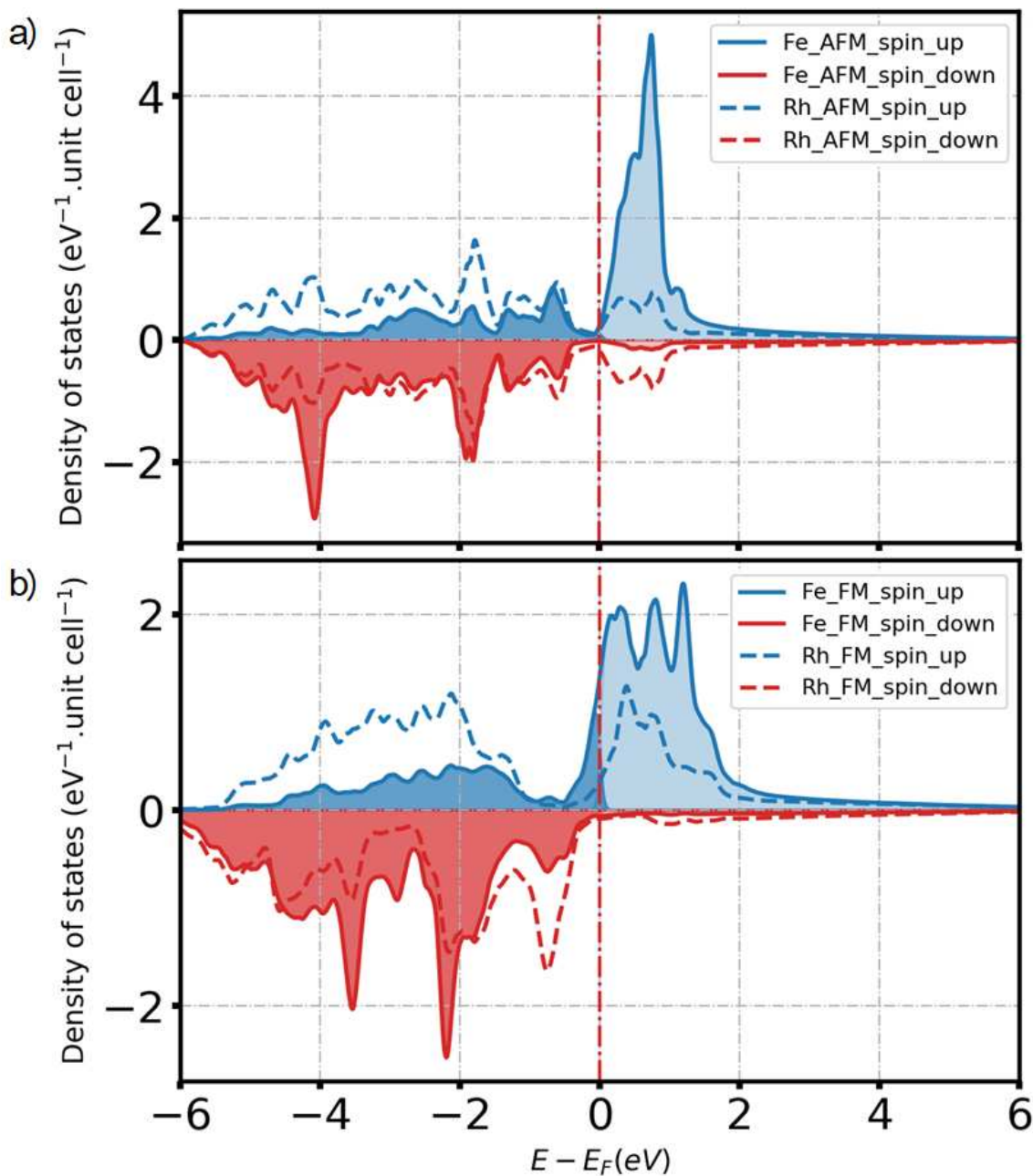


Figure 2.4: Hybridization of Fe and Rh in AFM and FM states of FeRh. a) Partial spin-resolved density of states in d band at Fe and Rh sites, for AFM state of FeRh. b) Partial spin-resolved density of states in d band at Fe and Rh sites, for FM state of FeRh. PDOS for Fe and Rh show quite similar peak positions indicating strong hybridization.

2.7 X-ray absorption spectral changes during FeRh phase transition

Fig. 2.5 shows the spin-resolved partial density of $3d$ states in the AFM (solid curve) and the FM (dashed curve) state of FeRh at room temperature calculated using the Elk code. Input file used for simulations is shown in Appendix A.5 and details about Elk code can be found in the documentation [212]. The key differences can be observed between the density of states of AFM and FM structure:

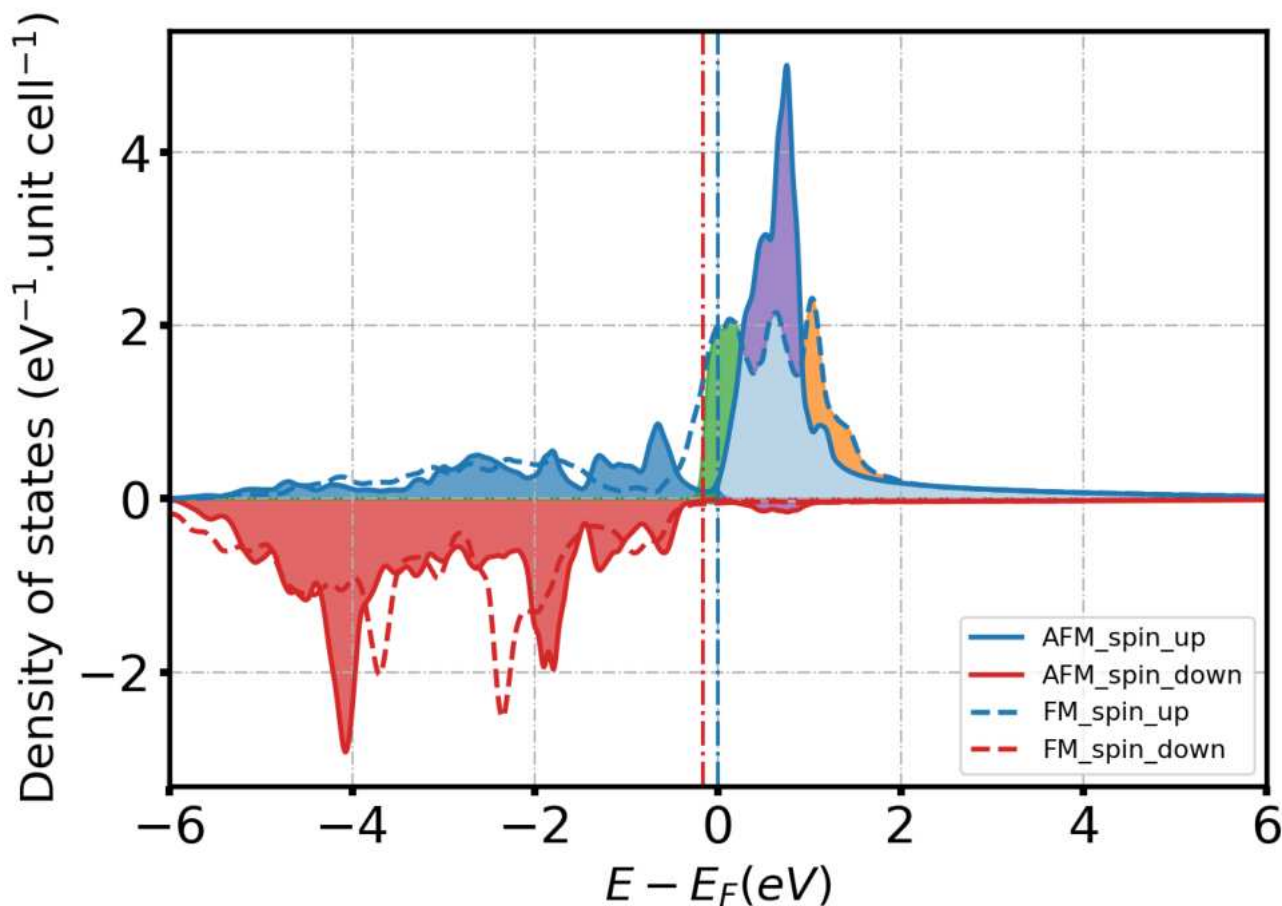


Figure 2.5: Partial density of states in FeRh. Spin-resolved PDOS for AFM and FM structure of FeRh around Fermi-energy (0 eV). Different shaded regions (green, purple, orange) in unoccupied PDOS (above 0 eV) represent the changes between AFM and FM PDOS, which can be probed by XAS. Vertical lines represent Fermi energy for AFM (blue) and FM (red) states

- In the AFM state, there are two distinguishable Fe sublattices based on spin quantization axis (+z or -z) while in FM state, there is only one type of Fe lattice.
- There is an increase in density of states near the Fermi energy for the FM state while the AFM state has fewer states near the Fermi energy.
- The antiferromagnetic band structure is narrower compared to the FM structure. The band narrowing is expected from the different exchange interactions. The band narrowing of exchange-split d-bands (ferromagnets or antiferromagnets) can be understood in terms of spin wave perturbation of a travelling electron due to the exchange interaction [228, 229].

Further, the narrower band in the antiferromagnetic state compared to the ferromagnetic state can be understood in terms of the weaker coupling between the two lattices of opposite spin polarization [207]. A change in exchange interaction leads to a spin- and energy-dependent shift of spectral weights clearly visible in the density of states.

Since the phase transition in FeRh involves a temperature change (either static heating or optical excitation), a volume expansion (0.5-1.5% depending on the substrate and thickness) and a change in magnetic ordering, we explore, in the following, the possibility to distinguish such changes in the electronic structure using X-ray absorption spectroscopy (XAS).

These different changes can be simulated separately to identify their quantitative contributions to the absorption:

- The thermal contribution is simulated by assuming changes in the Fermi-Dirac distribution and a chemical potential shift while ensuring electron conservation. The lattice constant and the magnetic phase remain unchanged.
- The structural contribution is simulated by calculating the density of states for different lattice constants and then calculating the spectral changes. The magnetic phase and the temperature remain unchanged.
- The magnetic contribution is simulated by calculating the density of states for AFM, FM and NM (nonmagnetic) phase and then calculating the spectral changes. The lattice constant and the temperature are kept unchanged.

The equation 2.17 can be used to calculate the absorption spectral changes. The spectral changes correspond to changes in the unoccupied partial density of states in 3d band of Fe because of the thermal, structural and/or magnetic contributions.

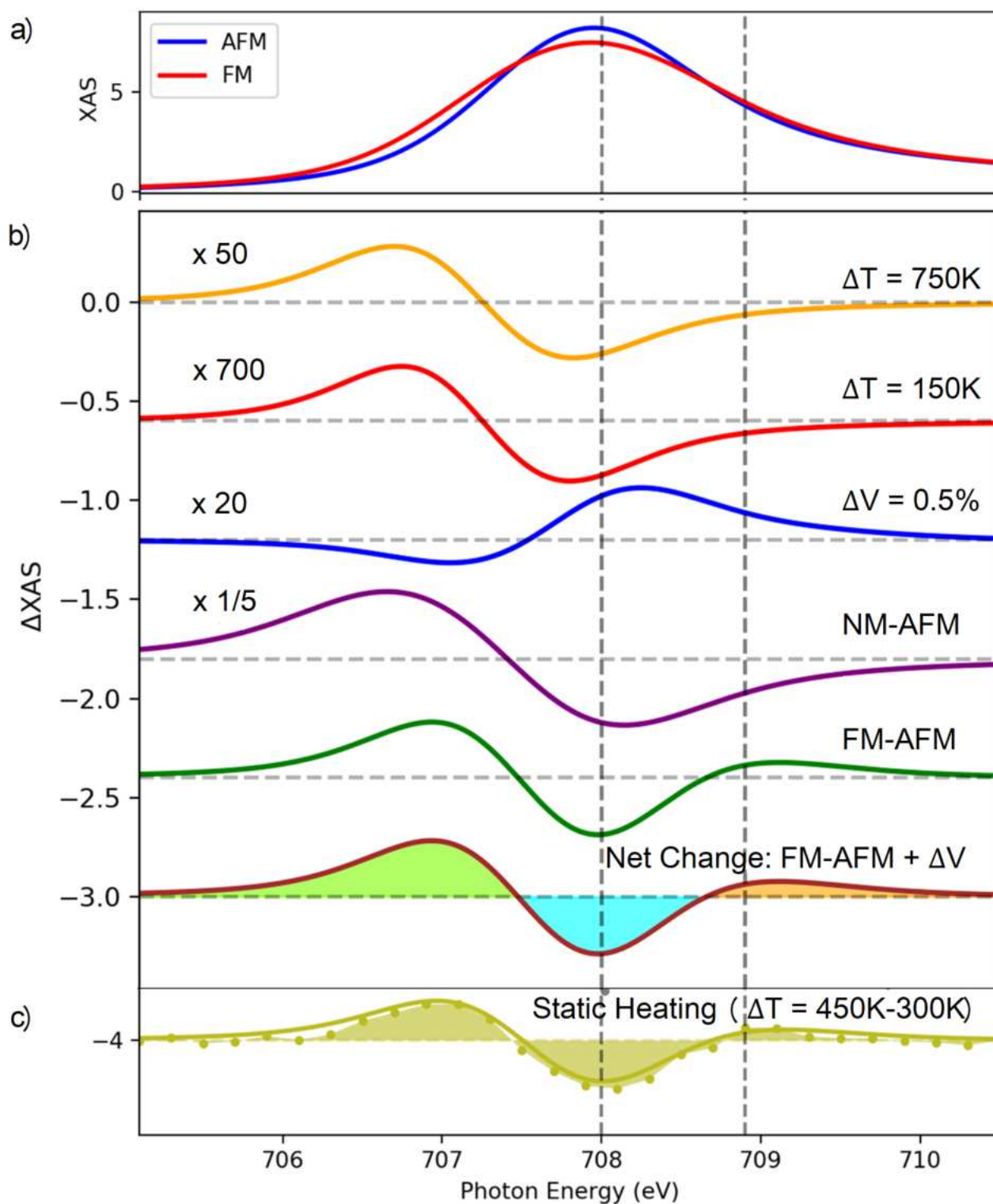


Figure 2.6: Simulated XAS spectra and spectral changes for AFM and FM state FeRh. a) The simulated XAS spectra at Fe L_3 edge for AFM and FM states of FeRh. b) The XAS spectral changes for FeRh phase transition due to temperature, volume and magnetic state (AFM, FM and NM (non-magnetic) changes). c) Comparison with experimental measurements for FeRh phase transition due to static heating (450 K) [68] (static heating data from courtesy of Christian Stamm).

Fig. 2.6 shows the simulated XAS changes (for 2p to 3d dipole transitions) of the FeRh band structure due to the different contributions. The spectra is convoluted with a Voigt lineshape broadening which accounts for the instrument Gaussian broadening of 0.3 eV (FWHM) and the lifetime Lorentzian broadening of 0.5 eV (FWHM) to simulate the experimental lineshape. A 2p core level exchange splitting of 0.3 eV and a core level spin-orbit splitting of 13 eV are taken into account to simulate the lineshape of spectral change. The simulated spectral change (Δ XAS) between the initial AFM state and the final FM state, in the phase transition in FeRh, is compared with the spectral change due to static-heating-induced phase transition in FeRh. Total spectral change and magnetic (FM-AFM) contribution to spectral change are normalized with respect to the spectral change in experimental data. Other contributions to the spectral changes are scaled accordingly.

- Δ XAS shows significant modifications at pre-edge and at the edge of the Fe L_3 edge while there is a small change visible at the post edge shoulder of the spectra.
- The spectral changes due to thermal (warm thermalized electrons) and lattice contributions have a dispersive (derivative-like) shape. The spectral modifications from the transition from AFM to non-magnetic state (NM) also have a derivative-like shape.
- In contrast, the spectral changes corresponding to a transition from AFM to FM state has a very different shape (green curve in Fig. 2.6) with prominent positive broad shoulder at the post edge (around 0.9 eV after resonance).
- Most significantly, the magnetic contributions (FM-AFM or NM-AFM) reflect the largest modifications and are at least an order of magnitude larger than thermal and lattice contributions.

The change in magnetic ordering and exchange interactions is imprinted as a strong electronic structure change as seen in Fig. 2.6 b). Thus, X-ray absorption spectroscopy can be used to probe the evolution of the magnetic phase transition in FeRh and to map the electronic band structure changes (without any XMCD contrast) which provide true time scales of exchange interactions. Further, the distinct positive feature at post edge can, uniquely, be used to follow the formation and evolution of FM band structure during the phase transition. As a benchmark, simulated spectral changes were compared with experimental spectral changes observed in equilibrium phase transition of FeRh due to static heating (Data obtained as courtesy of Christian Stamm. For experimental details of thermally-induced phase transition data, see [68]). As can be seen, the spectral shape calculated from simulations matches very nicely with the experimental observation. We will further compare the simulations with our non-equilibrium laser induced FeRh phase transition in chapter 6.

2.8 Resonant small angle X-ray scattering (SAXS)

Small angle X-ray scattering in forward transmission geometry is a microscopic probe of the structure with electronic, magnetic (spin) and lattice (phonon) degrees of freedom. The X-rays are predominantly scattered elastically from electrons giving rise to large charge/electronic signal while scattering due to spins contribute a very small portion (factor of $\frac{E_{X-ray}}{m_e c^2}$ less for non-resonant spin scattering). At X-ray resonances of probed structure, however, the magnetic contribution can be significantly enhanced and can become equal to the charge scattering signal. In ferromagnets, magnetic signal in SAXS is normally achieved by performing XMCD contrast type measurements: Here, either the helicity of circularly polarized X-rays or an external magnetic field is reversed and the difference signal gives the magnetic component of scattering. Note that this type of magnetic scattering contribution is formed by charge-magnetic interference which enhances the magnetic signal and is proportional to magnetization/spin and charge/electron density. Scattering with linearly polarized X-rays, on the other hand, contains magnetic contribution which is weaker and is quadratic in magnetization density. In this section, I will briefly discuss the resonant-SAXS and the magnetic contribution to scattering signal from samples probed by linearly polarized X-rays as seen in the experiments described in chapter 7.

The X-ray scattering signal is recorded with a 2D-array detector. The spatial resolution and signal-to-noise ratio (SNR) depends on X-ray wavelength, largest wavevector transfer or solid angle spanned by the detector and the detector pixel size. The wavevector transfer q ($=k_2 - k_1$, k is X-ray wavevector) is given by:

$$q = \frac{4\pi}{\lambda} \sin \frac{\theta}{2}, \quad (2.18)$$

where λ is the X-ray wavelength and θ is the angle between the incident and the scattered X-rays. In the hard-X-ray region, owing to the smaller wavelengths, the scattering provides atomic resolutions ($\sim \text{\AA}$) whereas soft X-ray scattering probes electronic structure and processes showing variations at nanometer length scales.

Elastic X-ray Scattering can be composed of resonant and non-resonant parts. Resonant elastic X-ray scattering can be thought as a second-order process (absorption of primary photon and simultaneous emission of secondary photon) and its amplitude can be calculated from quantum mechanics using Fermi-Golden rule and second order perturbation theory. Derivation for scattering amplitude calculations can be found in [230–233]. The scattering amplitude is directly proportional to the Fourier transformed electron and spin density. This means that the scattering contrast with a particular wavevector change (q), from an ensemble of atoms or structures, is obtained due to a contrast/difference between their physical properties (such as spin/electron density, magnetization, orientation) at a particular length scale (correlation length). On the other hand, a perfectly homogeneous sample will not scatter as the Fourier transform of a uniform density is the delta function at $q = 0$.

Following [233], the scattering length of elastic X-ray scattering signal up to first order in

dipole approximation (and neglecting non-resonant spin scattering) is given as:

$$f = -(\hat{\epsilon}' \cdot \hat{\epsilon}) r_e (F'_c + iF''_c) - \frac{3}{4\pi k} i(\hat{\epsilon}' \times \hat{\epsilon}) \cdot F_m [F_{-1}^1 - F_{+1}^1] \quad (2.19)$$

where first term is the total charge scattering and the second term is the dichroism like resonant magnetic term. $\hat{\epsilon}, \hat{\epsilon}'$ are the polarizations of incident and scattered waves. $k = \frac{2\pi}{\lambda}$ is the magnitude of the wavevector of X-ray (in elastic scattering, the magnitude remains the same for the incident and scattered X-rays and only the direction changes). F_m is the magnetic form factor. F'_c and F''_c are the real and imaginary parts of the charge scattering amplitude respectively, which can also be written as:

$$F'_c + iF''_c = F_c + \frac{3}{4\pi k} [F_{-1}^1 + F_{+1}^1] \quad (2.20)$$

where F_c is the non-resonant charge scattering part and F_{-1}^1 and F_{+1}^1 are the energy-dependent dipole transition strengths for resonant charge scattering. At the X-ray absorption edge (resonance), the contribution from non-resonant part F_c is negligible.

From the above equations, we can note that charge and magnetic form factors are out-of-phase (due to i) and have different polarization dependence (dot vs cross products). Thus, for horizontally linearly polarized X-ray (say along X direction), there is no interference between the charge and magnetic terms in small angle X-ray scattering (SAXS). Thus, the scattering signal can then be written as:

$$I_{SAXS} = (|f_{1c}|^2 + |f_{2c}|^2) \times S_c(q) + (|f_{1m}|^2 + |f_{2m}|^2) \times S_m(q), \quad (2.21)$$

where $f_{1c}, f_{2c} (f_{1m}, f_{2m})$ are the real and imaginary parts of energy-dependent charge(magnetic) atomic scattering lengths. $S_c(q)$ and $S_m(q)$ are the structure factors corresponding to the charge/electronic structure and the magnetic structure respectively. Here it has been assumed that only one type of atom contributes because of element specificity at the resonance.

Further, the polarization dependence of the magnetic scattering term $\hat{\epsilon}' \times \hat{\epsilon}$ can be represented as a 2×2 matrix, as shown in [233], by projecting the azimuthal scattering plane to the horizontal (π) and vertical (σ) scattering planes :

$$\hat{\epsilon}' \times \hat{\epsilon} : \begin{pmatrix} \hat{\epsilon}'_{\perp} \times \hat{\epsilon}_{\perp} & \hat{\epsilon}'_{\perp} \times \hat{\epsilon}_{\parallel} \\ \hat{\epsilon}'_{\parallel} \times \hat{\epsilon}_{\perp} & \hat{\epsilon}'_{\parallel} \times \hat{\epsilon}_{\parallel} \end{pmatrix} = \begin{pmatrix} 0 & \hat{k}_1 \\ -\hat{k}_2 & \hat{k}_2 \times \hat{k}_1 \end{pmatrix} \quad (2.22)$$

From Equation 2.22, we can see that, for small angle forward scattering ($\frac{|\vec{k}_2 - \vec{k}_1|}{k} \ll 1$), the leading term points in the direction of \hat{q} . Thus,

$$|(\hat{\epsilon}' \times \hat{\epsilon}) \cdot F_m|^2 \propto |F_{m_z}|^2 \quad (2.23)$$

Here, F_{m_z} is the form factor along beam direction (z). Thus, for small angles (SAXS) and for

linearly polarized X-rays as the probe, the main contribution to the magnetic scattering comes from magnetic moments projected along X-ray beam propagation. Scattering intensity is quadratic to the projected magnetic moments. One advantage of magnetic scattering measurements without magnetic field is that it can provide inherent time scales of the microscopic dynamics. XMCD-type measurements for the charge-magnetic interference type magnetic SAXS, with circularly polarized X-rays as the probe, need sample to be aligned in external magnetic field for the stronger XMCD signals. The external magnetic field for the alignment of domains adds another time scale to the SAXS measurements and may obscure the inherent time scales of the dynamics. Without external magnetic field, XMCD type contrast measurements give the weak magnetic scattering signal originating from the pinning centers (physical defects or grain boundaries). Ferromagnetic domains nucleating on these pinning centers still have constant phase relation between the charge and the magnetic scattering and give the finite average signal in the charge-magnetic interference. Ferromagnetic domains which are unpinned give zero average signal in XMCD in the absence of external magnetic field due to the random phase distribution. Thus, XMCD type scattering measurements without any external magnetic field might be interesting if one wants to learn about the inherent time scales of the dynamics at the pinning centers. In next section, we categorize the relative contributions to the scattering changes observed during the phase transition in FeRh.

2.9 Small angle X-ray scattering changes during FeRh phase transition

Time-resolved scattering contrast simulation of phase transitions is a more complicated problem because the structure factors ($S(q)$) and form factors ($f(E, Z)$) have strong scattering vector (q) and energy (E) dependence and are material/crystal structure specific. Even then, the simplified description of scattering dynamics of phase transitions can be obtained based on certain models and scaling behaviours (such as the Ising model) [78, 193, 234]. Numerical calculations to simulate the dynamics can be performed using quantum Monte Carlo methods [78, 193–195, 235]. Such model calculations are supposed to be valid for a large range of phenomena because of the assumed universality of the phase transitions. Here, I defer from such calculations but rather discuss a simplified description of resonant scattering changes related to the experimental results in chapter 7. As discussed in section 2.7, there are discrete features (such as post edge magnetic feature in Fig. 2.6) in the electronic band structure and X-ray absorption spectra of initial AFM state and final FM state of FeRh. These features in X-ray absorption spectra can be used to trace out the evolution of local electronic band structure during the phase transition of FeRh as shown in the chapter 6. Apart from the evolution of the local electronic band structure during the photo-induced phase transition, there is also the spatio-temporal dynamics of the nucleation and growth of the ferromagnetic domains during the phase transition in FeRh. Studying such spatio-temporal dynamics is useful to trace the connection between local changes in the electronic band structure and the macroscopic evolution of FM order parameter. The magnetic-SAXS measurements provide a way to measure the spatio-temporal dynamics by studying the spin-spin correlations in a wide range of length and time scales.

To discuss the contributions to transient scattering signal, we introduce the equivalent defini-

tion of scattering intensity in real space. There is an equivalence between the Fourier transformed scattering intensity and the equal time correlation function [236–238]. Using this equivalence, we can write the scattering intensity for the SAXS measurements with linearly polarized X-rays as the probe (no interference between the charge and the magnetic scattering), as follows:

$$I_{SAXS}(\vec{q}) \propto \int \left[(C_c(\vec{r}) + C_m(\vec{r})) \right] e^{i\vec{q} \cdot \vec{r}} d^3 \vec{r}, \quad (2.24)$$

where $C_c(\vec{r})$ and $C_m(\vec{r})$ are correlation functions for the charge/electron ($\rho_c(\vec{r})$) and the spin density ($\rho_m(\vec{r})$), respectively. Thus, scattering intensity can be further expanded in terms of real space charge and magnetic densities:

$$I_{SAXS}(\vec{q}) \propto \iint \left[\rho_c(\vec{R}) \rho_c(\vec{r} + \vec{R}) + \rho_m(\vec{R}) \rho_m(\vec{r} + \vec{R}) \right] d^3 \vec{R} e^{i\vec{q} \cdot \vec{r}} d^3 \vec{r}. \quad (2.25)$$

For the particular case of the SAXS measurements with the linearly polarized X-rays (no charge and magnetic interference) to probe the photo-induced phase transition in FeRh, the contributions to the transient scattering signal can be categorized in the four cases. These are illustrated in the Fig. 2.7:

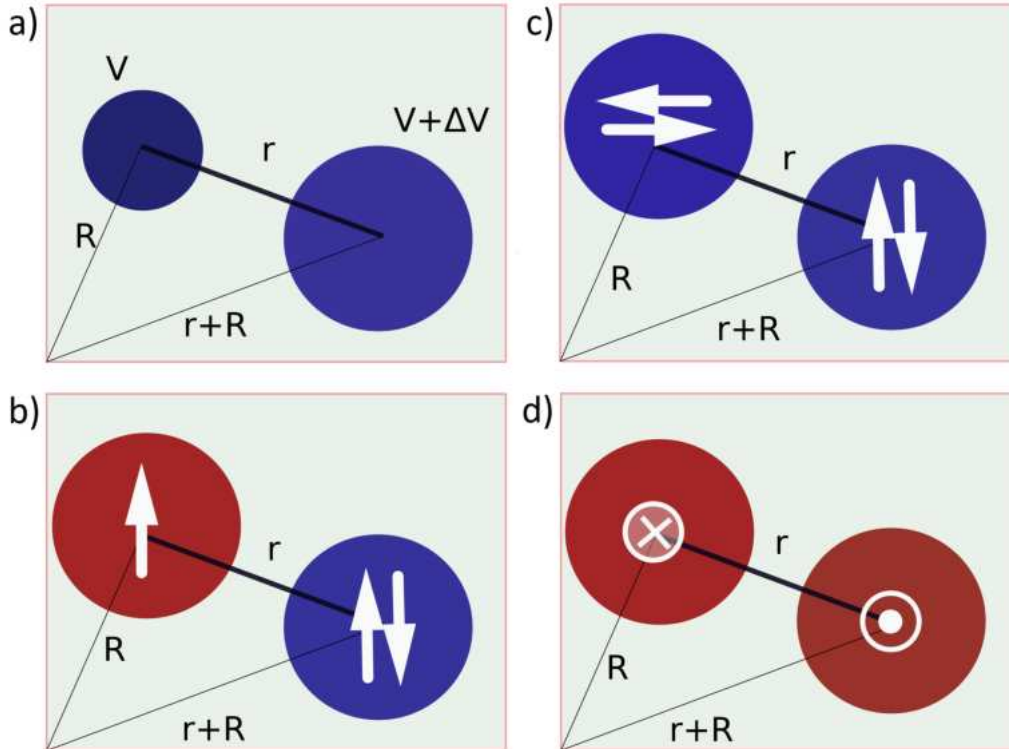


Figure 2.7: Various types of contributions to the the transient scattering signal during FeRh phase transition. a) Charge scattering contrast from density difference due to volume expansion. b) Magnetic scattering contrast due to absorption difference (electronic band structure modification) between AFM and FM domains. c). Magnetic scattering contrast due to orientation-difference in projected (in-plane) magnetic moments of AFM domains (analogous to XMLD in XAS). d) Magnetic scattering contrast due to orientation-difference in the projected (out-of-plane in the x-ray beam direction) magnetic moments of FM domains (analogous to XMCD in XAS).

Charge scattering contrast due to volume expansion:

Increase in the lattice parameter during the structural transition in FeRh leads to the decrease in the atomic density. Since the structural transition is a heterogeneous process, there is a scattering contrast between high density domains (which have not gone through structural transition) and low density domains (which have gone through the structural transition). Such scattering contrast contributes as a charge scattering and is independent of the spins (2.7 a). 0.5% volume expansion in FeRh phase transition gives the charge density change of 0.5%.

Magnetic scattering contrast from absorption difference between AFM and FM type domains:

As we have seen in section 2.7, electronic band structure is modified due to AFM and FM type exchange interactions in initial (AFM) and final (FM) states in FeRh, respectively. There is an absorption difference of up to ~5% at the Fe L_3 edge in XAS spectra measured at initial and final state of FeRh (cf. Fig. 2.6, Fig. 6.5, Fig. 6.3). This absorption and scattering originates from the different spin-polarized densities in the AFM and FM electronic band structures. The real part of the resonant scattering form factor (F') is related to imaginary form factor (F'' , related to the absorption) using the Kramer-Kronig relation:

$$F'(E) = F'(\infty) - \frac{2}{\pi} P \int_0^{\infty} \frac{E' F''(E')}{E^2 - E'^2} dE'. \quad (2.26)$$

Thus, absorption contrast also gives the scattering contrast between AFM domains (which have not gone through transition) and FM domains (which have gone through transition) at different length scales (2.7 b)). The absorption contrast of ~5% amounts to the ~5% change in spin-polarized electronic density.

Magnetic scattering contrast from relative orientation of AFM domains:

Relative orientation of magnetic moments of two AFM domains also contributes to a scattering signal. This is analogous to the X-ray magnetic linear dichroism (XMLD) signal which can be measured in XAS spectroscopy (2.7 c)). XMLD signal is around 1% of XAS signal and thus also of spin density [32].

Magnetic scattering contrast from relative orientation of FM domains:

Relative orientation of magnetic moments of two FM domains contributes to scattering signal analogous to the X-ray magnetic linear dichroism (XMCD) signal in XAS (2.7 d)). XMCD signal constitutes around 30% of the XAS spectra or spin density [68]. This shows that relative orientation of FM domains gives the largest spin density contrast and hence contributes the most to the transient scattering.

The transient scattering signal due to change in charge or magnetic density can be written as:

$$\begin{aligned} \Delta I_{SAXS}(\vec{q}) \propto & \iint \left[\Delta\rho_c(\vec{R})\rho_c(\vec{r} + \vec{R}) + \rho_c(\vec{R})\Delta\rho_c(\vec{r} + \vec{R}) + \Delta\rho_c(\vec{R})\Delta\rho_c(\vec{r} + \vec{R}) \right] d^3\vec{R} e^{i\vec{q}\cdot\vec{r}} d^3\vec{r} \\ & + \iint \left[\Delta\rho_m(\vec{R})\rho_m(\vec{r} + \vec{R}) + \rho_m(\vec{R})\Delta\rho_m(\vec{r} + \vec{R}) + \Delta\rho_m(\vec{R})\Delta\rho_m(\vec{r} + \vec{R}) \right] d^3\vec{R} e^{i\vec{q}\cdot\vec{r}} d^3\vec{r}. \end{aligned} \quad (2.27)$$

In the initial AFM state, the scattering contribution comes from the charge and magnetic roughness at various length scales. Making the assumption that transient scattering signal during the phase transition does not depend on the initial roughness, we can neglect the correlations between initial densities and transient change in densities. Thus transient scattering signal can be approximated as:

$$\begin{aligned} \Delta I_{SAXS}(\vec{q}) \propto & \iint \left[\Delta\rho_c(\vec{R})\Delta\rho_c(\vec{r} + \vec{R}) \right] d^3\vec{R} e^{i\vec{q}\cdot\vec{r}} d^3\vec{r} \\ & + \iint \left[\Delta\rho_m(\vec{R})\Delta\rho_m(\vec{r} + \vec{R}) \right] d^3\vec{R} e^{i\vec{q}\cdot\vec{r}} d^3\vec{r}. \end{aligned} \quad (2.28)$$

From equation 2.28, the transient scattering signal can be approximated as the square of the change in density at every length scale. Considering the four cases as illustrated in Fig. 2.7, we can estimate the relative contribution from charge and magnetic scattering as follows:

$$\frac{\Delta I_{SAXS-FeRh-c}(\vec{q})}{\Delta I_{SAXS-FeRh-m}(\vec{q})} \approx \frac{\left(\frac{0.5}{100}\right)^2}{\left(\frac{5}{100} + \frac{1}{100} + \frac{30}{100}\right)^2} \approx 0.0002. \quad (2.29)$$

Thus, transient scattering due to optical excitation of FeRh is predominantly because of the formation of the ferromagnetic domains. Only 0.02% of the signal comes from structural transition. The transient scattering due to the ferromagnetic domain formation gives a positive scattering signal as there is an effective increase in the spin density (compared to the initial state) at every length scale.

Another important aspect to note here is that the initial state was assumed to be fully AFM ordered. In practice, there are FM surface/interface layers present which give a scattering signal due to the demagnetization induced by the optical excitation. Since there is an effective decrease in the spin density, the scattering signal change due to the demagnetization of the FM interface is negative.

3 Experimental techniques

In this chapter, brief discussion is presented on the lasing process in X-ray region, European XFEL infrastructure, Spectroscopy and Coherent Scattering instrument (SCS), available experimental techniques at SCS instrument and THz detection.

3.1 X-ray free-electron lasing process

With the advent of XFELs, increase of photon flux, brightness and brilliance compared to synchrotron or femto-slicing sources has opened new avenues: studying element-specific dynamics with ultimate temporal and spatial resolution. The process of achieving such brightness and coherence stems from the coherent emission of X-ray radiation from the accelerated electrons as opposed to incoherent or partially coherent emission in synchrotron sources. The coherent emission process can be achieved through SASE (Self-Amplified Spontaneous Emission), self-seeding or external seeding processes. While external seeding (FERMI) and self-seeding modes (LCLS, European XFEL) of operation are still in development [112, 119, 239–241] for a broad range of X-ray wavelengths, the SASE mode of Free Electron Laser (FEL) operation has been established from XUV wavelengths (FLASH) to hard X-rays (European XFEL, LCLS, SACLA, PAL-XFEL SwissFEL) [107–111, 113, 120, 121]. Here, SASE process of coherent emission will be briefly described. A good description of such process can be found in [242] and the references therein.

Accelerated free-electrons with random statistical distribution in phase space (space and time) emit incoherent radiation called spontaneous emission. Undulators, containing periodic magnetic structures, can emit radiation which is incoherent or partially coherent depending on undulator tuning parameter. For sufficiently long undulators (~ 100 meters), a correct undulator parameter to generate partially coherent radiation, a high electron peak currents and a relatively small divergence and small electron bunch size, it is possible to achieve microbunching condition after travelling through a certain length of undulators. The microbunching process involves the change from a random distribution to high phase-space-correlations between electrons due to a sufficiently strong electric field which is generated by spontaneous emission. The oscillating electric field of emitted radiation acts as a modulator on the randomly distributed electrons. It accelerates or decelerates the electrons depending on their position in phase space thus bringing them together in space and time within the electron bunch, in the form of microbunch. Because of highly correlated electrons within the microbunch, spontaneous emission generated by these microbunches interferes constructively to generate coherent radiation which increases as $\sim N^2$

(where N is number of electrons in microbunches) as opposed to $\sim N$ in synchrotrons where there is no microbunching. Different electron bunches also participate in the coherent emission process because of the fact that relativistic electron bunches and emitted radiation, after traveling the undulator period (period of magnet), are exactly integer number of wavelengths apart from each other. Thus, newly generated radiation also adds up constructively at wavelength determined by undulator parameter. The power of this coherent radiation grows exponentially over the undulator length as more and more electron bunches participate in this coherent emission and more electrons within one electron bunch participate in the microbunching process. This complete process is termed self-amplified spontaneous emission (SASE).

Electrons in microbunches lose energy (deceleration) to the emitted radiation by interacting with the electric field of radiation. After certain undulator length, they start to slow down and lag behind the radiation by more than integral number of wavelengths of radiation. The emitted radiation from these electrons no longer interferes constructively. At this point, the SASE process achieves saturation. Emission from out-of-phase electrons in the remaining undulator length leads to a decrease in coherence.

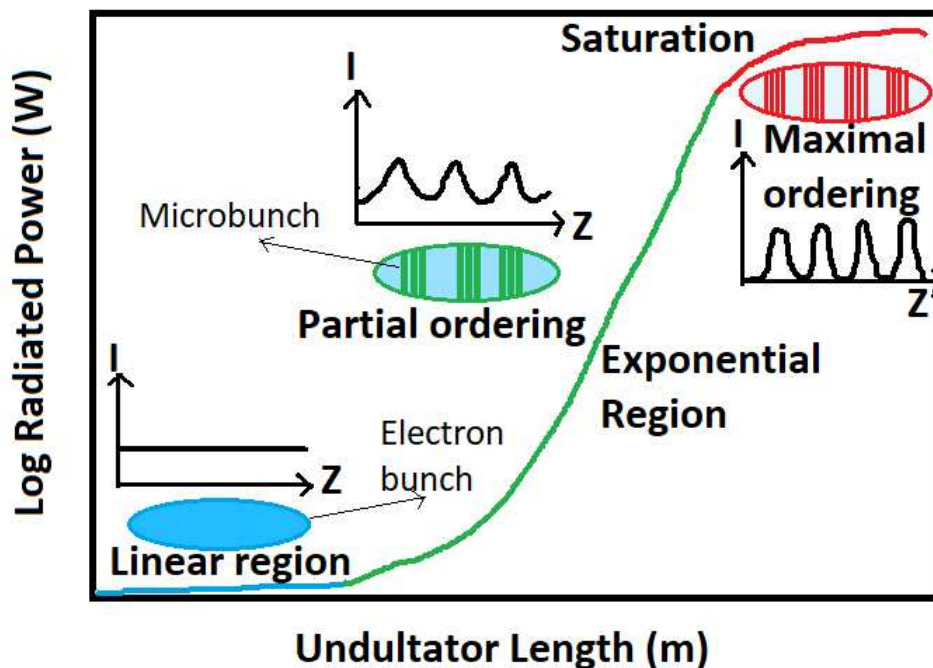


Figure 3.1: Lasing process for SASE Free-Electron lasers. Different gain regions across the undulator length show how the coherent radiation and power gain is obtained via micro-bunching process. Modified and adapted from [242].

There exist many more micro-bunches within one electron bunch. These micro-bunches within one electron bunch don't necessarily interfere constructively (this is why smaller divergence and bunch size in phase space is better for SASE) and can emit radiation at a slightly different wavelength (called SASE spikes within one pulse). This gives a finite energy spread to the undulator radiation. Other techniques like external seeding or self-seeding tend to make this bandwidth narrower and improve on the spatial coherence properties and peak powers of free-electron lasers [43, 112, 239, 240, 243]. The free-electron lasing process requires a very high stability in terms of

phase space fluctuations due to the external perturbations such as the temperature, pressure and magnetic field. These factor into the efficiency and output power of FELs. Such stability can be best achieved by superconducting accelerators.

3.2 European XFEL & current state of art instruments

European XFEL [107, 121] is one of the largest facilities for next generation high brilliance light sources. Free-electron lasing process is achieved by SASE as described in section 3.1. Currently there are six instruments operations at European XFEL and participate in external user proposals. These instruments receive the radiation from three different undulator sections (2 instruments each per undulator section) [244]. The possible FEL photon energy range varies from 0.26-3 keV for soft X-ray instruments (SCS, SQS) and 3 to over 25 keV for hard X-ray instruments (MID, HED, FXE, SPB), depending on the electron energy available from linear accelerator: lower the electron energy, lower the photon energy that can be reached. Normal modes of operation involve electron energies of 11.5 GeV, 14 GeV and 16.5 GeV for achieving different ranges of photon energies in the soft or hard X-ray regime. The mode of operation is the burst mode operation. The 600- μ s-long FEL trains come at fixed rate of 10 Hz and the number of X-ray pulses inside one train can be varied from 1 to 2700 pulses at up to 4.5 MHz, distributed over all instruments, depending on the need.

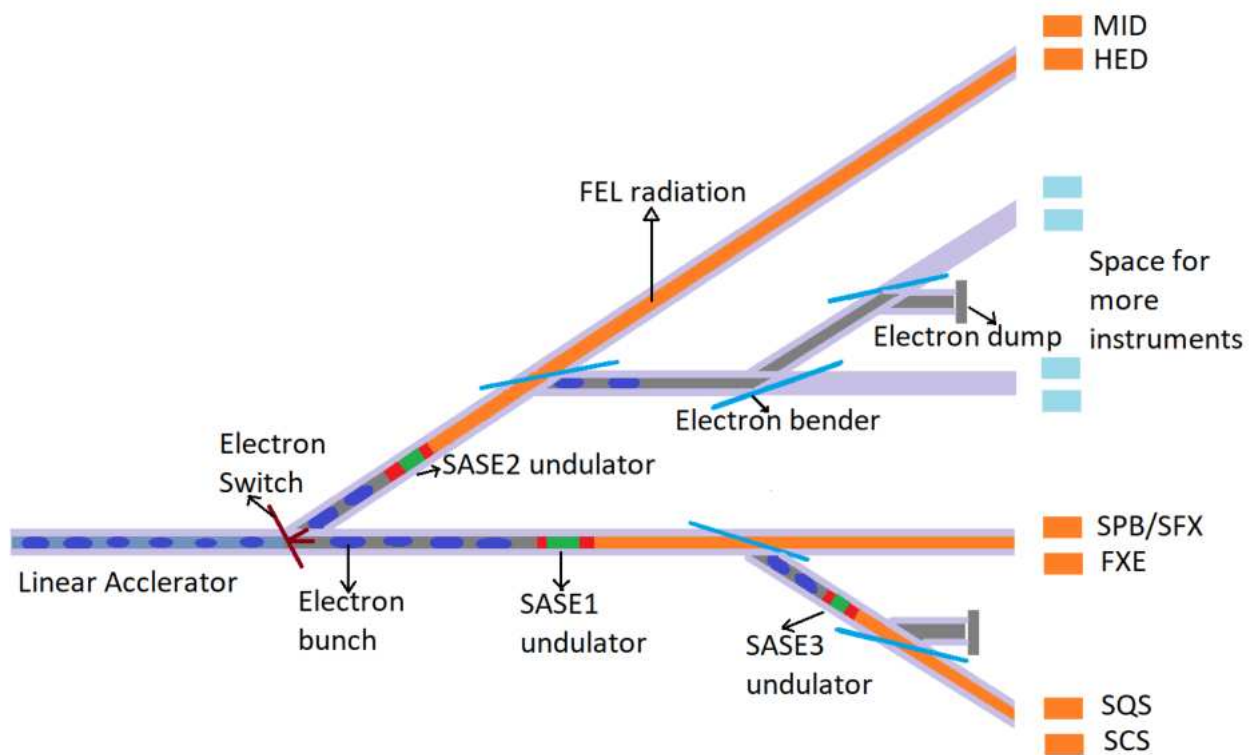


Figure 3.2: Schematic of current operational status of European XFEL. Accelerated electrons in Linear accelerator are distributed over different SASE tunnels using electron switch. FEL radiation is produced in SASE undulators and transported to different instruments. Electrons, after losing their energy during FEL process, are dumped at electron dump.

3.3 Spectroscopy and Coherent Scattering (SCS) instrument

The Spectroscopy and Coherent Scattering instrument (SCS) [114] is one of the two soft-X-ray instruments at European XFEL. It is dedicated to study the ultrafast phenomena in solids and liquids with nanometers resolution using various optical/X-ray pump and X-ray probe-based spectroscopy and imaging techniques. Time-resolved XAS and SAXS measurements for optically excited FeRh, as discussed in the thesis, were performed at SCS instrument. In this section, the SCS beam transport, beamline diagnostics, detectors and experimental stations will be described. Most of the control systems are interfaced with commercial Beckhoff system and software control is done through in-house developed Karabo framework.

3.3.1 X-ray beam transport and monochromator

FEL radiation generated in the 105 m long undulator section in the SASE3 tunnel is transported to the experimental hutch via various X-ray optical components under UHV (ultra-high vacuum) conditions [245]. For Soft X-rays, the penetration depth in the materials is of the order of few 100 nm. So, refractive optics cannot be used for long beam transport path because of high absorption losses. Materials have a refractive index smaller than (and close to) 1 for X-ray wavelengths. This means x-rays can go through total external reflection (in vacuum) near grazing incidence without any significant absorption losses. Thus, most x-ray optics for beam transport are used in reflection geometry at grazing incidence (mrad angles) for the highest efficiency. Grazing incidence (mrad) geometry necessitates the large reflective optics (few meters) and small clear aperture (few mm) of X-ray beam to transport the entire beam. As mentioned earlier, SASE FEL radiation has a large bandwidth (about 1%), soft X-ray monochromator is used to select a narrow bandwidth (~ 250 meV @ 1 keV) of radiation dispersively. This defines the resolving power of the SCS instrument for the most spectroscopy measurements [246]. Horizontal offset mirrors and pre-mirrors are used to align and transport the beam to experimental hutch. A wide range of attenuation levels (from 100 % to 0.0001%) of X-ray pulse energy can be achieved with the gas attenuator for all the energy range of SASE3. The gas attenuator normally contains nitrogen gas with maximum possible pressure of 13 mbar. Fig. 3.3 shows the in-vacuum components for beam transport from SASE3 tunnel to SCS hutch. Fig. 3.4 shows various components for X-ray experiments in the forward geometry in the SCS hutch. Some of them will be explained briefly in next subsections.

3.3.2 ALAS

For an easy alignment of the X-ray beam every time, a permanent retractable alignment system consisting has been implemented which consists of 473 nm, low divergence, collimated laser beam. This allows offline (without x-rays) positioning of beamline components and experimental stations.

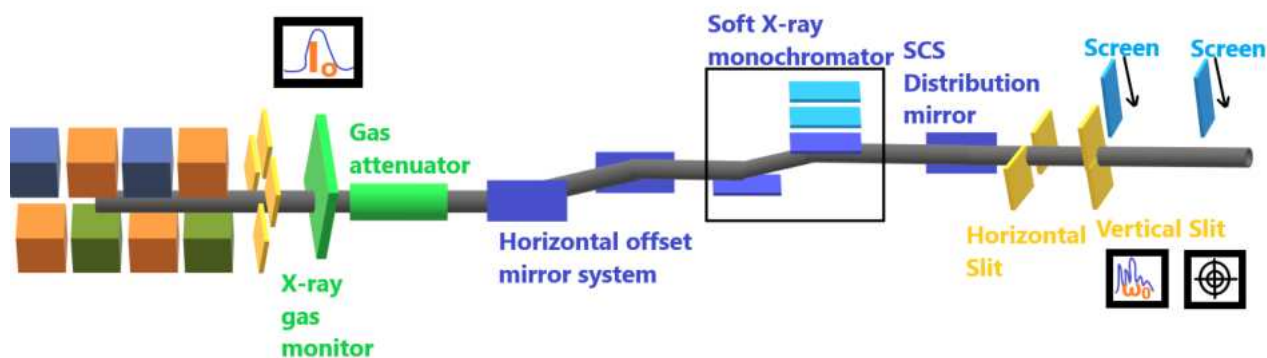


Figure 3.3: X-ray beam transport (Horizontal offset mirror system, SCS distribution mirror), X-ray monochromator (grating and slits) and X-ray diagnostics (X-ray gas monitor and gas attenuator) in the SASE3 tunnel for SCS instrument

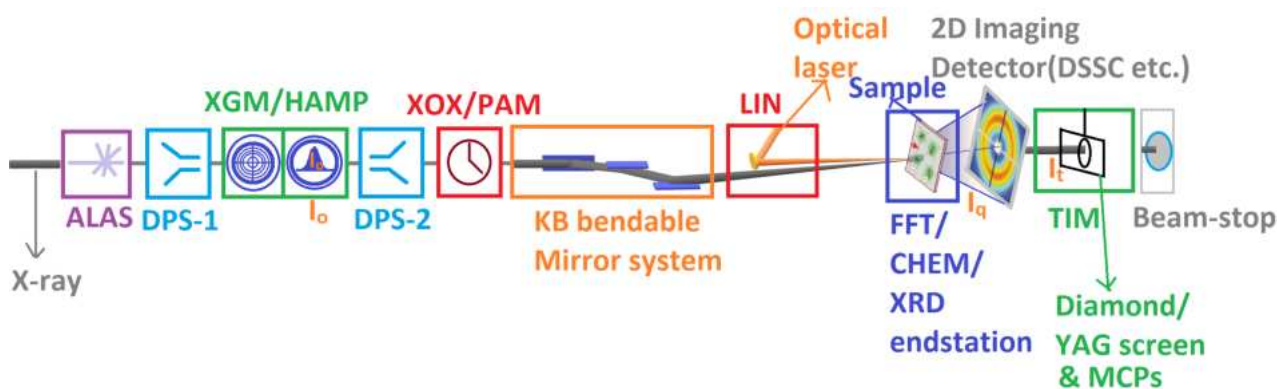


Figure 3.4: Schematic of SCS instrument in the experimental hutch for forward scattering geometry [247] including various components. (alignment laser (ALAS), DPS, X-ray gas monitor (XGM), X-ray focusing system (KB), laser in-coupling (LIN), experimental stations (FFT/CHEM/XRD), detectors (TIM, FCCD, DSSC etc) and beam stop)

3.3.3 X-ray gas monitor (XGM/HAMP)

The X-ray gas monitor (XGM) [248] is the first beam diagnostics component inside the experimental hutch. The XGM is capable of non-invasive pulse-resolved measurements of the horizontal and vertical position with a $\sim 10 \mu\text{m}$ accuracy and a 10% uncertainty in pulse energies. The XGM energy measurements integrated over all the pulses in the train (slow varying signal at 10 Hz) are absolutely calibrated while relative intensity measurements are performed for individual pulses within the train. For measurements of individual pulse energies (pulses within train) with lower relative uncertainty (1%), the huge aperture open multiplier (HAMP) is used. The fast pulse-resolved signal from HAMP is calibrated against the slow signal from XGM. The working principle of XGM/HAMP (Fig. 3.5) is based on the photo-ionization of dilute rare gases (Xe, Kr, Ar). Different gases are opted for depending on photo-ionization cross-section for particular energy range to achieve the maximum efficiency and minimum uncertainty. Energy ranges near the x-ray resonances of gases are excluded from the operational range of XGM to avoid the non-linearities. Pulse-resolved photo-electron and photo-ion currents are measured with (HAMP) or without (XGM) avalanche multiplication before the analog-to-digital converter (ADC).

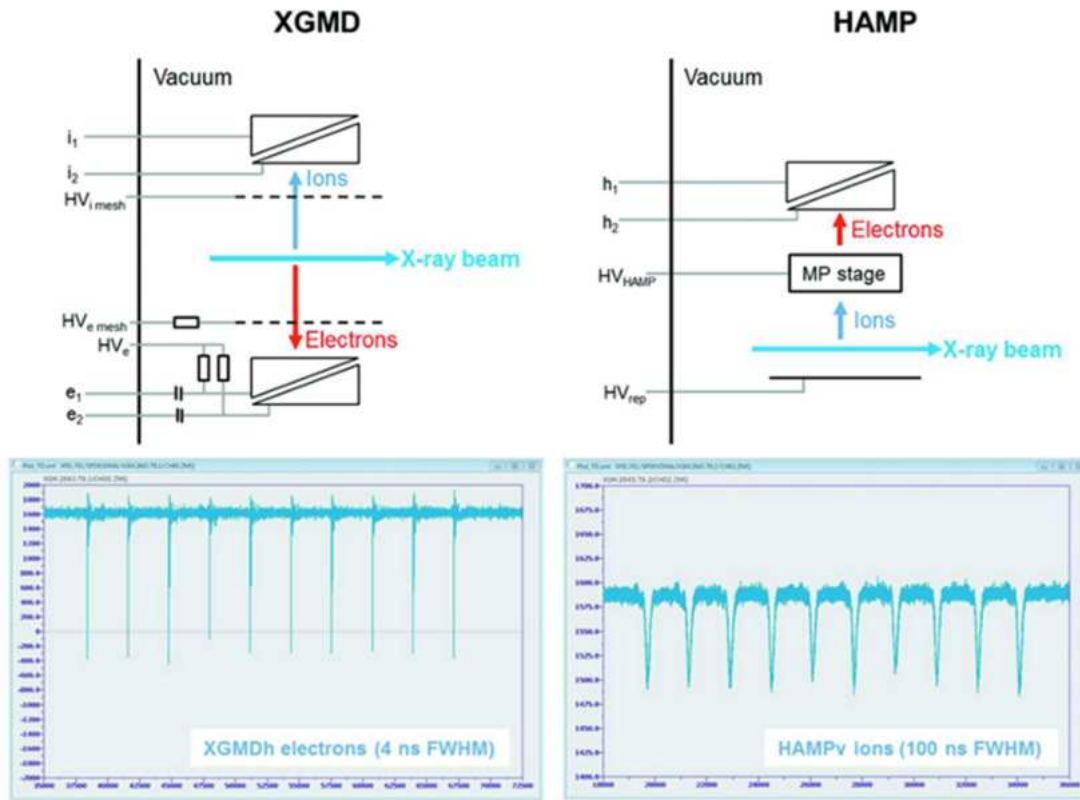


Figure 3.5: Schematic for the X-ray beam diagnostics using X-ray gas monitor (XGM) and Huge Aperture Multiplier (HAMP). Taken from [248]

3.3.4 DPS system

Some components of the beamline such as the XGM can have gas pressure of more than 10^{-4} mbar as compared to the UHV environment (better than 10^{-8} mbar). To accommodate for such pressure differences of 4-5 order of magnitude, differential pumping systems (DPS) are inserted between components. They are composed of several stages separated by multiple apertures.

3.3.5 Kirkpatrick-Baez (KB) focusing mirrors

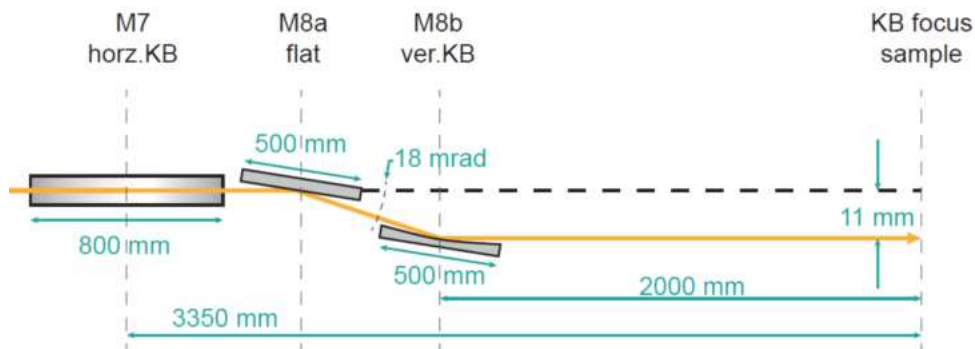


Figure 3.6: Schematic for X-ray focusing system in SCS hutch using KB mirrors

Kirkpatrick-Baez (KB) focusing system includes two ultra-polished mirrors for horizontal and vertical focusing of beam over full photon energy range. A precision bender system allows for changing independently the focal spot size of the beam in the horizontal and vertical direction from

$2\ \mu\text{m}$ to $500\ \mu\text{m}$ ($0\text{-}1.6 \times$ Rayleigh range) with a focal length from 1 m to 4 m. The minimum focus size has a very small dependence on the X-ray photon energy. A vertical offset mirror, in between two mirrors, keeps beam parallel to the horizontal plane [247, 249].

3.3.6 Laser in-coupling(LIN)

The laser in-coupling chamber is used to couple the optical pump laser in collinear or nearly collinear geometry to the X-ray beam for pump-probe experiments. Though, for certain experimental geometries (like zone-plate-based experiments) requiring a smaller focus size, it is also possible to directly couple the optical laser to experimental station in nearly collinear geometry (with the incidence angles as small as 10 deg).

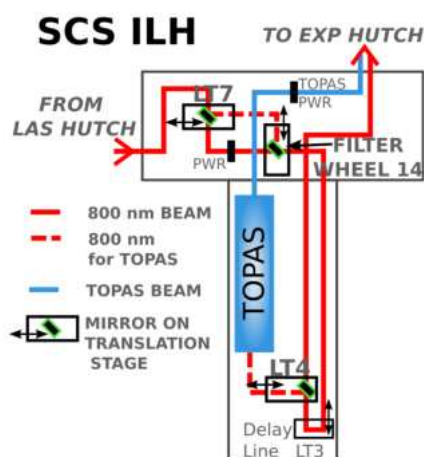


Figure 3.7: Schematic for optical laser delivery from instrument laser hutch to experiment hutch

3.3.7 Optical laser

For optical pump X-ray probe experiments, an in-house developed optical laser [250] with center wavelength around 800 nm and pulse duration of 15-300 fs (based on non-linear optical parametric amplifier (NOPA)), synchronized to the burst mode operation of the X-ray, can be delivered to experimental station. Current working modes of optical laser are 113 kHz and 1 MHz with pulse energy of 2 mJ and 0.2 mJ respectively. Further, there is also the possibility to obtain different pump wavelengths up to $10\ \mu\text{m}$ using the commercial OPA pumped by the 800 nm laser and seeded by the white light continuum (generated by the 800 nm laser).

3.3.8 Experimental station: forward scattering fixed target (FFT)

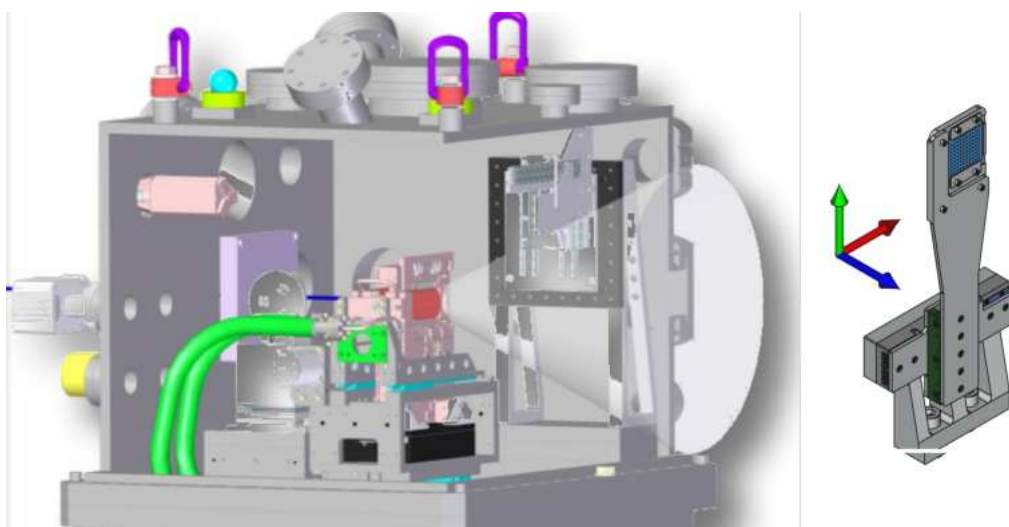


Figure 3.8: Schematic of inside of FFT experimental station for forward scattering experiments. Left: sample scanner (light pink and red), different in -vacuum motors and components, electromagnet and scattered beam. Right: Mounting stage for TZPG (transmission zone plate grating)

The forward scattering fixed target (FFT) chamber is designed for X-ray experiments in transmission geometry with solid samples (such as coherent diffraction imaging, holography, small angle X-ray scattering, X-ray absorption etc.). The samples can be mounted on a cart and inserted into (fast) sample scanner which makes it possible to change sample at a 10 Hz rate (thus every X-ray train) for destructive/irreversible type of non-linear optical/X-ray pump and X-ray probe experiments with very high optical/X-ray pump energies. Sample cart can be inserted through a load lock without breaking the vacuum. A water-cooled electromagnet in this chamber can be used to apply a maximum DC magnetic field of 350mT which can be switched on/off at 10 Hz. The sample holder can be installed with an heater for the experiments requiring a static heating of the samples. A cryostat is envisioned for low temperature experiments in the future. Transmission zone plate gratings (TZPG) can be mounted on the stage for zone-plate-based X-ray absorption spectroscopy. Motorized stages and components make it possible to control the experimental parameters remotely.

3.3.9 Detectors

In this section, detectors already implemented for forward geometry experiments at SCS will be described.

Fast charge coupled device (FCCD)

FCCD, a 2D imaging CCD detector, contains 1980×960 pixels of $30 \mu\text{m}$ size, capable of X-ray photon measurements at 10Hz. Smaller pixel size makes it possible to have better sampling of momentum transfer (q) in scattering or imaging experiments and thus higher resolution can be achieved. FCCD has a small hole to let the direct x-ray beam pass through. This makes it possible to do in-situ x-ray transmission measurements using transmission intensity monitor. FCCD detector integrates over all the pulses within the train and can only resolve single trains.

DEPMOS sensor with signal compression (DSSC)

DSSC is a pulse-resolved detector with single photon sensitivity in the highest gain over the X-ray photon energy range of 0.5-6 keV. The DSSC is capable of recording frames at a repetition rate of 4.5MHz in the burst mode. The currently implemented one Megapixel version consists of arrays of a miniSDD (silicon drift detectors). 1024×1024 hexagonal pixels, each pixel with the side length of $136 \mu\text{m}$, are equipped with 256 ASICs (application specific integrated circuits) over 16 tiles/ladders which are arranged in 4 quadrants in a windmill configuration [251]. These quadrants can be moved independently for the alignment and adjusting the center hole size. Hexagonal pixel geometry ensures that all the charge can be collected in a short amount of time and the pixel can be drained faster, making it ready for next incoming data. The detector has been calibrated in photon counts beforehand [252]. This provides us calibrated spread of photons over bins for different gain settings. Different possible fixed gain settings and differential gain setting of DSSC electronics make it possible to take measurements over a broader dynamic range. For the SAXS experiments (low photon counts requiring high photon sensitivity) described in the thesis, fixed gain setting of 0.5 photons per bin was applied. For XAS experiments (high photon counts), fixed gain setting of 10 photons per bin was applied. Future version of detector will contain nonlinear gain DEPFET sensors capable of ultimate dynamic range possible.

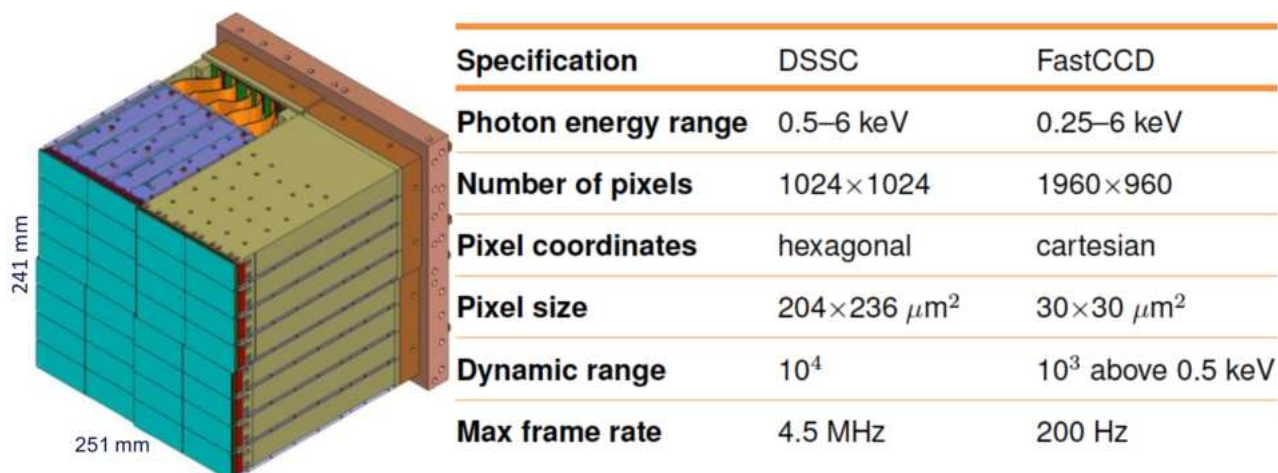


Figure 3.9: Left: Schematic for modular structure of DSSC. Right: Working specifications for FCCD and DSSC detectors [247].

Transmission intensity monitor (TIM)

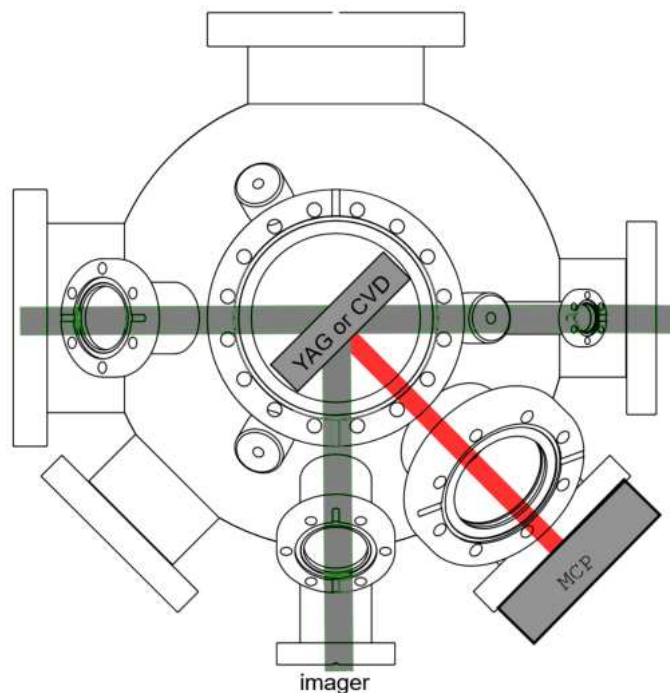


Figure 3.10: Schematic for X-ray fluorescence-based transmission intensity monitor for measuring (using multiple MCPs) the transmitted intensity in forward scattering experiments. Incident X-ray beam from left induced X-ray fluorescence at CVD diamond mounted at 45 degree. X-ray fluorescence is measured with MCPs.

The transmission intensity monitor is a micro-channel plate-(MCP)-based detector for measuring pulse-resolved signals of X-rays transmitted through the samples. The X-ray fluorescence from CVD diamond or YAG crystal, irradiated by incident X-rays, is measured by multiple MCP detectors. TIM can be used for pulse-resolved X-ray absorption spectroscopy in transmission geometry while performing scattering/imaging experiments using other 2D detectors with a central hole (like the FCCD or DSSC). In pulse-resolved MHz repetition rate XAS measurements, pulse-resolved incident energy is measured by HAMP while pulse-resolved transmitted intensity is measured by TIM. Transmission intensity monitor can measure x-ray pulse energies down to 10 nJ per pulse.

3.4 Soft X-ray experimental techniques at SCS instrument

In this section, experimental techniques in forward scattering geometry, which are already implemented and commissioned at the SCS instrument, will be described. In the future, other techniques such as X-ray diffraction, reflectivity, resonant inelastic X-ray scattering and X-ray emission spectroscopy will also be available in backward scattering geometry.

3.4.1 X-ray absorption spectroscopy with transmission intensity monitor

As described in chapter 2, X-ray absorption spectroscopy gives element specific information about the local chemical environment /electronic structure of the materials. With the advent of XFEL sources, it is possible to follow the dynamical processes such as electronic band structure modification, charge transfer dynamics and phase transitions with ultimate time resolution. At the SCS instrument, X-ray absorption spectroscopy (XAS) can be performed in two different ways. XAS spectra, can be measured in transmission geometry using the XGM/HAMP for incident intensity detection and the TIM for transmitted intensity detection. Such measurements are also possible in-situ with SAXS measurements. In order to obtain the femtosecond evolution of electronic band structure, time-resolved changes in XAS are obtained by probing the sample at twice the repetition rate of optical pump and then subtracting the unpumped signal (X-rays without optical pump) from pumped signal (X-ray with variable time delay with optical pump). Second and more sensitive way of measuring XAS spectra using transmission zone plate gratings is discussed in the following sub-section.

3.4.2 X-ray absorption spectroscopy with transmission zone-plate grating scheme

In the previous sub-section, the X-ray spectroscopy measurements were described where two separate detectors XGM/HAMP and TIM measure incident and transmitted intensity respectively. These measurements are limited by the photon sensitivity of XGM/HAMP and TIM detectors. Also, the incident pulse energy measurements using HAMP/XGM are done far upstream of the sample position. The KB focusing system between the sample position and XGM/HAMP also introduces additional noise. Thus, it would be ideal to perform the X-ray spectroscopy measurements where the incident and the transmitted intensity are measured by the same single photon-sensitive detector (low-noise read-out) without any additional X-ray optics in between a sample and detector. Here, we describe such a measurement scheme using the off-axis transmission zone-plate grating. In this scheme [253, 254] of highly sensitive photon-shot-noise-limited and pulse-resolved absorption measurement, a off-axis transmission zone plate grating (TZPG) splits the X-ray beam into 2 or even 3 first-order (zone-plate order) beams, one of which transmits through sample while the other being used as reference beam (Fig. 3.11). The off-axis geometry separates the zone plate orders of TZPG and ensures that the zeroth order or direct beam does not impinge on the detector to avoid the detector damage. Both reference and sample signals are measured simultaneously on single pulse-resolved 2D detector such as DSSC or FCCD. Electronic noise in CCD detectors is below that of generated by 1 photon, thus making the measurements limited only by Poisson noise or shot noise. This normalization scheme based on CCD detection improves the signal to noise ratio (SNR) by at least

an order of magnitude compared to the simple scheme described in previous subsection where the noise is limited by MCP and digitizer and not by photon shot noise. As a comparison, SNR of 500 has been observed with TZPG-XAS scheme using DSSC with sample-detector distance of 5.8 meters compared to SNR of 30 for measurements based on TIM and HAMP. Increased SNR improves significantly the sensitivity of the XAS ($\sim 0.2\%$ changes can be observed) and reduces the measurement time. Further improvement in SNR (upto 20000) has been estimated using larger CCD detector array with higher pixel density, lower read-out noise at larger sample-detector distance so as to cover the full detector area.

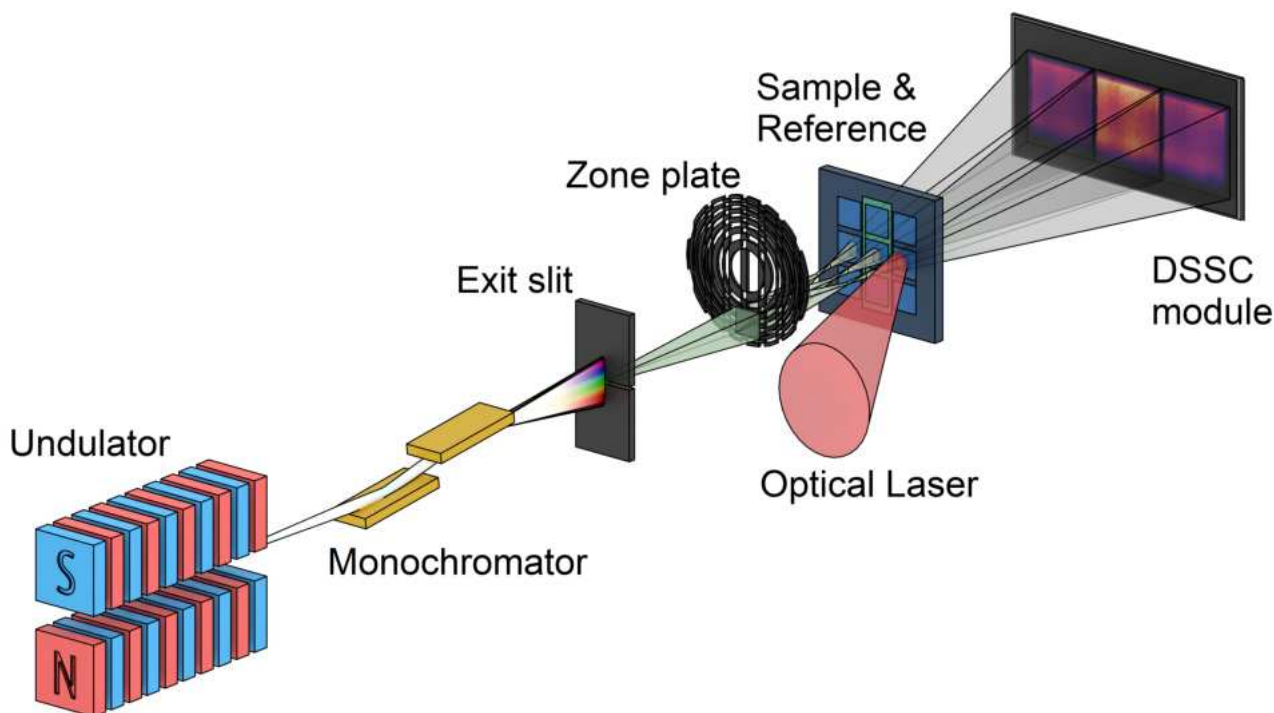


Figure 3.11: Schematic for time-resolved X-ray absorption spectroscopy based on transmission zone plate grating (TZPG) and 2D detector. This advanced off-axis geometry was used for the XAS measurements in this thesis. Off-axis geometry separates the zone-plate orders. Direct beam does not impinge on the detector. Zone-plate grating splits the zone plate orders into 2 or even 3 beams. One of the beam passed through the sample while other is used as a reference beam. Both beams are measured at the CCD detector.

3.4.3 Small angle X-ray scattering (SAXS)

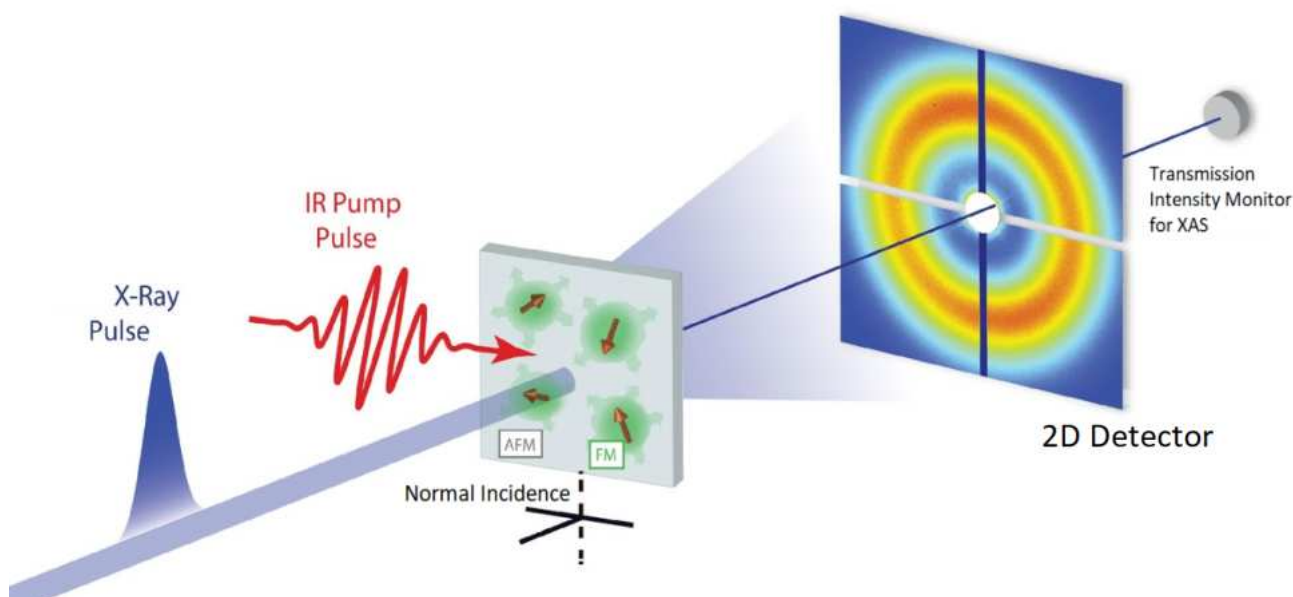


Figure 3.12: Schematic for time-resolved small angle x-ray scattering (SAXS) measurements. This geometry was used for SAXS measurements in this thesis.

Apart from understanding the ultrafast evolution of the local electronic structure via XAS, it is also important to delve into understanding temporal and spatial evolution of dynamical processes. Soft X-ray small angle X-ray scattering (SAXS) probes the correlation lengths of such dynamical processes in the material system, with chemical specificity and at high momentum transfer (q) in Fourier space which corresponds to nanometer resolution in real space. It provides the statistical view of the ensemble of states and their evolution in time. A time-resolved small angle x-ray scattering experiment at FELs gives ultimate temporal and spatial resolution. A 2D detector such as DSSC or FCCD, kept at an appropriate distance from sample, is used to record time-resolved scattering patterns at different scattering vectors originating from the different correlation lengths within the sample. Time-resolved small angle X-ray scattering (SAXS) with magnetic sensitivity probes the evolution of magnetic domains during the photo-induced dynamics as shown in chapter 7 in this thesis. Information on temporal evolution of magnetic domain sizes and their distribution, spin-spin correlations, correlation length scales and scaling laws of phase transitions can be extracted from the time-resolved SAXS data.

3.4.4 Time-resolved X-ray imaging & holography

In scattering experiments, only the intensity distribution in reciprocal space is measured over a large number of states while, for coherent X-ray experiments, phase information is lost. Phase distribution contains much more information about extent of coherent processes within the system. In the photo-induced systems where dynamics cease to be repeatable, one would need to single-out and reconstruct the individual events or pathways in the system. This information can be obtained using either complicated phase-retrieval-based reconstruction techniques (e.g. coherent diffraction imaging, ptychography) or lensless interferometric techniques such as holog-

raphy. Recording interferometric signal with reference structures allows one to directly reconstruct the image of nanostructures present in the system [255–257]. Further, time evolution of higher order correlations and fluctuations in the photo-induced dynamics can be measured with other imaging techniques such as X-ray photon correlation spectroscopy (XPCS) [258–262] and X-ray photon fluctuation spectroscopy (XPFS) [263]. The detailed description of these and other imaging techniques [264–267] is out-of-scope of this thesis.

3.5 Timing synchronization of XFEL: active timing correction

Large-scale FEL facilities such as European XFEL, where experiment stations and optical pump lasers are few kilometres away from the actual injector source, need sophisticated synchronization schemes for pump-probe experiments requiring few-fs timing stability. At European XFEL, the first synchronization stage involves synchronization between the linear accelerator's 1.3GHz radio frequency master oscillator (RF-MO) and the master laser oscillator (MLO) [268]. Master laser oscillator operates at the wavelength of 1550 nm, the pulse duration of 200 fs and the repetition rate of 216.667 MHz and it is used as a optical reference. The synchronization is achieved by novel laser-to-RF phase detection scheme based on Mach-Zehnder modulator (MZM). The secondary stage requires a RF and optical reference distribution to the RF and optical components in the accelerator. The local synchronization between the RF and optical distribution is again achieved by a laser-to-RF phase detection scheme. A real time femtosecond timing correction is performed via phase-locked loop (PLL) feedback. Beam arrival monitors (BAM) measure the arrival time of individual electron bunches using an electro-optic-modulator-based measurement of RF pulses, generated by a transient electric field of the electron bunch. They provide a slow and fast feedback to the phase-locked loop (PLL). The photoinjector laser oscillator is also synchronized with the RF-MO and optical reference signals and an active drift correction provides long-term stability. A secondary laser oscillator (SLO) in the experiment hall is also synchronized to the first master oscillator by an optical-fiber-based, balanced cross-correlation. All the optical laser systems in the experiment hutch are then synchronized to this secondary laser oscillator. Through active feedback corrections, one can achieve a few to tens of femtoseconds and also a long-term timing stability. This active feedback is especially crucial for the X-ray measurements performed at fixed time delay between X-ray and optical pump, for instance XAS measurements at fixed time delays done in chapter 6.

3.6 Timing jitter measurements using the pulse arrival monitor (PAM): passive timing correction

Even with the active-feedback-based timing correction between the electron bunch and the optical reference oscillator using the BAM, there are relative fast drifts/timing jitters of a few-fs within trains, mainly from the SASE process as well as the optical laser systems, which may still be present. These timing jitters can be monitored and corrected later using single-shot pulse-arrival monitors (PAM) [130, 269–272]. PAM measures the drift between the relative arrival time of the optical and X-ray pulses. Hereby, transient changes in the sample are induced by X-ray FEL pulses and probed by optical pulses. Spectral or spatial encoding techniques can be used for single-shot measurements of transient changes such as THz streaking, THz emission or transient reflectivity.

At the SCS instrument, it is envisioned to implement pulse arrival monitor based on transient reflectivity change of SiN or similar materials induced by X-ray pulses and probed by optical pulses using spectral encoding. Using PAM, it will be possible to correct for sub 10 fs single shot timing jitters. In a recent commissioning experiment for pulse-arrival jitter monitor, an intrinsic jitter of 14 fs between X-ray and PP laser pulses was measured. The major challenge of any pulse arrival

monitor (PAM), in soft X-ray range, is that it is destructive to the X-ray beam and can change its properties such as wave-front and its intensity. In the chapter 4, THz-emission-based time-arrival measurement technique will be described. This technique is potentially non-destructive. Using this technique, time arrival can be measured in-situ with the actual experiment at the same sample.

3.7 Spectral-encoding-based electro-optic sampling setup for THz detection

The spectral encoding method has been used for transient-reflectivity-based X-ray/optical cross-correlator [269]. A similar setup can be used to do single shot electro-optic sampling of THz pulses generated by FEL pulses. Fig. 3.13 illustrates the setup implemented for single-shot, spectral-encoding-based detection of THz pulses [273, 274]. THz pulses are generated using spintronic emitter by inverse spin Hall effect as explained in 2.1.2. Femtosecond optical pulse is stretched/chirped in pulse duration so that different wavelengths in the bandwidth come at given times. Now, this chirped pulse can be used to trace out the generated THz pulse in the electro-optic crystal where different wavelength of the chirped pulse gets modulated by the THz pulse at defined times. By performing differential measurements using the spectrometer, these modulations can be measured. These modulations provide a single-shot THz pulse which is encoded in the spectrum of the chirped optical pulse (4.1). In the chapter 4, such a detection scheme will be used to measure the relative arrival time between XUV and optical pulses.

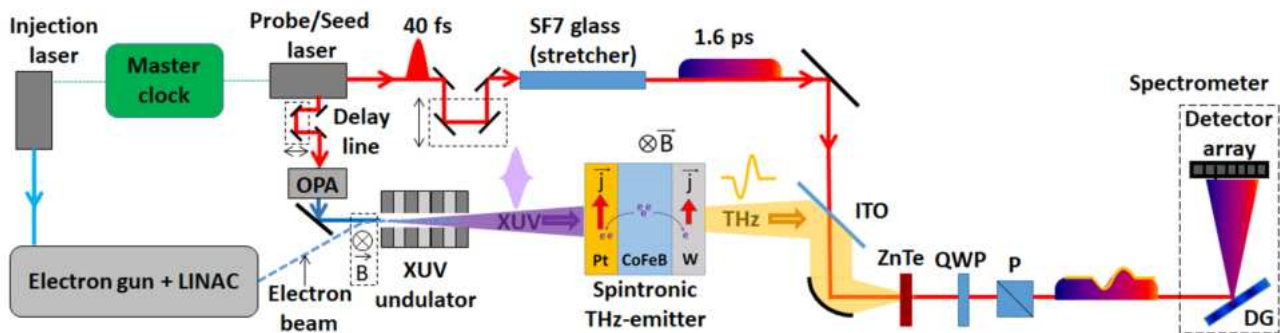


Figure 3.13: Experimental setup for single-shot spectral-encoding-based detection of THz pulses. Synchronized optical pulse is stretched using glass stretcher for spectral-encoding-based electro-optic sampling (in ZnTe) of THz pulses generated by spintronic THz emitter using XUV/FEL pulses. THz-Modulated stretched optical pulse spectrum is measured with spectrometer.

4 THz-wave decoding of XUV/FEL pulses

One main concern for pulse arrival monitors (PAM) based on transient reflectivity/transmissivity detection [269] is that they require high X-ray fluence ($>20 \text{ mJ/cm}^2$) to induce measurable changes, which is near the damage threshold of SiN membranes or any other materials within soft X-ray range at MHz repetition rate XFEL [130, 272]. Also, penetration depth in soft X-ray range is around 100 nm which further limits the measurement of the relative arrival time downstream to the solid-sample used for actual experiments. If PAM is implemented upstream before the sample position, using pick-off mirror (picking off a side portion of FEL pulse for PAM), it affects the X-ray experiments requiring wavefront stability. To measure the single-shot relative arrival time between X-ray and optical pulses, PAM must operate upstream to the sample position in parallel to the experiments and in non-invasive manner.

In this chapter, a novel timing jitter measurement scheme based on single-shot electro-optic sampling by spectral encoding of THz emission [273, 274] induced by FEL pulses is described. It, potentially, requires very small fluence ($<100 \mu\text{J/cm}^2$), a sample thickness of less than 100 nm (with responsive layer thickness being just 6 nm), does not affect wavefront as it uses full beam in transmission geometry. This potential scheme can, in principle, be implemented using same magnetic sample which is being used to study the ultrafast spin dynamics. This is because spin dynamics at the sub-picosecond or picosecond timescales is also a source of the THz emission. An experiment, demonstrating the potential sensitivity of such a scheme, was performed at EIS-TIMEX beamline of the seeded free-electron laser, FERMI at Trieste, Italy.

Fig. 3.13 in chapter 3 illustrates the setup implemented for single-shot spectral-encoding-based detection of THz pulses. XUV-FEL pulses (with 20 nm and 29 nm wavelength, 30 fs and 35 fs pulse duration, 25Hz repetition rate, 8 mm beam size, up to $42 \mu\text{J}$ energy) were used to excite a in-plane magnetized spintronic emitter (Pt (2 nm) /CoFeB (1.8 nm) /W (2 nm), 10 mm \times 10 mm size, grown on 500 μm z-cut sapphire substrate) placed inside an UHV chamber. The XUV pulses were incident at the normal to the sample. The spin current, generated inside the magnetic layer (CoFeB) by XUV excitation, is converted to radiative charge current or THz emission at the interfaces (Pt/CoFeB and W/CoFeB) due to the inverse spin Hall effect. The process of the THz emission has been explained in 2.1.2. A large XUV beam size of 8 mm ensured the fluence to be lower than 0.1 mJ/cm^2 . This avoided any demagnetization of the spintronic emitter which was saturated by applying 100 mT in-plane field. The setup was optimized to get the maximum amplitude of the THz pulses. The emitted THz pulses, in forward direction inside UHV chamber, were transported outside UHV chamber using a plane silver mirror. Plane mirror could be used in this case (in

place of a parabolic mirror) because of negligible or no divergence of THz beam generated by 8 mm size XUV beam. Further, THz pulses were reflected and focused onto electro-optic crystal by ITO (Indium Tin Oxide) coated substrate and parabolic mirror respectively. Chirped optical pulse is combined using the ITO coated substrate which transmits the optical pulses while reflecting THz pulses. THz pulses were probed using electro-optic sampling, in ambient conditions, with 800 nm chirped optical pulses of 1.6 ps duration at 50Hz. A 2 mm thick ZnTe crystal was used for electro-optic sampling, to ensure maximum sensitivity and large electro-optic modulation. The thick ZnTe crystal increases the sensitivity due to the increased modulation over total path length. Consequently, it also limits the bandwidth to 1 THz due to the mismatch between phase velocities of THz and optical pulses over the 2 mm path length. The optical background is recorded and subtracted by recording the optical probe at twice the repetition rate of XUV excitation. An Ocean-optic spectrometer (USB-2000) was used to record single shot spectra.

4.1 Calibration of spectral encoding setup and single-shot THz pulse extraction

Fig. 4.1 shows the calibration of the spectral encoding scheme which was used to extract the timing information and the THz pulse shape encoded in the wavelength of chirped optical pulse. When the time delay between the chirped optical pulse and the XUV pulse is varied using a delay stage, the single-shot modulation in the spectrum, measured with the spectrometer, changes its position linearly with the time delay and with respect to the wavelength. By linear fitting the wavelength position of maxima/minima of the modulation versus time delay, calibration for timing is obtained. The linear fit gives the conversion coefficient of 74 fs/nm.

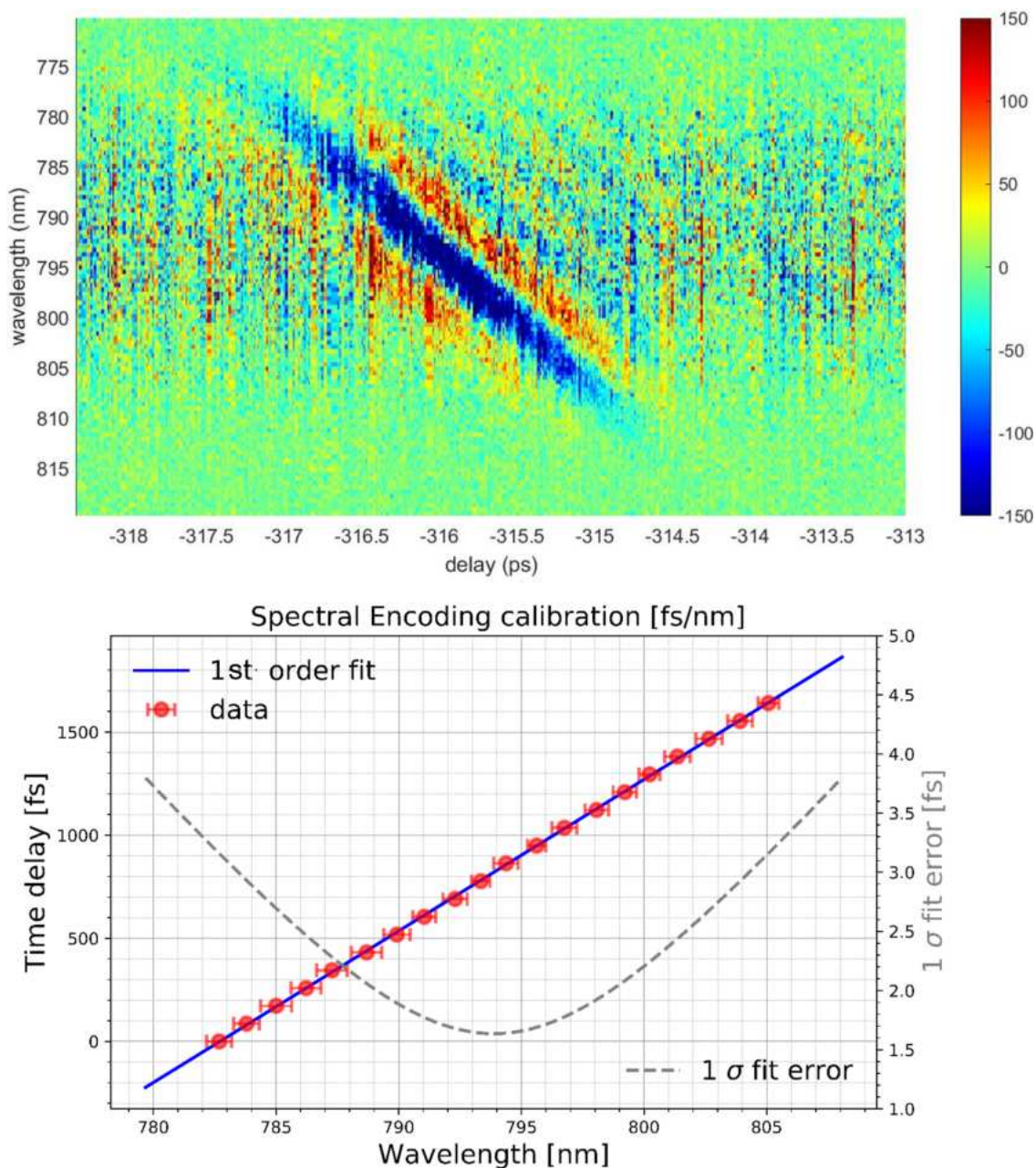


Figure 4.1: Spectral calibration. Top: Spectrally encoded THz waveforms (along y) vs delay stage movement to calibrate the setup. Bottom: Fitted (blue line) calibration of spectral encoding setup (to convert wavelength scale to time scale). Grey curve shows the error at each delay.

Fig. 4.2 shows the extracted THz pulse in the time and the frequency domains. Additional noise filtering based on frequency cut-off in the frequency domain has been applied. THz pulse simulation based on hot electron pulse generation from 30 fs excitation pulses, done by collaborators [275], shows a good match after including the transfer functions of the substrate (Sapphire) and the electro-optic crystal (ZnTe). The substrate and thick electro-optic crystal limit the measured bandwidth of emitted THz pulse due to mismatch between the phase velocities of THz and optical pulses over the total path-length of the electro-optic crystal.

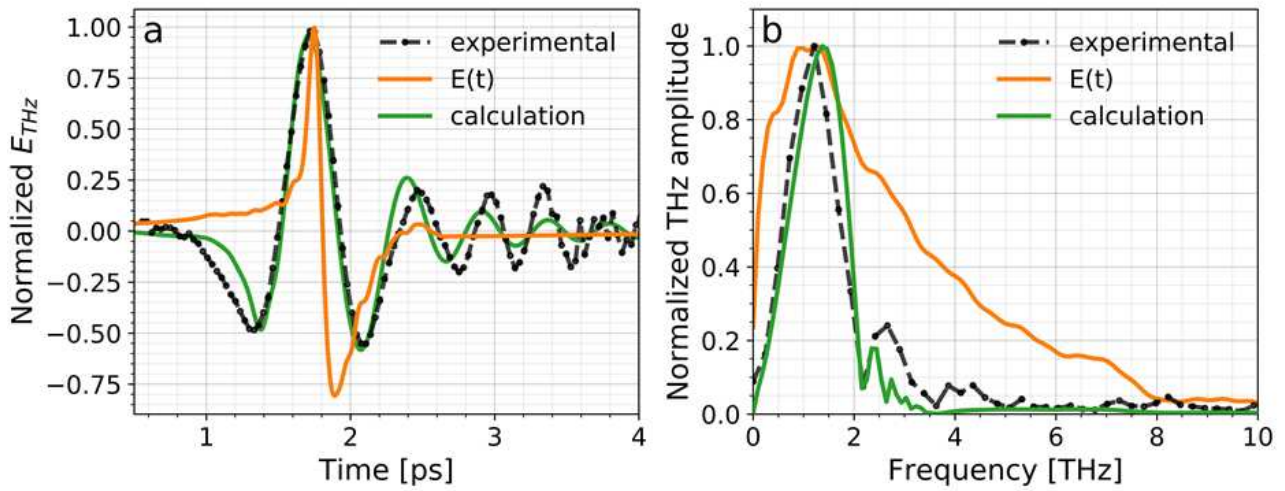


Figure 4.2: Averaged THz pulse generated by spintronic emitter excited by XUV pulses in time (a) and frequency (b) domain. THz pulse simulation (green and orange) as done by collaborators with and without transfer functions of substrate and electro-optic crystal respectively.

4.2 Application as the pulse arrival monitor

Fig. 4.3 a) and b) show relative arrival times of 3 consecutive THz pulses. The histogram (Fig. 4.3 c) of around 2500 pulses shows the timing jitter of THz pulses with $\sigma = 12.4$ fs which includes the intrinsic jitter of XUV pulses and our instrumentation. This determines the sensitivity of this measurement scheme.

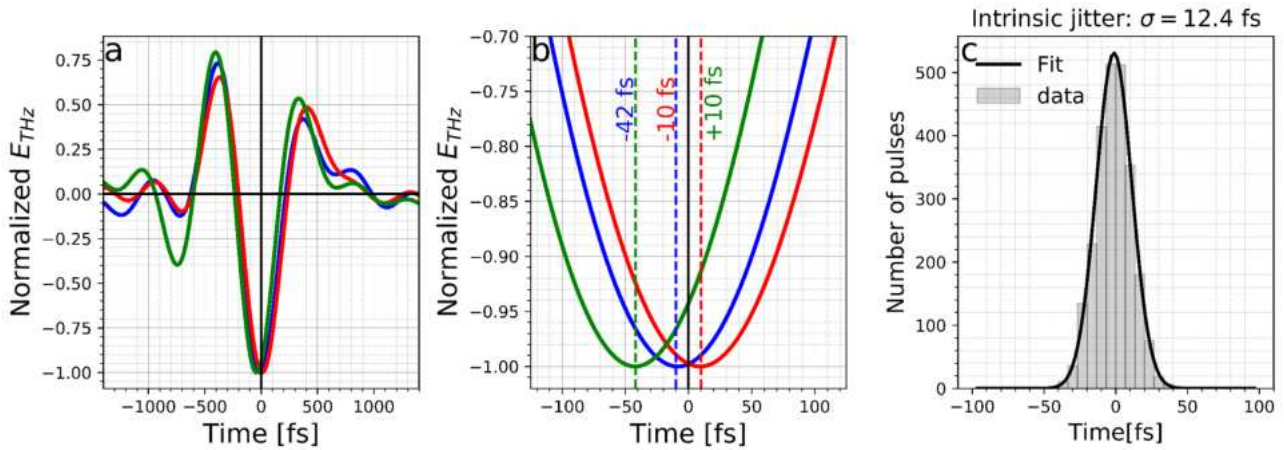


Figure 4.3: Arrival time jitter measured using THz pulses. a) Three consecutive THz pulses after spectral filtering. b) Minima of extracted single shot THz pulse is used to measure the timing jitter. c) Histogram of intrinsic jitter for 2500 XUV pulses.

To determine the robustness and reliability of the measurement setup, correlation measurements were performed where artificial saw-tooth type timing jitter was introduced in optical laser path. The estimated timing jitter from THz pulses was correlated with delay stage values. Figs. 4.4 b) and c) show that 40 fs artificial jitter can be estimated with very high degree of correlation whereas 10 fs artificial jitter (not including intrinsic jitter) is estimated with low degree of correlation. This is also to be expected as measurement sensitivity is between 0 and 10 fs.

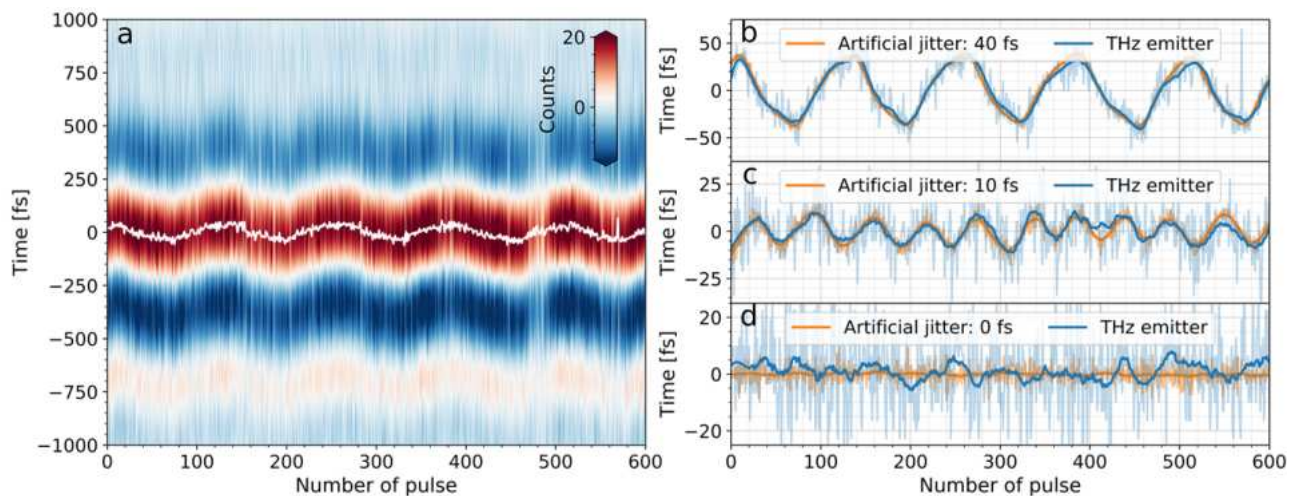


Figure 4.4: THz-detection-based FEL pulse arrival monitor. a) Single shot THz pulses for different 600 consecutive XUV shots with artificial jitter of 40 fs. Color coding represents THz field strength. White line shows the estimated jitter. b), c) and d) Artificial jitter (from delay stage) and THz-detection-based estimated jitter for 40 fs, 10 fs and 0 fs (intrinsic) amplitude.

4.3 Application as relative pulse intensity monitor

FEL pulses (specifically monochromatic SASE pulses), due to their stochastic nature, have very high intensity fluctuations. These fluctuations have to be normalized for every shot to achieve high signal to noise ratio in the measurements. It has already been shown, in the optical regime that the electric field of the THz pulse is directly proportional to the optical pulse intensity. This concept can be used to measure the shot-to-shot relative intensity of XUV/FEL pulses which normally requires sophisticated schemes such as gas monitors. As can be seen in Fig. 4.5, there is a very high degree of correlation between THz pulse amplitude and XUV pulse intensity.

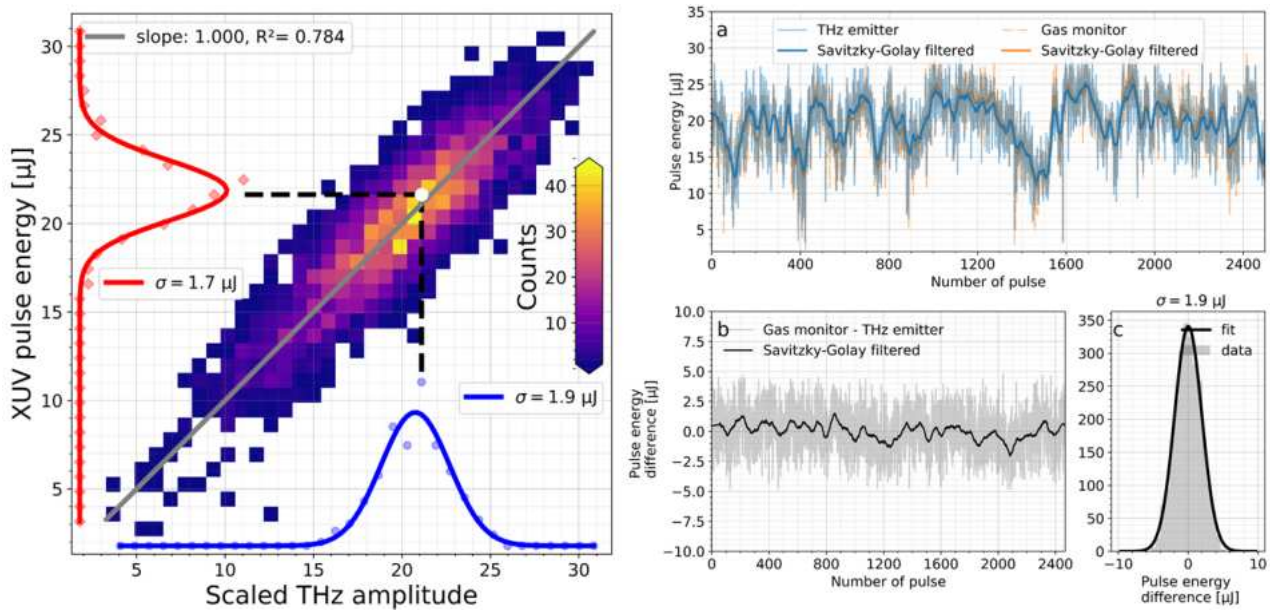


Figure 4.5: THz-based FEL pulse energy monitor. Left: Correlation plot for XUV pulse energy (through photo-emission) and scaled THz pulse amplitude. Right: a) Single shot XUV pulses overlaid with scaled THz amplitude. b) Single shot difference between XUV pulse energy and scaled THz amplitude. c) Histogram for intensity jitter in XUV pulse energy.

4.4 Discussion and outlook

In this chapter, it has been demonstrated that single-shot THz pulse emission from FEL pulses can be utilized to study different properties of FEL pulses. It was shown that pulse-resolved relative-arrival-time information between FEL and optical pulses can be obtained with better than 10 fs accuracy with very low FEL fluence. The timing accuracy observed in the experiment compares well with other methods [127, 130, 269–271, 276–279]. In addition, it can be used as single shot relative intensity monitor for FEL pulses.

Since bandwidth and shape of the THz pulse depends on the excitation pulse, this scheme should also be able to provide a measure of the pulse shape and pulse duration of FEL pulses which normally require complicated techniques [276, 280–284]. In the simulations done by collaborators and shown in [275], it was possible to differentiate between THz pulses generated by XUV pulses of different pulse durations or wavelengths. This remains to be investigated experimentally. Various choices of electro-optic crystals should be explored as electro-optic crystals affect the measurement sensitivity and bandwidth. Thick crystals give better sensitivity but poor bandwidth while thin crystals give good THz detection bandwidth but poor sensitivity.

Further, from the fact that the electric field of the THz pulse is directly proportional to XUV pulse intensity, it is speculated the THz emission process from XUV pulse excitation of the spintronic emitter should be similar to that in the optical regime based on hot electron pulse generation. In this experiment, there was no noticeable difference in THz generation from 20 nm and 29 nm XUV pulses compared to 800 nm optical pulses. This suggests that the THz intensity in spintronic emitter depends only on the absorbed energy density which is similar in case of the optical and XUV region. This hypothesis needs further investigation for different XUV and X-ray wavelengths. Since the penetration depth in the X-ray region becomes significantly larger, it can lead to a reduction in THz pulse energy using spintronic emitters. Thus, other materials like photoconductive antennas (InGaAs etc), photo dember samples (InAs) and organic crystals (DSTMS), which have shown high THz generation efficiency in the optical regime, should be explored in the XUV/ X-ray regime for their efficiency and working principles. More transparent materials with high THz emission efficiency are required for non-invasive measurements of the arrival time. It should also be noted that this technique, in principle, can also be extended to study the magnetization dynamics of the materials itself at the same time [92, 93].

With ultrafast, FEL-based experiments moving towards the attosecond regime, arrival time measurement techniques also need to be pushed for better sensitivity. Ultra-Broadband THz/far-infrared generation by attosecond pulses and single shot detection should be explored as one of the possibilities to achieve attosecond timing information and FEL pulse characteristics in the simplest way.

5 X-ray absorption spectral changes in thermally excited 3d transition metals

In the section 2.4, it was discussed how the X-ray absorption spectroscopy can be used to probe the element-specific electronic band structure changes in the materials of interest. In the section 2.7, different contributions to X-ray absorption spectral changes during the phase transition in FeRh were discussed. With the density functional theory simulations, it was shown that a temperature change can also induce certain electronic band structure changes. Modification in the temperature of the materials leads to a change in (various) macroscopic properties like the heat capacity, conductivity, magnetic properties and order parameters. Microscopically, this can be linked to changes in the band structure or the density of states at the Fermi energy or the chemical potential [95, 285–290].

There have been various attempts in simulating the band structure and X-ray absorption spectra of metals with as fine details as possible by taking into account of many-body effects, spin-orbit and exchange coupling effects, core-valence interactions and broadening [102, 213, 218, 220, 221, 290–296]. The broad and essentially featureless experimental absorption spectra at L edges due to lifetime broadening makes it difficult to refine the theoretical models for the metallic systems. Measuring electronic band structure changes may provide the the pathway to improve upon the theoretical modelling of metallic systems [285, 297, 298]. The measured spectral changes (due to thermal or optical excitation) might be expected to involve the finer details of the electronic structure which cannot be observed in broad absorption spectra. Simulating such modifications in spectra are expected to shed more light on the theoretical understanding of electronic effects in the band structure of transition metals.

As discussed in section 2.7, X-ray absorption spectral changes due to temperature changes can be simulated by assuming the Fermi-Dirac statistics. Assuming a constant total density of states, there is a possible shift in the Fermi level/chemical potential to conserve the number of electrons during thermal changes. Redistribution of electrons as per Fermi-Dirac distribution and Fermi level shift leads to changes in X-ray absorption spectra. Such changes can be simulated using density of states calculation from DFT and then calculating temperature-dependent X-ray absorption spectra using Equation 2.17. Here, the spin-resolved partial unoccupied density of states redistribute according to Fermi-Dirac distribution:

$$\Delta XAS_{DFT} = XAS_{DFT}(T + \Delta T) - XAS_{DFT}(T). \quad (5.1)$$

Also, following the Fermi-Dirac distribution, these changes can be empirically approximated by

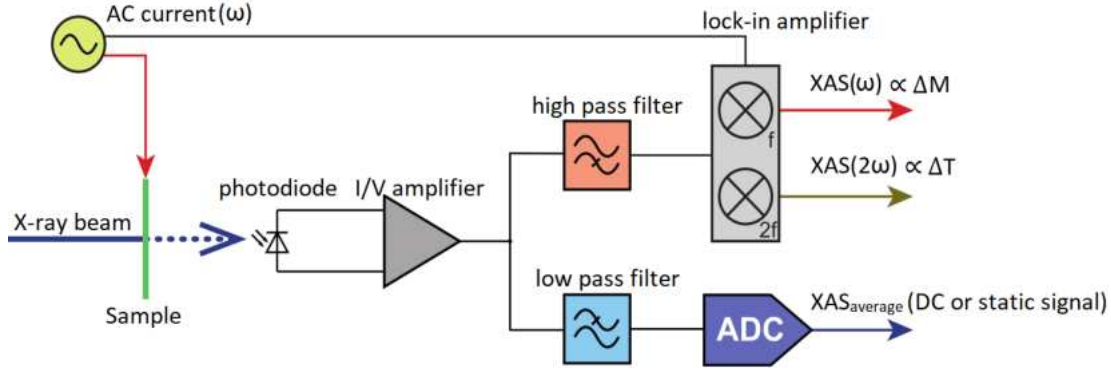


Figure 5.1: Schematic for the second harmonic lock-in measurements to measure temperature induced spectral changes. A sinusoidal current is passed through the sample placed in the X-ray beam. The transmitted intensity is monitored by a photodiode. DC or static signal gives X-ray absorption spectra. First and second harmonic measurements give current induced spin dynamics and temperature induced changes respectively. Adapted from figure by Dr. Christian Stamm [299].

convolving the experimental spectra with the difference in the Fermi distribution at the two different temperatures:

$$\Delta XAS_{\text{conv}} = XAS_{\text{exp}} * (F(T + \Delta T) - F(T)), \quad (5.2)$$

where $F(T)$ is the Fermi-Dirac distribution function given by:

$$F(E, T) = \frac{1}{\exp \frac{E - \mu}{k_B T} + 1}. \quad (5.3)$$

Here, μ is the Fermi level or the chemical potential. k_B is the Boltzmann constant. E is the energy of the valence bands. Under the assumptions that temperature induced electronic changes are small and simulated X-ray spectra are comparable to the experimental XAS spectra, the simulated spectral changes from the DFT or directly from the convolution of the experimental spectra should be similar.

In this chapter, such X-ray absorption spectral changes are simulated and compared to the experimental spectral changes for 3d transition metal thin films (Cobalt, Chromium, Titanium and Copper) measured by our collaborators (Dr. Christian Stamm et al.).

To measure the small temperature-induced spectral changes with very high sensitivity, a lock-in-measurement-based technique was used at 2nd harmonic (see Fig. 5.1). When an AC current of frequency ω is applied to the thin films, they get heated by the Joule heating. Joule heating is proportional to the square of the driving AC current. This apparent rectification of electric current leads to a temperature change (ΔT) which contains two components: the DC or static heating part (T_1) and the oscillating amplitude (T_2). Since the Joule heating is proportional to the square of the driving current, the oscillating component in temperature has double the frequency (second harmonic) of the driving AC current frequency:

$$\Delta T(t) \propto T_1 + T_2 \sin 2\omega t. \quad (5.4)$$

X-ray absorption measurements done via photodiode also contain the static and oscillating (1st and 2nd harmonic) components which can be separately measured using lock-in amplifier after passing through low and high pass filters (Fig. 5.1). The static signal, measured with an Analog to Digital converter (ADC), gives the XAS spectra. The measurement of first and second harmonic signals with a lock-in amplifier gives the spectral changes corresponding to current-induced and temperature-induced dynamics respectively. Current-induced dynamics in Pt/3d metal bilayers has been discussed in details by Christian Stamm et al. in [299]. In this chapter, we will focus on the temperature induced changes in XAS spectra observed in the second harmonic signal.

The X-ray absorption signal can be expanded in the multiples of harmonics of an applied AC current frequency:

$$\text{XAS} = \text{XAS}(0) + \text{XAS}(\omega) + \text{XAS}(2\omega) + \text{XAS}(3\omega) + \dots, \quad (5.5)$$

where XAS(0) is the static signal which gives the averaged XAS spectra. Amplitude of second harmonic component, XAS(2 ω), can be written as a Fourier transform:

$$\text{XAS}(2\omega) \propto \int \text{XAS}(t) \times e^{-i(2\omega)t} dt. \quad (5.6)$$

For small XAS changes corresponding to an oscillating temperature amplitude T₂, XAS(2 ω) can be approximated as:

$$\text{XAS}(2\omega) \approx \text{XAS}(T_0 + T_1 + T_2) - \text{XAS}(T_0 + T_1), \quad (5.7)$$

where T₀ is the room temperature and T₁ and T₂ are static and oscillating amplitudes of temperature change. The static temperature (T₀ + T₁) was taken from the DC resistivity measurements for cobalt [300]. In all other cases, it was taken to be 300K. The periodic temperature change(T₂) in Pt/Co bilayers due to sinusoidal current was estimated by fitting the experimental spectral changes over the full photon energy range (see Fig. 5.3 and Fig. 5.5). For the other bilayers (Pt/Ti, Pt/Cr and Pt/Cu), the estimate is only based on the eye and simulated spectral changes are only for the qualitative comparison with the experimental data. In the next sections in this chapter, we will discuss and interpret the shapes of the temperature-induced spectral changes and what are the similarities and differences between observed ΔXAS and simulated ΔXAS .

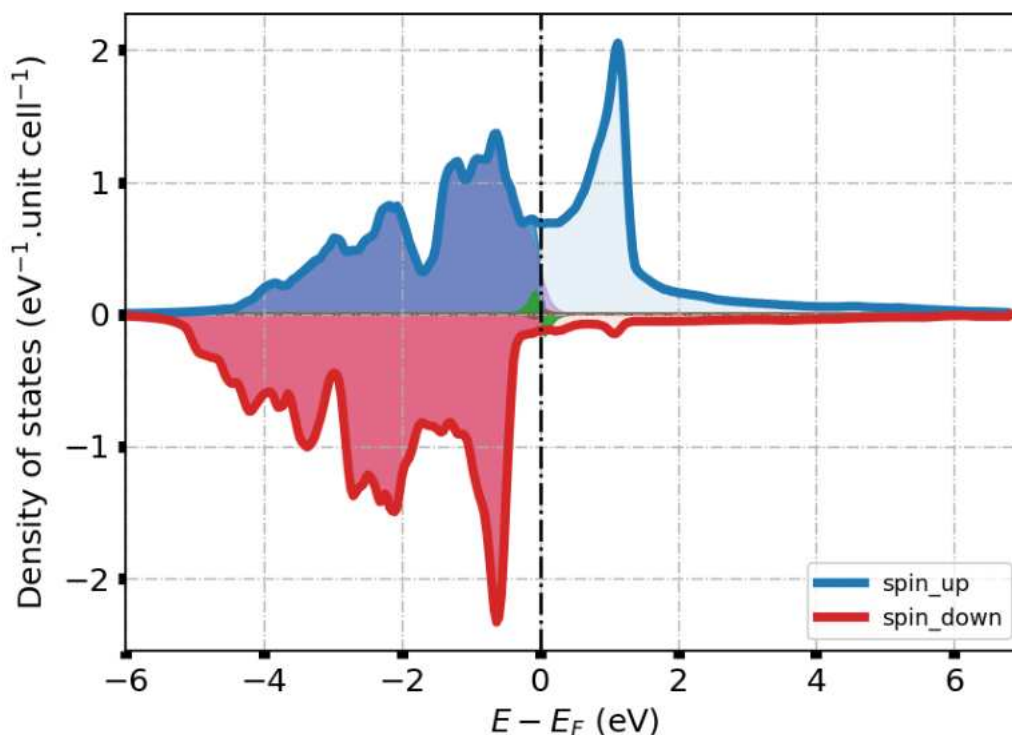


Figure 5.2: Spin-resolved partial density of states for hcp Co around Fermi energy (0eV). Blue and red shaded regions represent spin up and spin down DOS respectively. Dark-shaded regions below the Fermi energy represent the occupied states. Light-shaded regions above the Fermi energy represent unoccupied DOS. Small green and brown-shaded curves represent the temperature-induced DOS changes assuming the Fermi-Dirac distribution.

5.1 Pt/Co

Cobalt films show ferromagnetic ordering at room temperature. The Co/Pt structure is quite important for magnetic data storage devices. Here we simulate the thermally induced electronic band structure changes in Co and compare it with experimental data measured at Co/Pt bilayer. Fig 5.2 shows the spin-resolved partial density of states (PDOS) in the 3d band of ferromagnetic, hcp (hexagonal closed packed) cobalt, calculated through density functional theory simulations using the Elk code [212]. It can be seen that 3d bands are exchange-split by approximately 0.9 eV. The simulated PDOS for the hcp Co are similar to the DOS provided in [301]. The input file for density of state calculation can be seen in the appendix A.5.

Fig.5.3 (top) shows the simulated and measured XAS spectra and spectral changes at Co L edge. The spectra is convoluted with a Voigt lineshape broadening which accounts for the instrument Gaussian broadening of 0.2 eV (FWHM) and the lifetime Lorentzian broadening of 0.55 eV (FWHM) to simulate the experimental lineshape. A core level spin-orbit splitting of 14.85 eV to match the separation between L_3 and L_2 peaks in the measured XAS spectra. A core level exchange splitting of 0.5 eV was used in the simulations to simulate the asymmetry at L_3 peak in the Δ XAS spectra.

The simulated X-ray absorption spectra (green curve in Fig. 5.3, top) for ferromagnetic hexagonal closed-packed (hcp) cobalt fits reasonably well with line-shape of the experimental

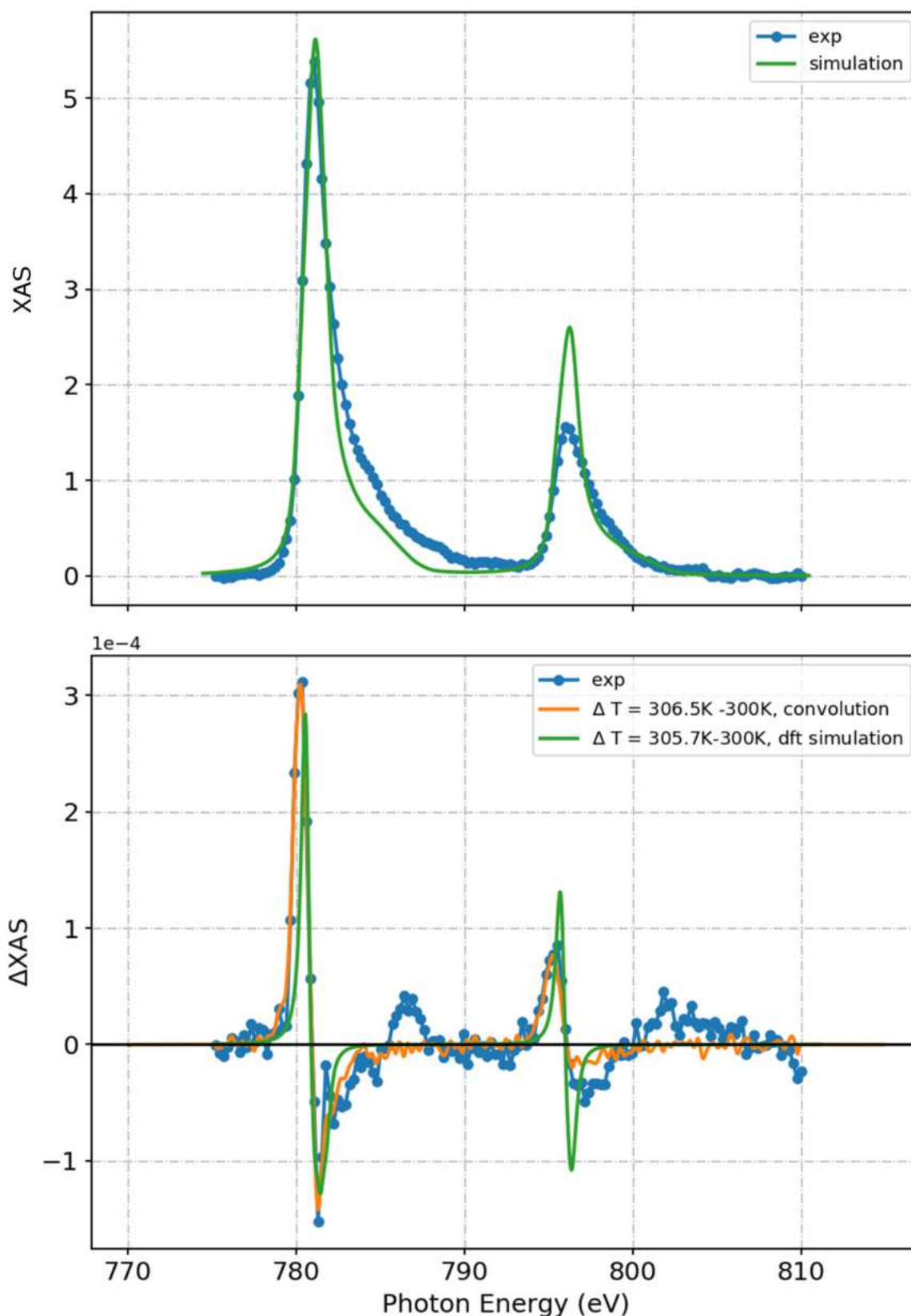


Figure 5.3: Electronic changes in Pt/Co. Top: XAS spectra at Co L edge (exp (blue) and simulation (green)). Bottom: 2ω XAS spectral changes due to AC current density of $j = 2.35 \times 10^6 \text{ cm}^{-2}$ (blue dots) and simulated spectral changes based on convolution (orange) and DFT (green).

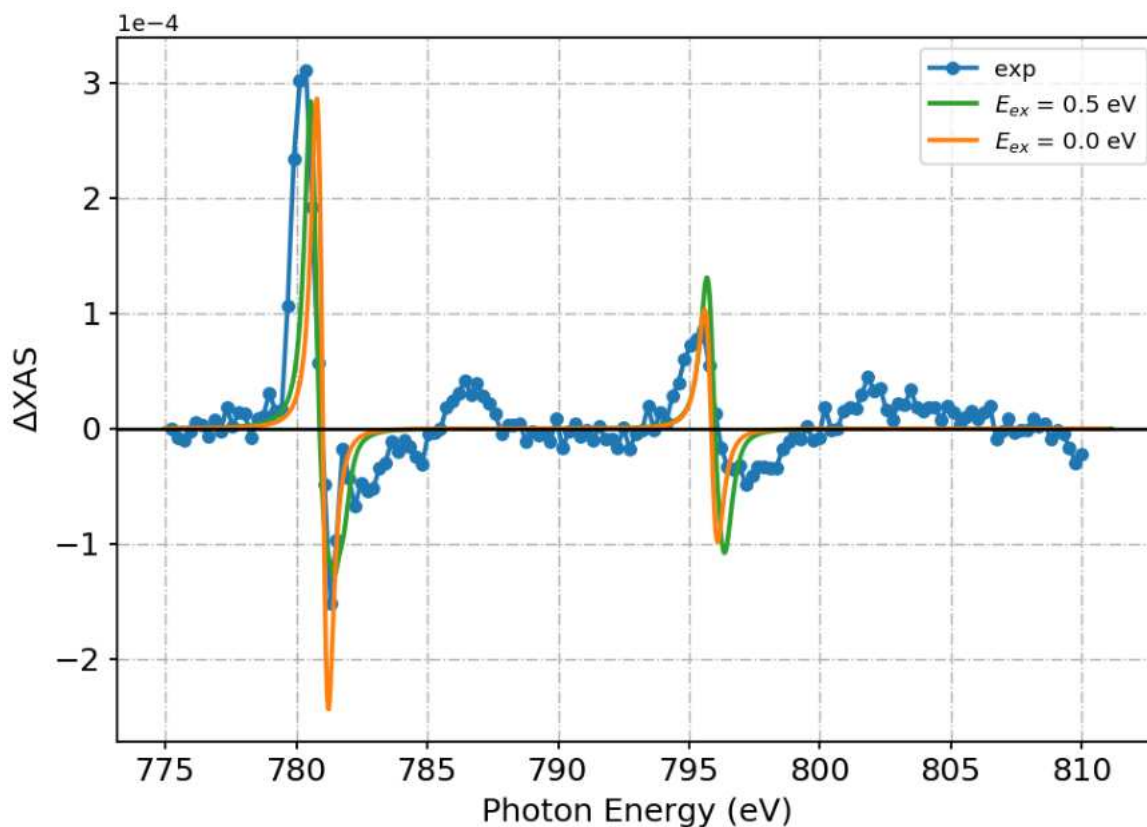


Figure 5.4: Effect of core level exchange splitting on XAS spectral changes in Co. Blue curve shows the experimentally measured spectral change. Green and orange curves show the DFT-based simulated spectral changes with and without core-level exchange splitting respectively. Including the exchange splitting makes the lineshape more asymmetric near the L_3 edge.

spectra. Certain broadening effects (like due to core hole-valence electron interactions) have not been included in simulations [302, 303]. The branching ratio (L_3/L_2) could not be simulated accurately under single electron approximation as it does not consider certain core-hole and many-body effects which lead to re-mixing of the core levels and thus redistributing the intensities between L_2 and L_3 absorption edges [291, 292, 304]. It can be anticipated that the simulation of spectral changes (ΔXAS) will also be affected by such a limitation.

Fig.5.4 shows the effect of core level exchange splitting on the temperature induced spectral changes in XAS. The exchange splitting in 2p core levels originates from the spin polarized potential of 3d valence bands [219]). When we compare the spectral changes with and without exchange splitting, we can see that the asymmetry at the L_3 peak (positive and negative part) is enhanced by the core level exchange splitting. The value of core-level exchange splitting was chosen to fit the asymmetry at L_3 edge. The asymmetry at L_2 edge is nearly unaffected by core level exchange splitting. This is probably because of the fact that L_3 levels are split into 4 equi-spaced energy levels while L_2 levels are split in only two equi-spaced levels. Thus, L_3 levels are affected more than L_2 . The effect of exchange splitting is not visible directly in the X-ray absorption spectra due to the lifetime broadening. This further emphasizes the fact that ΔXAS signal is more sensitive to the electronic band structure and contains the information beyond that can be obtained from the lifetime-broadening-limited XAS spectra. More input from transient XAS signal can be used to better simulate the electronic properties of 3d metals.

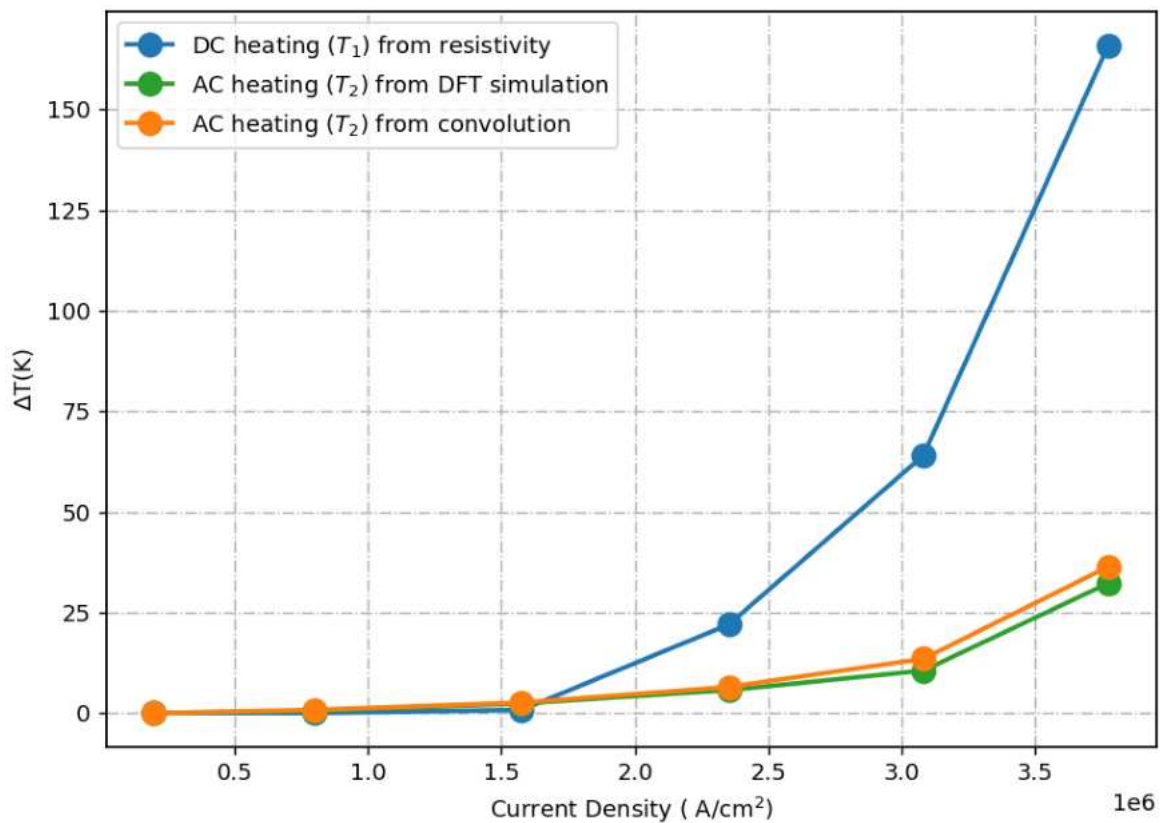


Figure 5.5: Estimated DC and AC heating components in the temperature change from resistivity measurements and simulations. Blue: Estimated DC heating due to AC current density from experimentally measured resistivity measurements. Green and orange: Estimated temperature change from XAS spectral fitting based on DFT and convolution respectively. Here, the resistivity-measurement-based DC heating components (blue) are used as the input in the simulation.

As evident from Fig. 5.3(bottom), the temperature-dependent X-ray absorption changes could be fitted using a convolution function consisting of the difference of Fermi-Dirac function at two temperatures (Orange curve in Fig. 5.3, bottom). Also, X-ray spectral changes, simulated using temperature-dependent Fermi distribution and DFT-based density of states, fit to the experimentally observed changes. Both calculations evidently miss small post edge features (positive bumps after L_3 and L_2 edges) observed in the experiment. These features are probably due to the change in unoccupied density of states far above the Fermi energy which is not accounted for in the Fermi-Dirac-distribution-based simulations and/or band structure calculations. Simulations are also not able to account for the width of the ΔXAS observed in the experiment. Both simulations give similar estimate of temperature increase for different current densities as shown in Fig. 5.5. Even between simulations and experiment, thermal changes in XAS of cobalt can be primarily attributed to change in Fermi distribution.

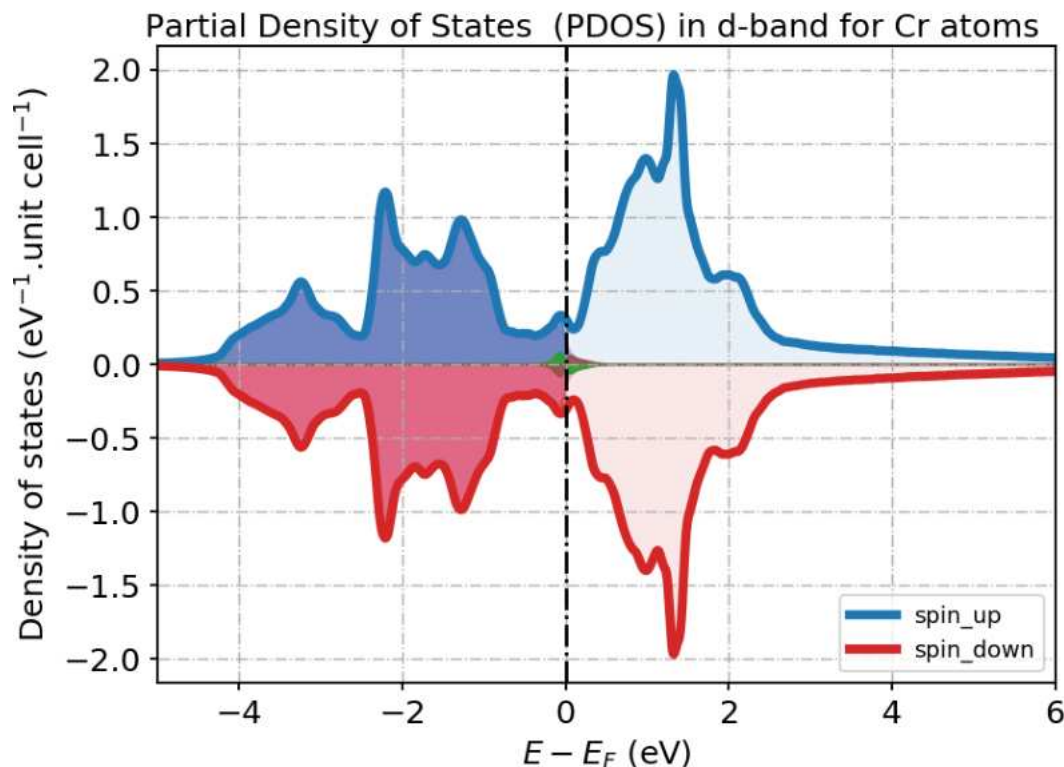


Figure 5.6: Partial density of states in 3d band for non-magnetic (NM) bcc Cr around Fermi energy (0 eV). Blue and red shaded regions represent spin up and spin down DOS respectively. Dark-shaded regions below the Fermi energy represent the occupied states. Light-shaded regions above the Fermi energy represent unoccupied DOS. Small green and brown-shaded curves represent the temperature-induced DOS changes assuming the Fermi-Dirac distribution.

5.2 Pt/Cr

Chromium shows a very characteristic spin density wave (SDW) structure at room temperature. While cobalt thin films show ferromagnetic ordering and have nearly 7.6 electrons in 3d band, Chromium thin films show the anti-ferromagnetic SDW structure and consist of the half-filled 3d band. Spin fluctuations in Cr and its band structure have been of scientific interest for quite long [305–309]. Here, we study the thermally-driven electronic structure changes due to thermal excitation and compare it with experimental spectra measured in Cr/Pt bilayer. DFT simulation, shown here, were performed assuming non-magnetic chromium with body centred cubic (bcc) structure. Fig 5.6 shows the partial density of states (PDOS) in the 3d band for non-magnetic (NM) bcc chromium. Broadening of DOS or band structure in non-magnetic chromium, compared to that of ferromagnetic cobalt, can be expected because of absence of exchange interactions [228].

Fig 5.7 shows the simulated and measured XAS spectra and spectral changes at Cr L edge. The spectra is convoluted with a Voigt lineshape broadening which accounts for the instrument Gaussian broadening of 0.15 eV (FWHM) and the lifetime Lorentzian broadening of 0.35 eV (FWHM) to simulate the experimental lineshape. A core level spin-orbit splitting of 8.6 eV was used in the simulations to match the separation between L_3 and L_2 peaks in the measured XAS spectra. Input file for density of state calculation can be seen in Appendix A.5.

The simulated XAS line shape (in Fig. 5.7(top)) is narrower compared to the measured XAS and the simulated L_3/L_2 intensity ratio is quite different from the observed one. This is because of the core-level spin mixing as a result of the small spin-orbit splitting and core-hole effects. Further, the spin density fluctuations in chromium [305–309] can't be considered in the simple DFT framework and needs more sophisticated tools like DMFT. Even the XAS simulations using the PDOS from AFM band structure calculation of bcc Cr (not shown) did not reproduce the measured spectra.

We detect a pronounced change of the absorption spectrum upon current injection, as shown in the Fig.5.7 (bottom). The lineshapes (but not the intensity) of Δ XAS spectra in Fig.5.7(bottom) could be reproduced from the convolution of measured XAS spectra. It underestimates the peak intensity at L_2 edge which is surprising as it uses the experimental branching ratio from the measured XAS spectra. This is probably due to the fact that density of states in orbitals taking part in L_3 and L_2 transition change in the different way. This leads to different intensity ratio in case of measured Δ XAS compared to measured XAS spectra. Simple convolution does not take into account of the distinctive orbital-dependent changes in density of states. The DFT-based simulations of Δ XAS spectra does not simulate the post edge features observed in the measured spectra while also underestimating the broadening.

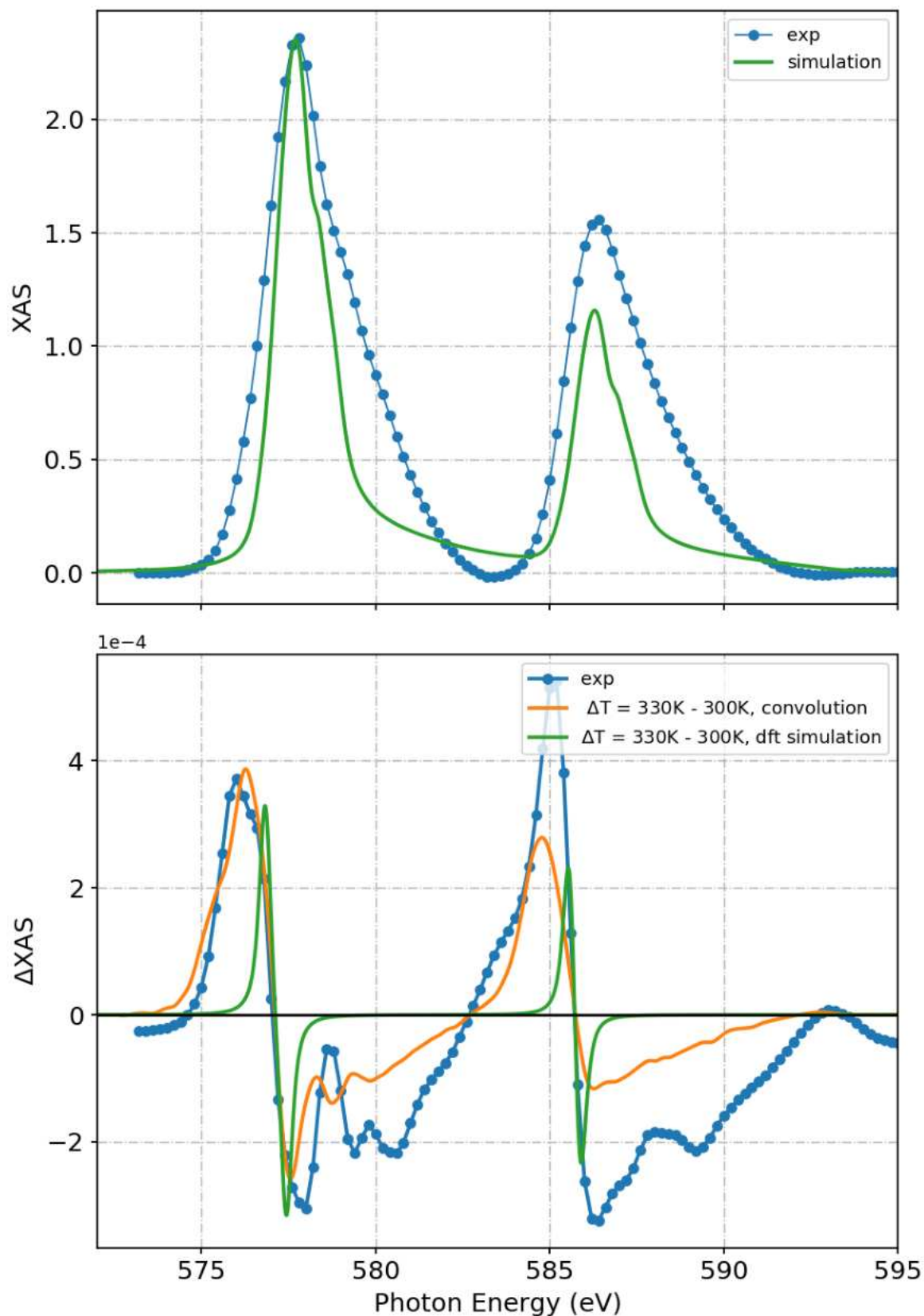


Figure 5.7: Electronic changes in Pt/Cr. Top: XAS spectra at Cr L edge (exp (blue) and simulation (green)). Bottom: 2ω XAS spectral changes due to AC current density (blue) and simulated spectral changes based on convolution (orange) and DFT (green).

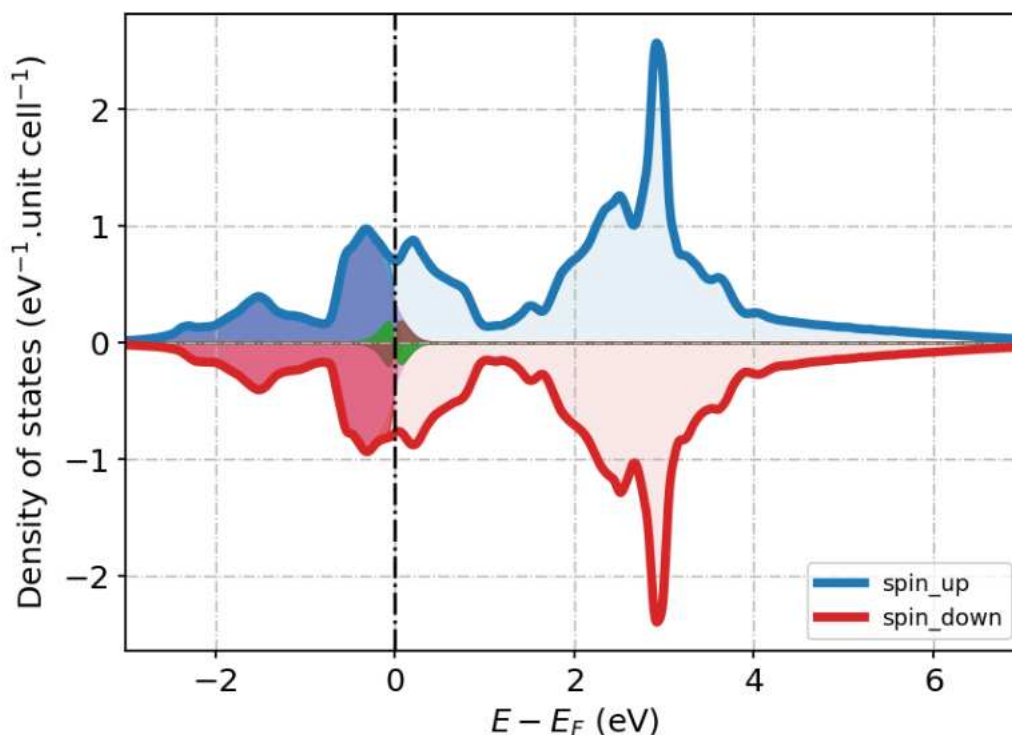


Figure 5.8: Partial density of states in 3d band for non-magnetic hcp Ti around Fermi energy (0 eV). Blue and red shaded regions represent spin up and spin down DOS respectively. Dark-shaded regions below the Fermi energy represent the occupied states. Light-shaded regions above the Fermi energy represent unoccupied DOS. Small green and brown-shaded curves represent the temperature-induced DOS changes assuming the Fermi-Dirac distribution.

5.3 Pt/Ti

Titanium, due to its corrosion resistance properties, has various industrial applications such as paints, catalyst etc. Being an early member of 3d transition series, it has a large number of unoccupied d states. Here, we compare the simulations for spectral changes in thermally excited Ti with experimental measurements on Ti/Pt bilayer. Fig 5.8 shows the partial density of states (PDOS) in 3d band for non-magnetic (NM) hcp (hexagonal close-packing) titanium. Fig 5.9 shows the simulated and measured XAS spectra and spectral changes at Ti L edge. The spectra is convoluted with a Voigt lineshape broadening which accounts for the instrument Gaussian broadening of 0.15 eV (FWHM) and the lifetime Lorentzian broadening of 0.3 eV (FWHM) to simulate the experimental lineshape. Core level spin-orbit splitting of 5.8 eV was used in the simulations to match the separation between L_3 and L_2 peaks in the measured XAS spectra. The input file for density of state calculation can be seen in Appendix A.5. As shown in Fig.5.9 (top), the simulated XAS lineshape of non-magnetic hexagonal closed-packed (hcp) titanium differs from the experiment lineshape. The density of states simulations (Fig 5.8) show a large number of unoccupied states available above from the Fermi energy. This leads to peak-splitting in XAS spectra. More accurate density of states simulations are needed to take into account of the correct bandwidth of band structure. Also, the mixing of core levels due to small spin-orbit splitting affects the intensity ratio between L_3 and L_2 edges [294]. The simulated Δ XAS spectral line shapes in Fig. 5.9(bottom) cannot

explain the broad shouldered pre-edge feature observed in the experiment at L_3 and L_2 edges. This indicates that certain thermal changes in Ti/Pt lie deep into band structure away from the Fermi energy. The double peaked structure in DFT-based XAS simulation is not present in the corresponding Δ XAS simulation. However, situation is reversed in the experimental observations where the double-peaked structure is present in Δ XAS spectra and not in the XAS spectra. Another important feature is the extra peak near 467 eV which is present in the convolution of measured XAS spectra (orange curve in 5.9 (bottom)). This peak corresponds to the small peak observed in the XAS spectra at same photon energy. Such a pronounced peak is not observed in the measured Δ XAS spectra. The spectral changes are qualitatively different from the ones observed in the Pt/Co sample, and consequently the model of a Fermi-Dirac broadening of the XAS line is not sufficient to explain the experimental data.

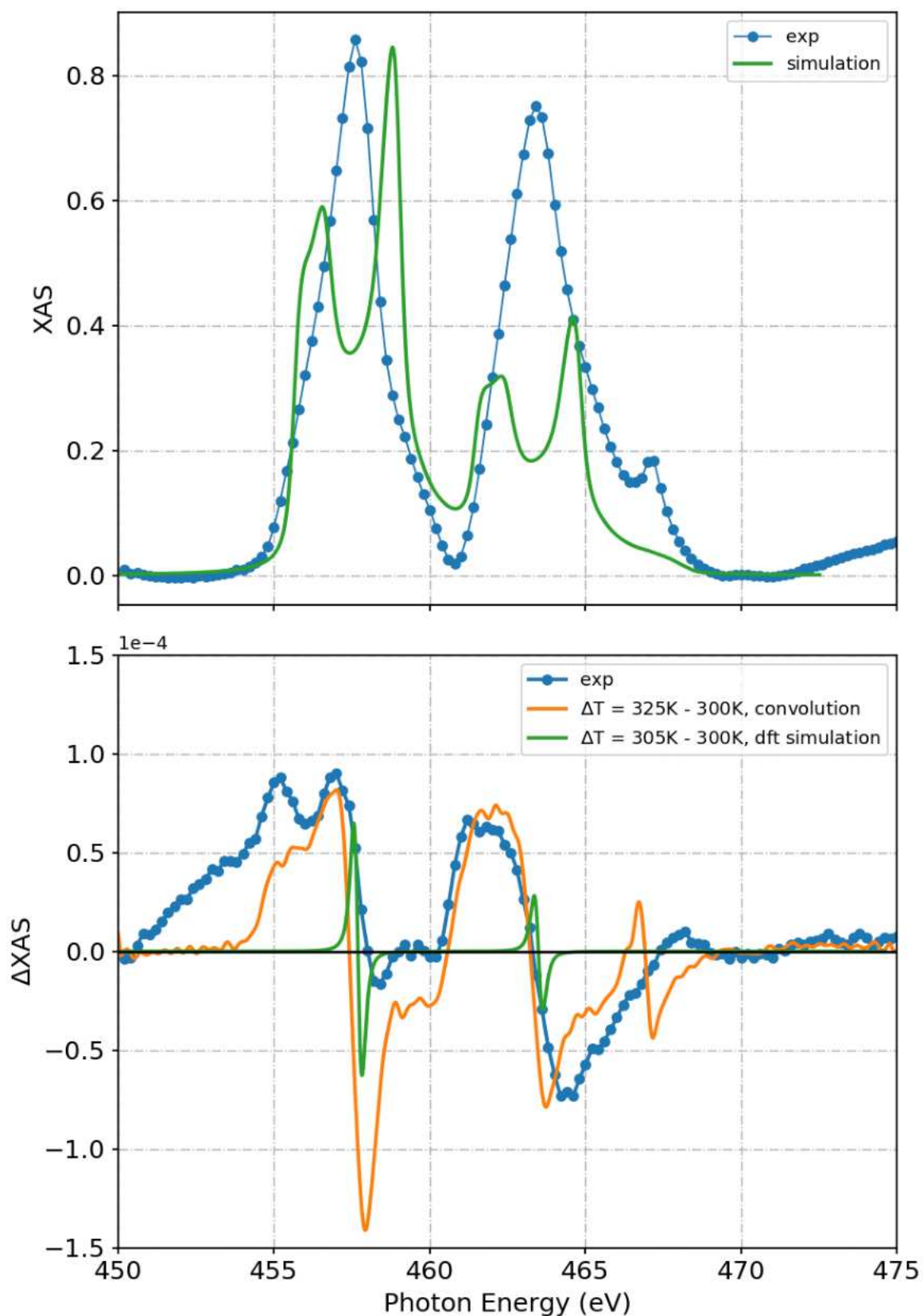


Figure 5.9: Electronic changes in Pt/Ti. Top: XAS spectra at Ti L edge (exp (blue) and simulation (green)). Bottom: 2ω XAS spectral changes due to AC current density (blue) and simulated spectral changes based on convolution (orange) and DFT (green).

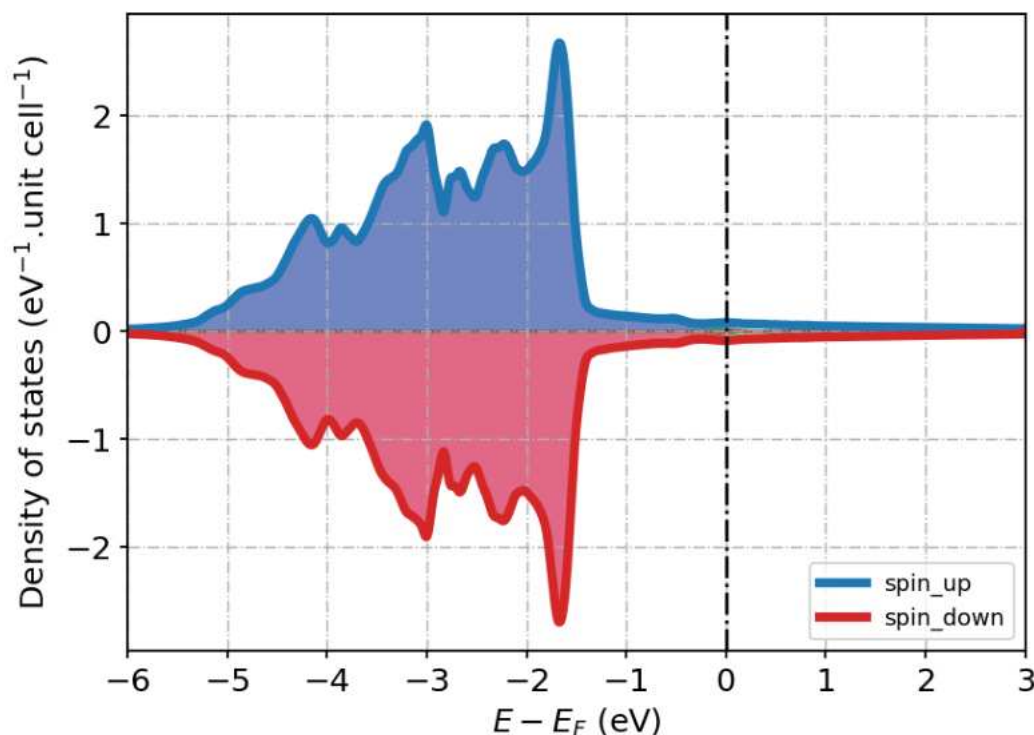


Figure 5.10: Partial density of states in 3d band for nonmagnetic (NM) fcc Cu around Fermi energy (0 eV). Blue and red shaded regions represent spin up and spin down DOS respectively. Dark-shaded regions below the Fermi energy represent the occupied states. Light-shaded regions above the Fermi energy represent unoccupied DOS. Small green and brown-shaded curves represent the temperature-induced DOS changes assuming the Fermi-Dirac distribution.

5.4 Pt/Cu

Copper, due to its high electrical conductivity, has applications in electronics and solar industry. Being at the end of 3d transition metal series, it has a very small number of unoccupied states which are essentially due to hybridization with the s-p states. Here, we simulate the temperature induced changes in Cu and compare it with the experimental measurements of Cu/Pt bilayers. Fig 5.10 shows the partial density of states (PDOS) in the 3d band for non-magnetic (NM) fcc (face-centered close-packing) copper. As can be seen, there are very few 3d states available above the Fermi energy and have s-p like delocalized character. Most of the 3d states lie deep below the Fermi energy.

Fig 5.11 shows the simulated and measured XAS spectra and the spectral changes at Cu L_3 edge. The spectra is convoluted with a Voigt lineshape broadening which accounts for the instrument Gaussian broadening of 0.2 eV (FWHM) and the lifetime Lorentzian broadening of 0.7 eV (FWHM) to simulate the experimental lineshape. A core level spin-orbit splitting of 19.6 eV was used in the simulations. The input file for the density of state calculation can be seen in Appendix A.5. The simulated L_3 line shape of nonmagnetic face centred cubic (fcc) copper matches with the experimental XAS apart from certain post edge features. The broadening of electronic band structure of Cu is not simulated properly within DFT framework due to strong hybridization with the delocalized s-p states. Proper electronic correlations should be taken into account in DMFT

framework. The lineshape of Δ XAS is fitted well with the convolution-based Fermi-broadening while DFT-based calculation lacks the post edge asymmetric elongated tail, seen in experiment. Additionally, the convolution-based transient XAS simulation shows the pre-feature which is not present in the measured Δ XAS signal.

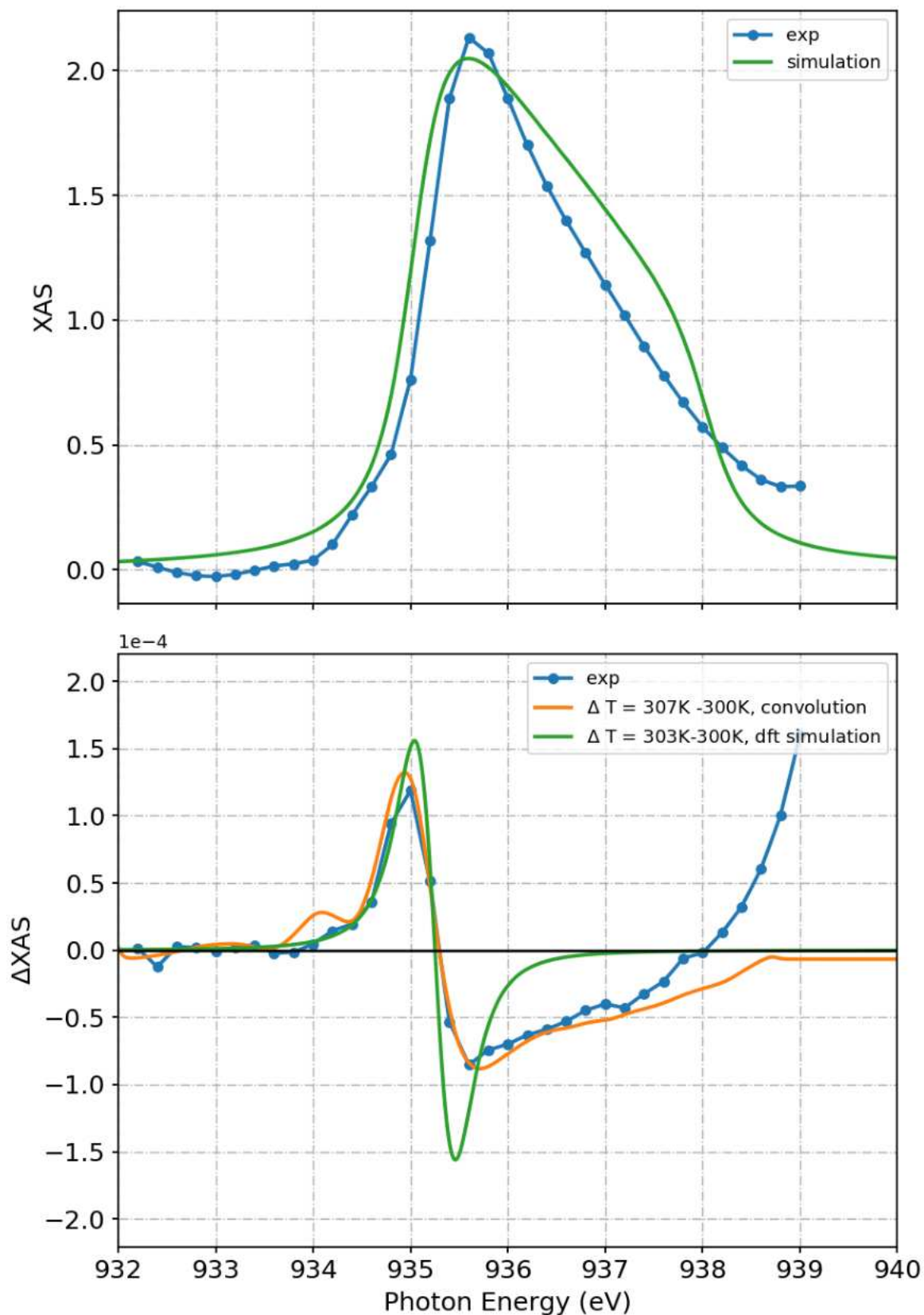


Figure 5.11: Electronic changes in Pt/Cu. Top: XAS spectra at Cu L_3 edge (exp (blue) and simulation (green)). Bottom: 2ω XAS spectral changes due to AC current density (blue) and simulated spectral changes based on convolution (orange) and DFT (green).

5.5 Discussion and outlook

We compare X-ray absorption spectra and thermally-induced spectral changes in 3d transition metals with DFT-based lines shapes simulated under single electron theory and dipole approximation. Also, the spectral changes are compared with the direct convolution of measured XAS spectra with the temperature-dependent change in the Fermi-Dirac distribution. DFT-based single-electron-based XAS description of 3d transition metals lacks certain core-level interactions which is evident in failing to describe the line shape of Ti (as such interactions become more relevant/dominant because of the small spin orbit splitting) and the intensity ratios of Co, Cr (core-valence interactions and many body effects): XAS simulations using the independent particle approximation seem to be valid for certain elements in the middle of 3d transition metal series (Fe, Co and Ni), while lacking certain features for the other elements. This is because core-hole and many body effects are more prominent from half-filled 3d bands towards early transition metals. Despite the lack of certain interactions, DFT-based simulations give a good description of the line-shapes of spectral changes in Co and Fe (see section 2.7). Further it is evident that certain spectral changes (such as post edge features in Δ XAS of Co and Cr or pre-edge changes in Δ XAS of Ti) cannot be described with the Fermi-broadening-based electron reshuffling and probably occur via a temperature-dependent evolution of near- Fermi states and band structure itself. Theoretically, such changes should probably be described by time-dependent DFT/DMFT calculations. Nevertheless, such a simple description is able to provide us a temperature estimate of spectral changes for different current densities as shown for Cobalt. This method could potentially be very useful for estimating the (dynamic) temperature evolution during ultrafast laser induced dynamics in metals as the spectral changes not only depend on temperature difference but also on the initial temperature. Convolution of measured XAS spectra already contains most details of many body effects and electronic correlations. Thus, it gives a very direct insight in electronic band structure changes which deviate from the Fermi-Dirac distribution. Although, care must be taken in interpretation because convolution based simulation assumed isotropic changes in orbital-resolved density of states whereas temperature induced changes can be orbital-dependent such as suspected in case of Cr from the change in branching ratio between XAS spectra and Δ XAS spectra. This can be used as more accurate estimate of temperature. However, to understand the microscopic properties such as electronic correlations, exchange interactions and many body effects which govern the electronic band structure, a full DFT/DMFT-based model should be used. Comparing the DFT-based Δ XAS simulations with the observations will certainly help to improve our understanding of many-body effects and the itinerant behaviour of the metals. It should be noted that, as can be seen in all cases, the temperature-dependent spectral changes constitute a very small fraction of the spectra (1 in 10000 or 0.01%). We will see in the next chapter that these changes are orders of magnitude smaller than the spectral changes induced by modification of exchange interactions during phase transition of FeRh (~5%).

6 Time resolved X-ray absorption spectroscopy of optically excited FeRh

In this chapter, the results from time resolved resonant soft X-ray absorption spectroscopy (XAS) of the laser-induced phase transition of FeRh are described. The time scales of different interactions and microscopic dynamics during FeRh phase transition are discussed.

Time-resolved X-ray absorption spectroscopy, near Fe L_3 edge, of the phase transition in optically excited FeRh was performed using the transmission zone plate grating (TZPG)-based method at the SCS instrument as described in section 3.4.2. A FeRh sample of thickness 70 nm was used for this experiment. Epitaxial (001) FeRh thin films were deposited on a 100 nm thick epitaxial SiC (001) membranes using magnetron sputtering by our collaborators Dr. Jon Ander Arregi and Vojtěch Uhlíř. In-plane and out-of-plane epitaxial texture and lattice parameters were determined using the X-ray diffraction measurements. The thickness of the FeRh films was determined by the X-ray reflectivity measurements. Magneto-optical Kerr (MOKE) microscopy was used to characterize the phase transition and the temperature-hysteresis in the FeRh samples. The sample growth and characterization data for FeRh can be seen in Appendix A.4. The penetration depth of 800 nm optical laser pump is around 20 nm. 70 nm thick FeRh film ensures that back interface FM layer is not pumped directly with the optical laser. The attenuation length of the X-ray probe pulse across the Fe L_3 edge varies from 24 nm to 94 nm (Fig. 6.1 b)). Thus, the last 35 nm thickness of 70 nm thick FeRh thin film contributes only a small fraction (less than 10%) near Fe L_3 edge to the transient absorption signal. Also, a 70 nm thick sample has a sharp transition and narrow hysteresis region compared to thinner samples as can be seen from magneto-optical (MOKE) characterization (See Fig. A.12). This ensures that the transition temperature is always above the room temperature during the heating or the cooling cycles and the initial AFM state is recovered after cooling. X-ray and optical pulses are employed in nearly collinear geometry and impinge from the capping layer side on the membrane of size of $500 \mu\text{m} \times 500 \mu\text{m}$. The pulse resolved DSSC detector was used to record the reference and absorption signals simultaneously.

Fig. 6.1 a) shows the pulse sequence used in the experiment. First X-ray pulse probes the initial AFM state in the FeRh thin film. Second X-ray pulse probes the transient or intermediate state in the FeRh film which is pumped by optical pulse with central wavelength around 800 nm and pulse duration around 35 fs. The time delay (Δt in Fig. 6.1 a)) between second X-ray pulse and optical pulse is varied using a delay stage. Difference signal ΔXAS is obtained by subtracting the initial absorption signal probed by the first x-ray pulse from the transient absorption signal probed by the second X-ray pulse. The third X-ray pulse (optically unpumped) gives the long time (70 μs) final state of the transition. Recurring dynamics was recorded by measuring multiple trains and

then binned in photon energy or time delays accordingly.

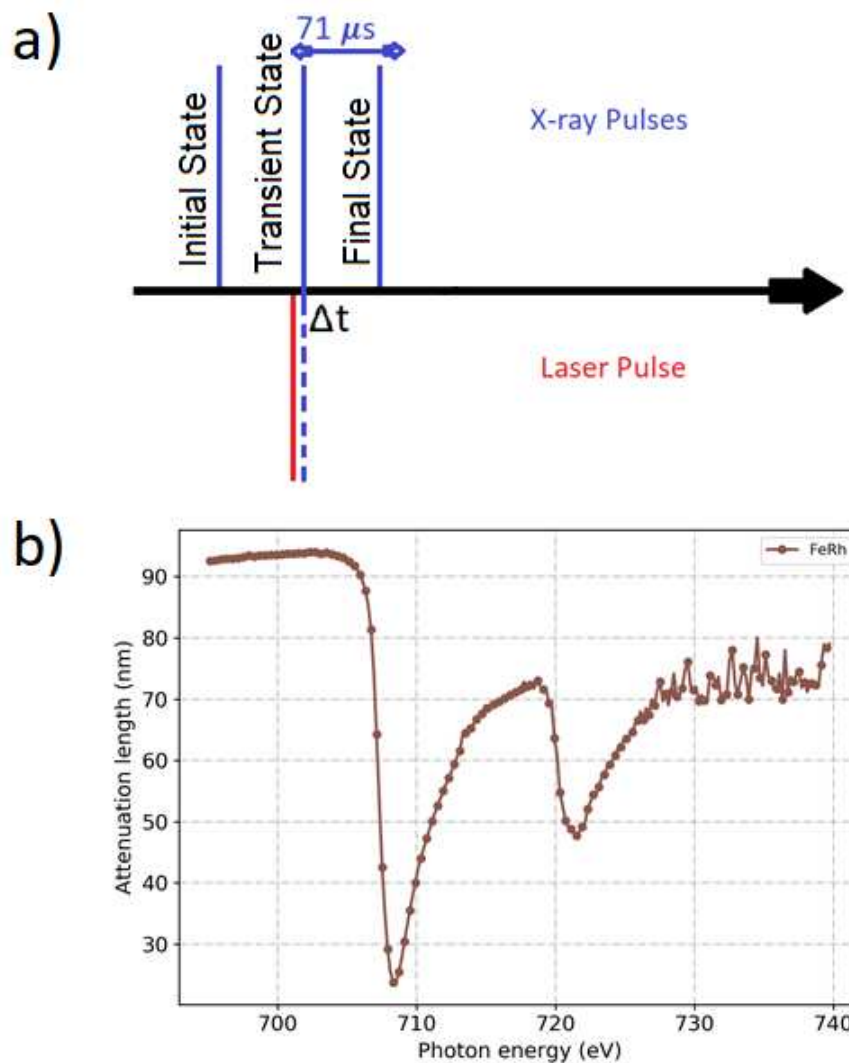


Figure 6.1: a) X-ray and optical pulse sequence within one train. Blue vertical lines represent X-ray pulses while red vertical line represents optical pulse. Δt represents the time delay between optical and X-ray pulse. X-axis represents time. b) Attenuation depth of X-rays in FeRh across Fe L_3 edge measured by X-ray absorption spectroscopy. Absorption of substrate, heat sink and the capping layer is taken into account.

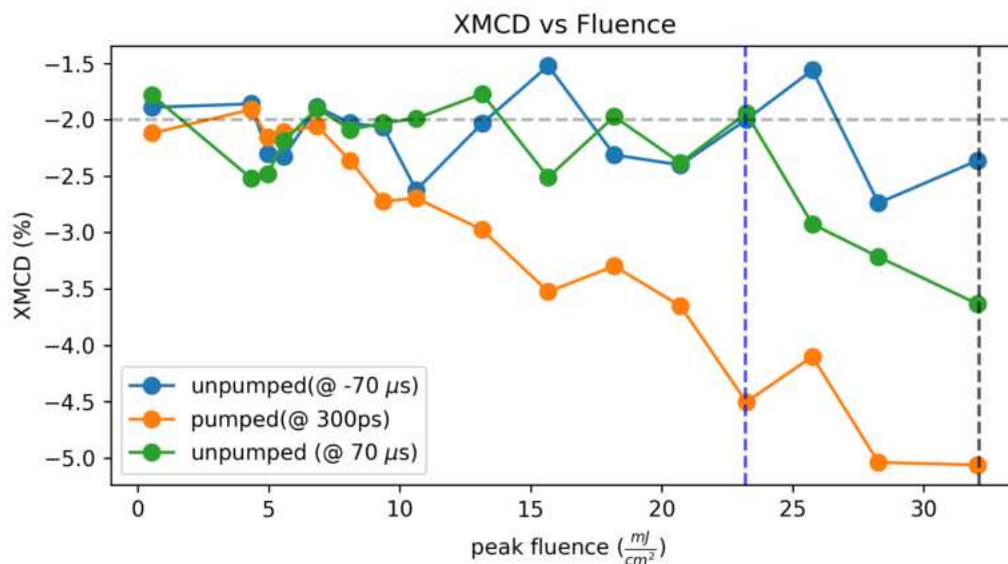


Figure 6.2: X-ray magnetic circular dichroism (XMCD) versus optical laser fluence measurement. Initial state (blue), 300 ps after laser excitation (orange), Final state 70 μ s after optical excitation (green). Dashed blue vertical line represents selected laser pump fluence. Dashed black vertical line represents damage threshold. Initial XMCD of around 2%, as measured by partial circularly polarized X-rays, is due to the ferromagnetic interface layer.

As shown in Fig. 6.2, XMCD measurements were performed to determine the optimal fluence and damage threshold of sample. Partial circularly polarized X-ray pulses for XMCD measurements were obtained using Fe thin film polarizer [310]. XMCD signal was measured at fixed delay of 300 ps and at Fe L_3 edge (708 eV). The peak fluence was determined by laser pulse energy and beam size measurements done via a laser pulse-energy monitor and knife edge scans, respectively. A optical beam size (FWHM) of around 180 μ m and a X-ray beam size (FWHM) of around 50 μ m was used. The damage threshold (for optical pump pulse) for the FeRh membranes was found to be at the peak fluence of 32 mJ/cm². Peak fluence of 23 mJ/cm² was chosen for the measurements to reach the FM state in the probed volume and get maximum magnetic contribution: The selected fluence shows a maximum XMCD contrast (orange curve in Fig. 6.2) while mitigating the long term heating effects after 70 μ s (i.e. blue curve and green curve in Fig. 6.2 are still similar). The X-ray fluence was kept \sim 1 mJ/cm².

6.1 Energy scans across Fe L_3 edge at fixed time delays

Photon energy scans near the Fe L_3 edge were performed at fixed time delays as shown in Fig. 6.3. The X-ray photon energy was varied using continuous synchronized monochromator-undulator scans. The monochromator resolving power of around 3000 gives an energy resolution of ~ 250 meV. Now we compare the initial AFM state and final FM state reached by optically pumping the FeRh films with the aforementioned fluence and pulse sequence settings.

It can be observed from Fig. 6.3 a) and b) that the experimental lineshape is well-matched with the calculated X-ray absorption spectra. Spectral changes from initial AFM state, at fixed delays of 300 ps and 70 μ s, as shown in Fig. 6.3 e), are similar to spectral change observed in simulations where final state is considered to be fully saturated FM state (Fig. 6.3 d)). There are no distinct features observed in the spectral changes measured at time delays of 300 ps and 70 μ s. This indicates that the AFM to FM transition is completed in the probed sample region. This observation is also consistent with the spectral changes observed in the thermally-driven FeRh phase transition (last plot in Fig. 6.3 e)). This suggests that the long-range ferromagnetic ordering is fully established at 300 ps.

The transient spectra at very early times (less than a picosecond) show a dispersive lineshape which is an indication of heated electrons and/or disordering of the initial AFM order parameter as expected from simulations (Fig. 2.6). Looking at the size of spectral change, the contribution from actual band structure modification is at least an order of magnitude larger than the contribution from heated electrons (cf. section 2.7 and chapter 5). This means that modification in exchange interactions (such as AFM to FM type interactions) strongly modifies the band structure and correspondingly the spectral weights in the XAS spectra.

Moving to shortly later time delays (850 fs and 1.85 ps), the spectral shape modifies evidently in the post edge region, above 0.9 eV of absolute maximum, becoming more flat and non-dispersive like. As discussed before in section 2.7, this positive trend indicates the starting phase of FM ordering. Short range FM order is established due to FM type local exchange interactions. These FM fluctuations (short range FM order) further grow at later times where this positive peak further evolves and also shifts towards 0.9 eV.

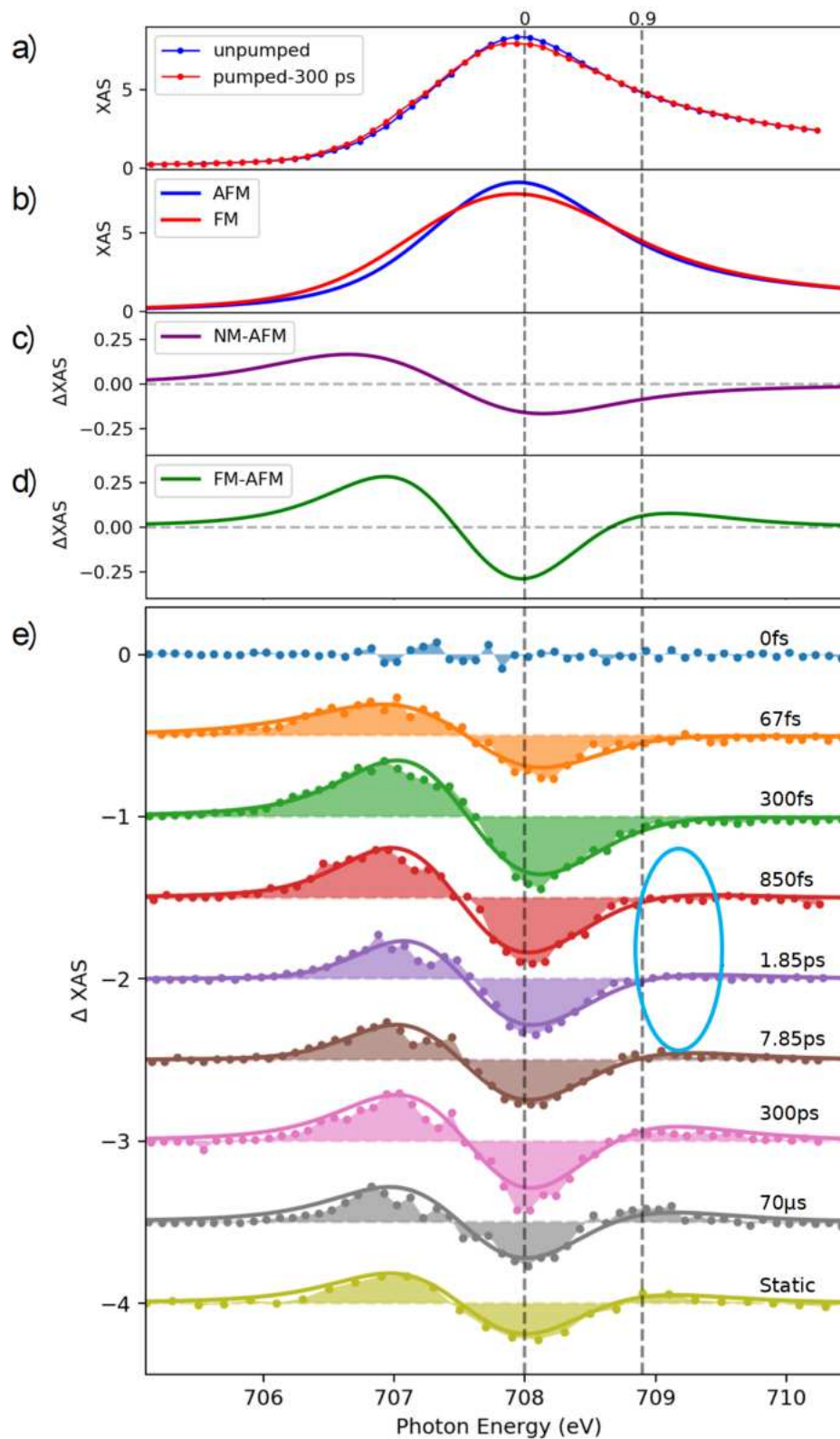


Figure 6.3: X-ray absorption spectroscopy near Fe L_3 edge at fixed time delays. a) XAS scans for pumped (after 300 ps) and unpumped state. b) Simulated XAS spectra for AFM and FM state of FeRh, convolved with a Voigt lineshape broadening. c) Simulated spectral changes between NM (non-magnetic) and AFM state. d) Simulated spectral change between FM and AFM state. Post edge positive feature is only present here and is indicative of FM exchange. e) XAS transients at different fixed time delays showing the evolution of the electronic band structure during the FeRh phase transition. Bottom transient spectrum obtained by static heating for comparison (static data from Christian Stamm [68]). Solid lines are guide to eye.

Hot electron dynamics and band structure modification during the phase transition may involve the charge transfer from Fe to Rh as suggested in the simulations by Pressacco et al. [95]. To look at the net charge transfer, the transient change in the number of 3d holes was calculated by the total integration of spectral change across Fe L_3 edge (Fig. 6.4). It was found that there is nearly no change (within error bars of 0.3%) in the number of 3d electrons for the different time delays. This indicates that there is no (or not significant) net charge transfer between Fe and Rh during any stage of the phase transition in FeRh. This is contrary to what has been suggested through TDDFT simulations in [95].

In summary, we have identified and observed the characteristic post-edge feature of the AFM to FM phase transition in the transient absorption spectra measured across Fe L_3 edge. We have observed band structure modification in FeRh using tr-XAS at sub-picosecond to 70 μ s time delays which we have identified (from simulations) to be coming from change in exchange interactions. We have found no evidence of net charge transfer from Fe to Rh during the phase transition in FeRh. In the next section, time delay scans at characteristic energy points of maximum change showing dynamics of hot-electron relaxation, melting of order parameter (pre-edge: 1.1 eV below Fe L_3 edge, on edge: at Fe L_3 edge) and onset of FM exchange interactions (post edge, 0.9 eV above Fe L_3 edge) will be discussed.

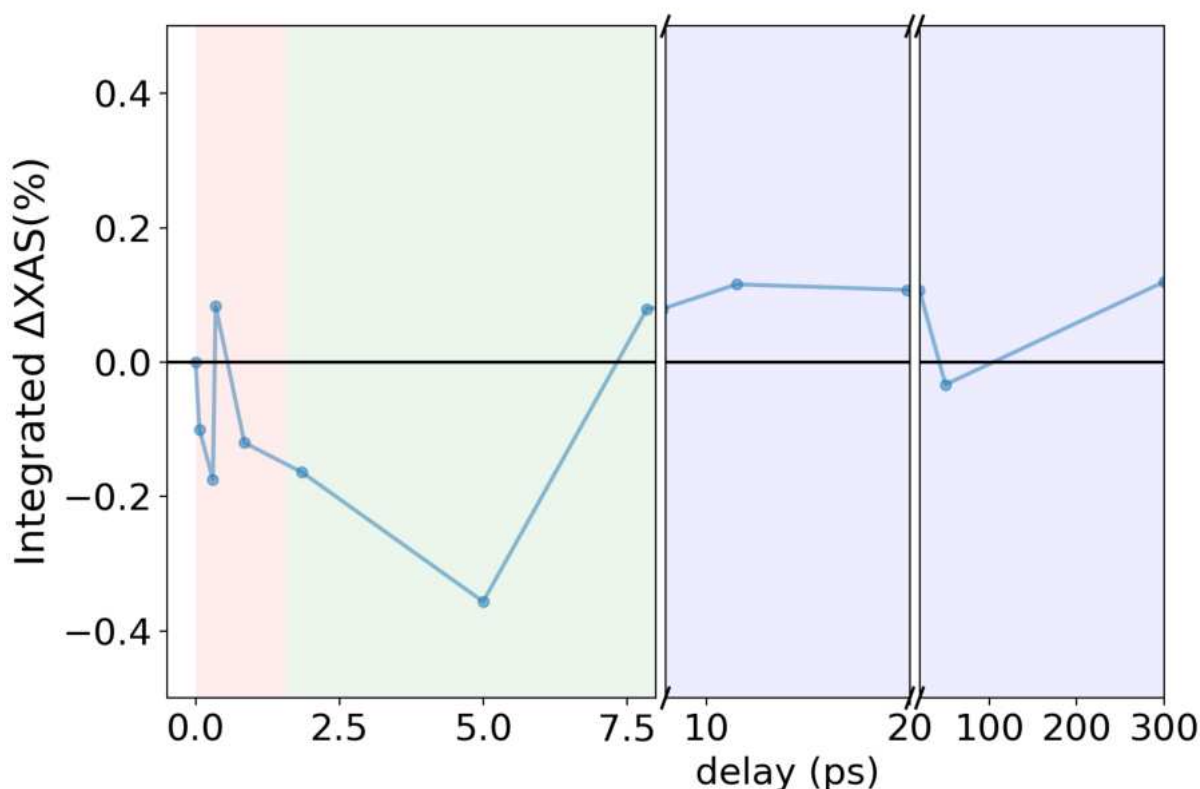


Figure 6.4: Integrated transient XAS (%) to calculate change in the number of 3d electrons at Fe sublattice. % change is within the 0.3% error bars of the measurements

6.2 Time delay scans at fixed energies around Fe L_3 edge

From energy scans at fixed time delays in last section, we have seen that there are characteristic changes at given energies across the Fe L_3 edge. Following the dynamics at the pre-edge and on the Fe L_3 edge gives insight into the band structure changes. 5% change in the transient is an order of magnitude larger than solely due to warm thermalized electrons (cf. chapter 5 and Fig. 2.6). Tracing the dynamics at the post edge shows the broadening of band structure and the occurrence of the FM exchange in the system. This allows us to unfold the electronic structure dynamics during the phase transition. Thus, in this section, we further investigate the time scales of the electronic structure dynamics during phase transition. Time delay scans were performed at the pre-edge (-1.1 eV), at the Fe L_3 edge (0 eV) and at the post edge(+0.9 eV) of the XAS spectra as shown in the Fig. 6.5.

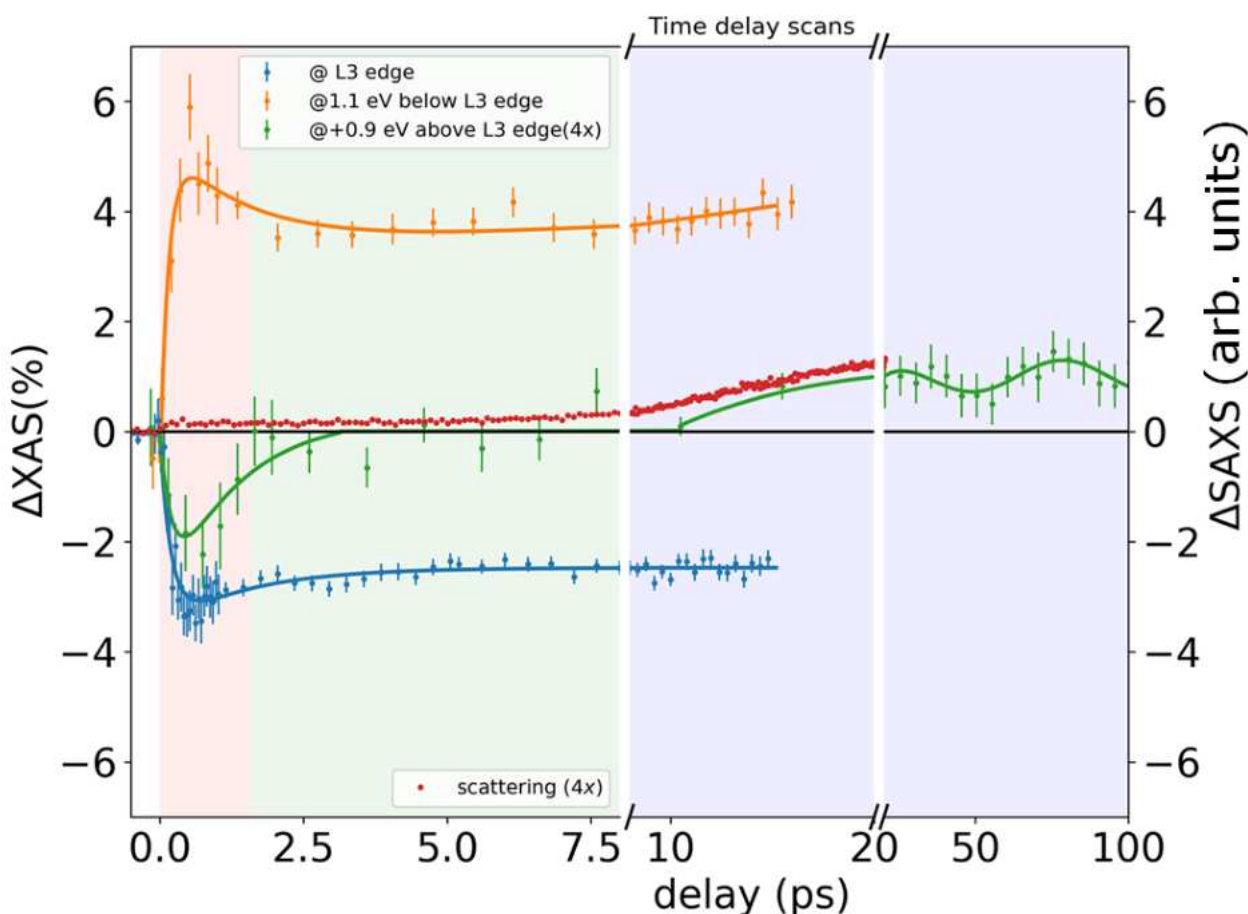


Figure 6.5: Time delay scans measuring % change in absorption at pre-edge (orange), at edge (blue) and post edge (green) of Fe L_3 edge and q-integrated change in scattering at Fe L_3 edge (red). Different color shaded regions indicate different dynamics. Red: Melting of Fe sublattice/disordering. Green: Thermalization and onset of FM fluctuations. Blue: Long range FM ordering.

Delay scans were fitted with piece-wise exponential functions and rate constants. The fit functions were convolved with an error function to take into account of the time resolution of 200 fs. The extracted time constants are tabulated in Table 6.1.

We observe the initial decay (rise) of transient absorption at the edge (pre-edge) at time scales of 200 fs. We assign this large rapid change in the band structure within the electron thermalization

Energy	τ_1	τ_2	τ_3
@ L_3 edge	0.188 ps	1.48 ps	-
@ 1.1 eV below L_3 edge	0.146 ps	1.45 ps	-
@ 0.9 eV above L_3 edge	0.21 ps	1.22 ps	7.63 ps

Table 6.1: Time constants for different time delay scans. τ_1 represents timescale of melting/disordering. τ_2 represents recovery/thermalization timescale. τ_3 represents the time scale of long range correlations after 10.5 ps.

timescale to the decay of AFM order parameter and melting of two Fe sub-lattices. The time scale of 200 fs may be limited by our time resolution. Further, Δ XAS signal does not recover to initial state but relaxes to a transient state at the time scale of ~ 1.5 ps. This is the time scale of energy transfer between electron and lattice subsystems and their thermalization. This spectral change does not return to initial state upto even 70 μ s as also shown in energy scans.

From the delay scan at post edge magnetic feature (green curve in 6.5, also see Fig. 6.3 d) and section 2.7 for details), it can be observed that the transient signal rises after the electronic subsystem relaxes but during the thermalization of electron-lattice subsystems. The increase in the transient signal from negative towards zero signifies the change in AFM type exchange interactions which also lifts the band narrowing. The transient signal at post-edge does not change significantly between 3 to 10 ps and fluctuates near zero. We observe neither the deterministic positive signal at the post edge (the feature for the long range FM correlations, cf. Fig. 2.6) nor the deterministic negative signal (the feature for fully disordered state or remaining AFM exchange in the heated state, cf. Fig. 2.6) between 3 to 10 ps. Thus, we assign this fluctuating region to the short range FM correlations/fluctuations. (see discussion for more details).

Further cooling of the electronic system and the lattice expansion results in building up of long-range correlations of the FM order parameter after 10 ps, which is observed by deterministic positive increase in the transient signal at the post-edge of the XAS spectra. The role of long range and higher order interaction has also been discussed, theoretically in [311]. As mentioned in [101], the magnitude of the FM exchange interaction is strongly dependent on the lattice parameter. Thus, the onset of long-range interactions is expected to take place on the time scale of lattice expansion. This time scale is therefore consistent with the time scale of lattice expansion (14 ps), reported in [89] and the time scale of nucleation and growth of FM region as shown by integrated magnetic scattering in Fig. 6.5 (red curve). The nucleation and growth dynamics of FM domains, investigated with SAXS, is presented and discussed in the next chapter. As a small remark, small oscillations (within the error bars) of time period 58 ps (17 GHz) are extracted from the fit of the Δ XAS scan at post edge (20-100 ps delay range in green curve in Fig. 6.5). The origin of these modulations is beyond the scope of this thesis.

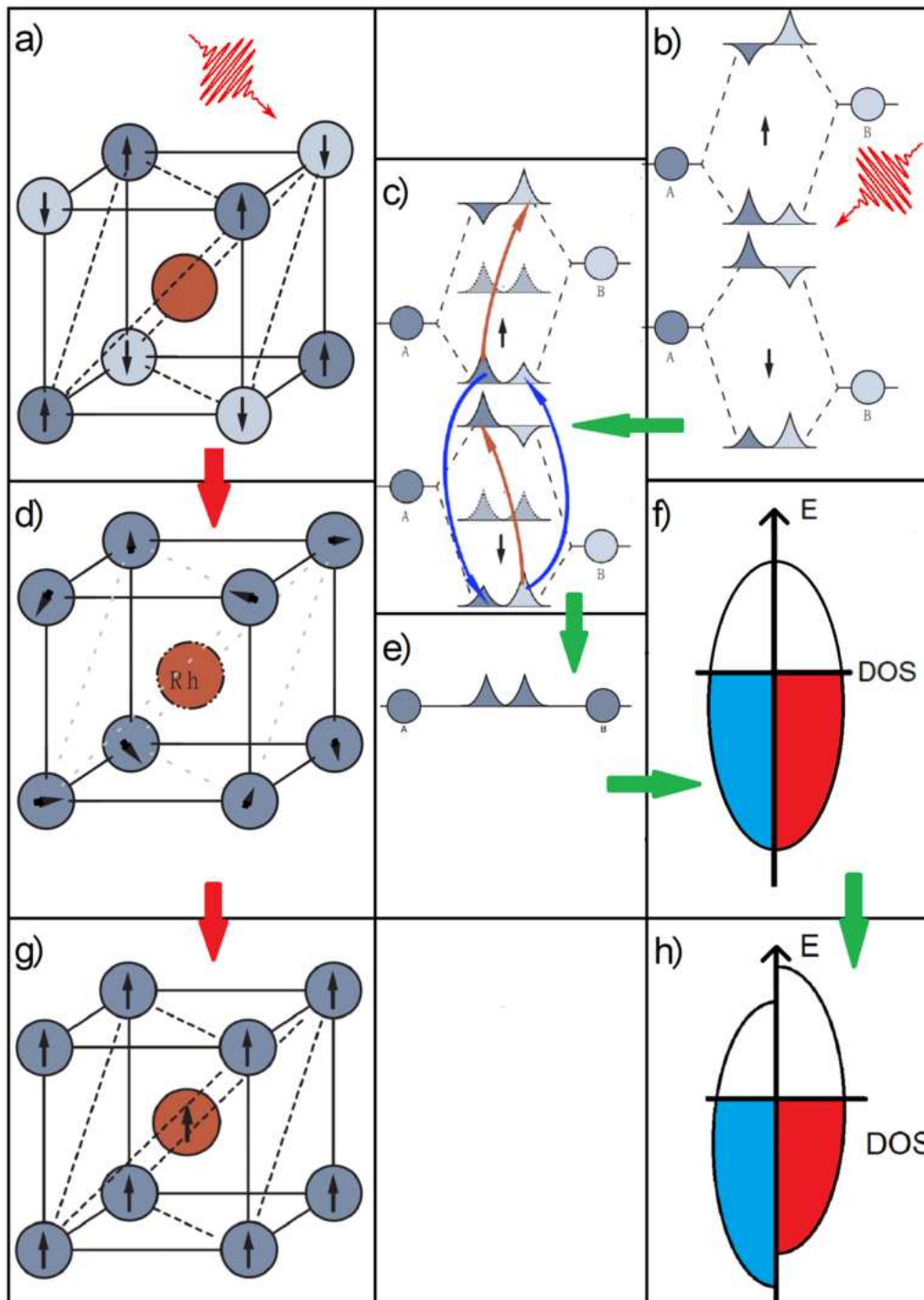


Figure 6.6: Illustration of change in spectral weights during phase transition in FeRh AFM-II(a) disordered(d) and FM (g) structure of FeRh as the phase transition progresses. b) Illustration of AFM state (spin up and spin down bands) using covalent bonding picture of neutral diatomic molecule (adapted from [222]). A and B represent two Fe sublattices. Lower symmetric sites are bonding orbitals while upper antisymmetric sites are anti-bonding orbitals. c) Change in spectral weights and exchange modification after optical excitation due to inter-site spin transfer (brown arrows) or spin flip scattering (blue arrow). e) FeRh sublattices become equivalent in disordered state with equal spectral weights for both lattice sites and spin sub-bands. f) Band structure picture of disordered/spin depolarized state. h) Band picture of exchange splitting in FM state where both Fe sub-lattices are still equivalent.

6.3 Discussion

We observe the spectral changes during phase transition of FeRh using time-resolved X-ray absorption spectroscopy near Fe L_3 edge. The nature of exchange interaction (AFM or FM) and its magnitude govern the electronic structure changes. The transient absorption, observed without external magnetic field and magnetic contrast, provides inherent timescales of interactions between electron, lattice and spin subsystems. Evolution of exchange interactions and FM state, in particular case of FeRh phase transition, could be traced via changes in electronic structure studied through DFT simulations.

The transfer of spectral weights during the phase transition of FeRh can be illustrated using a bonding and anti-bonding orbital picture of a diatomic molecule as shown in Fig. 6.6. We can relate the experimental results in this chapter to the microscopic mechanism of exchange interaction modification, based on theoretical simulations in section 2.7 as well as in [101], as follows:

Depolarization of AFM state and melting of Fe sub-lattices at 200 fs timescale:

We illustrate the depolarization of the AFM state using the diatomic molecule picture of the antiferromagnetism as discussed in the section 2.6. During optical excitation, the electrons from a bonding orbital at one site (occupied spin band of majority spin) can be excited to an anti-bonding orbitals on the other site (un-occupied spin band of minority carrier) by the effect called optically induced inter-site spin transfer (OISTR) (Brown arrows in Fig. 6.6c)). Such an effect has already been observed and used to explain the ultrafast demagnetization in ferromagnets [135, 139, 168–170]. Here, it tends to reduce the effective spin polarization on both Fe sub-lattices. Due to the occupation of anti-bonding orbitals on both sites, there is a decrease in the overlap integrals, which leads to change in spectral weights and subsequently the weakening of AFM exchange interaction between the two Fe sublattices. Other competing processes such as Elliott-Yafet spin flip scattering (blue arrows in Fig. 6.6c)) also tend to reduce the spin polarization and modify the spectral weights [60]. It should be noted that optical excitation should lead to modification of the exchange interactions of both types, Fe-Fe and Fe-Rh. This is because of the strong hybridization between Fe and Rh [101, 227] (cf. section 2.6, see Fig. 2.4). In the extreme case, a redistribution of spectral weights ultimately leads to the non-bonding of the molecule as the exchange interaction does not lower the energy anymore (Fig. 6.6 e)). Equivalently, the band structure picture would correspond to the two equivalent Fe sub-lattices with no exchange splitting (Fig. 6.6 f)). From an experimental point of view, it is not possible to say, if the AFM exchange interaction is reduced or fully quenched in the excited state. This means that the excited AFM state may not fully depolarize similar to the ultrafast demagnetization process in ferromagnets. Fig. 6.7 shows the outcome of the TDDFT simulations performed by Dr. Viktor Valmispild. The TDDFT simulates the time evolution of the initial AFM state in FeRh excited by single optical pulse of 35 fs pulse duration (FWHM). Fig. 6.7 a) shows the spin-resolved occupied density of states of Fe sublattice in initial AFM and excited states of FeRh. The density of states above initial Fermi-level are occupied in the excited state. The available density of states above initial Fermi level are spin-dependent due to the exchange splitting: the minority spin band has more available states above Fermi level. Thus, the spin-dependent population of DOS above Fermi-level leads to the spin-depolarization at Fe sublattice. Fig. 6.7 b) shows the evolution

of magnetic moment at Fe sublattice for 3 different fluences of optical pulse (vector potential in TDDFT). It can be seen that the magnetic moment at Fe sublattice gets reduced within 60 fs. The timescale of depolarization is weekly dependent on the fluence levels of optical excitation: more is the fluence, the faster is the demagnetization.

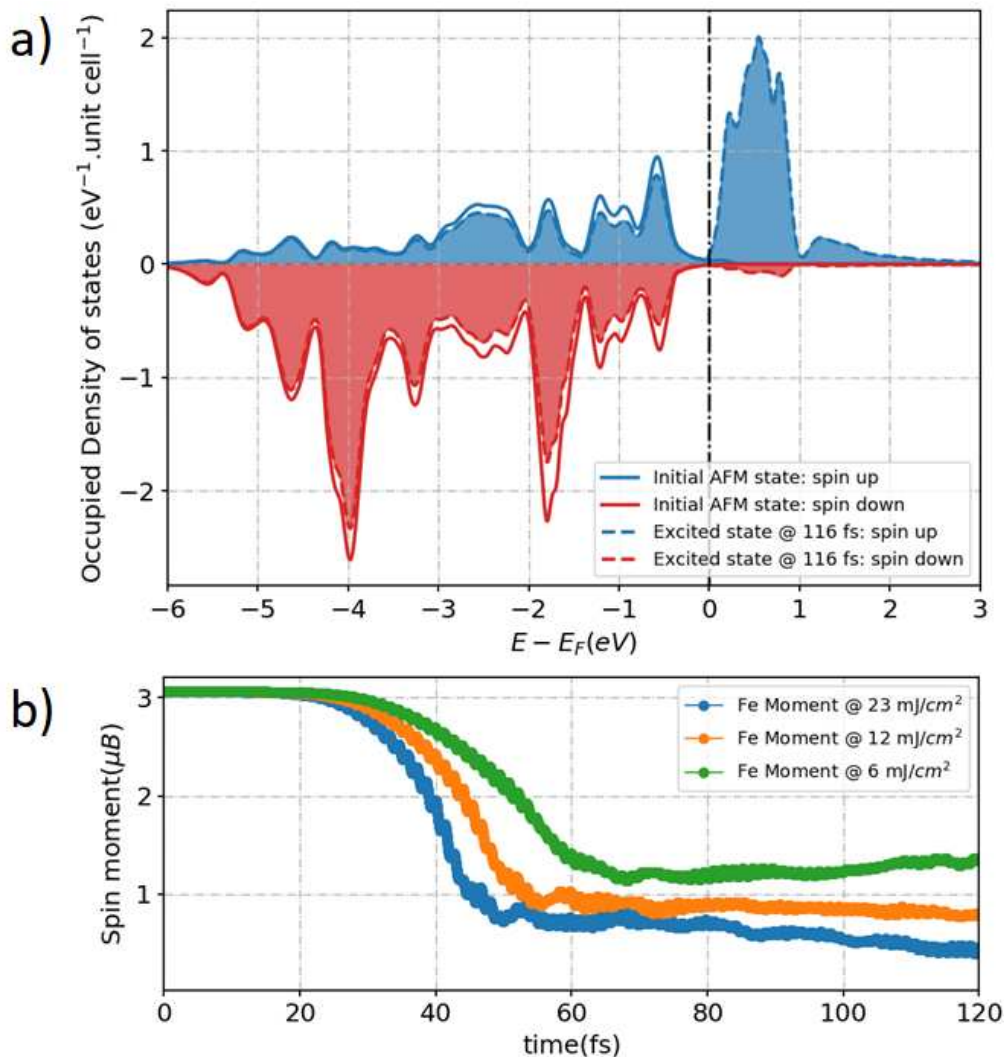


Figure 6.7: TDDFT simulations performed by Dr. Viktor Valmispild for the time evolution of optically excited AFM state. a) Spin-resolved occupied density of states of initial AFM state (solid lines, unfilled) and excited state at 116 fs (dashed lines, shaded) at Fe sublattice. Density of states are occupied above initial Fermi-level in the excited state as shown by shaded region. This leads to the spin depolarization at each Fe sublattice. b) Time evolution of magnetic moment of Fe sublattice for three fluence levels of optical pulse applied in the TDDFT simulation.

Thermalization of electronic and lattice subsystems at 1.5 ps timescale:

Even after the electronic relaxation within 200 fs, the electron and lattice subsystems are still not in the equilibrium with each other. There is the energy flow from electron subsystem to lattice which leads to the cooling of both the subsystems. As the both subsystems cool down and the energy flows into the lattice, the nearest neighbour exchange interactions (Fe-Rh, which is of FM type), second nearest neighbour interaction (Fe-Fe, which is of AFM type)) and spin polarization are expected to recover. This means that spectral weights should also recover but that is not what we observe in the experiment. We observe that the band structure changes, compared to initial

AFM state, remain there for 100s of ps at the pre-edge and on the Fe L_3 edge while a second spectral change at the post edge is recovered and tends to the final positive value. This spectral change near post edge indicates, as per the simulations, is due to onset of ferromagnetic interactions. As is evident from two temperature model (see Appendix, Fig. A.3), the lattice temperature rises above the transition temperature. Consequently, the structural transition/volume expansion leads to a further weakening of the strongly volume-dependent Fe-Fe AFM interaction [101]. On the other hand, as mentioned by Sandratskii [101], the Fe-Rh interaction is of FM type and is not strongly volume dependent. Such FM interaction leads to spin polarization pockets over Rh atomic volume due to strong hybridization between Fe and Rh while still rendering the total Rh moment zero. At this point, Fe-Rh FM interaction, which does not strongly depend on lattice parameter, takes over the AFM type Fe-Fe interactions with an increasing spin polarization on Rh site. This makes the net exchange interaction of FM type [101] and later governs the ordering state above the phase transition.

FM fluctuations after thermalization, from 3 ps to 10 ps:

As observed from near zero signal in green curve of Fig. 6.5 between 3 to 10 ps, the band structure does not change significantly over this time. We have local FM exchange and Rh becomes spin-polarized leading to short range order with FM fluctuations. As observed from the hard X-ray diffraction study [89], lattice expansion takes time and completes at the time scale of 10-15 ps. Thus, long range ordering cannot take place until then and FM fluctuations persist until 10 ps similar to time scale of the lattice expansion. Also worth mentioning here is that structural transition take place as normal first order phase transition as the lattice temperature rises. Though, from electronic point of view, electronic temperature crosses the Curie temperature before cooling down, so FM fluctuations in electronic band structure persist for long time.

Long range FM ordering from 10 ps onwards:

As the lattice expansion completes at 10 ps timescale and electronic temperature of FeRh system decreases, FM fluctuations subside. This leads to formation of long range FM state in FeRh and also modifies the local electronic structure as indicated by growing positive feature in time delay scan at post edge. This clearly indicates that long range correlations also affect local electronic band structure.

After observing how exchange interactions are modified during the phase transition, next chapter will focus on making the connection between microscopic ferromagnetic state to macroscopic magnetization state using time-resolved small angle X-ray scattering.

7 Time-resolved small angle X-ray scattering of optically excited FeRh

After discussing the time scales of dynamical processes, the evolution of electronic band structure and exchange interactions during the FeRh phase transition in the previous chapter, the picture of the onset of FM fluctuations, domain formation and growth which connects the microscopic state to the macroscopic state still remains in question. To measure spatial dynamics, time-resolved SAXS was employed at the Fe L_3 edge. SAXS experiments were performed during two different beamtimes using the pulse-resolved DSSC detector and the FCCD detector with 30 nm and 70 nm thick FeRh samples, respectively. The measurements were performed in normal incidence geometry. A peak fluence level of 8 mJ/cm^2 was used for the scattering experiments with collinear X-ray and optical beams. The X-ray probe fluence was kept below 1 mJ/cm^2 . The DSSC detector was kept at 513 mm distance from the sample while the FCCD detector was placed at 150 mm distance to cover the same range in the momentum transfer (q). The observed scattering signal was azimuthally isotropic without any preferential direction. Thus, the scattering signal was integrated along the azimuthal angle (ϕ) and binned in the time delays or the momentum transfer (q) to analyze the temporal and the spatial evolution of FM scattering during the phase transition in the photo-induced FeRh.

7.1 Time- and momentum-resolved magnetic scattering

7.1.1 q -integrated scattering

We start with the discussion of the time evolution of magnetic scattering in 70 nm FeRh thin films which were also used for the X-ray absorption spectroscopy in the chapter 6. The momentum- and time-resolved scattering for 70 nm thin films recorded with the FCCD detector is shown in Fig. 7.1 a). As discussed in section 2.9, the positive scattering difference signal observed is mainly due to formation of FM domains. Due to normalization problem because of calibration issues (linearity, temperature-dependent background etc.) of the FCCD detector, it was not possible to do in-depth analysis of momentum-resolved scattering. The data shown in Fig. 7.2 a) is the ratio of difference scattering signal (pumped-unpumped) and unpumped scattering signal averaged over full q - range, in order to improve the data quality. This normalization does not affect the dynamics of q -integrated scattering qualitatively but then the analysis of q -resolved scattering in a quantitative manner is not possible in this case.

The time evolution of q -integrated scattering is shown in Fig. 7.2 a) for 70 nm thin films. The region of integration has been marked in Fig. 7.1 a). The timescale of FM magnetic scattering is found to be ~ 10 ps which is similar to the time scale of long range FM ordering as observed in XAS at post-edge (Fig. 6.5). This time scale is also found to be similar to the time scale of lattice/volume expansion (~ 14 ps) observed by hard X-ray diffraction [89].

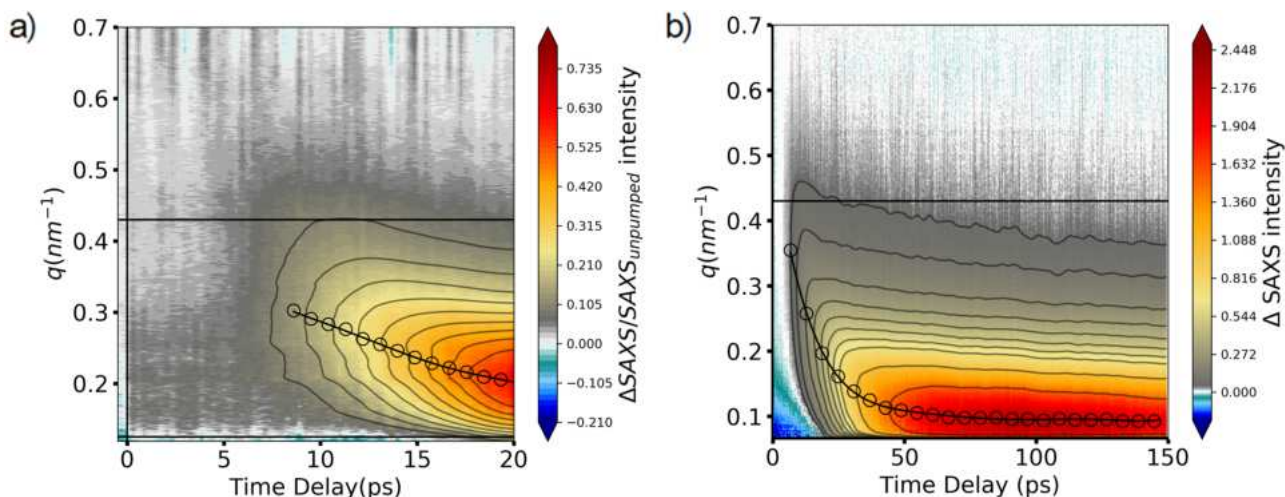


Figure 7.1: SAXS colomaps. a) Time- and q -resolved small angle X-ray scattering at the Fe L_3 edge using the FCCD detector measured at 70 nm FeRh sample with an optical fluence of 8 mJ/cm^2 in normal incidence geometry. b) Time- and q -resolved small angle X-ray scattering at Fe L_3 edge measured using DSSC detector at 30 nm FeRh sample with optical fluence of 8 mJ/cm^2 . For both figures: Horizontal black lines show the region of integration for q -integrated scattering. Color bars are in arb. units. Circles and corresponding fitted curve show the trend of momentum transfer (q) with maximum scattering intensity depicting the growth of FM domains. Contours show the iso-scattering-intensity curves. Negative values represent demagnetization of the interface layer whereas positive values represent FM scattering.

Now, we discuss the time evolution of magnetic scattering measured by DSSC detector for 30 nm FeRh films. The time- and q -resolved magnetic scattering colormap is shown in Fig. 7.1 b). Here, the magnetic scattering signal is obtained by taking only the difference between pumped and unpumped scattering signal. This makes it possible to do a q -resolved analysis. Further, as evident from Fig. 7.2 a), the time evolution of the integrated magnetic scattering is the same for 30 nm and 70 nm films, at least upto 20 ps. This suggests that the dynamics of the domain growth is quite similar in both films. Having this in mind, we will have a closer look on the temporal and spatial dynamics of the phase transition using magnetic scattering at 30 nm films recorded using the DSSC detector in this and following sections.

From the magnetic scattering colormap in Fig. 7.1 b), it can be observed that the FM scattering starts at high q range and shifts towards lower q range indicating variation of domain sizes and correlation length scales over time. This has also been observed before in static measurements of thermally induced phase transition [69]. This similarity suggests that the photo-induced phase transition is still thermally driven.

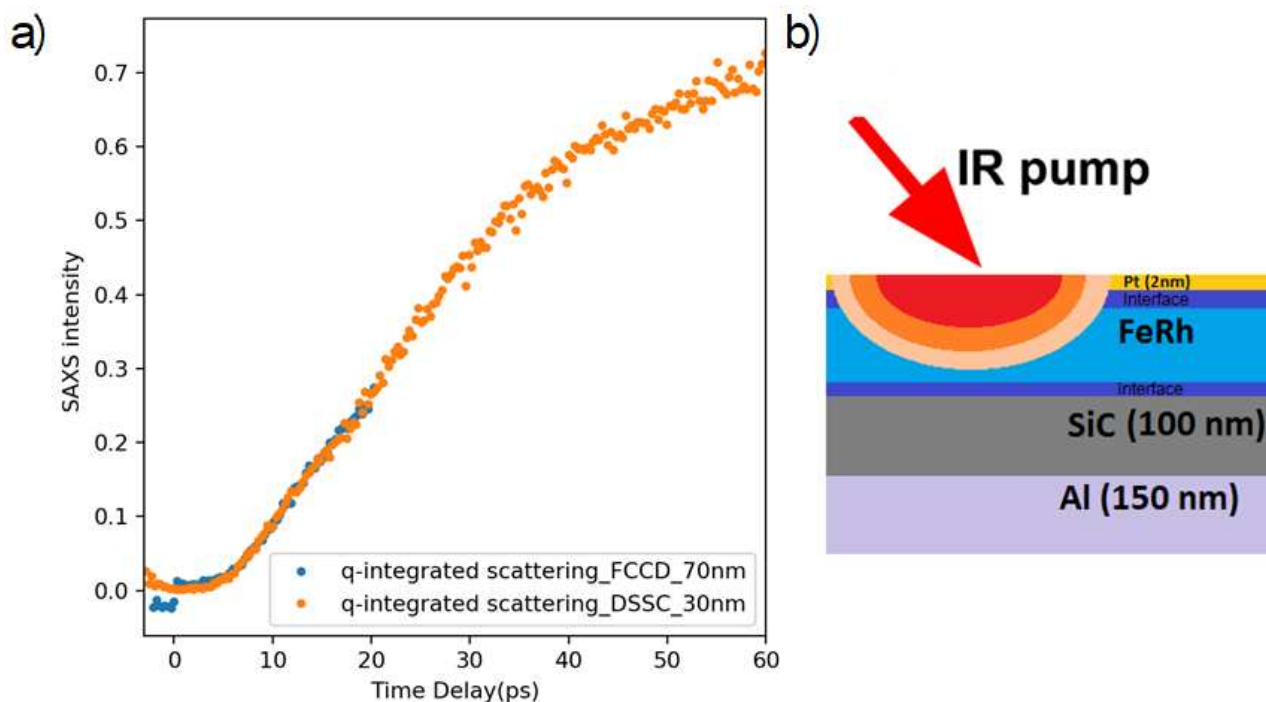


Figure 7.2: Integrated magnetic scattering and sample structure. a) q-integrated magnetic scattering for SAXS measurements on two different samples of thickness 70 nm and 30 nm using different detectors, with integration region shown in Figs. 7.1 a) and b). b) Sample structure showing different layers and in-homogeneous optical excitation of FeRh thin film. Dark blue regions show FM interfaces.

7.1.2 q-resolved magnetic scattering at fixed time delays

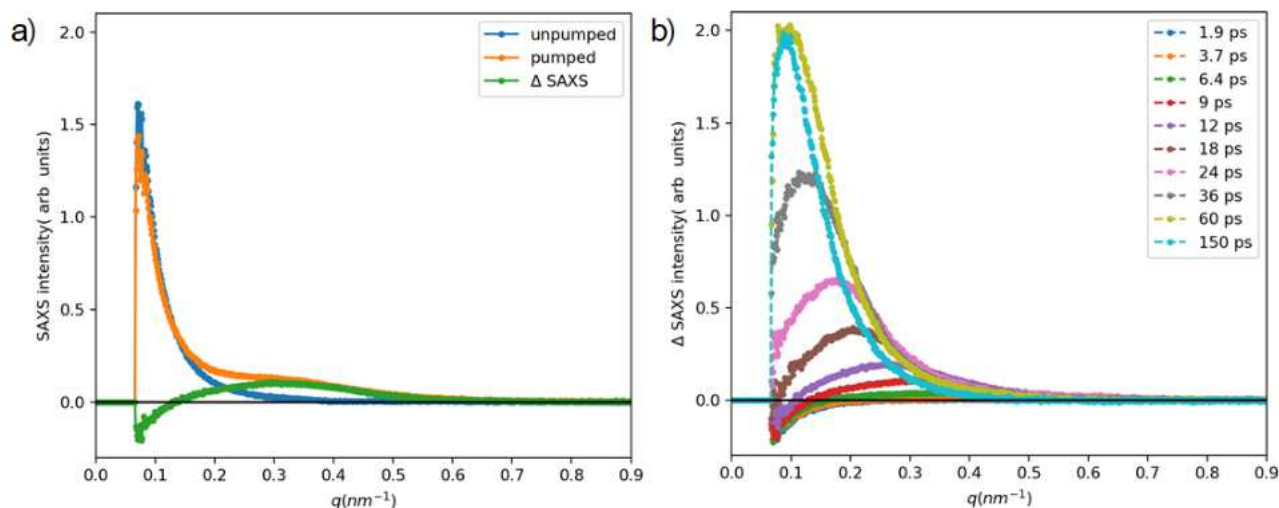


Figure 7.3: q-resolved SAXS. a) q-resolved SAXS line cuts at fixed delay of 11.3 ps with average over ± 0.3 ps showing scattering for optical pumped (orange), unpumped (blue) states and their difference (green). b) q-resolved SAXS line cuts at different fixed delays with average over ± 0.3 ps showing change in scattering due to optical excitation. Positive signal corresponds to magnetic scattering due to FM domains while negative signal, observed up to 18 ps, corresponds to demagnetization of FM interface layers.

Fig. 7.3 a) shows the q-resolved scattering at initial unpumped state, the transient pumped state 11.3 ps after optical excitation and the difference between transient and initial state. The

scattering at initial state is due to charge and magnetic roughness which shows significant change after the optical excitation. We attribute the negative signal at the low- q in the difference scattering to the demagnetization of the ferromagnetic interface layer (see the sample structure in Fig. 7.2 b)), as explained in the Sec. 2.9. The positive signal at high- q is contribution from the generation of ferromagnetic ordering. The q -resolved Δ SAXS signals for various time-delays are shown in Fig. 7.3 b). The time evolution of the distribution shows a shift in the peak position from the higher momentum transfer (q) to a lower momentum transfer (q) indicating the increase in the size of FM domains and correlation length scales. After clipping the negative contribution at low- q due to demagnetization, Fig. 7.4 a) shows only FM contribution from domain nucleation and growth. The q -resolved magnetic scattering is shown for fixed time delays with an average over ± 0.3 ps around the time delay.

It can be clearly seen that FM magnetic scattering appears at a time scale of 3 ps over a broad q range with nearly uniform intensity, which corresponds to initial FM fluctuations, which are present at a wide range of length scale. The appearance of FM fluctuations in scattering at the time scale of 3 ps is in conformity with the transient signal observed in X-ray absorption measurements. The competing exchange interactions at the time scale of 3 ps destabilize the two Fe sublattices and cause the FM fluctuations giving the magnetic scattering signal over broad q -range. The spectral weights near the post edge (green shaded area in Fig. 6.5) in the transient XAS signal remain near zero and don't change significantly until 10 ps.

At later times (> 4.6 ps), this FM scattering signal takes the shape of well-defined distribution peaked at a certain q . At this time scale, FM fluctuations start to subside and condense into nucleation centers to minimize the global free energy of the whole system. The time scale of the onset of nucleation (~ 4 ps) is similar to that of onset of lattice expansion (~ 3 ps), as studied by hard X-ray diffraction [89]. As already emphasized, this again suggests that ferromagnetic order generation goes hand-in-hand with lattice expansion. Lattice expansion also helps in cooling down the electronic system and magnetic fluctuations by absorbing more energy without the temperature increase (first order phase transition).

Finally, the scattering distribution shifts to lower q at later time delays indicating long range correlations and increasing domain sizes. Also, the distribution gets narrower in q with increasing time delays. The change in variance of distribution indicates that the shape of domains is modified due to domain wall motion.

7.1.3 Time-resolved magnetic scattering in fixed q ranges

In Fig. 7.4 b), the delay scan traces are shown for different q ranges averaged over $\pm 0.05 \text{ nm}^{-1}$. It can be seen that smaller domains (larger q scattering) are formed at early times while large domains (smaller q scattering) are formed later. Smaller domains also decay faster by coalescence (coarsening dynamics) to form large domains.

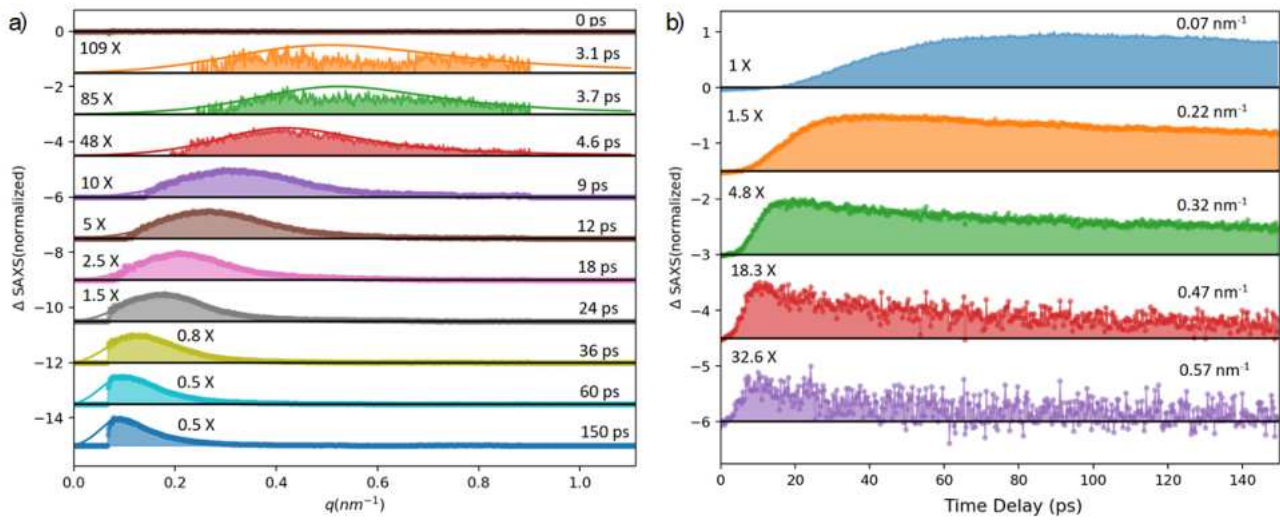


Figure 7.4: q-resolved and time-resolved line-cut waterfall plots of SAXS. a) q-resolved SAXS line cuts at different fixed delays with average over ± 0.3 ps showing normalized magnetic scattering after optical excitation. The negative signal due to demagnetization of interface layers has been removed/clipped. Solid lines show the fitting of the scattering signal using the equation 7.1. b) Time-resolved scattering line-cuts at fixed q averaged over $\pm 0.05 \text{ nm}^{-1}$ showing normalized FM scattering change after optical excitation. Multiplication factors for each scan are shown within the figures.

7.1.4 Fitting of q-resolved scattering distribution

Now, for the further analysis in reciprocal or real space, it is instructive to fit and fill the missing low q -information due to centre hole in DSSC by extrapolation. The fitted distribution can then be used to obtain the domain size evolution, properly normalized correlation function and correlation lengths as will be shown in following sections.

The q -resolved scattering distributions, shown in 7.4 a), are fitted with a modified form of Lorentzian function:

$$\Delta I_{SAXS}(q) = I_0 \times \frac{q}{\left(1 + \left(\frac{q-\mu}{\sigma}\right)^2\right)^2}. \quad (7.1)$$

This form of fitting function is motivated from the fact that the Fourier transform of an universal exponential scaling function [194, 238], which is valid near a critical point, is Lorentzian. As can be observed from solid lines in Fig. 7.4 a), the function fits the spectra at all time delays greater than 4.6 ps quite well. The fitting function can be used to extrapolate the data to $q = 0$, for the time delays up to 60 ps where the peak of the distribution is still visible. After 60 ps, the fit cannot compensate for the missing information as peak of the distribution is missing as well. Thus, we limit our analysis for the time delays up to 60 ps. In the following sections, this fitted distribution will be used to analyze the evolution of domain sizes and correlation lengths up to 60 ps.

7.2 Time evolution of domain size and distribution

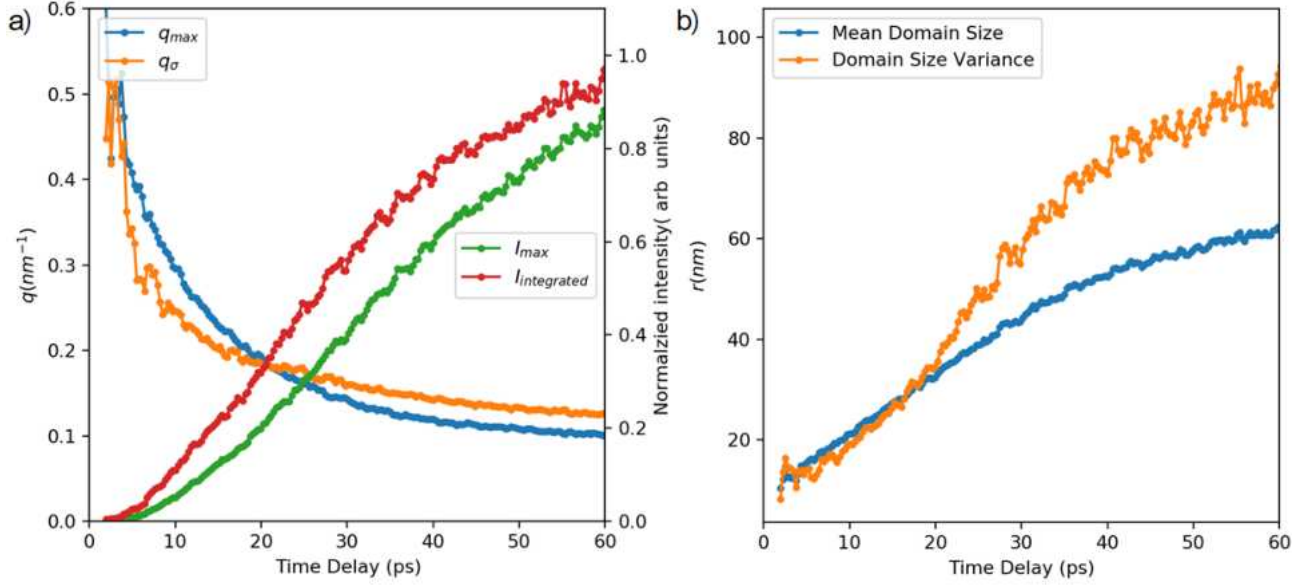


Figure 7.5: Domain size evolution obtained from fitting the q -resolved scattering line cuts. a) Time evolution of q_{max} corresponding to maximum intensity I_{max} , variance of distribution in q space q_{σ} and integrated scattering change $I_{integrated}$. b) Time evolution of domain size and variance of distribution in real space obtained using the relations shown in equations 7.2 and 7.3.

The fit function of q -resolved scattering (Equation 7.1) is used to determine the position (q_{max}) of maximum intensity (I_0). q_{σ} is defined as the FWHM of the fitted distribution. $I_{integrated}$ is the q -integrated total intensity of the fitted distribution which is proportional to the square of the magnetization component in the beam direction. As it can be seen from Fig. 7.5 a), q_{σ} and q_{max} decrease with time depicting that the scattering intensity shifts to lower q and its variance gets narrower.

Using the relation between real space and reciprocal space variables, mean domain size and domain size variance can be defined as follows:

$$r_{mean} = \frac{2\pi}{q_{max}} \quad (7.2)$$

$$r_{FWHM} = \frac{2\pi}{q_1} - \frac{2\pi}{q_2}, \quad (7.3)$$

where q_1 and q_2 correspond to q values at the FWHM intensity of fitted distributions. As seen in Fig. 7.5 b), domain sizes of 10 nm to 60 nm with variation of 10 nm to 90 nm respectively could be seen in the experiment. The domain size growth is nearly linear at early times and slows down at around 25 ps when the mean domain size reaches 40 nm. The variance of the FM domain distribution increases monotonically after laser excitation. The variance of the domain distribution increases rapidly compared to the mean domain size indicating the increase in the roughness/polydispersity of the FM domains. Without any external magnetic field, dipolar fields govern the FM domain growth and it becomes energetically less favourable after certain domain size limit is reached.

7.3 Correlation length evolution and dynamical power-law scaling

An equal time spatial correlation function can be constructed, using the Fourier transform of scattering intensity, to understand the spatial and temporal evolution of the ferromagnetic domains. This section will focus on the spin-spin correlations (equal time spatial correlations due to spins) and their time evolution.

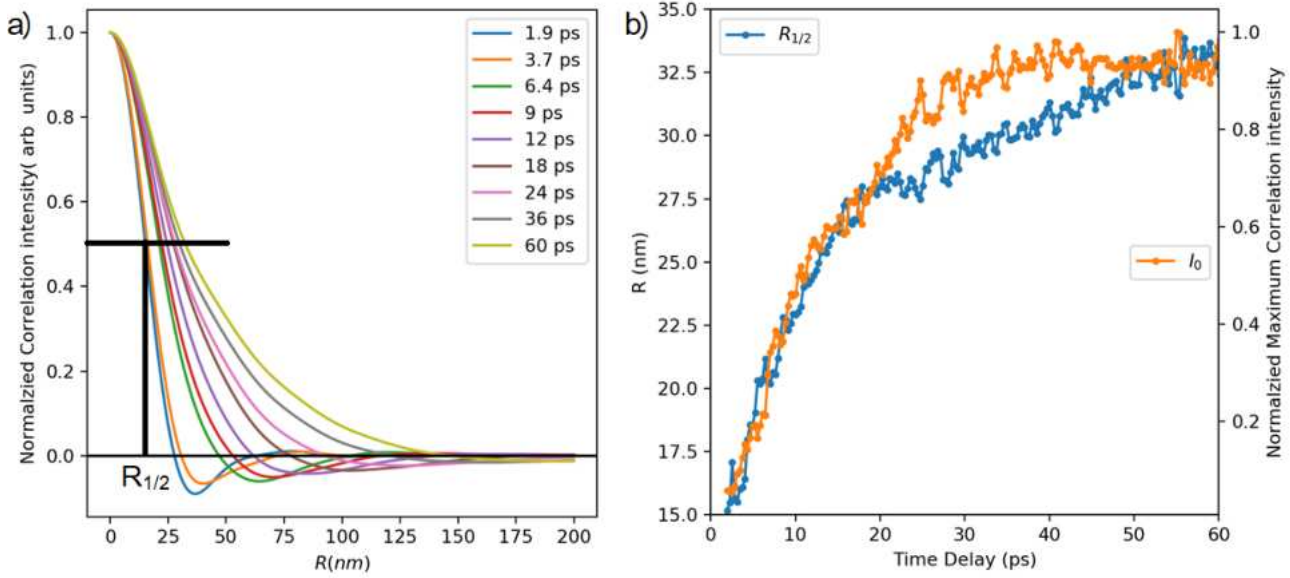


Figure 7.6: Correlation function and correlation length. a) Normalized correlation function at different fixed time delays calculated by the spherically symmetric Fourier transform of the fitted distribution of q -resolved scattering linecuts 7.4. b) Time evolution of the correlation length $R_{1/2}$ showing different growth rates and time evolution of the maximum intensity I_0 of correlation function

As shown in section 2.9, the correlation function, ($C_m(\vec{r})$) can be defined as the Fourier transform of the scattering intensity. Also, as discussed in section 2.9, the scattering intensity mainly represents FM scattering so that the correlation function can be called the spin-spin correlation function displaying the correlations between spin densities at different length scales [236]. Assuming spherical symmetry, the Fourier transform of scattering intensity can be written as:

$$C_m(\vec{r}) = \int [I_{SAXS}(\vec{q})] e^{-i\vec{q}\cdot\vec{r}} d^3\vec{q} \approx C_m(r) = \int \left[\frac{q \times I_{SAXS}(q)}{2\pi^2 r} \right] \times \sin\left(\frac{q \times r}{2\pi}\right) dq, \quad (7.4)$$

where r is length in nm and q is reciprocal space momentum transfer in nm^{-1} .

The correlation function, calculated for different time delays, is shown in Fig. 7.6 a). The spurious negative part/ringing of the correlation function around zero is probably due to the high q -cutoff. The correlation length, at particular time delay, can be defined as the length corresponding to the half of the maximum correlation signal (HWHM). Correlation length ($R_{1/2}$) for normalized correlation function $C_m(r)$ is defined as (also shown in Fig. 7.6 a)):

$$C_m(r = R_{1/2}) = 0.5. \quad (7.5)$$

As can be observed from Fig. 7.6 a), the normalized correlation function decays slowly over the length scale with increasing time delays. This also becomes clear from Fig. 7.6 b) where the time evolution of the correlation length ($R_{1/2}$) and maximum intensity (I_0) are plotted. The time evolution of correlation length shows two distinct regimes of growth rate and evolution changes from fast growth upto 23 ps to slower growth afterwards.

The change in the growth rate of correlation length near 23 ps corresponds to the correlation length of nearly 28 nm. This is close to the 30 nm thickness of the FeRh film. Thus, this sharp change in growth rate may also be due to a dimensional cross-over from 3D to 2D. The FM correlations/domains can initially expand over a three dimensional region of 30 nm. Later, they can only expand further laterally in two dimensions due to the thickness constraint of FeRh film. This may result in the slower growth of correlations. However, this concept needs further investigations for different thickness of FeRh thin films to ensure that such dimensional cross-over indeed occurs.

In analogy with continuous phase transitions, the time evolution (t) of correlation length/coarsening dynamics can be approximated as a power law with given exponents β :

$$R_{1/2}(t) = \alpha \times (t)^\beta. \quad (7.6)$$

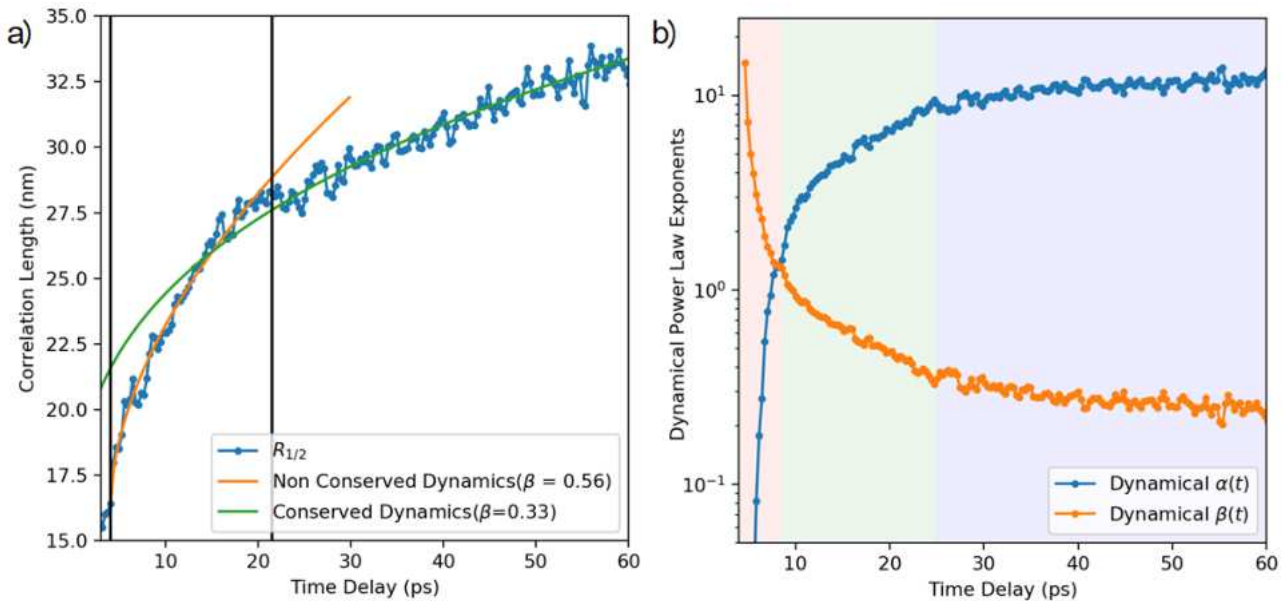


Figure 7.7: Power law scaling of correlation length. a) Fitting of the correlation length evolution with power-law scaling of Ising type system. Initial dynamics coincides with non-conserved order parameter while later it converts to slower dynamics with conserved order parameter. b) Continuous power law scaling for the correlation length indicates continuous change in power law exponent β and dynamical slowing down of the transition. Three different regions of dynamics can be defined: An exponential slowing down (red), power law slowing from 1 to 0.3 (green) at faster rate, power law slowing down from 0.3 to 0.2 at slower rate.

Fig. 7.7 a) shows that the initial evolution of the correlation length can be fitted with $\beta = 0.56$ while the later evolution can be fitted with $\beta = 0.33$. Comparing the conserved (Kawasaki/spin exchange) dynamics with the non-conserved (Glauber/spin flip) dynamics in Ising like system [194], the following observations can be made:

- The initial dynamics correspond to the Glauber-type dynamics with a non-conserved order parameter. Here FM regions are formed from fluctuating regions. This increases the total volume of ferromagnetic domains.
- Evolution at later time scale corresponds to the Kawasaki-type dynamics with a conserved order parameter. The FM domains grow in size by merging smaller FM domains. This is called coalescence. Here, the total volume of FM domains remains conserved.

Further, for the case of a non-equilibrium phase transitions, one can define a dynamical power law exponent ($\beta \rightarrow \beta(t)$) which changes continuously with time delay:

$$R_{1/2}(t) = \alpha(t) \times (t)^{\beta(t)}. \quad (7.7)$$

Experimentally, the dynamical exponent $\beta(t)$ can be determined as:

$$\beta(t) = \frac{\alpha(t) \times (t)^{\beta(t)} \times t}{\int \alpha(t) \times (t)^{\beta(t)} d(t)} - 1 = \frac{R_{1/2}(t) \times t}{\int R_{1/2}(t) d(t)} - 1. \quad (7.8)$$

Fig. 7.7 b) shows the calculated dynamical coefficients $\beta(t)$ and $\alpha(t)$ in log y-x plot. We can see a continuous slowing down of the dynamics. As mentioned in section 2.2, the scaling laws of coarsening dynamics for first-order phase transitions in crystalline materials may not be so universal due to the crystalline anisotropies. This becomes quite clear from Fig. 7.7 b) where the dynamical exponent continuously changes from 14 to 0.2 as the transition progresses. Also, abnormally high values of the exponent are due to the highly non-equilibrium nature of the nucleation dynamics at early time scales. The dynamics can be separated into three regions (colored areas in Fig 7.7 b):

- **3-8 ps: Decay of FM fluctuations** into well-defined domains by nucleation where the exponential slowdown of dynamics is observed. The dynamical exponent β decays from 14 to 1.
- **8-23 ps: The formation of new FM domains from disordered domains** where the non-conserved order parameter of Glauber type dynamics is dominant. The dynamical exponent β decays from 1 to 0.3.
- **>23 ps: The formation of large FM domains by coalescence** where conserved order parameter of Kawasaki type dynamics dominates. Dynamical exponent β decays from 0.3 to 0.2. In addition, the growth rate probably slows down due to the dimensional cross-over. A exponent near 0.25 (1/4) suggests that surface diffusion (in terms of 2D expansion of the correlations) might be dominant at this timescale due to the thickness constraint [197]. Thus, this may also be related to the dimensional cross-over from 3D to 2D.

7.4 Statistically-similar behaviour of phase transition

The FeRh phase transition shows statistically similar behaviour during the coarsening dynamics which means that all the spatial dynamics can be scaled to a single curve using a single time-dependent scaling parameter. The functional form of the scattering distribution remains the same (Equation 7.1). Such statistically similar behaviour has been observed before in other phase transitions and is quite characteristic of the first-order phase transitions [194, 312]. We observe from Fig 7.8 that q -resolved scans can be scaled down to an approximately single curve using the variance as the scaling parameter.

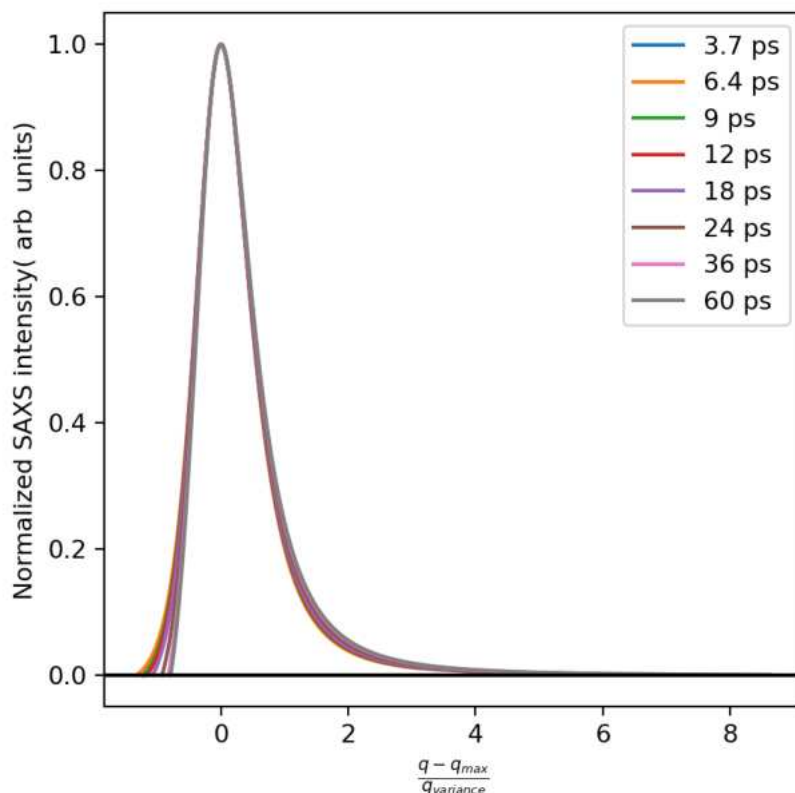


Figure 7.8: Statistical similarity in FeRh phase transition: Evidence of the statistically similar nature of the transition near a critical point by scaling with the variance q_{σ} .

7.5 Final remarks on photo-induced phase transition in FeRh

Finally, combining the results from the time-resolved XAS and SAXS measurements, the various stages of FeRh phase transition can be described as follows:

- **0-200 fs: Initial melting of the two Fe sub-lattices** into one indistinguishable Fe lattice by coherent (OISTR) or incoherent (spin flip scattering) processes. This is indicated by XAS measurements (Fig. 6.5) but not visible in SAXS.
- **1.5 ps: Thermalization of the electronic and lattice subsystems.** Again, this is indicated by XAS measurements (Fig. 6.5) and not visible in SAXS measurements. At this timescale, the FM interaction between Fe-Rh starts to dominate over AFM type interaction between Fe-Fe. This is supported by onset of lattice expansion [101].
- **3-10 ps: FM fluctuations and nucleations** supported by the ongoing structural transition [89]. In XAS measurements (green curve in Fig. 6.5), spectral weight does not change over this time. Competing exchange interactions support the local FM interaction. In SAXS measurements (Fig. 7.4 a)), the scattering intensity is distributed over the wide q-range. FM fluctuations condense into FM nucleation centers where the exponential slow down of the power law scaling is observed in SAXS (Fig. 7.7 b)). The dynamical power law exponent β decays to 1.
- **10-23 ps: Build-up of long-range FM correlations** indicated in XAS measurements by appearance of magnetic feature (post edge at 0.9 eV above Fe L_3 edge). The formation of the new FM domains from disordered domains progresses at higher growth rate. Here, the Glauber type dynamics is dominant and the order parameter is not conserved. The dynamical exponent β decays from 1 to 0.3.
- **23 ps and longer: The formation of large FM domains** at slower growth rate occurs by coalescence where the Kawasaki type dynamics is dominant and the order parameter is nearly conserved. The dynamical exponent β decays from 0.3 to 0.2 (Fig. 7.7 b)). A possible dimensional cross-over from 3D to 2D is observed as a further slowing down in growth rate occurs when correlations in one of 3-dimensions are limited by the film thickness.

7.6 Discussion and outlook

By using tr-XAS and tr-SAXS studies at the Fe L_3 edge, we were able to distinguish different stages and time scales of FeRh phase transition starting from the depolarization of AFM order, the onset of FM interactions to long-range correlations, and the nucleation and growth dynamics of FM domains. The electronic band structure of FeRh is modified at ultrafast time scales but there is no indication of sub-picosecond onset of the FM interaction which rather comes up at the same time scale as the lattice expansion. This suggests that speed limit of ferromagnetic order generation is set by speed of lattice expansion.

Still, we have not conclusively examined the role of Fe-Rh exchange interaction and hybridization during the phase transition. Numerous theoretical and experimental studies have investigated the role of Rh in the phase transition, though it remains an open question whether and how Rh is involved in the formation of FM order. In a recent photo-emission study [95] supported by time-dependent DFT calculations, it was suggested that the transition is preceded by a charge transfer from Rh to Fe. However, we have found no evidence of a change in the number of holes at the Fe site, within the experimental limits (0.3%). In a theoretical study [101], it was suggested that Rh is already polarized within atomic volume because of implicit Fe-Rh FM interactions even though there is no explicit net magnetic moment on Rh. Only canting of magnetic moments at Fe sites after the optical excitation leads to a finite magnetic moment at Rh due to the imbalance between spin up and spin down states of Fe sublattices. It would be nice to experimentally verify this prediction by measuring higher order multipole moments which should be non-zero as opposed to zero magnetic dipole moment at the Rh site. Further, since generation of ferromagnetic order also leads to change in angular momentum at Fe and Rh sites, it also raises the question how the angular momentum is gained at Fe and Rh sites? A reasonable assumption based on speed limit of magnetic transition, is that Rh and Fe both gain angular momentum from the lattice, due to strong spin orbit coupling of Rh. Another possible channel for the angular momentum transfer could be between Fe and Rh itself because of their strong hybridization. However, for spin polarized angular momentum transfer, there is need for symmetry breaking which is not present at the initial AFM state. Hopefully, measurements at the Rh site, possible in the future, will be able to answer these outstanding questions.

8 Summary

In this work, the microscopic evolution of the optically induced magneto-structural phase transition in FeRh was investigated. The electronic structure evolution of the unoccupied states was measured with time-resolved X-ray absorption spectroscopy (tr-XAS) at Fe L_3 edge. It was related to the modification of the exchange interaction and generation of ferromagnetic order with the help of X-ray absorption spectral simulations based on density functional theory. X-ray absorption spectra were calculated under dipole approximation and one-electron theory for different temperatures, lattice constants and magnetic states (FM and AFM). The theoretical calculations suggested that most significant contribution to electronic band structure change comes from the modification of magnetic ordering and thus exchange interactions. The experiments were performed on epitaxial FeRh thin films grown on single crystalline SiC membranes. A direct measurement of XAS spectral changes without the need for magnetic contrast and magnetic field provide the inherent timescales of the competing interactions. It was demonstrated that the electronic structure and exchange interactions in FeRh can be modified at ultrafast time scales by laser excitation. At later time scales, long range correlations also clearly modify the local electronic structure as observed at the post edge to the Fe L_3 edge. Competition between the ferromagnetic exchange (Fe-Rh) and the antiferromagnetic exchange (Fe-Fe) leads to the short range FM state at picosecond time scale after the laser excitation, but long-range ferromagnetic state can only be stabilized at the time scale of 10 ps, which is similar to time scale of lattice expansion (14 ps) observed in other experiments.

Connection was made between the microscopic ferromagnetic state and macroscopic magnetization by studying the spatial evolution of ferromagnetic domains using time-resolved small angle X-ray scattering (tr-SAXS). It was shown that difference signal (pumped-unpumped) gives primarily the ferromagnetic contribution of the phase transition. Nucleation and growth dynamics of FM domains, with range of 10 nm to 60 nm domains, was observed up to 100 ps timescales. FM domains which nucleate from the condensation/cooling of non-equilibrium FM fluctuations around 3-4 ps grow at different rates at later times. The correlation functions and correlation length evolution, calculated by the Fourier transform of fitted SAXS intensity, give three regions of dynamical slowing down of phase transition. The physics behind the dynamics can be sought out by comparing the evolution of correlation length with Ising model. In the first region from 3 to around 8 ps, where there is an exponential down in the evolution of correlation length, the dynamical exponent decays from 14 to 1. In this region, non-equilibrium FM fluctuations condense into FM nucleation centers. In intermediary region from 8 to around 23 ps, where growth rate is slower, the dynamical exponent decays from 1 to 0.3. In this region, nucleated domains grow

in size and the FM order parameter does not remain conserved. In the last region from 23 ps onwards, the dynamical exponent decays from 0.3 to 0.2. In this region, FM domains grow at the expense of smaller FM domains by coalescence. The FM order parameter, in this region, remains nearly conserved as formation of new FM phase saturates. Thus, tr-XAS and tr-SAXS measurements give unified microscopic picture of spatial and temporal evolution of the photo-induced phase transition in FeRh. Nevertheless, more experimental and theoretical investigations, at the Rh L or M edge, are needed to clarify the dynamics of FM ordering and role of Rh in stabilizing the FM state of FeRh at higher temperature.

In another part of thesis, X-ray spectral simulations were performed in order to simulate the thermal changes in X-ray absorption spectra of 3d transition metals (Ti, Co, Cr, Cu). It was observed that thermal changes in X-ray spectra, for most part, can be explained by electron reshuffling according to the Fermi-Dirac distribution. Some small features in spectral changes, specifically in case of Ti and Cr, might involve actual band structure changes. Further theoretical investigations are needed in this regard (such as using time dependent density functional theory (TDDFT) or dynamical mean field theory (DMFT)) to accurately calculate the electronic correlations and many-body effects.

In relation to ongoing efforts to achieve sub-femtosecond time resolution in FEL experiments, novel arrival time measurement scheme based on spectral encoding of THz pulse emission excited by FEL pulses was presented. This scheme was shown to be capable of in-situ pulse-resolved timing jitter measurements with just $\mu\text{J}/\text{cm}^2$ fluence and time resolution of few femtoseconds. It makes it more suitable for future MHz rep rate FEL facilities comparing to other transient reflectivity techniques which require fluence near damage threshold ($\sim 20 \text{ mJ}/\text{cm}^2$). Further, it was shown that this technique can be used parasitically for FEL pulse diagnostics. Further investigations on different materials are needed to improve the sensitivity of in-situ measurement scheme and to extend the measurements to broad FEL energy range and pulse duration.

Zusammenfassung

In dieser Arbeit wurde die mikroskopische Entwicklung des optisch induzierten magnetostrukturellen Phasenübergangs in FeRh untersucht. Die elektronische Strukturentwicklung der unbesetzten Zustände wurde mit zeitaufgelöster Röntgenabsorptionsspektroskopie (tr-XAS) an der Fe L_3 -Kante gemessen. Mit Hilfe von Röntgenabsorptionsspektralsimulationen wurde die elektronische Strukturentwicklung auf die Modifikation der Austauschwechselwirkung und die Erzeugung ferromagnetischer Ordnung bezogen. Röntgenabsorptionsspektren wurden unter Dipolnäherung und Ein-Elektronen-Theorie für verschiedene Temperaturen, Gitterkonstanten und magnetische Zustände (FM und AFM) berechnet. Die theoretischen Berechnungen legten nahe, dass der wichtigste Beitrag zur Änderung der elektronischen Bandstruktur von der Modifikation der magnetischen Ordnung und damit von Austauschwechselwirkungen stammt. Die Experimente wurden an epitaktischen FeRh-Dünnschichten durchgeführt, die auf einkristallinen SiC-Membranen aufgewachsen waren. Eine direkte Messung von XAS-Spektraländerungen liefert die inhärenten Zeitskalen der konkurrierenden Wechselwirkungen des AFM-FM Phasenübergangs ohne die Notwendigkeit von magnetischem Kontrast und angelegtem Magnetfeld. Es wurde gezeigt, dass die elektronische Struktur und Austauschwechselwirkungen in FeRh durch Laseranregung auf ultraschnellen Zeitskalen modifiziert werden können. Auf späteren Zeitskalen ändern weitreichende Korrelationen auch deutlich die lokale elektronische Struktur, wie sie an der oberhalb der Fe L_3 -Kante beobachtet wird. Die Konkurrenz zwischen dem ferromagnetischen Austausch (Fe-Rh) und dem antiferromagnetischen Austausch (Fe-Fe) führt zu dem kurzreichweitigen FM-Zustand auf der Pikosekunden-Zeitskala nach der Laseranregung, aber der langreichweitige ferromagnetische Zustand kann nur auf der Zeitskala von 10 ps stabilisiert werden, was mit der Zeitskala der Gitterexpansion (14 ps) korrespondiert, die in anderen Experimenten beobachtet wurde.

Eine Verbindung zwischen dem mikroskopischen ferromagnetischen Zustand und der makroskopischen Magnetisierung wurde hergestellt, indem die räumliche Entwicklung ferromagnetischer Domänen unter Verwendung zeitaufgelöster Röntgenkleinwinkelstreuung (tr-SAXS) untersucht wurde. Es wurde gezeigt, dass das Differenzsignal (gepumpt-ungepumpt) hauptsächlich den ferromagnetischen Beitrag des Phasenübergangs liefert. Die Nukleations- und Wachstumsdynamik von FM-Domänen in einem Bereich von 10 nm bis 60 nm wurde auf Zeitskalen von bis zu 100 ps beobachtet. FM-Domänen, die aus der Kondensation/Abkühlung von Nichtgleichgewichts-FM-Fluktuationen um die 3-4 ps entstehen, wachsen mit unterschiedlichen Geschwindigkeiten zu späteren Zeitpunkten. Die Korrelationsfunktionen und die Korrelationslängenentwicklung, berechnet durch die Fourier-Transformation der angepassten SAXS-Intensität, ergeben drei Bereiche der dynamischen Verlangsamung des Phasenübergangs. Die Physik hinter der Dynamik kann durch einen Vergleich der Entwicklung der Korrelationslänge mit dem Ising-Modell ermittelt werden. Im ersten Bereich von 3 bis etwa 8 ps, wo die Entwicklung der Korrelationslänge exponentiell

abwärts verläuft, fällt der dynamische Exponent von 14 auf 1 ab. In diesem Bereich kondensieren Nichtgleichgewichts-FM-Fluktuationen zu FM-Nukleationszentren. Im darauf folgenden Bereich von 8 bis etwa 23 ps, wo die Wachstumsrate langsamer ist, fällt der dynamische Exponent von 1 auf 0,3 ab. In dieser Region nehmen nukleierte Domänen an Größe zu, und der FM-Ordnungsparameter ist nicht konserviert. Auf längeren Zeitskalen ab 23 ps fällt der dynamische Exponent von 0,3 auf 0,2 ab. In diesem Bereich wachsen die FM-Domänen auf Kosten kleinerer FM-Domänen durch Koaleszenz. Der FM-Ordnungsparameter bleibt in diesem Bereich der FM-Phasensättigungen nahezu erhalten. Somit liefern tr-XAS- und tr-SAXS-Messungen ein einheitliches mikroskopisches Bild der räumlichen und zeitlichen Entwicklung des photoinduzierten Phasenübergangs in FeRh. Nichtsdestotrotz sind weitere experimentelle und theoretische Untersuchungen an der Rh-L- oder -M-Kante erforderlich, um die Dynamik der FM-Ordnung und die Rolle von Rh bei der Stabilisierung des FM-Zustands von FeRh bei höheren Temperaturen zu klären.

Im Zusammenhang mit den laufenden Bemühungen, eine Zeitauflösung von Sub-Femtosekunden in XFEL-Experimenten zu erreichen, wurde ein neuartiges Schema zur Messung der Ankunftszeit von Röntgen- und Laser-Pulsen vorgestellt, welche auf der spektralen Kodierung der von XFEL-Pulsen in der Probe erzeugten THz-Strahlung basiert. Es wurde gezeigt, dass das in-situ pulsaufgelöste Timing-Jitter-Messprinzip mit Energiedichten im Bereich von $\mu\text{J}/\text{cm}^2$ auskommt und eine Zeitauflösung von wenigen Femtosekunden ermöglicht. Diese Methode eignet sich besser für zukünftige FEL-Anlagen mit Wiederholungsrate im MHz-Bereich im Vergleich zu anderen transienten Reflektivitätstechniken, die höhere Energiedichten nahe der Schadensschwelle von Materialien erfordern ($\sim 20 \text{ mJ}/\text{cm}^2$). Weiterhin konnte gezeigt werden, dass diese Technik parasitär für die XFEL-Pulsdiagnostik eingesetzt werden kann. Weitere Untersuchungen an verschiedenen Materialien sind erforderlich, um die Empfindlichkeit der Methode weiter zu steigern und die Messungen auf einen breiteren Bereich von Photonenenergien und Pulsdauern auszudehnen.

A Appendix

A.1 Two-temperature model

The dynamical response of materials upon ultrafast optical excitation involves various degrees of freedom which interact at different time scales and can vary from attoseconds to many picoseconds or even longer [54]. Such dynamical response and corresponding time scales, at macroscopic level can (phenomenologically) be simulated by considering the macroscopic properties (temperature, heat conduction, heat capacity), relaxation times and thermalization times of different degrees of freedom. [35, 57, 313–318].

The two-temperature model (2TM) describes the phenomenological non-equilibrium/quasi-equilibrium energy transfer between the electron and lattice subsystems in metals excited by femtosecond optical pulses. It is assumed that the optical pulse initially excites the electronic subsystem and the energy transfer between electron and lattice is defined by the electron-lattice coupling parameter G_{el} . Since the electronic relaxation rates (via electron-electron and electron-phonon scattering) in metals are at ~ 10 - 100 fs time scales, this assumption of quasi-equilibrium within the electronic subsystem holds for metals at time scales greater than ~ 100 fs. For the time scales greater than ~ 100 fs, the electronic subsystem can be assumed to follow the Fermi-Dirac distribution. The electronic and lattice subsystems can be considered in their own equilibrium(quasi-equilibrium), thus defining the macroscopic temperatures (T_e , T_l) for the electronic and lattice subsystem.

Fig. A.1 illustrates the different processes and the time scales for the electronic and lattice subsystems described by the 2TM model. The electronic subsystem undergoes ultrafast heating or so called "hot electron dynamics" at ~ 100 fs timescale followed by the thermalization with the lattice at ~ 2 - 10 ps time scales, depending on electron-phonon coupling strength. The electron and lattice subsystems relax to the initial state at $\sim ns$ - μs timescales. Following [315], the dual-hyperbolic 2TM can be written as following:

$$C_e(T_e, T_l) \frac{\partial T_e(t)}{\partial t} = -\nabla \cdot Q_e - G_{ep}(T_e - T_l) + S(t), \quad (\text{A.1})$$

$$\tau_e \frac{\partial Q_e}{\partial t} + Q_e = -K_e \nabla T_e, \quad (\text{A.2})$$

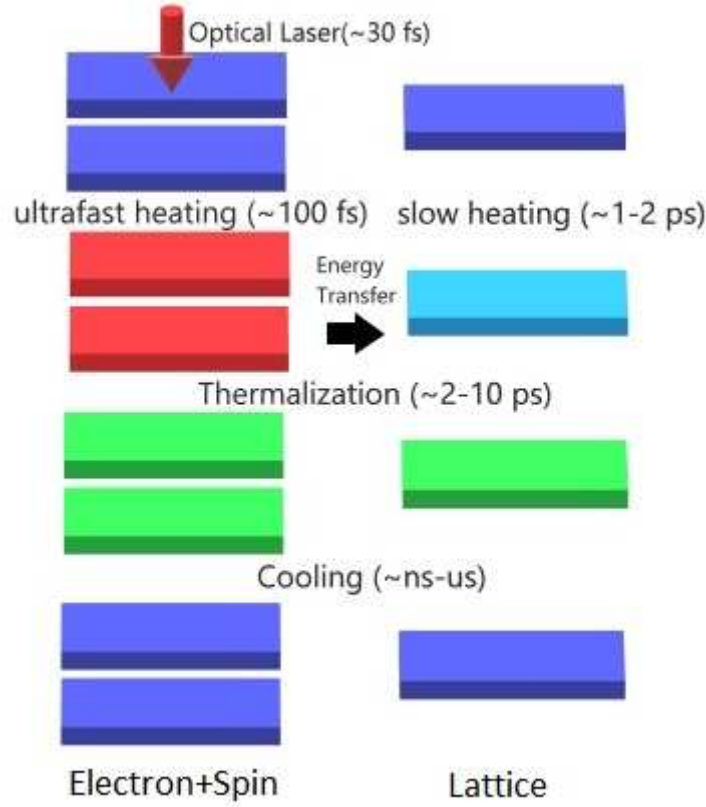


Figure A.1: Illustration of Two Temperature Model. Electron, Spin (blocks in left) and Lattice (blocks in right) subsystems follow the coupled dynamics after optical excitation of electronic subsystem. Time scales for energy transfer between these subsystems can be related to microscopic mechanisms. Electron and spin temperatures are assumed in equilibrium with each other. Different colours represent different temperature

$$C_l(T_e, T_l) \times \frac{\partial T_l(t)}{\partial t} = G_{ep}(T_e - T_l), \quad (\text{A.3})$$

$$\tau_l \frac{\partial Q_l}{\partial t} + Q_l = -K_l \nabla T_l. \quad (\text{A.4})$$

Equations A.1 and A.3 represent the energy balance in the electron and lattice subsystems including the external excitation source while equations A.2 and A.4 represent the energy flow/flux across the system due to the temperature gradient in electron and lattice subsystems. Here, C_e , C_l are the electronic and lattice heat capacities, Q_e , Q_l are the electronic and lattice heat fluxes, K_e , K_l are the electronic and lattice thermal conductivities and τ_e , τ_l are the electronic and lattice relaxation times. G_{ep} is the electron-phonon coupling factor and $S(t)$ is the optical excitation function given as:

$$S(z, t) = \sqrt{\frac{4 \ln 2}{\pi}} \frac{F(1-R)}{\delta t_p} \times e^{-\frac{z}{\delta} - 4 \ln 2 \left(\frac{t-2t_p}{t_p}\right)^2}. \quad (\text{A.5})$$

Here, F is the fluence, R is the reflectivity from front surface, δ is the penetration depth, t_p is the pulse duration and z is the depth along normal to material surface.

We consider the following assumptions for treating the energy transfer in metals excited by optical pulses:

- For metals, the electronic relaxation time (τ_e) is around 10 fs and thus can be neglected for dynamics at timescale of around 100 fs and laser pulse duration of order of around 30 fs.
- The thermal conduction due to lattice can also be neglected as electronic conduction is main contributing factor in metals.
- The electron-phonon coupling factor G_{ep} can be written as $G_{ep} = \frac{C_e(T_e, T_l)}{\tau_{ep}}$ where τ_{ep} is the electron-phonon thermalization time.
- For looking at the dynamics on ps timescales, we can neglect the spatial dependence of the energy transfer because the spot size of the X-ray probe beam is around 3 times smaller than the optical pump beam. Thus, temperature profile only varies with thickness (z) and time (t).
- The thermal conductivity does not have any explicit thickness(z) dependence.

Based on the above assumptions, the dual hyperbolic 2TM model can be reduced to the following parabolic 2TM equations:

$$C_e(T_e, T_l) \frac{\partial T_e(z, t)}{\partial t} = K_e(T_e, T_l) \frac{\partial^2 T_e}{\partial z^2} - \frac{C_e(T_e, T_l)}{\tau_{ep}} (T_e - T_l) + S(z, t), \quad (\text{A.6})$$

$$C_l(T_e, T_l) \frac{\partial T_l(z, t)}{\partial t} = \frac{C_e(T_e, T_l)}{\tau_{ep}} (T_e - T_l). \quad (\text{A.7})$$

By taking proper boundary conditions, these equations can be solved numerically to find the time- and depth-dependent temperature profiles of the electronic and lattice subsystems. A good illustration on numerical solution and comparison of different two-temperature models (parabolic, hyperbolic, dual hyperbolic, semi-classical etc.) can be found in [313–316].

In sections A.2 and A.3, this two temperature model will be used to describe the thermal response and order parameter profile for the first order phase transition in FeRh excited by optical pulses.

A.2 Two temperature model for phase transitions

For first order phase transitions, the thermodynamics variables such as specific heat capacity, electrical resistivity and thermal conductivity show discontinuities at transition temperatures [66, 67, 75, 288, 319, 320]. This affects the heat flow in the material and the temperature profiles of electronic and lattice subsystems. These discontinuities can be modelled by piecewise continuous functions.

The temperature-dependent profiles of heat capacities and thermal conductivities of FeRh, which undergoes a magnetic and structural phase transition near 353K and has a Curie temperature of near 690K, can be modelled as follows:

$$C_e(T_e, T_l) = \begin{cases} \gamma_{AFM} \times T_e, & T_e \leq 675K \text{ \& } T_l \leq 353K \\ \gamma_{FM} \times T_e, & T_e \leq 675K \text{ \& } T_l \geq 373K \\ F_1(\gamma_{AFM}, \gamma_{PM}, T_e, 675, 705), & 675K < T_e < 705K \text{ \& } T_l < 353K \\ F_1(\gamma_{FM}, \gamma_{PM}, T_e, 675, 705), & 675K < T_e < 705K \text{ \& } T_l > 373K \\ F_1(\gamma_{AFM}, \gamma_{FM}, T_l, 353, 373) \times \frac{T_e}{T_l}, & T_e < 675K \text{ \& } 353K < T_l < 373K \\ F_1\left(\frac{F_1(\gamma_{AFM}, \gamma_{FM}, T_l, 353, 373)}{T_l}, \gamma_{PM}, T_e, 675, 705\right), & 675K < T_e < 705K \text{ \& } 353K < T_l < 373K \\ \gamma_{PM} \times T_e, & T_e \geq 705K \end{cases} \quad (A.8)$$

$$C_l(T_l) = \begin{cases} C_{total}(T_l) - \gamma_{AFM} \times T_l - C_{mag}, & T_l \leq 353K \\ C_{total}(T_l) - \gamma_{FM} \times T_l - C_{mag}, & T_l \geq 373K \\ C_{total}(T_l) - F_1(\gamma_{AFM}, \gamma_{FM}, T_l, 353, 373) - C_{mag}, & 353K < T_l < 373K \end{cases} \quad (A.9)$$

The temperature-dependent heat capacity(C) and Sommerfeld coefficients(γ) for the AFM and FM phase were taken from experimental measurements of [75]. The values for disordered/paramagnetic phase were taken from a theoretical study of [223] after normalizing with respect to the experimental values of AFM and FM phases.

The temperature-dependence of thermal conductivity (κ_e) is calculated from temperature-dependent electrical resistivity(ρ_e) given in [67], assuming the Wiedemann-Franz law:

$$\kappa_e(T_e, T_l) = \frac{2.44 \times T_e}{\rho_e(T_e, T_l)}. \quad (A.10)$$

$$\rho_e(T_e, T_l) = \begin{cases} \mu_{AFM} \times T_e, & T_e \leq 675K \text{ \& } T_l \leq 353K \\ \mu_{FM} \times T_e, & T_e \leq 675K \text{ \& } T_l > 373K \\ F_2(\mu_{AFM}, \rho_{PM}, T_e, 675, 705), & 675K < T_e < 705K \text{ \& } T_l < 353K \\ F_2(\mu_{FM}, \rho_{PM}, T_e, 675, 705), & 675K < T_e < 705K \text{ \& } T_l > 373K \\ F_1(\mu_{AFM}, \mu_{FM}, T_l, 353, 373) \times \frac{T_e}{T_l}, & T_e < 675K \text{ \& } 353K < T_l < 373K \\ F_2\left(\frac{F_1(\mu_{AFM}, \mu_{FM}, T_l, 353, 373)}{T_l}, \rho_{PM}, T_e, 675, 705\right), & 675K < T_e < 705K \text{ \& } 353K < T_l < 373K \\ \rho_{PM}, & T_e > 705K \end{cases} \quad (\text{A.11})$$

F_1 and F_2 in above equations are the polynomial functions to make the heat capacities and thermal conductivity continuous (in second order derivative) during the phase transition. μ_{AFM} and μ_{FM} are the slopes of ρ_e vs T curve obtained from [67]. Parameters used in the 2TM model shown in the Table A.1.

Wavelength	λ	800 nm
Pulse Duration	t_p	35 fs
Penetration depth	δ	20 nm
Thermalization time	τ_{ep}	1.5 ps
Magnetic heat capacity	C_{mag}	6 J/K/mol
Electronic Sommerfeld Coefficient in AFM phase	γ_{AFM}	$3.5 \times 10^{-3} \text{ J/K}^2/\text{mol}$
Electronic Sommerfeld Coefficient in FM phase	γ_{FM}	$8.5 \times 10^{-3} \text{ J/K}^2/\text{mol}$
Electronic Sommerfeld Coefficient in PM phase	γ_{PM}	$28 \times 10^{-3} \text{ J/K}^2/\text{mol}$

Table A.1: Parameters used in 2TM model

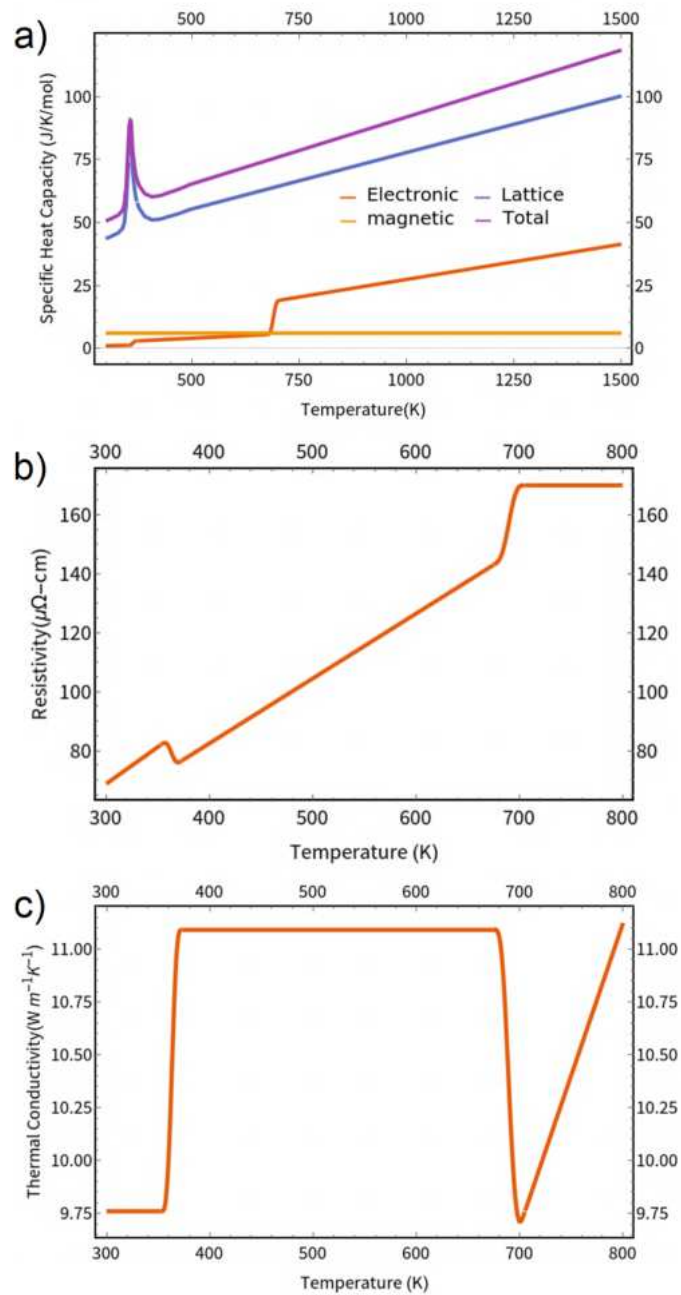


Figure A.2: Temperature dependence of physical properties for two temperature model for FeRh. a) specific heat capacities for different subsystems. Magnetic heat capacity contribution is small and is assumed to be constant. b) electronic resistivity. c) electronic thermal conductivity. Data digitized from [75] and [67].

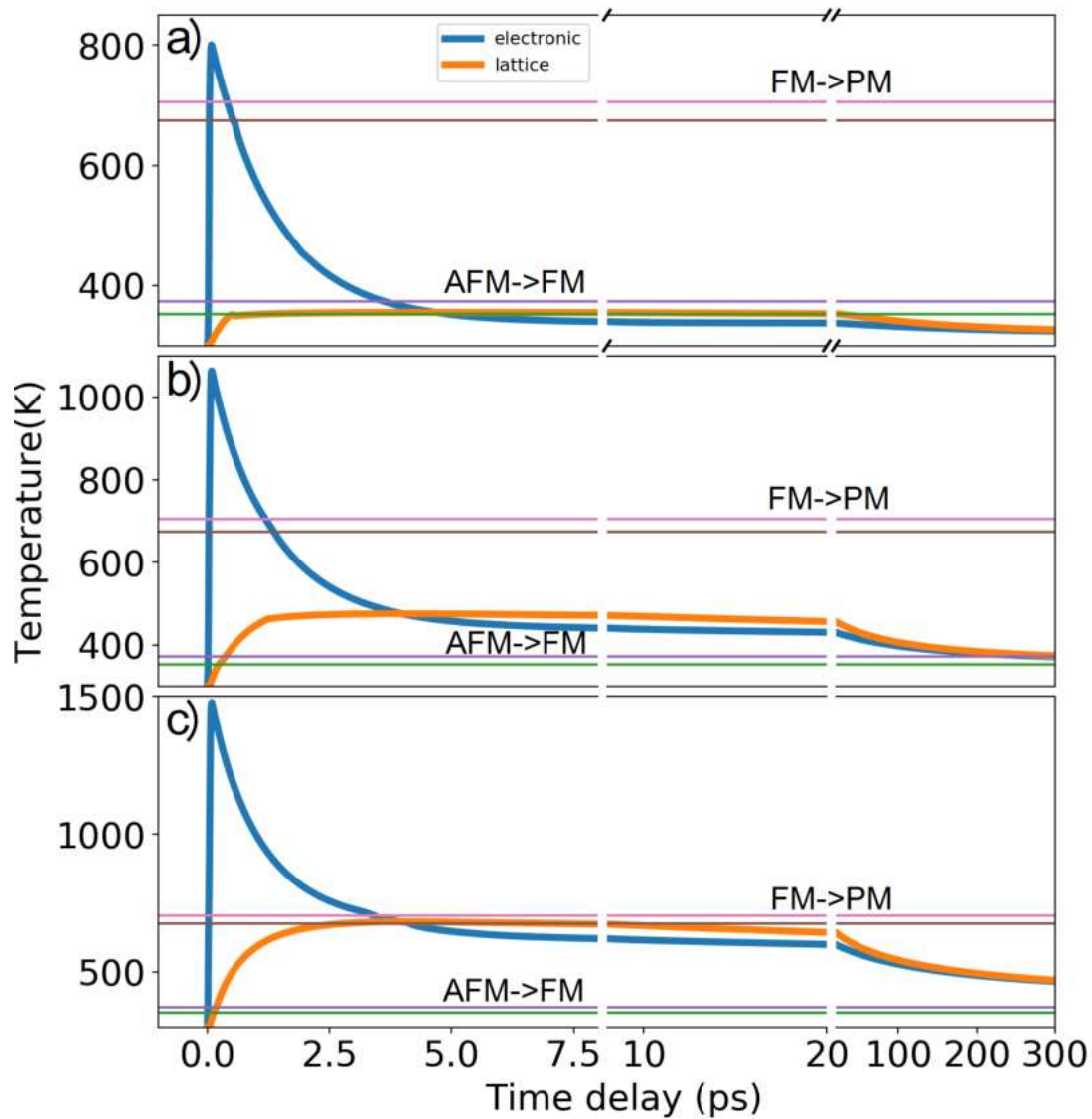


Figure A.3: Parabolic 2TM model for FeRh phase transition. Time evolution of electronic and lattice temperature for various fluence levels. The fluence threshold is calculated at 300 ps after optical excitation. a) below threshold b) at threshold (for the SAXS measurements in this thesis) c) above threshold (for the XAS measurements in this thesis). Horizontal lines represent transition hysteresis for AFM-FM ordering (near 363 K) or ordering- \rightarrow disordering (near 690K).

Now using the 2TM model and above equations for heat capacities and thermal conductivities, we can simulate the temperature profiles for the FeRh phase transition with optical excitation. In the Fig. A.3, the electron and lattice temperature dynamics is shown for three different excitation fluences. Here, the threshold fluence means that lattice temperature is above transition temperature when measured at around 300 ps. It can be seen that the electronic temperature goes beyond the Curie temperature of 690K before cooling down which means that the FeRh electronic system should follow an order (AFM)-disorder-order (AFM or FM depending on fluence) dynamics at picosecond timescales. From the dynamics of the electronic and lattice temperature at different fluences, it can

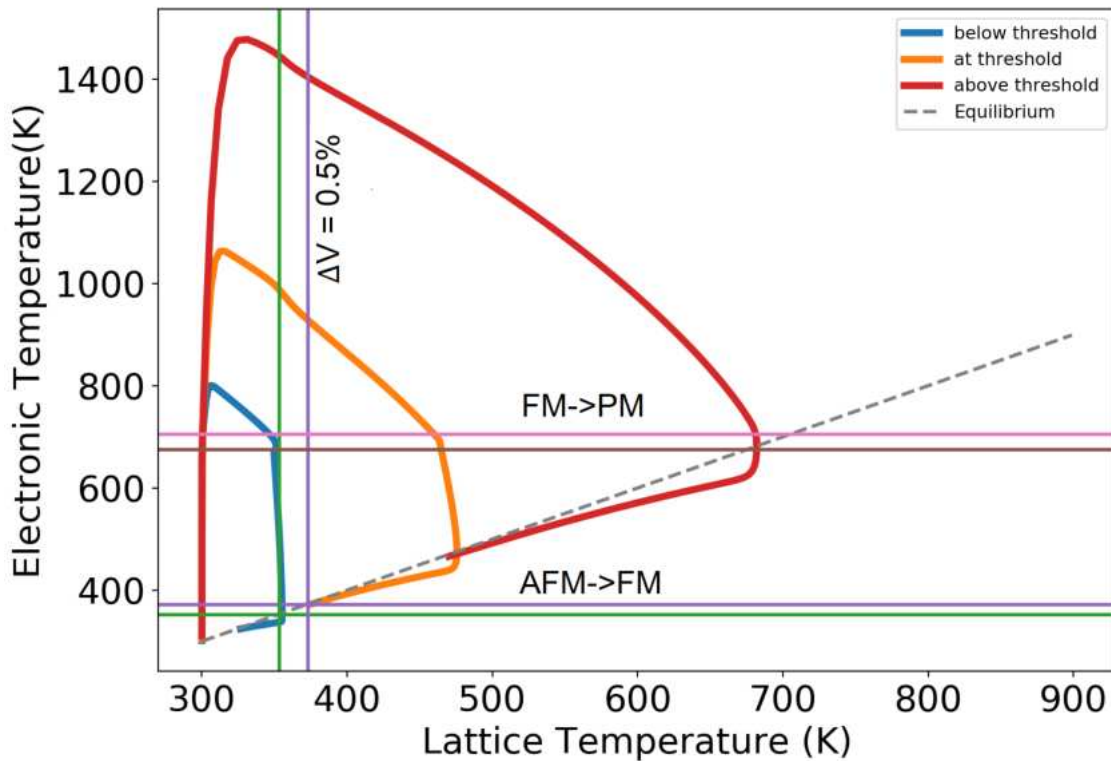


Figure A.4: Coupled temperature evolution during FeRh phase transition. Evolution of electronic and lattice temperatures for different fluences. Horizontal lines in represent transition hysteresis region from AFM-FM ordering (near 363K) or ordering to disordering (near 690K). Vertical lines represent structural transition region. Dashed grey line represents thermal equilibrium between subsystems. Highest electronic temperature of ~ 1400 K is reached within 200 fs after optical excitation. FM fluctuations arise at ~ 3 ps when electronic temperature reaches near the Curie temperature (690K). As electronic system cools down together with lattice temperature in equilibrium, FM fluctuation condense to nucleation centers.

be observed that the electronic temperature reaches near a Curie temperature (around 690K) for FeRh while lattice temperature not necessarily crosses the AFM-FM transition temperature (around 360K). This implies that AFM-FM transition of the optically excited FeRh eventually go through fully or partially disordered state before relaxing to FM state. This is in contrast to equilibrium phase transition obtained through static heating where the transition occurs through phase coexistence of AFM and FM domains and nucleation and growth mechanism.

A.3 Temperature and magnetic order parameter profiles from 2TM model

The optical excitation has a small penetration depth for metallic systems. For FeRh thin films, 800 nm excitation wavelength has a penetration depth of around 20 nm. Because of this attenuation, there is large temperature gradient across the thin film. In Fig. A.5, we plot the depth profiles for the temperature of the electronic and lattice subsystems.

Further, based on the electronic and lattice temperature profiles, the magnetic order parameter $\Phi_m(T_e, T_l)$ depth profile can be also plotted for the FeRh phase transition as follows:

$$\Phi_m(T_e, T_l) = \begin{cases} -(1 - (\frac{T_e}{705})^{4.5}), & T_e \leq 675K \text{ \& } T_l \leq 353K \\ (1 - (\frac{T_e}{705})^{4.5}), & T_e \leq 675K \text{ \& } T_l \geq 373K \\ F_3[-(1 - (\frac{T_e}{705})^{4.5}), 0, T_e, 675, 705], & 675K < T_e < 705K \text{ \& } T_l < 353K \\ F_3[(1 - (\frac{T_e}{705})^{4.5}), 0, T_e, 675, 705], & 675K < T_e < 705K \text{ \& } T_l > 373K \\ F_3[-(1 - (\frac{T_e}{705})^{4.5}), (1 - (\frac{T_e}{705})^{4.5}), T_l, 353, 373] \times \frac{T_e}{T_l}, & T_e < 675K \text{ \& } 353K < T_l < 373K \\ F_3[F_3(-(1 - (\frac{T_e}{705})^{4.5}), (1 - (\frac{T_e}{705})^{4.5}), T_l, 353, 373), & 675K < T_e < 705K \text{ \& } \\ & 0, T_e, 675, 705] & 353K < T_l < 373K \\ 0, & T_e \geq 705K \end{cases}, \quad (\text{A.12})$$

where F_3 is a polynomial function to make the order parameter continuous during the phase transition. Here the negative, positive and zero order parameter means antiferromagnetic, ferromagnetic and disordered phase, respectively.

From the depth-resolved temperature and the order parameter profile shown in Fig. A.5, it can be observed that it takes quite a long time for demagnetization of the complete film (around 100 ps) as expected because optical penetration depth is around 20 nm. Though, initial 40 nm thickness is demagnetized relatively quickly under 20 ps. From the point of view of X-ray probe, the penetration depth at Fe L_3 edge is around 35 nm. Thus, we would observe mostly dynamics happening within 35 nm thickness. Further, from zoomed in order parameter profile, it can be seen that FM state starts to grow from middle of the film and not from top surface. Though, in practice, inherent symmetry breaking at surface may lead to the FM state earlier than the bulk.

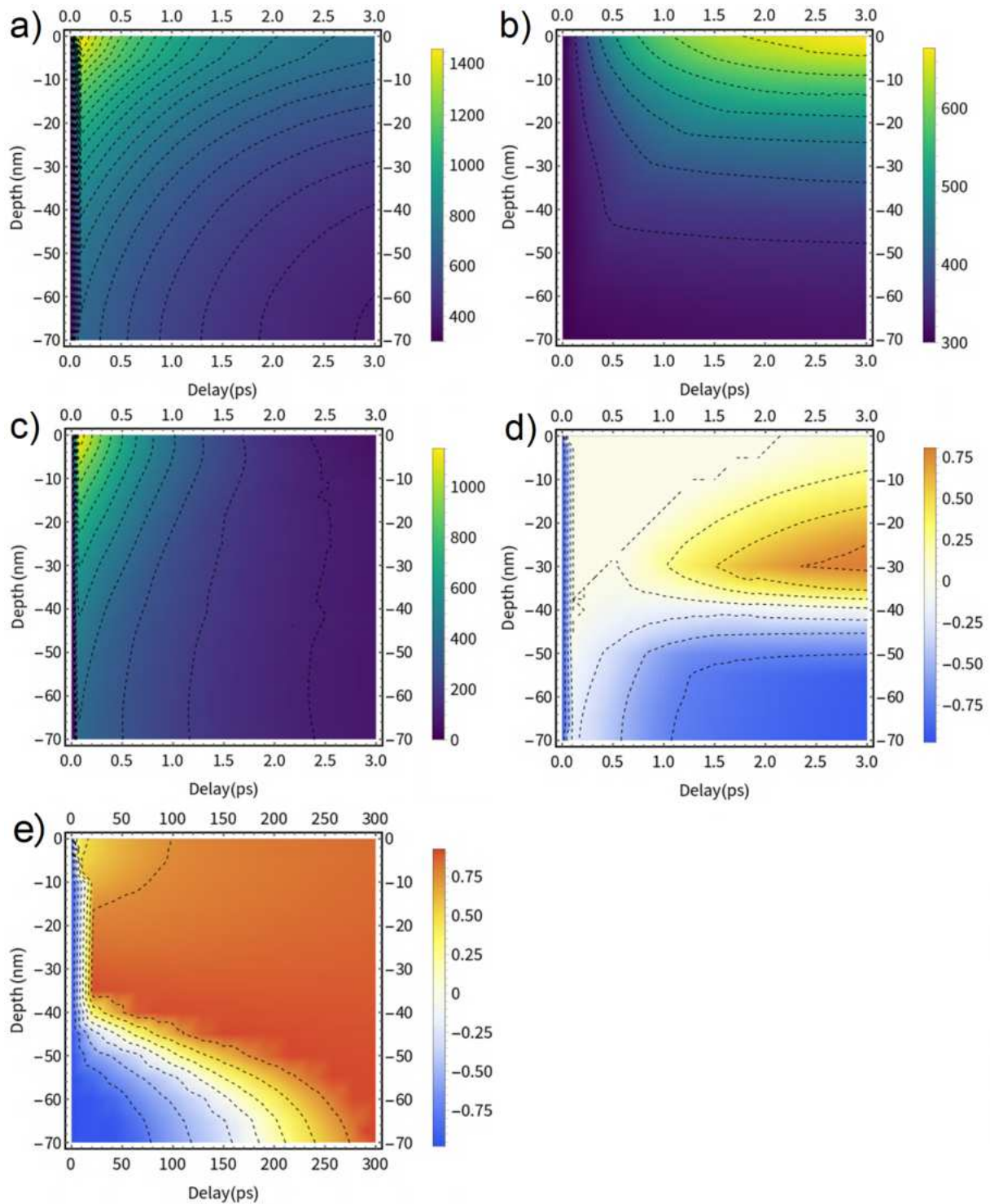


Figure A.5: Temperature (in K) and normalized order parameter (-ve: AFM, 0: PM, +ve: FM) profiles: Time evolution and depth profiles of electronic temperature (a) lattice temperature (b) difference (electronic-lattice) (c) and magnetic order parameter (short (d) & long time (e)). The FM order parameter is formed in the middle of the film according to the 2TM model. Initial 30 nm of the film is already magnetized within 20 ps while the remaining part takes longer time up to several 100 ps.

A.4 Synthesis and characterization of FeRh thin films

The samples were fabricated and characterized by collaborators Dr. Jon Ander Arregi and Dr. Vojtěch Uhlíř at CEITEC, Brno, Czech Republic. A short summary of the synthesis and characterizations is reproduced here for completeness.

A.4.1 Epitaxial growth of FeRh on SiC

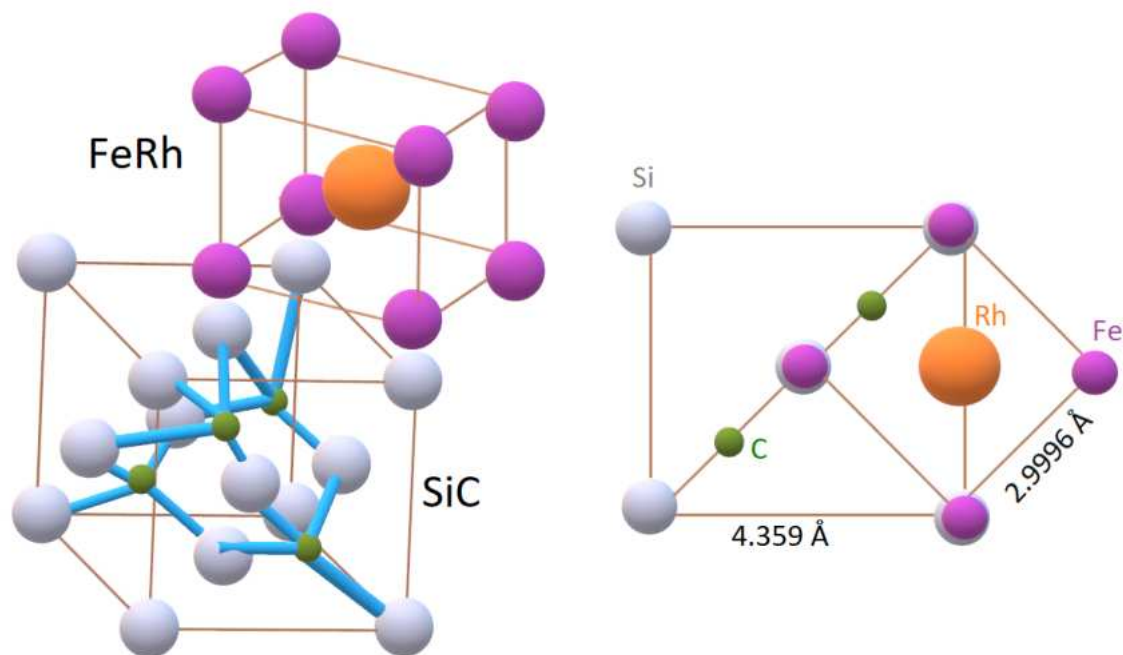


Figure A.6: Epitaxy of FeRh on SiC. 3D and 2D (from top) representation of epitaxial growth of single crystalline (001) FeRh lattice rotated along the diagonal (45 degree) of single crystalline 3C-SiC lattice (substrate).

The FeRh samples were deposited via magnetron sputtering on 100 nm thick epitaxial SiC (001) membranes on 200 μm thick single-crystal Si (001) frame (Silson Ltd.). The substrates were introduced in a chamber with a base pressure lower than 5×10^{-8} mbar and pre-heated to 623 K for 1h prior to deposition. The epitaxial growth of FeRh was subsequently performed at the same temperature using an equiatomic FeRh target at a fixed Ar pressure of 2.8×10^{-3} mbar. The deposition rate at a sputter power of 50W was 0.03 nm/s. FeRh layers were annealed after growth at 923K for 30 to 60 min (depending on FeRh thickness, with longer annealing for thicker films) in the same chamber to obtain the desired CsCl type (B2 ordering) crystal structure. The samples were subsequently cooled down below 373K and covered with a protective 3 nm thick Pt capping layer. After the static characterizations (described later), a 150 nm Al heat sink layer was deposited at the back-side using electron beam evaporation.

X-ray symmetric $\theta/2\theta$ scans shown in Fig. A.7 (a) show the FeRh (001) out of plane texture grown on 3C-SiC (001) /Si (001). Further, the azimuthal(ϕ) scans shown in Fig. A.7 (b) confirm the in-plane four-fold symmetry with FeRh (110) direction being parallel to SiC (110), as evident from 45-degree shift between SiC (113) and FeRh (112).

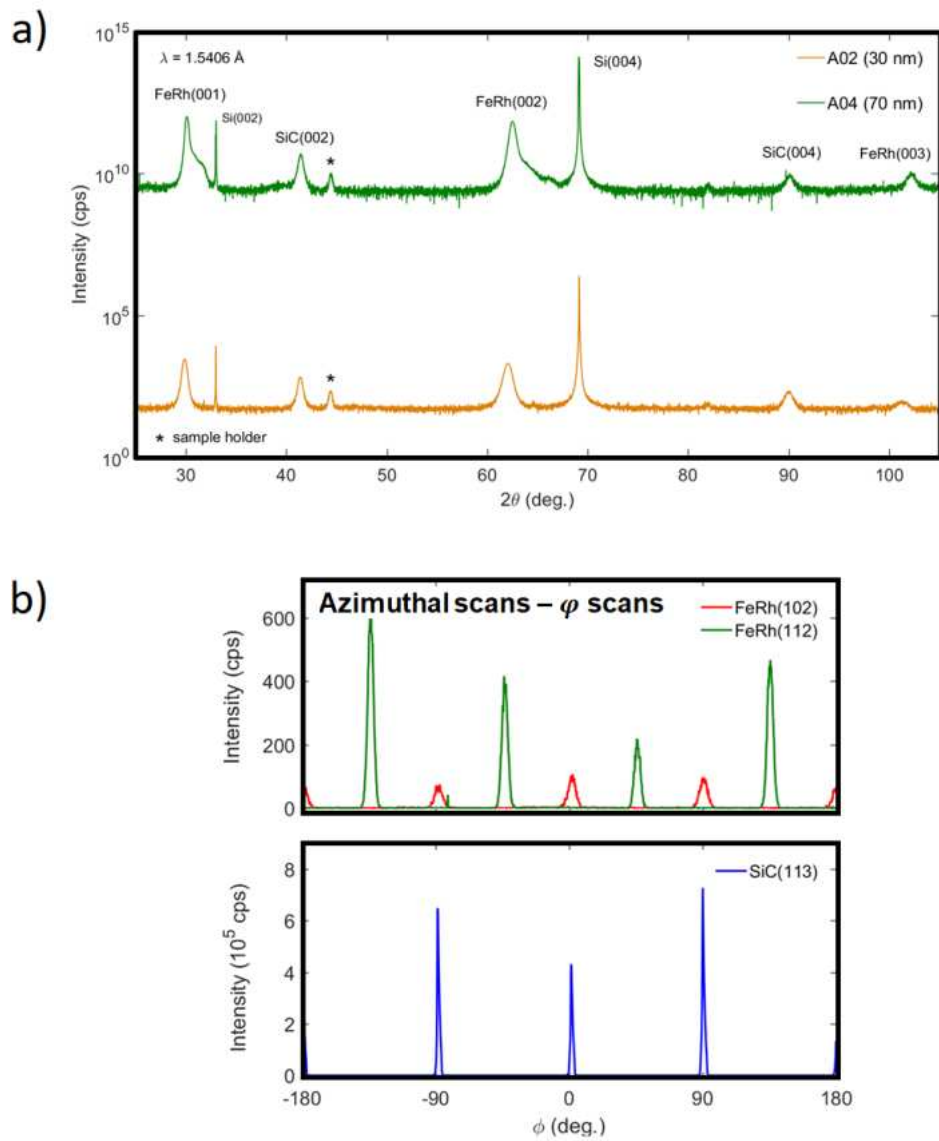


Figure A.7: X-ray diffraction characterization of crystalline FeRh by out of plane symmetric (a) and in-plane azimuthal(b) scans

A.4.2 Lattice parameter and thickness determination

X-ray reflectivity (XRR) and x-ray diffraction (XRD) using a Rigaku SmartLab 9 kW diffractometer with Cu K_α radiation ($\lambda = 1.5406 \text{ \AA}$) were employed for the structural characterization of the samples [321]. The instrument uses a double-bounce Ge (022) monochromator and a 5° Soller slit in the incident and diffractive optics, respectively. X-ray reciprocal space map measurements at 300 K and 400 K were employed for the investigation of the anti-ferromagnetic and ferromagnetic lattices of the FeRh films, respectively. For the high-temperature XRD measurements, the sample was placed in a high-temperature chamber with a controllable ceramic heater with a hemispherical dome made of graphite, using a N_2 gas environment for improved temperature homogeneity. XRD with reciprocal space mapping (geometry shown in Fig. A.8) is used to determine the in-plane (a) and out-of plane (c) lattice parameter of FeRh and SiC as shown in Fig. A.9. Estimated parameter are shown in Fig. A.10.

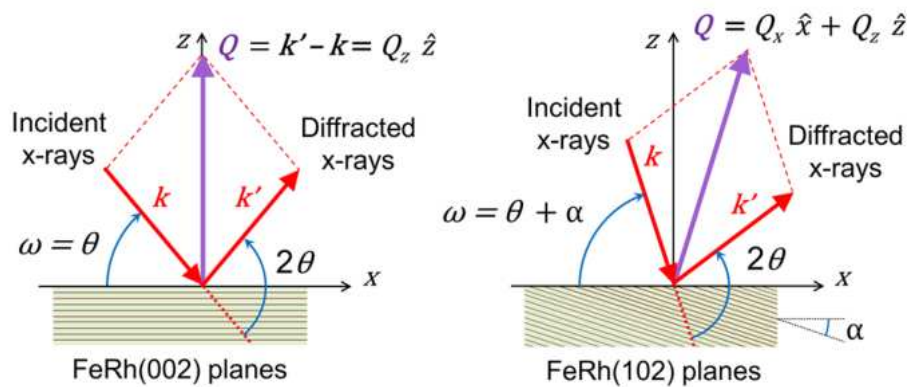


Figure A.8: Geometry for reciprocal space mapping in XRD measurements for out of plane (a) and in plane lattice parameter (a and b) determination.

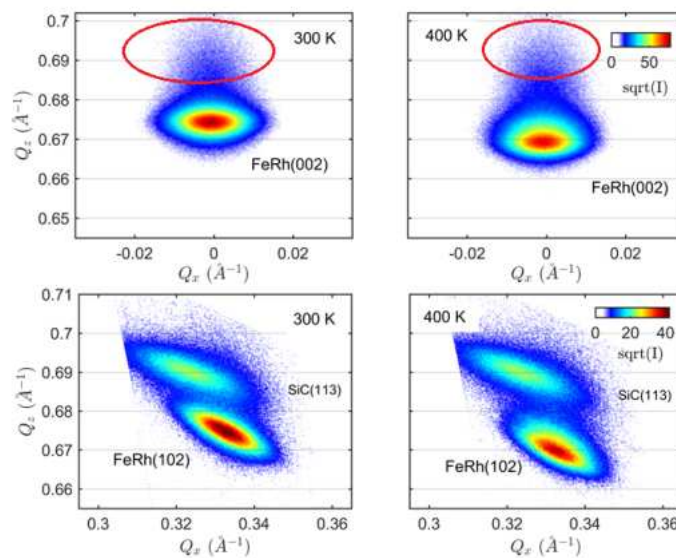


Figure A.9: FeRh lattice parameters determination. Reciprocal space maps around different FeRh crystal planes (002 and 102) and temperature (300K and 400K) for lattice parameter determination before and after FeRh phase transition

	Sample	FeRh thickness (nm)	300 K			400 K		
			c (Å)	a (Å)	c/a	c (Å)	a (Å)	c/a
FeRh lattice	A02	29.7 ± 0.3	2.9852	2.9818	1.0012	2.9973	2.9960	1.0004
	A04	67 ± 1	2.9671	2.9996	0.9891	2.9857	2.9978	0.9959
	Sample	FeRh thickness (nm)	300 K			400 K		
			c (Å)	a (Å)	c/a	c (Å)	a (Å)	c/a
SiC lattice	A02	29.7 ± 0.3	4.3553	4.3487	1.0015	-	-	-
	A04	67 ± 1	4.3534	4.3591	0.9987	-	-	-

Figure A.10: Estimated in plane (a) and out of plane (c) lattice parameters for FeRh (before and after transition) and SiC for different FeRh thickness (30 and 70 nm)

Kiessig fringes from X-ray reflectivity measurements were used to determine the accurate thickness and roughness of the FeRh, Pt and SiC as shown in Fig. A.11. For the 70 nm thick sample, fringes were not clearly visible so thickness was determined by a calibration of deposition rate with respect to estimated values of other samples.

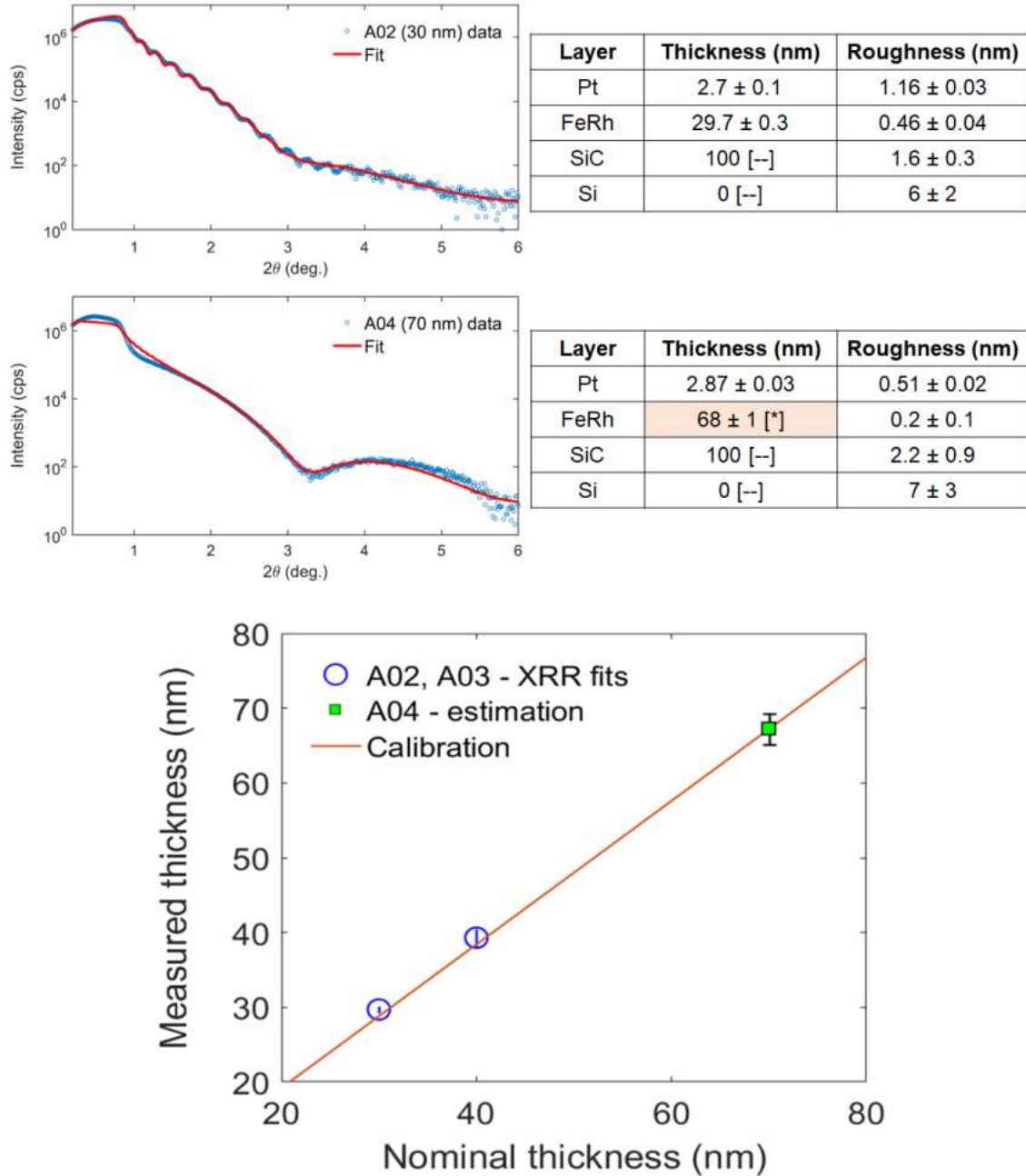


Figure A.11: Top: X-ray reflectivity measurements for thickness measurements. Corresponding table shows the estimated thickness of different layers in the sample structure. red-shaded part with * is based on the extrapolated estimation and not the direct fitting of fringes. Thickness values of substrates (- -) are taken as fixed values. Bottom: Estimated thickness for 70 nm nominally thick FeRh using an extrapolation of calibrated of growth rate based on other thicknesses.

A.4.3 Phase transition characterization with magneto-optical Kerr effect

The temperature-driven phase transition of the membrane-window areas of the FeRh films was verified using a magneto-optical Kerr effect (MOKE) microscope from Evico Magnetics with a 20× magnification microscope objective lens. The sample temperature was adjusted in between 300-410K using a custom-made Peltier heater stage. The measurement of field-dependent magnetization hysteresis loops during heating and cooling characterized the temperature-dependent magnetization order parameter as shown in Fig. A.12 [322]. It can be observed that the transition temperature is lower for thinner samples due to the higher in-plane strain, which favours the FM state.

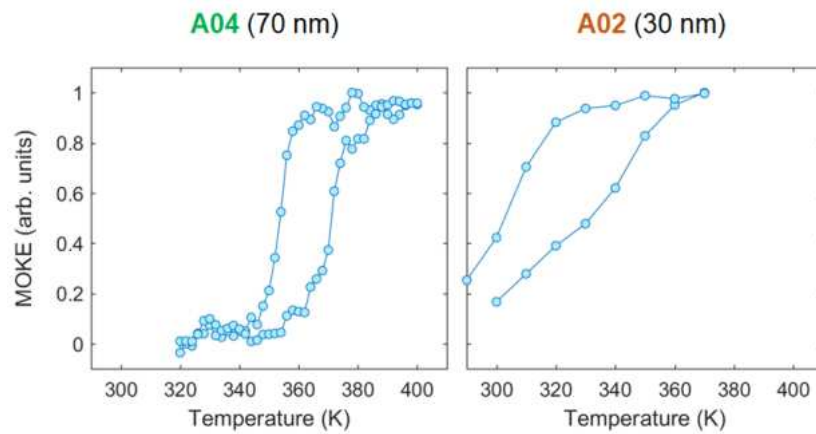


Figure A.12: Characterization of magnetic phase transition in FeRh using static MOKE microscopy. Temperature-dependent MOKE hysteresis for 70 nm (left) and 30 nm (right) FeRh samples

A.5 Input file for calculation of density of states using Elk

```
!Ground state calculation and partial density of states
tasks
0
10
!Spin polarized density of states
spinpol
.true.
! Spin orbit coupling is included
spinorb
.true.
! Core levels are solved with spin polarized Dirac equation
spincore
.true.
! Maximum angular momentum cutoff for DOS
lmaxdos
3
!Maximum angular moment cutoff at muffin tin radius
lmaxi
3
! Conduction stated included
lorbcnd
.true.
!radial step for mesh size
lradstp
3
!Maximum no of iterations for one step
maxitoepl
1000
! maximum no of self consistent loops
maxscl
1000
! Mixing type for finding the roots ( 3 = Broyden mixing)
mixtype
3
ncbse
3
nvbse
3
nxoapwlo
1
!Fermi distribution type smearing
tempk
```

```

300.0
!use GGA
xctype
22
!rgkmax default 7.0
rgkmax
8.0
! default 1.d-6
epspot
5.d-9
ngridk
16      16      16
! scratch space
scrpath
'/tmp/'
!start with a large magnetic field and reduce at each iteration
bfieldc
0.0      0.0      1.d-3 (0.0 for NM (non-magnetic phase))
reducebf
0.8
! large number of empty states necessary for "continuum" absorption
nempty
60

      !FeRh-AFM lattice constant parameters & AFM phase (calculation-1)
avec
0.0      1.0      0.9826150426
1.0      0.0      0.9826150426
1.0      1.0      0.0
scale
5.6958257823
atoms
2 : nspecies
'Fe.in' : spfname
2 : natoms
0.0      0.0      0.0      0.0      0.0      0.01 : atposl, bfcmt
0.5      0.5      0.5      0.0      0.0      -0.01 : atposl, bfcmt
'Rh.in' : spfname
2 : natoms
0.25     0.25     0.25     0.0      0.0      0.0 : atposl, bfcmt
0.75     0.75     0.75     0.0      0.0      -0.0 : atposl, bfcmt

```

!FeRh- AFM lattice constant parameters & FM phase (calculation-2)

avec

0.0 1.0 0.9826150426

1.0 0.0 0.9826150426

1.0 1.0 0.0

scale

5.6958257823

atoms

2 : nspecies

'Fe.in' : spfname

2 : natoms

0.0 0.0 0.0 0.0 0.0 0.01 : atposl, bfcmt

0.5 0.5 0.5 0.0 0.0 0.01 : atposl, bfcmt

'Rh.in' : spfname

2 : natoms

0.25 0.25 0.25 0.0 0.0 0.01 : atposl, bfcmt

0.75 0.75 0.75 0.0 0.0 0.01 : atposl, bfcmt

!FeRh-AFM lattice constant parameters & NM phase (calculation-3)

avec

0.0 1.0 0.9826150426

1.0 0.0 0.9826150426

1.0 1.0 0.0

scale

5.6958257823

atoms

2 : nspecies

'Fe.in' : spfname

2 : natoms

0.0 0.0 0.0 0.0 0.0 0.1 : atposl, bfcmt

0.5 0.5 0.5 0.0 0.0 0.0 : atposl, bfcmt

'Rh.in' : spfname

2 : natoms

0.25 0.25 0.25 0.0 0.0 0.0 : atposl, bfcmt

0.75 0.75 0.75 0.0 0.0 0.0 : atposl, bfcmt

!FeRh-FM lattice constant parameters & AFM phase (calculation-4)

avec

0.0 1.0 0.9895466914

1.0 0.0 0.9895466914

1.0 1.0 0.0

scale

5.6945029735

atoms

2 : nspecies

'Fe.in' : spfname

2 : natoms

0.0 0.0 0.0 0.0 0.0 0.01 : atposl, bfcmt

0.5 0.5 0.5 0.0 0.0 -0.01 : atposl, bfcmt

'Rh.in' : spfname

2 : natoms

0.25 0.25 0.25 0.0 0.0 0.0 : atposl, bfcmt

0.75 0.75 0.75 0.0 0.0 -0.0 : atposl, bfcmt

!FeRh- FM lattice constant parameters & FM phase (calculation-5)

avec

0.0 1.0 0.9895466914

1.0 0.0 0.9895466914

1.0 1.0 0.0

scale

5.6945029735

atoms

2 : nspecies

'Fe.in' : spfname

2 : natoms

0.0 0.0 0.0 0.0 0.0 0.01 : atposl, bfcmt

0.5 0.5 0.5 0.0 0.0 0.01 : atposl, bfcmt

'Rh.in' : spfname

2 : natoms

0.25 0.25 0.25 0.0 0.0 0.01 : atposl, bfcmt

0.75 0.75 0.75 0.0 0.0 0.01 : atposl, bfcmt

!FeRh- FM lattice constant parameters & NM phase (calculation-6)

avec

0.0 1.0 0.9895466914

1.0 0.0 0.9895466914

1.0 1.0 0.0

scale

5.6945029735

atoms

2 : nspecies

'Fe.in' : spfname

2 : natoms

0.0 0.0 0.0 0.0 0.0 0.1 : atposl, bfcmt

0.5 0.5 0.5 0.0 0.0 0.0 : atposl, bfcmt

'Rh.in' : spfname

2 : natoms

0.25 0.25 0.25 0.0 0.0 0.0 : atposl, bfcmt

0.75 0.75 0.75 0.0 0.0 0.0 : atposl, bfcmt

! hcp-Co lattice constant parameters & FM phase (calculation-7)

avec

0.5 -0.86602540378 0.0

0.5 0.86602540378 0.0

0.0 0.0 1.0

scale1

4.73773237

scale2

4.73773237

scale3

7.69024047

atoms

1 : nspecies

'Co.in' : spfname

2 : natoms

0.0 0.0 0.0 0.0 0.0 1.d-2 : atposl, bfcmt

0.33333333 0.66666667 0.5 0.0 0.0 1.d-2 : atposl, bfcmt

! bcc-Cr lattice constant parameters & NM phase (calculation-8)

avec

1.0 0.0 0.0

0.0 1.0 0.0

0.0 0.0 1.0

scale

5.499102627

atoms

1 : nspecies

'Cr.in' : spfname

2 : natoms

0.0 0.0 0.0 0.0 0.0 0.0 : atposl, bfcmt

0.5 0.5 0.5 0.0 0.0 0.0 : atposl, bfcmt

! hcp-Ti lattice constant parameters & NM phase (calculation-9)

avec

```

0.5      -0.86602540378      0.0
0.5      0.86602540378      0.0
0.0      0.0      1.0
scale1
5.576
scale2
5.576
scale3
8.847
atoms
1 : nspecies
'Ti.in' : spfname
2 : natoms
0.0      0.0      0.0      0.0      0.0      0.0 : atposl, bfcmt
0.33333333      0.66666667      0.5      0.0      0.0      0.0 : atposl, bfcmt

```

!fcc-Cu lattice constant parameters & NM phase (calculation-10)

```

avec
1.0      0.0      0.0
0.0      1.0      0.0
0.0      0.0      1.0
scale
6.824202627
atoms
1 : nspecies
'Cu.in' : spfname
4 : natoms
0.0      0.0      0.0      0.0      0.0      0.0 : atposl, bfcmt
0.5      0.5      0.0      0.0      0.0      0.0 : atposl, bfcmt
0.5      0.0      0.5      0.0      0.0      0.0 : atposl, bfcmt
0.0      0.5      0.5      0.0      0.0      0.0 : atposl, bfcmt

```

All the units are in atomic units. More details about different parameters can be found in the documentation of the elk code. Species files ('Fe.in', 'Rh.in', 'Co.in', 'Cr.in', 'Ti.in', 'Cu.in') can be found as standard files in elk code [212]. These calculations were run at Maxwell cluster of DESY, utilizing the parallel computing. The calculation generates different output files. Density of states are written in PDOS.OUT type files. Eigenvalues for core states are written in EVALCORE.OUT. Fermi energy is written in EFERMI.OUT and summary of calculations such as convergence, magnetic moments are written in INFO.OUT. Convergence of magnetic moments should be verified for correct simulations. For calculating XAS spectra and comparing XAS spectra from different calculations, Fermi energy values as well as eigenvalues of core levels should be properly taken into account. Partial density of states (PDOS) from these calculations are used to calculate the XAS spectra.

Bibliography

- [1] Jorge Puebla et al. “Spintronic devices for energy-efficient data storage and energy harvesting”. In: *Communications Materials* 1 (1 Dec. 2020). DOI: 10.1038/s43246-020-0022-5.
- [2] Ryan F. Need et al. “Using structural phase transitions to enhance the coercivity of ferromagnetic films”. In: *APL Materials* 7 (10 Oct. 2019). ISSN: 2166532X. DOI: 10.1063/1.5118893.
- [3] Thomas Thomson, Leon Abelman, and Hans Groenland. “MAGNETIC DATA STORAGE: PAST PRESENT AND FUTURE”. In: *Magnetic Nanostructures in Modern Technology* (2008), pp. 237–306.
- [4] A J Thompson S Best. “The future of magnetic data storage technology”. In: *IBM J. Res. Develop.* 44 (3 2000).
- [5] Noah Kent et al. “Creation and observation of Hopfions in magnetic multilayer systems”. In: *Nature Communications* 12 (1 Dec. 2021). ISSN: 20411723. DOI: 10.1038/s41467-021-21846-5.
- [6] Börge Göbel et al. “Topological Hall signatures of magnetic hopfions”. In: *Physical Review Research* 2 (1 Mar. 2020). ISSN: 26431564. DOI: 10.1103/physrevresearch.2.013315.
- [7] Scott J. F. “Multiferroic memories”. In: *Nature Materials* 6 (2007).
- [8] “Memory with a spin”. In: *Nature Nanotechnology* 10 (3 Mar. 2015), p. 185. ISSN: 17483395. DOI: 10.1038/nnano.2015.50.
- [9] Jairo Sinova et al. “Spin Hall effects”. In: *Reviews of Modern Physics* 87 (4 Oct. 2015), pp. 1213–1260. ISSN: 15390756. DOI: 10.1103/RevModPhys.87.1213.
- [10] David Foster et al. “Two-dimensional skyrmion bags in liquid crystals and ferromagnets”. In: *Nature Physics* 15 (7 July 2019), pp. 655–659. ISSN: 17452481. DOI: 10.1038/s41567-019-0476-x.
- [11] H. S. Philip Wong and Sayeef Salahuddin. “Memory leads the way to better computing”. In: *Nature Nanotechnology* 10 (3 Mar. 2015), pp. 191–194. ISSN: 17483395. DOI: 10.1038/nnano.2015.29.
- [12] Jairo Sinova, Tomas Jungwirth, and Olena Gomonay. “Antiferromagnetic spintronics”. In: *Physica Status Solidi - Rapid Research Letters* 11 (4 Apr. 2017). ISSN: 18626270. DOI: 10.1002/pssr.201770322.
- [13] Du Xiang, Tao Liu, and Wei Chen. “Fused computing and storage in a 2D transistor”. In: *Nature Nanotechnology* 14 (7 July 2019), pp. 642–643. ISSN: 17483395. DOI: 10.1038/s41565-019-0476-0.
- [14] P Wadley et al. “Electrical switching of an antiferromagnet”. In: *Science* 351 (6273 2016), p. 2021. URL: <https://www.science.org>.

- [15] Stuart Parkin and See Hun Yang. “Memory on the racetrack”. In: *Nature Nanotechnology* 10 (3 Mar. 2015), pp. 195–198. ISSN: 17483395. DOI: 10.1038/nnano.2015.41.
- [16] Andrew D. Kent and Daniel C. Worledge. “A new spin on magnetic memories”. In: *Nature Nanotechnology* 10 (3 Mar. 2015), pp. 187–191. ISSN: 17483395. DOI: 10.1038/nnano.2015.24.
- [17] Fumihiro Matsukura, Yoshinori Tokura, and Hideo Ohno. “Control of magnetism by electric fields”. In: *Nature Nanotechnology* 10 (3 Mar. 2015), pp. 209–220. ISSN: 17483395. DOI: 10.1038/nnano.2015.22.
- [18] J. Joshua Yang, Dmitri B. Strukov, and Duncan R. Stewart. “Memristive devices for computing”. In: *Nature Nanotechnology* 8 (1 2013), pp. 13–24. ISSN: 17483395. DOI: 10.1038/nnano.2012.240.
- [19] Kamil Olejník et al. “Terahertz electrical writing speed in an antiferromagnetic memory”. In: *Science Advances* 4:eaar3566 (2018). URL: <https://www.science.org>.
- [20] P Vettiger et al. “The "Millipede" -Nanotechnology Entering Data Storage”. In: *IEEE TRANSACTIONS ON NANOTECHNOLOGY* 1 (1 2002).
- [21] Garello Kevin, Yasin Farrukh, and Kar Gouri Sankar. “Spin-Orbit Torque MRAM for ultrafast embedded memories: from fundamentals to large scale technology integration”. In: 2019. ISBN: 9781728109817. URL: 10.1109/IMW.2019.8739466.
- [22] S. Urazhdin et al. “Nanomagnonic devices based on the spin-transfer torque”. In: *Nature Nanotechnology* 9 (7 2014), pp. 509–513. ISSN: 17483395. DOI: 10.1038/nnano.2014.88.
- [23] Anjan Barman et al. “The 2021 Magnonics Roadmap”. In: *Journal of Physics Condensed Matter* 33 (41 Oct. 2021). ISSN: 1361648X. DOI: 10.1088/1361-648X/abec1a.
- [24] E. Y. Vedmedenko et al. “The 2020 magnetism roadmap”. In: *Journal of Physics D: Applied Physics* 53 (45 Nov. 2020). ISSN: 13616463. DOI: 10.1088/1361-6463/ab9d98.
- [25] C. Back et al. “The 2020 skyrmionics roadmap”. In: *Journal of Physics D: Applied Physics* 53 (36 Sept. 2020). ISSN: 13616463. DOI: 10.1088/1361-6463/ab8418.
- [26] Jiahao Han et al. “Mutual control of coherent spin waves and magnetic domain walls in a magnonic device”. In: *Science* 366 (2019), p. 2021. URL: <https://www.science.org>.
- [27] Zhenyi Zheng et al. “Field-free spin-orbit torque-induced switching of perpendicular magnetization in a ferrimagnetic layer with a vertical composition gradient”. In: *Nature Communications* 12 (1 Dec. 2021). ISSN: 20411723. DOI: 10.1038/s41467-021-24854-7.
- [28] Sevdnur Arpacı et al. “Observation of current-induced switching in non-collinear antiferromagnetic IrMn₃ by differential voltage measurements”. In: *Nature Communications* 12 (1 Dec. 2021). ISSN: 20411723. DOI: 10.1038/s41467-021-24237-y.
- [29] Jiacheng Shi et al. “Electrical manipulation of the magnetic order in antiferromagnetic PtMn pillars”. In: *Nature Electronics* 3 (2 Feb. 2020), pp. 92–98. ISSN: 25201131. DOI: 10.1038/s41928-020-0367-2.
- [30] Ralph M. DeFrancesco. “Biological cells as storage devices”. In: 2012, pp. 897–898. ISBN: 9780769546544. DOI: 10.1109/ITNG.2012.154.

- [31] Guillaume Prenat et al. “Beyond STT-MRAM, spin orbit torque RAM SOT-MRAM for high speed and high reliability applications”. In: *Spintronics-based Computing* (Jan. 2015), pp. 145–158. DOI: 10.1007/978-3-319-15180-9_4.
- [32] X. Marti et al. “Room-temperature antiferromagnetic memory resistor”. In: *Nature Materials* 13.4 (2014), pp. 367–374. ISSN: 14764660. DOI: 10.1038/nmat3861.
- [33] R. O. Cherifi et al. “Electric-field control of magnetic order above room temperature”. In: *Nature Materials* 13.4 (2014), pp. 345–351. ISSN: 14764660. DOI: 10.1038/nmat3870.
- [34] Zexin Feng, Han Yan, and Zhiqi Liu. *Electric-Field Control of Magnetic Order: From FeRh to Topological Antiferromagnetic Spintronics*. Jan. 2019. DOI: 10.1002/aelm.201800466.
- [35] E Beaurepaire et al. “Ultrafast Spin Dynamics in Ferromagnetic Nickel”. In: *PHYSICAL REVIEW LETTERS* 76.22 (1996), pp. 4250–4253.
- [36] Victor Lopez-Dominguez, Hamid Almasi, and Pedram Khalili Amiri. “Picosecond Electric-Field-Induced Switching of Antiferromagnets”. In: *Physical Review Applied* 11.2 (Feb. 2019). ISSN: 23317019. DOI: 10.1103/PhysRevApplied.11.024019.
- [37] C. D. Stanciu et al. “All-optical magnetic recording with circularly polarized light”. In: *Physical Review Letters* 99.4 (July 2007). ISSN: 00319007. DOI: 10.1103/PhysRevLett.99.047601.
- [38] Tobias Kampfrath et al. “Coherent terahertz control of antiferromagnetic spin waves”. In: *Nature Photonics* 5.1 (Jan. 2011), pp. 31–34. ISSN: 17494885. DOI: 10.1038/nphoton.2010.259.
- [39] S. Mangin et al. “Engineered materials for all-optical helicity-dependent magnetic switching”. In: *Nature Materials* 13.3 (2014), pp. 286–292. ISSN: 14764660. DOI: 10.1038/nmat3864.
- [40] Patrick W. Granitzka et al. “Magnetic Switching in Granular FePt Layers Promoted by Near-Field Laser Enhancement”. In: *Nano Letters* 17.4 (Apr. 2017), pp. 2426–2432. ISSN: 15306992. DOI: 10.1021/acs.nanolett.7b00052.
- [41] J. H. Mentink. *Manipulating magnetism by ultrafast control of the exchange interaction*. Oct. 2017. DOI: 10.1088/1361-648X/aa8abf.
- [42] Takahiro Moriyama et al. “Sequential write-read operations in FeRh antiferromagnetic memory”. In: *Applied Physics Letters* 107.12 (Sept. 2015). ISSN: 00036951. DOI: 10.1063/1.4931567.
- [43] Jon Gorchon et al. “Single shot ultrafast all optical magnetization switching of ferromagnetic Co/Pt multilayers”. In: *Applied Physics Letters* 111.4 (July 2017). ISSN: 00036951. DOI: 10.1063/1.4994802.
- [44] A. Stupakiewicz et al. “Ultrafast nonthermal photo-magnetic recording in a transparent medium”. In: *Nature* 542.7639 (Feb. 2017), pp. 71–74. ISSN: 14764687. DOI: 10.1038/nature20807.
- [45] Andrei Kirilyuk, Alexey V. Kimel, and Theo Rasing. “Ultrafast optical manipulation of magnetic order”. In: *Reviews of Modern Physics* 82.3 (Sept. 2010), pp. 2731–2784. ISSN: 15390756. DOI: 10.1103/RevModPhys.82.2731.
- [46] Youri L.W. van Hees et al. “Deterministic all-optical magnetization writing facilitated by non-local transfer of spin angular momentum”. In: *Nature Communications* 11 (1 Dec. 2020). ISSN: 20411723. DOI: 10.1038/s41467-020-17676-6.

- [47] Eva Grimaldi et al. “Single-shot dynamics of spin–orbit torque and spin transfer torque switching in three-terminal magnetic tunnel junctions”. In: *Nature Nanotechnology* 15 (2 Feb. 2020), pp. 111–117. ISSN: 17483395. DOI: 10.1038/s41565-019-0607-7.
- [48] Fabian D. Natterer et al. “Reading and writing single-atom magnets”. In: *Nature* 543 (7644 Mar. 2017), pp. 226–228. ISSN: 14764687. DOI: 10.1038/nature21371.
- [49] T. Seifert et al. “Terahertz Spin Currents and Inverse Spin Hall Effect in Thin-Film Heterostructures Containing Complex Magnetic Compounds”. In: *SPIN* 7 (3 Sept. 2017). ISSN: 20103255. DOI: 10.1142/S2010324717400100.
- [50] Joachim. Stöhr and Hans Christoph. Siegmann. *Magnetism : from fundamentals to nanoscale dynamics*. Springer, 2006, p. 820. ISBN: 9783540302827.
- [51] Yuyan Wang et al. “Time-Resolved Detection of Multilevel Switching of the Magnetization and Exchange Bias Driven by Spin-Orbit Torques”. In: *Research Square* (2021). DOI: 10.21203/rs.3.rs-882472/v1. URL: <https://doi.org/10.21203/rs.3.rs-882472/v1>.
- [52] A. Cavalleri et al. “Femtosecond structural dynamics in vo2 during an ultrafast solid-solid phase transition”. In: *Physical Review Letters* 87 (23 Dec. 2001), pp. 237401-1-237401–4. ISSN: 10797114. DOI: 10.1103/PhysRevLett.87.237401.
- [53] D. Fausti et al. “Light-induced superconductivity in a stripe-ordered cuprate”. In: *Science* 331 (6014 Jan. 2011), pp. 189–191. ISSN: 00368075. DOI: 10.1126/science.1197294.
- [54] Frances Hellman et al. “Interface-induced phenomena in magnetism”. In: *Reviews of Modern Physics* 89.2 (June 2017). ISSN: 15390756. DOI: 10.1103/RevModPhys.89.025006.
- [55] E. Carpene et al. “Dynamics of electron-magnon interaction and ultrafast demagnetization in thin iron films”. In: *Physical Review B - Condensed Matter and Materials Physics* 78.17 (Nov. 2008). ISSN: 10980121. DOI: 10.1103/PhysRevB.78.174422.
- [56] Sven Essert and Hans Christian Schneider. “Electron-phonon scattering dynamics in ferromagnetic metals and their influence on ultrafast demagnetization processes”. In: *Physical Review B - Condensed Matter and Materials Physics* 84.22 (Dec. 2011). ISSN: 10980121. DOI: 10.1103/PhysRevB.84.224405.
- [57] B. Koopmans et al. “Explaining the paradoxical diversity of ultrafast laser-induced demagnetization”. In: *Nature Materials* 9.3 (2010), pp. 259–265. ISSN: 14764660. DOI: 10.1038/nmat2593.
- [58] G P Zhang and W Hübner. “Laser-Induced Ultrafast Demagnetization in Ferromagnetic Metals”. In: *PHYSICAL REVIEW LETTERS* 85.14 (2000), pp. 3025–3028.
- [59] M. Battiato, K. Carva, and P. M. Oppeneer. “Superdiffusive spin transport as a mechanism of ultrafast demagnetization”. In: *Physical Review Letters* 105.2 (July 2010). ISSN: 00319007. DOI: 10.1103/PhysRevLett.105.027203.
- [60] Stefan Günther et al. “Testing spin-flip scattering as a possible mechanism of ultrafast demagnetization in ordered magnetic alloys”. In: *Physical Review B - Condensed Matter and Materials Physics* 90 (18 Nov. 2014). ISSN: 1550235X. DOI: 10.1103/PhysRevB.90.180407.

- [61] Michael Krauß et al. “Ultrafast demagnetization of ferromagnetic transition metals: The role of the Coulomb interaction”. In: *Physical Review B - Condensed Matter and Materials Physics* 80.18 (Nov. 2009). ISSN: 10980121. DOI: 10.1103/PhysRevB.80.180407.
- [62] B. Pfau et al. “Ultrafast optical demagnetization manipulates nanoscale spin structure in domain walls”. In: *Nature Communications* 3 (2012). ISSN: 20411723. DOI: 10.1038/ncomms2108.
- [63] Beatrice Andres and Martin Weinelt. “Spin-resolved electronic structure of 3d transition metals during ultrafast demagnetization”. In: *Journal of Magnetism and Magnetic Materials* 501 (May 2020). ISSN: 03048853. DOI: 10.1016/j.jmmm.2020.166475.
- [64] A. Fognini et al. “Ultrafast reduction of the total magnetization in iron”. In: *Applied Physics Letters* 104.3 (Jan. 2014). ISSN: 00036951. DOI: 10.1063/1.4862476.
- [65] J. S. Kouvel. “Unusual nature of the abrupt magnetic transition in FeRh and its pseudobinary variants”. In: *Journal of Applied Physics* 37 (3 1966), pp. 1257–1258. ISSN: 00218979. DOI: 10.1063/1.1708424.
- [66] J. M. Lommel. “Magnetic and electrical properties of FeRh thin films”. In: *Journal of Applied Physics* 37.3 (1966), pp. 1483–1484. ISSN: 00218979. DOI: 10.1063/1.1708527.
- [67] Schinkel C J, Hartog R, and Hochstenbach F H A M. “On the magnetic and electrical properties of nearly equiatomic ordered FeRh alloys”. In: *Journal of Physics F: Metal Physics* 4 (1974), p. 1412.
- [68] C. Stamm et al. “Antiferromagnetic-ferromagnetic phase transition in FeRh probed by x-ray magnetic circular dichroism”. In: *Physical Review B - Condensed Matter and Materials Physics* 77.18 (May 2008). ISSN: 10980121. DOI: 10.1103/PhysRevB.77.184401.
- [69] C. Baldasseroni et al. “Temperature-driven nucleation of ferromagnetic domains in FeRh thin films”. In: *Applied Physics Letters* 100.26 (June 2012). ISSN: 00036951. DOI: 10.1063/1.4730957.
- [70] R. C. Temple et al. “Antiferromagnetic-ferromagnetic phase domain development in nanopatterned FeRh islands”. In: *Physical Review Materials* 2.10 (Oct. 2018). ISSN: 24759953. DOI: 10.1103/PhysRevMaterials.2.104406.
- [71] C. Bordel et al. “Fe spin reorientation across the metamagnetic transition in strained FeRh thin films”. In: *Physical Review Letters* 109.11 (Sept. 2012). ISSN: 00319007. DOI: 10.1103/PhysRevLett.109.117201.
- [72] David J. Keavney et al. “Phase coexistence and kinetic arrest in the magnetostructural transition of the ordered alloy FeRh”. In: *Scientific Reports* 8.1 (Dec. 2018). ISSN: 20452322. DOI: 10.1038/s41598-018-20101-0.
- [73] A. X. Gray et al. “Electronic structure changes across the metamagnetic transition in FeRh via hard X-ray photoemission”. In: *Physical Review Letters* 108.25 (June 2012). ISSN: 00319007. DOI: 10.1103/PhysRevLett.108.257208.
- [74] Grazhdankina N. P. “MAGNETIC FIRST ORDER PHASE TRANSITIONS”. In: *Soviet Physics Uspekhi* 11.5 (1969), pp. 727–745.

- [75] David W. Cooke et al. “Calorimetry of epitaxial thin films”. In: *Review of Scientific Instruments* 82.2 (Feb. 2011). ISSN: 00346748. DOI: 10.1063/1.3554440.
- [76] S. O. Mariager et al. “Imaging the antiferromagnetic to ferromagnetic first order phase transition of FeRh”. In: (Jan. 2013). URL: <http://arxiv.org/abs/1301.4164>.
- [77] Sen Yang, Xiaobing Ren, and Xiaoping Song. “Evidence for first-order nature of the ferromagnetic transition in Ni, Fe, Co, and CoFe₂O₄”. In: *Physical Review B - Condensed Matter and Materials Physics* 78.17 (Nov. 2008). ISSN: 10980121. DOI: 10.1103/PhysRevB.78.174427.
- [78] Landau David P. and Binder Kurt. *A Guide to Monte Carlo Simulations in Statistical Physics, Third Edition*. 3rd edition. Cambridge University Press, 2009. ISBN: 978-0-511-65176-2.
- [79] Kurt Binder. “Theory of first-order phase transitions”. In: *Rep. Prog. Phys* 50 (1987), pp. 783–859. URL: <http://iopscience.iop.org/0034-4885/50/7/001>.
- [80] K Binder. “NUCLEATION THEORY AND DYNAMICS OF FIRST-ORDER PHASE TRANSITIONS NEAR A CRITICAL POINT”. In: *Journal de Physique Colloques* (1980), pp. 4–51. DOI: 10.1051/jphyscol:1980409. URL: <https://hal.archives-ouvertes.fr/jpa-00219924>.
- [81] Vitaly V Slezov. *Kinetics of First-order Phase Transitions*. WILEY-VCH Verlag GmbH & Co. KGaA, 2009. ISBN: 978-3-527-40775-0.
- [82] Yukio Noda, Shinji Nishihara, and Yasusada Yamada. “Critical Behavior and Scaling Law in Ordering Process of the First order Phase Transition in Cu₃Au Alloy”. In: *Journal of Physical Society of Japan* 53.12 (1984), pp. 4241–4249.
- [83] Jan Ulrich Thiele, Stefan Maat, and Eric E. Fullerton. “FeRh/FePt exchange spring films for thermally assisted magnetic recording media”. In: *Applied Physics Letters* 82 (17 Apr. 2003), pp. 2859–2861. ISSN: 00036951. DOI: 10.1063/1.1571232.
- [84] Yuyan Wang et al. “Spin pumping during the antiferromagnetic–ferromagnetic phase transition of iron–rhodium”. In: *Nature Communications* 11.1 (Dec. 2020). ISSN: 20411723. DOI: 10.1038/s41467-019-14061-w.
- [85] Jan Ulrich Thiele, Matthias Buess, and Christian H. Back. “Spin dynamics of the antiferromagnetic-to-ferromagnetic phase transition in FeRh on a sub-picosecond time scale”. In: *Applied Physics Letters* 85.14 (Oct. 2004), pp. 2857–2859. ISSN: 00036951. DOI: 10.1063/1.1799244.
- [86] Ganping Ju et al. “Ultrafast generation of ferromagnetic order via a laser-induced phase transformation in FeRh thin films”. In: *Physical Review Letters* 93.19 (Nov. 2004). ISSN: 00319007. DOI: 10.1103/PhysRevLett.93.197403.
- [87] Bastiaan Bergman et al. “Identifying growth mechanisms for laser-induced magnetization in FeRh”. In: *Physical Review B - Condensed Matter and Materials Physics* 73.6 (2006). ISSN: 10980121. DOI: 10.1103/PhysRevB.73.060407.
- [88] I. Radu et al. “Laser-induced generation and quenching of magnetization on FeRh studied with time-resolved x-ray magnetic circular dichroism”. In: *Physical Review B - Condensed Matter and Materials Physics* 81.10 (Mar. 2010). ISSN: 10980121. DOI: 10.1103/PhysRevB.81.104415.

- [89] S. O. Mariager et al. “Structural and magnetic dynamics of a laser induced phase transition in FeRh”. In: *Physical Review Letters* 108.8 (Feb. 2012). ISSN: 00319007. DOI: 10.1103/PhysRevLett.108.087201.
- [90] A. A. Ünal et al. “Laser-driven formation of transient local ferromagnetism in FeRh thin films”. In: *Ultramicroscopy* 183 (Dec. 2017), pp. 104–108. ISSN: 18792723. DOI: 10.1016/j.ultramic.2017.03.024.
- [91] Florian Quirin et al. “Structural dynamics in FeRh during a laser-induced metamagnetic phase transition”. In: *Physical Review B - Condensed Matter and Materials Physics* 85.2 (Jan. 2012). ISSN: 10980121. DOI: 10.1103/PhysRevB.85.020103.
- [92] G Li et al. “Multiscale dynamics at the antiferromagnetic-ferromagnetic phase transition in FeRh”. In: *arXiv:2001.06799* (2020).
- [93] N. Awari et al. “Monitoring laser-induced magnetization in FeRh by transient terahertz emission spectroscopy”. In: *Applied Physics Letters* 117.12 (Sept. 2020). ISSN: 00036951. DOI: 10.1063/5.0019663.
- [94] Federico Pressacco et al. “Laser induced phase transition in epitaxial FeRh layers studied by pump-probe valence band photoemission”. In: *Structural Dynamics* 5.3 (May 2018). ISSN: 23297778. DOI: 10.1063/1.5027809.
- [95] Federico Pressacco et al. “Subpicosecond metamagnetic phase transition in FeRh driven by non-equilibrium electron dynamics”. In: *Nature Communications* 12.1 (Dec. 2021). ISSN: 20411723. DOI: 10.1038/s41467-021-25347-3.
- [96] L. H. Lewis, C. H. Marrows, and S. Langridge. *Coupled magnetic, structural, and electronic phase transitions in FeRh*. July 2016. DOI: 10.1088/0022-3727/49/32/323002.
- [97] Philip W Anderson. “Theory of Magnetic Exchange Interactions: Exchange in Insulators and Semiconductors”. In: *Solid State Physics* 14 (1963), pp. 99–214.
- [98] White Robert M. (*Springer series in solid-state sciences*) *Robert M. White - Quantum theory of magnetism: magnetic properties of materials*. Springer, 2007.
- [99] Stephen Blundell. *Magnetism in condensed matter by*. Oxford University Press, 2001.
- [100] David Jeffrey Griffiths. *Introduction to quantum mechanics*. 2nd Edition. Pearson, 2014, p. 468. ISBN: 1292024089.
- [101] Leonid M. Sandratskii and Phivos Mavropoulos. “Magnetic excitations and femtomagnetism of FeRh: A first-principles study”. In: *Physical Review B - Condensed Matter and Materials Physics* 83.17 (May 2011). ISSN: 10980121. DOI: 10.1103/PhysRevB.83.174408.
- [102] M Alouani and M A Khan. “X-ray emission and absorption in intermetallic compounds: FeAl and FeRh”. In: *J. Phys. F: Met. Phys* 17 (1987), pp. 519–541.
- [103] Rohit P Prasankumar and Antoinette J Taylor. *Optical Techniques for Solid-state Materials Characterization*. CRC Press, 2012.
- [104] J. Lloyd-Hughes et al. “The 2021 ultrafast spectroscopic probes of condensed matter roadmap”. In: *Journal of Physics Condensed Matter* 33 (35 Sept. 2021). ISSN: 1361648X. DOI: 10.1088/1361-648X/abfe21.

- [105] A Nitzan et al. “First Operation of a Free-Electron Laser”. In: *Prog. Theor. Phys* 12 (1977), p. 160.
- [106] Saldin E. L., Schneidmiller E. A., and Yurkov M. V. *The Physics of Free Electron Lasers*. Springer-Verlag Berlin Heidelberg GmbH, 2000.
- [107] Massimo. Altarelli and Deutsches Elektronen-Synchrotron (Center). X-Ray Free-Electron Laser Project. *XFEL : the European X-ray free-electron laser : technical design report*. 2006, p. 630.
- [108] Brian W.J. Mcneil and Neil R. Thompson. “X-ray free-electron lasers”. In: *Nature Photonics* 4 (12 Dec. 2010), pp. 814–821. ISSN: 17494885. DOI: 10.1038/nphoton.2010.239.
- [109] G. Margaritondo and Primoz Rebernik Ribic. “A simplified description of X-ray free-electron lasers”. In: *Journal of Synchrotron Radiation* 18 (2 Mar. 2011), pp. 101–108. ISSN: 09090495. DOI: 10.1107/S090904951004896X.
- [110] Tetsuya Ishikawa et al. “A compact X-ray free-electron laser emitting in the sub-ångström region”. In: *Nature Photonics* 6 (8 Aug. 2012), pp. 540–544. ISSN: 17494885. DOI: 10.1038/nphoton.2012.141.
- [111] Zhiron Huang and Ingolf Lindau. “Free-electron lasers: SACLA hard-X-ray compact FEL”. In: *Nature Photonics* 6 (8 Aug. 2012), pp. 505–506. ISSN: 17494885. DOI: 10.1038/nphoton.2012.184.
- [112] E. Allaria et al. “Two-stage seeded soft-X-ray free-electron laser”. In: *Nature Photonics* 7 (11 Nov. 2013), pp. 913–918. ISSN: 17494885. DOI: 10.1038/nphoton.2013.277.
- [113] B. W.J. McNeil, N. R. Thompson, and D. J. Dunning. “Transform-limited x-ray pulse generation from a high-brightness self-amplified spontaneous-emission free-electron laser”. In: *Physical Review Letters* 110 (13 Mar. 2013). ISSN: 00319007. DOI: 10.1103/PhysRevLett.110.134802.
- [114] A Scherz and O Krupin. *CONCEPTUAL DESIGN REPORT Scientific Instrument Spectroscopy and Coherent Scattering (SCS)*. European XFEL, 2013.
- [115] Peter Schmüser et al. *Springer Tracts in Modern Physics 258 Free-Electron Lasers in the Ultraviolet and X-Ray Regime*. 2nd. Springer, 2014. URL: www.mpe-garching.mpg.de/index.html.
- [116] C. Pellegrini. “X-ray free-electron lasers: From dreams to reality”. In: *Physica Scripta* (T169 Mar. 2016). ISSN: 02811847. DOI: 10.1088/1402-4896/aa5281.
- [117] Eberhard J Jaeschke et al. *Synchrotron Light Sources and Free-Electron Lasers*. Springer Reference, 2016.
- [118] Kiyoshi Ueda. (Ed.) “X-Ray Free-Electron Laser(Special Issue)”. In: *Applied Sciences* (2018). URL: http://www.mdpi.com/journal/applsci/special...issues/xray_fe.
- [119] Ichiro Inoue et al. “Generation of narrow-band X-ray free-electron laser via reflection self-seeding”. In: *Nature Photonics* 13 (5 May 2019), pp. 319–322. ISSN: 17494893. DOI: 10.1038/s41566-019-0365-y.

- [120] W. Decking et al. “A MHz-repetition-rate hard X-ray free-electron laser driven by a superconducting linear accelerator”. In: *Nature Photonics* 14 (6 June 2020), pp. 391–397. ISSN: 17494893. DOI: 10.1038/s41566-020-0607-z.
- [121] *European XFEL Annual Report 2020*. European XFEL, 2020.
- [122] Adams Bernhard W. *Nonlinear Optics, Quantum Optics, and Ultrafast Phenomena with X-Rays*. Springer US, 2003. DOI: 10.1007/978-1-4615-0387-3.
- [123] Daniel J. Higley et al. “Femtosecond X-ray magnetic circular dichroism absorption spectroscopy at an X-ray free electron laser”. In: *Review of Scientific Instruments* 87.3 (Mar. 2016). ISSN: 10897623. DOI: 10.1063/1.4944410.
- [124] C. Gutt et al. “Resonant magnetic scattering with soft x-ray pulses from a free-electron laser operating at 1.59 nm”. In: *Physical Review B - Condensed Matter and Materials Physics* 79.21 (June 2009). ISSN: 10980121. DOI: 10.1103/PhysRevB.79.212406.
- [125] L. Müller et al. “Ultrafast Dynamics of Magnetic Domain Structures Probed by Coherent Free-Electron Laser Light”. In: *Synchrotron Radiation News* 26 (6 Nov. 2013), pp. 27–32. ISSN: 08940886. DOI: 10.1080/08940886.2013.850384.
- [126] Tetsuo Katayama et al. “Femtosecond x-ray absorption spectroscopy with hard x-ray free electron laser”. In: *Applied Physics Letters* 103 (13 Sept. 2013). ISSN: 00036951. DOI: 10.1063/1.4821108.
- [127] C. Behrens et al. “Few-femtosecond time-resolved measurements of X-ray free-electron lasers”. In: *Nature Communications* 5 (Apr. 2014). ISSN: 20411723. DOI: 10.1038/ncomms4762.
- [128] Ichiro Inoue et al. “Observation of femtosecond X-ray interactions with matter using an X-ray-X-ray pump-probe scheme”. In: *Proceedings of the National Academy of Sciences of the United States of America* 113 (6 Feb. 2016), pp. 1492–1497. ISSN: 10916490. DOI: 10.1073/pnas.1516426113.
- [129] Bergmann Uwe, Yachandra Vittal K., and Yano Junko. *X-Ray Free Electron Lasers: Applications in Materials, Chemistry and Biology*. CPI Group (UK) Ltd, Croydon, CR0 4YY, UK., Aug. 2017, P001–P004. DOI: 10.1039/9781782624097-FP001.
- [130] Ryan N. Coffee et al. “Development of ultrafast capabilities for X-ray free-electron lasers at the linac coherent light source”. In: *Philosophical Transactions of the Royal Society A: Mathematical, Physical and Engineering Sciences* 377 (2145 May 2019). ISSN: 1364503X. DOI: 10.1098/rsta.2018.0386.
- [131] Iwao Matsuda and Yuya Kubota. “Recent Progress in Spectroscopies Using Soft X-ray Free-electron Lasers”. In: *Chemistry Letters* 50 (7 July 2021), pp. 1336–1344. ISSN: 13480715. DOI: 10.1246/cl.200881.
- [132] A. J. Schellekens and B. Koopmans. “Comparing ultrafast demagnetization rates between competing models for finite temperature magnetism”. In: *Physical Review Letters* 110 (21 May 2013). ISSN: 00319007. DOI: 10.1103/PhysRevLett.110.217204.
- [133] D. Steiauf and M. Fähnle. “Elliott-Yafet mechanism and the discussion of femtosecond magnetization dynamics”. In: *Physical Review B - Condensed Matter and Materials Physics* 79 (14 Apr. 2009). ISSN: 10980121. DOI: 10.1103/PhysRevB.79.140401.

- [134] R J Elliott. “Theory of the Effect of Spin-Orbit Coupling on Magnetic Resonance in Some Semiconductors*”. In: *Physical Review* 96 (2 1954).
- [135] Felix Willems et al. “Optical inter-site spin transfer probed by energy and spin-resolved transient absorption spectroscopy”. In: *Nature Communications* 11 (1 Dec. 2020). ISSN: 20411723. DOI: 10.1038/s41467-020-14691-5.
- [136] B. Y. Mueller et al. “Driving force of ultrafast magnetization dynamics”. In: *New Journal of Physics* 13 (Dec. 2011). ISSN: 13672630. DOI: 10.1088/1367-2630/13/12/123010.
- [137] C. E. Graves et al. “Nanoscale spin reversal by non-local angular momentum transfer following ultrafast laser excitation in ferrimagnetic GdFeCo”. In: *Nature Materials* 12.4 (2013), pp. 293–298. ISSN: 14764660. DOI: 10.1038/nmat3597.
- [138] C. Stamm et al. “Femtosecond modification of electron localization and transfer of angular momentum in nickel”. In: *Nature Materials* 6 (10 2007), pp. 740–743. ISSN: 14764660. DOI: 10.1038/nmat1985.
- [139] K. Krieger et al. “Laser-Induced Demagnetization at Ultrashort Time Scales: Predictions of TDDFT”. In: *Journal of Chemical Theory and Computation* 11 (10 Aug. 2015), pp. 4870–4874. ISSN: 15499626. DOI: 10.1021/acs.jctc.5b00621.
- [140] Loïc Le Guyader et al. “State-resolved ultrafast charge and spin dynamics in [Co/Pd] multilayers”. In: *arXiv:2110.15615v1* (Oct. 2021). URL: <http://arxiv.org/abs/2110.15615>.
- [141] Michael Haag, Christian Illg, and Manfred Fähnle. “Role of electron-magnon scatterings in ultrafast demagnetization”. In: *Physical Review B - Condensed Matter and Materials Physics* 90 (1 July 2014). ISSN: 1550235X. DOI: 10.1103/PhysRevB.90.014417.
- [142] G. Malinowski et al. “Control of speed and efficiency of ultrafast demagnetization by direct transfer of spin angular momentum”. In: *Nature Physics* 4 (11 2008), pp. 855–858. ISSN: 17452481. DOI: 10.1038/nphys1092.
- [143] J. H. Mentink et al. “Ultrafast spin dynamics in multisublattice magnets”. In: *Physical Review Letters* 108 (5 Jan. 2012). ISSN: 00319007. DOI: 10.1103/PhysRevLett.108.057202.
- [144] Christian Illg, Michael Haag, and Manfred Fähnle. “Ultrafast demagnetization after laser irradiation in transition metals: Ab initio calculations of the spin-flip electron-phonon scattering with reduced exchange splitting”. In: *Physical Review B - Condensed Matter and Materials Physics* 88 (21 Dec. 2013). ISSN: 10980121. DOI: 10.1103/PhysRevB.88.214404.
- [145] Emrah Turgut et al. “Controlling the competition between optically induced ultrafast spin-flip scattering and spin transport in magnetic multilayers”. In: *Physical Review Letters* 110.19 (May 2013). ISSN: 00319007. DOI: 10.1103/PhysRevLett.110.197201.
- [146] Emrah Turgut et al. “Stoner versus Heisenberg: Ultrafast exchange reduction and magnon generation during laser-induced demagnetization”. In: *Physical Review B* 94 (22 Dec. 2016). ISSN: 24699969. DOI: 10.1103/PhysRevB.94.220408.
- [147] Stefan Mathias et al. “Probing the timescale of the exchange interaction in a ferromagnetic alloy”. In: *PNAS* 109 (13 2012). ISSN: 4792-4797. DOI: 10.1073/pnas.1201371109/-/DCSupplemental.

- [148] Dennis Rudolf et al. “Ultrafast magnetization enhancement in metallic multilayers driven by superdiffusive spin current”. In: *Nature Communications* 3 (2012). ISSN: 20411723. DOI: 10.1038/ncomms2029.
- [149] K. Carva, M. Battiato, and P. M. Oppeneer. “Ab initio investigation of the Elliott-Yafet electron-phonon mechanism in laser-induced ultrafast demagnetization”. In: *Physical Review Letters* 107 (20 Nov. 2011). ISSN: 00319007. DOI: 10.1103/PhysRevLett.107.207201.
- [150] Pablo Maldonado et al. “Theory of out-of-equilibrium ultrafast relaxation dynamics in metals”. In: *Physical Review B* 96.17 (Nov. 2017). ISSN: 24699969. DOI: 10.1103/PhysRevB.96.174439.
- [151] K. Carva et al. “Ab initio theory of electron-phonon mediated ultrafast spin relaxation of laser-excited hot electrons in transition-metal ferromagnets”. In: *Physical Review B - Condensed Matter and Materials Physics* 87 (18 May 2013). ISSN: 10980121. DOI: 10.1103/PhysRevB.87.184425.
- [152] Jean Yves Bigot, Mircea Vomir, and Eric Beaurepaire. “Coherent ultrafast magnetism induced by femtosecond laser pulses”. In: *Nature Physics* 5.7 (2009), pp. 515–520. ISSN: 17452481. DOI: 10.1038/nphys1285.
- [153] E. Carpene et al. “Ultrafast demagnetization of metals: Collapsed exchange versus collective excitations”. In: *Physical Review B - Condensed Matter and Materials Physics* 91 (17 May 2015). ISSN: 1550235X. DOI: 10.1103/PhysRevB.91.174414.
- [154] I. Radu et al. “Transient ferromagnetic-like state mediating ultrafast reversal of antiferromagnetically coupled spins”. In: *Nature* 472 (7342 Apr. 2011), pp. 205–209. ISSN: 00280836. DOI: 10.1038/nature09901.
- [155] Stefan Mathias et al. “Probing the timescale of the exchange interaction in a ferromagnetic alloy”. In: *PNAS* 109.13 (2012), pp. 4792–4797. ISSN: 4792-4797. DOI: 10.1073/pnas.1201371109/-/DCSupplemental.
- [156] P. Elliott et al. “The microscopic origin of spin-orbit mediated spin-flips”. In: *Journal of Magnetism and Magnetic Materials* 502 (May 2020). ISSN: 03048853. DOI: 10.1016/j.jmmm.2020.166473.
- [157] M. Fähnle and C. Illg. *Electron theory of fast and ultrafast dissipative magnetization dynamics*. Dec. 2011. DOI: 10.1088/0953-8984/23/49/493201.
- [158] U. Atxitia et al. “Evidence for thermal mechanisms in laser-induced femtosecond spin dynamics”. In: *Physical Review B - Condensed Matter and Materials Physics* 81.17 (May 2010). ISSN: 10980121. DOI: 10.1103/PhysRevB.81.174401.
- [159] N. Berggaard et al. “Ultrafast angular momentum transfer in multisublattice ferrimagnets”. In: *Nature Communications* 5 (Mar. 2014). ISSN: 20411723. DOI: 10.1038/ncomms4466.
- [160] V. Shokeen et al. “Spin Flips versus Spin Transport in Nonthermal Electrons Excited by Ultrashort Optical Pulses in Transition Metals”. In: *Physical Review Letters* 119 (10 Sept. 2017). ISSN: 10797114. DOI: 10.1103/PhysRevLett.119.107203.
- [161] A. Eschenlohr et al. “Ultrafast spin transport as key to femtosecond demagnetization”. In: *Nature Materials* 12 (4 Apr. 2013), pp. 332–336. ISSN: 14761122. DOI: 10.1038/nmat3546.

- [162] R. Gort et al. “Early Stages of Ultrafast Spin Dynamics in a 3d Ferromagnet”. In: *Physical Review Letters* 121 (8 Aug. 2018). ISSN: 10797114. DOI: 10.1103/PhysRevLett.121.087206.
- [163] Andrei Kirilyuk, Alexey V. Kimel, and Theo Rasing. “Laser-induced magnetization dynamics and reversal in ferrimagnetic alloys”. In: *Reports on Progress in Physics* 76 (2 Feb. 2013). ISSN: 00344885. DOI: 10.1088/0034-4885/76/2/026501.
- [164] B. Koopmans et al. “Unifying ultrafast magnetization dynamics”. In: *Physical Review Letters* 95.26 (Dec. 2005). ISSN: 00319007. DOI: 10.1103/PhysRevLett.95.267207.
- [165] E. Iacocca et al. “Spin-current-mediated rapid magnon localisation and coalescence after ultrafast optical pumping of ferrimagnetic alloys”. In: *Nature Communications* 10.1 (Dec. 2019). ISSN: 20411723. DOI: 10.1038/s41467-019-09577-0.
- [166] M Hofherr et al. “Ultrafast optically induced spin transfer in ferromagnetic alloys”. In: *Science Advances* 6:eaay8717 (2020). URL: <https://www.science.org>.
- [167] E. Golias et al. “Ultrafast Optically Induced Ferromagnetic State in an Elemental Antiferromagnet”. In: *Physical Review Letters* 126 (10 Mar. 2021). ISSN: 10797114. DOI: 10.1103/PhysRevLett.126.107202.
- [168] John Kay Dewhurst et al. “Laser-induced intersite spin transfer”. In: *Nano Letters* 18 (3 Mar. 2018), pp. 1842–1848. ISSN: 15306992. DOI: 10.1021/acs.nanolett.7b05118.
- [169] P. Elliott et al. “Ultrafast laser induced local magnetization dynamics in Heusler compounds”. In: *Scientific Reports* 6 (Dec. 2016). ISSN: 20452322. DOI: 10.1038/srep38911.
- [170] K. Krieger et al. “Ultrafast demagnetization in bulk versus thin films: An ab initio study”. In: *Journal of Physics Condensed Matter* 29 (22 Apr. 2017). ISSN: 1361648X. DOI: 10.1088/1361-648X/aa66f2.
- [171] Dykanov M. I. and Perel V. I. “Possibility of Orienting Electron Spins with Current”. In: *JETP Letters* 13 (11 1971), pp. 657–660.
- [172] E. Saitoh et al. “Conversion of spin current into charge current at room temperature: Inverse spin-Hall effect”. In: *Applied Physics Letters* 88 (18 May 2006). ISSN: 00036951. DOI: 10.1063/1.2199473.
- [173] Axel Hoffmann. “Spin hall effects in metals”. In: *IEEE Transactions on Magnetics* 49 (10 2013), pp. 5172–5193. ISSN: 00189464. DOI: 10.1109/TMAG.2013.2262947.
- [174] Y. Niimi et al. “Giant spin hall effect induced by skew scattering from bismuth impurities inside thin film CuBi alloys”. In: *Physical Review Letters* 109 (15 Oct. 2012). ISSN: 00319007. DOI: 10.1103/PhysRevLett.109.156602.
- [175] M. Obstbaum et al. “Tuning spin hall angles by alloying”. In: *Physical Review Letters* 117 (16 Oct. 2016). ISSN: 10797114. DOI: 10.1103/PhysRevLett.117.167204.
- [176] Chi Feng Pai et al. “Spin transfer torque devices utilizing the giant spin Hall effect of tungsten”. In: *Applied Physics Letters* 101 (12 Sept. 2012). ISSN: 00036951. DOI: 10.1063/1.4753947.
- [177] Luqiao Liu et al. “Spin-Torque Switching with the Giant Spin Hall Effect of Tantalum”. In: *Science* 336 (2012), p. 2021. URL: www.sciencemag.orgSCIENCEVOL.
- [178] Wanjun Jiang et al. “Blowing magnetic skyrmion bubbles”. In: *Science* 349 (6245 2015), p. 2021. URL: <https://www.science.org>.

- [179] Michihiko Yamanouchi et al. “Three terminal magnetic tunnel junction utilizing the spin Hall effect of iridium-doped copper”. In: *Applied Physics Letters* 102 (21 May 2013). ISSN: 00036951. DOI: 10.1063/1.4808033.
- [180] Satoru Emori et al. “Current-driven dynamics of chiral ferromagnetic domain walls”. In: *Nature Materials* 12 (7 July 2013), pp. 611–616. ISSN: 14761122. DOI: 10.1038/nmat3675.
- [181] D. H. Wei et al. “The spin Hall effect as a probe of nonlinear spin fluctuations”. In: *Nature Communications* 3 (2012). ISSN: 20411723. DOI: 10.1038/ncomms2063.
- [182] T. Seifert et al. “Efficient metallic spintronic emitters of ultrabroadband terahertz radiation”. In: *Nature Photonics* 10.7 (June 2016), pp. 483–488. ISSN: 17494893. DOI: 10.1038/nphoton.2016.91.
- [183] T. Seifert et al. “Ultrabroadband single-cycle terahertz pulses with peak fields of 300 kV cm⁻¹ from a metallic spintronic emitter”. In: *Applied Physics Letters* 110 (25 June 2017). ISSN: 00036951. DOI: 10.1063/1.4986755.
- [184] Yoshinori Tokura. “Photoinduced phase transition: A tool for generating a hidden state of matter”. In: *Journal of the Physical Society of Japan* 75 (1 Jan. 2006). ISSN: 00319015. DOI: 10.1143/JPSJ.75.011001.
- [185] Nathaniel F. Brady et al. “Heterogeneous nucleation and growth dynamics in the light-induced phase transition in vanadium dioxide”. In: *Journal of Physics Condensed Matter* 28.12 (Mar. 2016). ISSN: 1361648X. DOI: 10.1088/0953-8984/28/12/125603.
- [186] Brian T. O’Callahan et al. “Inhomogeneity of the ultrafast insulator-to-metal transition dynamics of VO₂”. In: *Nature Communications* 6 (Apr. 2015). ISSN: 20411723. DOI: 10.1038/ncomms7849.
- [187] A. Cavalleri et al. “Evidence for a structurally-driven insulator-to-metal transition in VO₂: A view from the ultrafast timescale [2]”. In: *Physical Review B - Condensed Matter and Materials Physics* 70 (16 Oct. 2004), pp. 1–4. ISSN: 01631829. DOI: 10.1103/PhysRevB.70.161102.
- [188] G. Bridoux et al. “Light-induced metal-insulator transition in SrTiO₃ by photoresistance spectroscopy”. In: *Physical Review B - Condensed Matter and Materials Physics* 92 (15 Oct. 2015). ISSN: 1550235X. DOI: 10.1103/PhysRevB.92.155202.
- [189] Jure Demsar. “Emergent phenomena: Light-induced superconductivity”. In: *Nature Physics* 12 (3 Mar. 2016), pp. 202–203. ISSN: 17452481. DOI: 10.1038/nphys3687.
- [190] Kazuki Isoyama et al. “Light-induced enhancement of superconductivity in iron-based superconductor FeSe_{0.5}Te_{0.5}”. In: *Communications Physics* 4 (1 Dec. 2021). ISSN: 23993650. DOI: 10.1038/s42005-021-00663-8.
- [191] D. Nicoletti et al. “Optically induced superconductivity in striped La_{2-x}Ba_xCuO₄ by polarization-selective excitation in the near infrared”. In: *Physical Review B - Condensed Matter and Materials Physics* 90 (10 Sept. 2014). ISSN: 1550235X. DOI: 10.1103/PhysRevB.90.100503.
- [192] Yasutomo J. Uemura. “Dynamic superconductivity responses in photoexcited optical conductivity and Nernst effect”. In: *Physical Review Materials* 3 (10 Oct. 2019). ISSN: 24759953. DOI: 10.1103/PhysRevMaterials.3.104801.
- [193] Puri Sanjay and Wadhawan Vinod. *Kinetics of Phase Transitions*. 2009.

- [194] Roberto Livi and Paolo Politi. *Nonequilibrium statistical physics: A modern perspective*. Cambridge University Press, Jan. 2017, pp. 1–420. ISBN: 9781107278974. DOI: 10.1017/9781107278974.
- [195] A. J. Bray. “Theory of phase-ordering kinetics”. In: *Advances in Physics* 51 (2 Mar. 2002), pp. 481–587. ISSN: 00018732. DOI: 10.1080/00018730110117433.
- [196] Landau L. D. and Lifshitz E. M. *Physical Kinetics*. Pergamon Press, 1981.
- [197] James P Sethna. *Statistical Mechanics: Entropy, Order Parameters, and Complexity*. 2nd. Oxford University Press, 2021.
- [198] Andrew D Rutenberg and Benjamin P Vollmayr-Lee. “Anisotropic Coarsening: Grain Shapes and Nonuniversal Persistence”. In: *PHYSICAL REVIEW LETTERS* 83 (19 1999).
- [199] Parr Robert G. and Yang Weitao. *DENSITY-FUNCTIONAL THEORY OF ATOMS AND MOLECULES*. Oxford University Press Inc, 1989.
- [200] R O Jones and O Gunnarsson. “The density functional formalism, its applications and prospects”. In: *Reviews of Modern Physics* 61.3 (1989).
- [201] John P Perdew, Kieron Burke, and Yue Wang. “Generalized gradient approximation for the exchange-correlation hole of a many-electron system”. In: *Physical Review B* 54.33 (1996).
- [202] John P Perdew et al. “Atoms, molecules, solids, and surfaces: Applications of the generalized gradient approximation for exchange and correlation”. In: *PHYSICAL REVIEW B* 46.11 (1992), pp. 15–1992.
- [203] John P Perdew, Kieron Burke, and Matthias Ernzerhof. “Generalized Gradient Approximation Made Simple”. In: *Physical Review Letters* 77.18 (1996).
- [204] Charlotte Froese Fischer. “Numerical Solution of General Hartree-Fock Equations for Atoms”. In: *JOURNAL OF COMPUTATIONAL PHYSICS* 27 (1978), pp. 221–240.
- [205] W Kohn and L J Sham. “Self-Consistent Equations Including Exchange and Correlation Effects*”. In: *Physical Review* 140.4A (1965), A1133.
- [206] P Hohenberg and W Konnt. “Inhomogeneous Electron Gas”. In: *Physical Review* 136.3B (1964).
- [207] Vladimir A. Gubanov, Alexandr I. Liechtenstein, and Andrei V. Postnikov. *Magnetism and the Electronic Structure of Crystals*. Vol. 98. Springer Series in Solid-State Sciences. Berlin, Heidelberg: Springer Berlin Heidelberg, 1992. ISBN: 978-3-642-84413-3. DOI: 10.1007/978-3-642-84411-9. URL: <http://link.springer.com/10.1007/978-3-642-84411-9>.
- [208] V O Lume and O Krogh Andersen. “Linear methods in band theory*”. In: *Physical Review B* 12 (8 1975).
- [209] Markus Betzinger et al. “Local exact exchange potentials within the all-electron FLAPW method and a comparison with pseudopotential results”. In: *Physical Review B - Condensed Matter and Materials Physics* 83 (4 Jan. 2011). ISSN: 10980121. DOI: 10.1103/PhysRevB.83.045105.
- [210] A B Shick, A I Liechtenstein, and W E Pickett. “Implementation of the LDAU method using the full-potential linearized augmented plane-wave basis”. In: *Physical Review B* 60 (15 1999).

- [211] M. Weinert et al. “FLAPW: Applications and implementations”. In: *Journal of Physics Condensed Matter* 21 (8 2009). ISSN: 09538984. DOI: 10.1088/0953-8984/21/8/084201.
- [212] *The Elk Code*. <http://elk.sourceforge.net/>.
- [213] Groot Frank de and Kotani Akio. *Core Level Spectroscopy of Solids*. CRC Press, 2008. ISBN: 978-0-8493-9071-5.
- [214] J. J. (Jun John) Sakurai and San Fu Tuan. *Modern quantum mechanics*. Addison-Wesley Pub. Co, 1994, p. 500. ISBN: 0201539292.
- [215] Gerrit van der Laan and Adriana I. Figueroa. *X-ray magnetic circular dichroism - A versatile tool to study magnetism*. Oct. 2014. DOI: 10.1016/j.ccr.2014.03.018.
- [216] J T M Walraven. *Atomic Physics lectures University of Amsterdam*. Tech. rep. 2018.
- [217] Messiah Albert. *Quantum Mechanics, Vol 2*. North Holland Publishing Company, Amsterdam, 1962, p. 992.
- [218] Ondřej Šipr, Jiří Vackář, and Ján Minár. “Finite lifetime broadening of calculated X-ray absorption spectra: Possible artefacts close to the edge”. In: *Journal of Synchrotron Radiation* 25 (2 Mar. 2018), pp. 523–528. ISSN: 16005775. DOI: 10.1107/S1600577518000048.
- [219] J. Kuneš and P. M. Oppeneer. “Anisotropic x-ray magnetic linear dichroism at the L edges of cubic Fe, Co, and Ni: Ab Initio calculations and model theory”. In: *Physical Review B - Condensed Matter and Materials Physics* 67 (2 2003). ISSN: 1550235X. DOI: 10.1103/PhysRevB.67.024431.
- [220] J G Tobin and F O Schumann. “Element-specific magnetometry with photoelectron dichroism: FeCo and FeNi”. In: *Surface Science* 478 (2001), pp. 211–228. URL: www.elsevier.nl/locate/susc.
- [221] J G Tobin et al. “Direct extraction of exchange splittings from magnetic X-ray dichroism in photoelectron spectroscopy”. In: *Surface Science* 395 (1998), pp. L227–L235.
- [222] Kübler Jürgen. *Theory of Itinerant Electron Magnetism*. Revised Edition. Oxford University Press, 2000.
- [223] C Koenig. “Self-consistent band structure of paramagnetic, ferromagnetic and antiferromagnetic ordered FeRh”. In: *J. Phys. F: Met. Phys* 12 (1982), pp. 1123–1137.
- [224] Hidekazu Takahashi et al. “Theoretical Investigation on Electronic and Magnetic Structures of FeRh”. In: *Journal of the Magnetism Society of Japan* 40.4 (2016), pp. 77–80.
- [225] A Szajek and J A Morkowski. “The electronic and magnetic properties of the metamagnetic ordered alloy FeRh”. In: *Physica B* 193 (1994), pp. 81–91.
- [226] Ulrich Aschauer et al. “Strain-induced structural instability in FeRh”. In: *Physical Review B* 94 (1 July 2016). ISSN: 24699969. DOI: 10.1103/PhysRevB.94.014109.
- [227] M. Wolloch et al. “Impact of lattice dynamics on the phase stability of metamagnetic FeRh: Bulk and thin films”. In: *Physical Review B* 94 (17 Nov. 2016). ISSN: 24699969. DOI: 10.1103/PhysRevB.94.174435.
- [228] Wolfram Thomas and Callaway Joseph. “Exchange Narrowing of d Bands in Ferronagnets*”. In: *Physical Review* 127 (5 1962).

- [229] Wolfram Thomas and Callaway Joseph. “Exchange Narrowing of d Bands in Antiferromagnets*”. In: *Physical Review* 130 (1 1963).
- [230] J. Fink et al. “Resonant elastic soft x-ray scattering”. In: *Reports on Progress in Physics* 76.5 (May 2013). ISSN: 00344885. DOI: 10.1088/0034-4885/76/5/056502.
- [231] S. Grenier and Y. Joly. “Basics of resonant elastic X-ray scattering theory”. In: vol. 519. Institute of Physics Publishing, 2014. DOI: 10.1088/1742-6596/519/1/012001.
- [232] J P Hannon et al. “X-Ray Resonance Exchange Scattering”. In: *Physical Review Letters* 61 (10 1988).
- [233] Lovesey S. W. and Collins S.P. *X-Ray Scattering and Absorption by Magnetic Materials*. Oxford University Press, USA, 1996.
- [234] Camille Aron et al. “Scaling and super-universality in the coarsening dynamics of the 3D random field Ising model”. In: *Journal of Statistical Mechanics: Theory and Experiment* 2008.5 (May 2008). ISSN: 17425468. DOI: 10.1088/1742-5468/2008/05/P05016.
- [235] Nishimori Hidetoshi and Ortiz Gerardo. *Elements of Phase Transitions and Critical Phenomena*. Oxford University Press, 2011. ISBN: 978-0-19-957722-4.
- [236] Egami T. and Billinge S.J.L. *PERGAMON MATERIALS SERIES VOLUME 7 UNDERNEATH THE BRAGG PEAKS Structural Analysis of Complex Materials*. Pergamon, 2003. ISBN: 0-08-042698-0.
- [237] Franz Schwabl. *Statistical Mechanics*. 2nd. Springer Berlin Heidelberg New York, 2006.
- [238] Kerson Huang. *Statistical mechanics*. 2nd. John Wiley & Sons, Inc, 1987. ISBN: 0-471-81518-7.
- [239] Gianluca Geloni, Vitali Kocharyan, and Evgeni Saldin. “A novel self-seeding scheme for hard X-ray FELs”. In: *Journal of Modern Optics* 58 (16 Sept. 2011), pp. 1391–1403. ISSN: 09500340. DOI: 10.1080/09500340.2011.586473.
- [240] J. Amann et al. “Demonstration of self-seeding in a hard-X-ray free-electron laser”. In: *Nature Photonics* 6 (10 Oct. 2012), pp. 693–698. ISSN: 17494885. DOI: 10.1038/nphoton.2012.180.
- [241] Paola Finetti et al. “Pulse duration of seeded free-electron lasers”. In: *Physical Review X* 7 (2 June 2017). ISSN: 21603308. DOI: 10.1103/PhysRevX.7.021043.
- [242] David Attwood and Anne Sakdinawat. *X-Rays and Extreme Ultraviolet Radiation: Principles and Applications*. 2nd ed. Cambridge University Press, 2017. DOI: 10.1017/CBO9781107477629.
- [243] Gianluca Geloni. “Self-Seeded Free-Electron Lasers”. In: *Synchrotron Light Sources and Free-Electron Lasers: Accelerator Physics, Instrumentation and Science Applications*. Ed. by Eberhard J. Jaeschke et al. Cham: Springer International Publishing, 2016, pp. 161–193. ISBN: 978-3-319-14394-1. DOI: 10.1007/978-3-319-14394-1_4. URL: https://doi.org/10.1007/978-3-319-14394-1_4.
- [244] Thomas Tschentscher et al. “Photon Beam Transport and Scientific Instruments at the European XFEL”. In: *Appl. Sci.. Applied Sciences* ARTICLE (2017). DOI: 10.3390/app7060592. URL: <https://xfel.tind.io/record/1421>.
- [245] Daniele La Civita et al. “SASE3: soft X-ray Beamline at European XFEL”. In: (2014), Proc. SPIE 9210, X-Ray Free-Electron Lasers: Beam Diagnostics, Beamline Instrumentation, and Applications II, 921002. DOI: 10.1117/12.2061693. URL: <https://xfel.tind.io/record/239>.

- [246] Natalia Gerasimova. “Diffraction Orders of the SASE3 Monochromator”. In: XFEL.EU TR-2014-003 (2014), pp. 1–36. DOI: 10.3204/XFEL.EU/TR-2014-003. URL: <https://xfel.tind.io/record/311>.
- [247] A. Scherz et al. “Conceptual Design Report: Scientific Instrument Spectroscopy and Coherent Scattering (SCS)”. In: XFEL.EU TR-2013-006 (2013), pp. 1–147. DOI: 10.3204/XFEL.EU/TR-2013-006. URL: <https://xfel.tind.io/record/370>.
- [248] Theophilos Maltezopoulos et al. “Operation of X-ray gas monitors at the European XFEL”. In: *J. Synchrotron Rad.. Journal of Synchrotron Radiation* (2019). DOI: 10.1107/S1600577519003795. URL: <https://xfel.tind.io/record/1978>.
- [249] Giuseppe Mercurio et al. “First commissioning results of the KB mirrors at the SCS instrument of the European XFEL”. In: *Proceedings of SPIE PROCEEDING* (2019). DOI: 10.1117/12.2530725. URL: <https://xfel.tind.io/record/2095>.
- [250] M. J. Lederer et al. “Pump-probe laser development for the European X-Ray Free-Electron Laser Facility”. In: *Proceedings of SPIE* (2012). DOI: 10.1117/12.928961. URL: <https://xfel.tind.io/record/428>.
- [251] Matteo Porro et al. “The MiniSDD-Based 1-Mpixel Camera of the DSSC Project for the European XFEL”. In: *IEEE Trans. Nucl. Sci., IEEE Transactions on Nuclear Science* ARTICLE (2021). DOI: 10.1109/TNS.2021.3076602. URL: <https://xfel.tind.io/record/2560>.
- [252] Mattia Donato. “Commissioning and Characterization of the First DSSC Ladder X-Ray Camera Prototype for the European XFEL”. In: THESIS (2019). DOI: nbn:de:gbv:18-95174. URL: <https://xfel.tind.io/record/1972>.
- [253] W. F. Schlotter et al. “Balanced Detection in Femtosecond X-ray Absorption Spectroscopy to Reach the Ultimate Sensitivity Limit”. In: (June 2020). URL: <http://arxiv.org/abs/2006.13968>.
- [254] L. Le Guyader et al. “Beam-splitting off-axis zone plate for time-resolved X-ray absorption spectroscopy at the SCS instrument”. In: (2020). URL: <https://xfel.tind.io/record/2125>.
- [255] S. Eisebitt et al. “Polarization effects in coherent scattering from magnetic specimen: Implications for x-ray holography, lensless imaging, and correlation spectroscopy”. In: *Physical Review B - Condensed Matter and Materials Physics* 68.10 (2003). ISSN: 1550235X. DOI: 10.1103/PhysRevB.68.104419.
- [256] Eisebitt S. et al. “Lensless imaging of magnetic nanostructures by X-ray spectro-holography”. In: *Nature* 432 (Dec. 2004), pp. 881–885. ISSN: 00280836. DOI: 10.1038/nature03129.
- [257] Tianhan Wang et al. “Femtosecond single-shot imaging of nanoscale ferromagnetic order in co/pd multilayers using resonant x-ray holography”. In: *Physical Review Letters* 108 (26 June 2012). ISSN: 10797114. DOI: 10.1103/PhysRevLett.108.267403.
- [258] W. Roseker et al. “Towards ultrafast dynamics with split-pulse X-ray photon correlation spectroscopy at free electron laser sources”. In: *Nature Communications* 9 (1 Dec. 2018). ISSN: 20411723. DOI: 10.1038/s41467-018-04178-9.
- [259] Wojciech Roseker et al. “Double-pulse speckle contrast correlations with near Fourier transform limited free-electron laser light using hard X-ray split-and-delay”. In: *Scientific Reports* 10 (1 Dec. 2020). ISSN: 20452322. DOI: 10.1038/s41598-020-61926-y.

- [260] Yanwen Sun et al. “Realizing split-pulse X-ray photon correlation spectroscopy to measure ultrafast dynamics in complex matter”. In: *Physical Review Research* 2 (2 Apr. 2020). ISSN: 26431564. DOI: 10.1103/PhysRevResearch.2.023099.
- [261] Francesco Dallari et al. “Analysis strategies for mhz XPCS at the European XFEL”. In: *Applied Sciences (Switzerland)* 11 (17 Sept. 2021). ISSN: 20763417. DOI: 10.3390/app11178037.
- [262] Yuya Shinohara et al. “Split-pulse X-ray photon correlation spectroscopy with seeded X-rays from X-ray laser to study atomic-level dynamics”. In: *Nature Communications* 11 (1 Dec. 2020). ISSN: 20411723. DOI: 10.1038/s41467-020-20036-z.
- [263] L. Shen et al. “A snapshot review—Fluctuations in quantum materials: from skyrmions to superconductivity”. In: *MRS Advances* 6 (8 May 2021), pp. 221–233. ISSN: 20598521. DOI: 10.1557/s43580-021-00051-y.
- [264] Haidan Wen, Mathew J Cherukara, and Martin V Holt. “Time-Resolved X-Ray Microscopy for Materials Science Keywords”. In: *Annu. Rev. Mater. Res.* 49 (2019), pp. 389–415. DOI: 10.1146/annurev-matsci-070616. URL: <https://doi.org/10.1146/annurev-matsci-070616->.
- [265] Buzzi Michele et al. “Probing dynamics in quantum materials with femtosecond X-rays”. In: *Nature Reviews Materials* (2018).
- [266] Zhang Jiang et al. “Reconstruction of evolving nanostructures in ultrathin films with X-ray waveguide fluorescence holography”. In: *Nature Communications* 11 (1 Dec. 2020). ISSN: 20411723. DOI: 10.1038/s41467-020-16980-5.
- [267] Jörg Zegenhagen. “X-ray standing waves technique: Fourier imaging active sites”. In: *Japanese Journal of Applied Physics* 58 (11 2019). ISSN: 13474065. DOI: 10.7567/1347-4065/ab4dec.
- [268] T Lamb et al. “LARGE-SCALE OPTICAL SYNCHRONIZATION SYSTEM OF THE EUROPEAN XFEL WITH FEMTOSECOND PRECISION”. In: *10th Int. Particle Accelerator Conf. 2019*, pp. 3835–3838. ISBN: 9783954502080. DOI: 10.18429/JACoW-IPAC2019-THPRB018.
- [269] M. R. Bionta et al. “Spectral encoding method for measuring the relative arrival time between x-ray/optical pulses”. In: *Review of Scientific Instruments* 85 (8 2014). ISSN: 10897623. DOI: 10.1063/1.4893657.
- [270] Henry J. Kirkwood et al. “Initial observations of the femtosecond timing jitter at the European XFEL”. In: *Optics Letters* 44 (7 Apr. 2019), p. 1650. ISSN: 0146-9592. DOI: 10.1364/ol.44.001650.
- [271] M. Harmand et al. “Achieving few-femtosecond time-sorting at hard X-ray free-electron lasers”. In: *Nature Photonics* 7.3 (Mar. 2013), pp. 215–218. ISSN: 17494885. DOI: 10.1038/nphoton.2013.11.
- [272] Li Tao, Craig Levin, and Ryan Coffee. “Ionizing radiation induces femtosecond time scale modulations of a material’s optical properties”. In: SPIE-Intl Soc Optical Eng, Sept. 2018, p. 2. ISBN: 9781510620971. DOI: 10.1117/12.2319435.
- [273] Zhiping Jiang and X. C. Zhang. “Electro-optic measurement of THz field pulses with a chirped optical beam”. In: *Applied Physics Letters* 72 (16 1998), pp. 1945–1947. ISSN: 00036951. DOI: 10.1063/1.121231.

- [274] S. Kovalev et al. “Probing ultra-fast processes with high dynamic range at 4th-generation light sources: Arrival time and intensity binning at unprecedented repetition rates”. In: *Structural Dynamics* 4 (2 Mar. 2017). ISSN: 23297778. DOI: 10.1063/1.4978042.
- [275] I Ilyakov et al. “Terahertz tomography of femtosecond extreme-ultraviolet light pulses (Submitted 2021)”. In: (2021).
- [276] Ulrike Frühling et al. “Single-shot terahertz-field-driven X-ray streak camera”. In: *Nature Photonics* 3 (9 Sept. 2009), pp. 523–528. ISSN: 17494885. DOI: 10.1038/nphoton.2009.160.
- [277] F. Tavella et al. “Few-femtosecond timing at fourth-generation X-ray light sources”. In: *Nature Photonics* 5 (3 Mar. 2011), pp. 162–165. ISSN: 17494885. DOI: 10.1038/nphoton.2010.311.
- [278] S. Cunovic et al. “Time-to-space mapping in a gas medium for the temporal characterization of vacuum-ultraviolet pulses”. In: *Applied Physics Letters* 90 (12 2007). ISSN: 00036951. DOI: 10.1063/1.2714999.
- [279] Tokushi Sato et al. “Femtosecond timing synchronization at megahertz repetition rates for an x-ray free-electron laser”. In: *Optica* 7 (6 June 2020), p. 716. ISSN: 2334-2536. DOI: 10.1364/optica.396728.
- [280] Ulrike Frühling. “Light-field streaking for FELs”. In: *Journal of Physics B: Atomic, Molecular and Optical Physics* 44 (24 Dec. 2011). ISSN: 09534075. DOI: 10.1088/0953-4075/44/24/243001.
- [281] I. Grguraš et al. “Ultrafast X-ray pulse characterization at free-electron lasers”. In: *Nature Photonics* 6 (12 Dec. 2012), pp. 852–857. ISSN: 17494885. DOI: 10.1038/nphoton.2012.276.
- [282] Rosen Ivanov et al. “Single-shot temporal characterization of XUV pulses with duration from 10 fs to 350 fs at FLASH”. In: *Journal of Physics B: Atomic, Molecular and Optical Physics* 53 (18 Sept. 2020). ISSN: 13616455. DOI: 10.1088/1361-6455/ab9c38.
- [283] R. Riedel et al. “Single-shot pulse duration monitor for extreme ultraviolet and X-ray free-electron lasers”. In: *Nature Communications* 4 (2013). ISSN: 20411723. DOI: 10.1038/ncomms2754.
- [284] R. Heider et al. “Megahertz-compatible angular streaking with few-femtosecond resolution at x-ray free-electron lasers”. In: *Phys. Rev. A. Physical Review A* ARTICLE (2019). DOI: 10.1103/PhysRevA.100.053420. URL: <https://xfel.tind.io/record/2005>.
- [285] J. Honolka et al. “Spin-spiral state of a Mn monolayer on W(110) studied by soft x-ray absorption spectroscopy at variable temperature”. In: *Physical Review B* 103 (17 May 2021). ISSN: 24699969. DOI: 10.1103/PhysRevB.103.174419.
- [286] Zhibin Lin and Leonid V. Zhigilei. “Temperature dependences of the electron-phonon coupling, electron heat capacity and thermal conductivity in Ni under femtosecond laser irradiation”. In: *Applied Surface Science* 253.15 (May 2007), pp. 6295–6300. ISSN: 01694332. DOI: 10.1016/j.apsusc.2007.01.032.
- [287] E. Şaşıoğlu et al. “Exchange interactions and temperature dependence of magnetization in half-metallic Heusler alloys”. In: *Physical Review B - Condensed Matter and Materials Physics* 72 (18 Nov. 2005). ISSN: 10980121. DOI: 10.1103/PhysRevB.72.184415.

- [288] S. Mankovsky et al. “Temperature-dependent transport properties of FeRh”. In: *Physical Review B* 95.15 (Apr. 2017). ISSN: 24699969. DOI: 10.1103/PhysRevB.95.155139.
- [289] S. Mankovsky, S. Polesya, and H. Ebert. “Exchange coupling constants at finite temperature”. In: *Physical Review B* 102 (13 Oct. 2020). ISSN: 24699969. DOI: 10.1103/PhysRevB.102.134434.
- [290] A. I. Lichtenstein, M. I. Katsnelson, and G. Kotliar. “Finite-Temperature Magnetism of Transition Metals: An ab initio Dynamical Mean-Field Theory”. In: *Physical Review Letters* 87 (6 Aug. 2001), pp. 67205-1-67205-4. ISSN: 10797114. DOI: 10.1103/PhysRevLett.87.067205.
- [291] O. Šipr et al. “Many-body effects in X-ray absorption and magnetic circular dichroism spectra within the LSDA+DMFT framework”. In: *Physical Review B - Condensed Matter and Materials Physics* 84 (11 Sept. 2011). ISSN: 10980121. DOI: 10.1103/PhysRevB.84.115102.
- [292] O. Bunău and Y. Joly. “Full potential x-ray absorption calculations using time dependent density functional theory”. In: *Journal of Physics Condensed Matter* 24.21 (May 2012). ISSN: 09538984. DOI: 10.1088/0953-8984/24/21/215502.
- [293] H Ebert et al. “L-edge x-ray absorption in fcc and bcc Cu metal: Comparison of experimental and first-principles theoretical results”. In: *PHYSICAL REVIEW B* 53.33 (1996).
- [294] Andreas Scherz. “Spin dependent x-ray absorption spectroscopy of 3d transition metals systematics and applications”. PhD thesis. Free University of Berlin, 2003.
- [295] Gerrit Van Der Laan. “Sum rules and beyond”. In: *Journal of Electron Spectroscopy and Related Phenomena* 101.103 (1999), pp. 859–868.
- [296] M I Katsnelson and A I Lichtenstein. “LDA++ approach to the electronic structure of magnets: correlation effects in iron”. In: *J. Phys.: Condens. Matter* 11 (1999), pp. 1037–1048.
- [297] B. I. Cho et al. “Electronic structure of warm dense copper studied by ultrafast X-ray absorption spectroscopy”. In: *Physical Review Letters* 106 (16 Apr. 2011). ISSN: 00319007. DOI: 10.1103/PhysRevLett.106.167601.
- [298] N. Rothenbach et al. “Effect of lattice excitations on transient near edge X-ray absorption spectroscopy”. In: *PHYSICAL REVIEW B* 104 (Nov. 2021), pp. 144302-1-144302-9. ISSN: 2469-9950. DOI: 10.1103/physrevb.104.144302. URL: <http://arxiv.org/abs/1911.06201>.
- [299] C. Stamm et al. “X-ray spectroscopy of current-induced spin-orbit torques and spin accumulation in Pt/3d -transition-metal bilayers”. In: *Physical Review B* 100.2 (July 2019). ISSN: 24699969. DOI: 10.1103/PhysRevB.100.024426.
- [300] N Agarwal et al. “X-ray absorption spectroscopy of thermal effects in 3d transition metals (in preparation)”. In: (2021).
- [301] Dimitris A Papaconstantopoulos. *Handbook of the Band Structure of Elemental Solids*. 2nd. Springer, 2015. ISBN: 978-1-4419-8263-6.
- [302] M. O. Krause. “Atomic radiative and radiationless yields for K and L shells”. In: *Journal of Physical and Chemical Reference Data* 8 (2 1979), pp. 307–327. ISSN: 15297845. DOI: 10.1063/1.555594.
- [303] Krause M.O. and Oliver J. H. “Natural widths of atomic K and L levels, $K\alpha$ X-ray lines and several KLL Auger lines”. In: *Journal of Physical and Chemical Reference Data* 8 (2 1979), pp. 329–338.

- [304] C T Chen et al. “Experimental Confirmation of the X-Ray Magnetic Circular Dichroism Sum Rules for Iron and Cobalt”. In: *Physical Review Letters* 75 (1 1995), pp. 152–155.
- [305] Eric Fawcett. “Spin-density-wave antiferromagnetism in chromium”. In: *Rev Mod. Phys* 60 (1 1988).
- [306] G Grimvall et al. “Spin fluctuations in paramagnetic chromium determined from entropy considerations S-100 gg Stockholm, Sujeden”. In: *Physical Review B* 47 (22 1993).
- [307] J P Hill, G Helgesen, and Doon Gibbs. “X-ray-scattering study of charge-and spin-density waves in chromium”. In: *PHYSICAL REVIEW B* 51 (16 1995), pp. 15–1995.
- [308] B J Sternlieb et al. “Silent Satellites: Critical Fluctuations in Chromium”. In: *Physical Review Letters* 75 (3 1995).
- [309] B. J. Sternlieb et al. “Critical dynamics at the spin-density-wave transition of chromium”. In: *Journal of Applied Physics* 79 (8 PART 2A Apr. 1996), pp. 4802–4804. ISSN: 00218979. DOI: 10.1063/1.361677.
- [310] L. Müller et al. “Note: Soft X-ray transmission polarizer based on ferromagnetic thin films”. In: *Review of Scientific Instruments* 89 (3 Mar. 2018). ISSN: 10897623. DOI: 10.1063/1.5018396.
- [311] Joseph Barker and Roy W. Chantrell. “Higher-order exchange interactions leading to metamagnetism in FeRh”. In: *Physical Review B - Condensed Matter and Materials Physics* 92.9 (Sept. 2015). ISSN: 1550235X. DOI: 10.1103/PhysRevB.92.094402.
- [312] Matteo Mitrano et al. “Ultrafast time-resolved x-ray scattering reveals diffusive charge order dynamics in La 2-x Ba x Cu O 4”. In: *Science Advances* 5:eaax3346 (2019). URL: <https://www.science.org>.
- [313] J. K. Chen and J. E. Beraun. “Numerical study of ultrashort laser pulse interactions with metal films”. In: *Numerical Heat Transfer; Part A: Applications* 40.1 (July 2001), pp. 1–20. ISSN: 10407782. DOI: 10.1080/104077801300348842.
- [314] J. K. Chen, J. E. Beraun, and C. L. Tham. “Investigation of thermal response caused by pulse laser heating”. In: *Numerical Heat Transfer; Part A: Applications* 44.7 (2003), pp. 705–722. ISSN: 15210634. DOI: 10.1080/716100520.
- [315] J. K. Chen, D. Y. Tzou, and J. E. Beraun. “A semiclassical two-temperature model for ultrafast laser heating”. In: *International Journal of Heat and Mass Transfer* 49.1-2 (Jan. 2006), pp. 307–316. ISSN: 00179310. DOI: 10.1016/j.ijheatmasstransfer.2005.06.022.
- [316] Yunpeng Ren, J. K. Chen, and Yuwen Zhang. “Modeling of ultrafast phase changes in metal films induced by an ultrashort laser pulse using a semi-classical two-temperature model”. In: *International Journal of Heat and Mass Transfer* 55.5-6 (Feb. 2012), pp. 1620–1627. ISSN: 00179310. DOI: 10.1016/j.ijheatmasstransfer.2011.11.018.
- [317] J K Chen, W P Latham, and J E Beraun. “The role of electron-phonon coupling in ultrafast laser heating”. In: *JOURNAL OF LASER APPLICATIONS* 17.1 (2005). URL: http://jla.aip.org/about/about_the_journal.
- [318] S. L. Johnson et al. “Watching ultrafast responses of structure and magnetism in condensed matter with momentum-resolved probes”. In: *Structural Dynamics* 4.6 (Nov. 2017). ISSN: 23297778. DOI: 10.1063/1.4996176.

- [319] David W. Cooke et al. “Thermodynamic measurements of Fe-Rh alloys”. In: *Physical Review Letters* 109.25 (Dec. 2012). ISSN: 00319007. DOI: 10.1103/PhysRevLett.109.255901.
- [320] A I Zakharov et al. “MAGNETIC AND MAGNETOELASTIC PROPERTIES OF A METAMAGNETIC IRON-RHODIUM ALLOY”. In: *J. Exptl. Theoret. Phys. (U.S.S.R.)* 19.6 (1964).
- [321] Jon Ander Arregi, Ondřej Caha, and Vojtěch Uhlíř. “Evolution of strain across the magnetostructural phase transition in epitaxial FeRh films on different substrates”. In: *Physical Review B* 101.17 (May 2020). ISSN: 24699969. DOI: 10.1103/PhysRevB.101.174413.
- [322] Jon Ander Arregi et al. “Magnetization reversal and confinement effects across the metamagnetic phase transition in mesoscale FeRh structures”. In: *Journal of Physics D: Applied Physics* 51.10 (Feb. 2018). ISSN: 13616463. DOI: 10.1088/1361-6463/aaaa5a.



NAMAN AGARWAL

✉ Email address: nanu0907@gmail.com

🌐 Website: <https://scholar.google.com/citations?user=AbTyugsAAAAJ&hl=en>

🌐 LinkedIn: <https://www.linkedin.com/in/naman-agarwal-aos/>

Nationality: Indian

EDUCATION AND TRAINING

[Jul 2017 – Jan 2022] **Doctoral researcher in Physics**
European X-ray Free Electron Laser , IMPRS-UFAST & University of Hamburg, Germany

[Aug 2012 – Jul 2017] **Integrated Master of Science in Physics**
UM-DAE CEBS, University of Mumbai, India

WORK EXPERIENCE

[Jul 2017 – Jan 2022] **Doctoral Thesis**
Dr. Andreas Scherz (European XFEL), Prof. Alexander Lichtenstein (University of Hamburg)

[Jun 2016 – Dec 2016] **Master thesis : Electric Field Control of Skyrmion phase in Cu₂OSeO₃**
Professor Henrik M. Ronnow, LQM, EPFL, Lausanne, Switzerland

[Jan 2016 – Apr 2016] **Semester Project-2: Study of Fabry Perot resonators using supercontinuum laser**
Dr. Sushil Mujumdar, TIFR, Mumbai, India

[Aug 2015 – Nov 2015] **Semester project-1: Density functional theory**
Dr. Swapan K. Ghosh, UM-DAE-CBS, Mumbai, India

[May 2015 – Jul 2015] **Summer research fellowship: Mueller Polarimetric Imaging on turbid mediums**
Dr. Razvigor Ossikovski, Ecole Polytechnique, Paris-Saclay, France

[May 2014 – Jul 2014] **Summer research fellowship: Magnetic and electric properties of CoCr₂O₄ and related multiferroic materials**
Dr. A. Sundaresan, JNCASR, Bangalore, India

[May 2013 – Jul 2013] **Summer Project: Sensor calibration and testing**
Dr. R. Nagarajan, UM-DAE CBS, Mumbai, India

CONFERENCES AND SEMINARS

Intermag-2021

Ultrafast dynamics in electronic band structure of optically excited epitaxial FeRh: X-ray absorption spectroscopy and density functional theory approach (ID: FD-05)

MMM-2020

Probing the Laser-driven Antiferromagnetic to Ferromagnetic Phase Transition of FeRh with Femtosecond Time-resolved Small Angle X-ray Scattering (tr-SAXS) and X-ray Absorption Spectroscopy (tr-XAS) (ID: G3-06)

JEMS-2020

Probing the antiferromagnetic to ferromagnetic phase transition of FeRh with femtosecond time-resolved small angle X-ray scattering (tr-SAXS) and X-ray absorption spectroscopy (tr-XAS) (ID:3887)

POSTER PRESENTATIONS

UXSS-2019

(Beamtime proposal practice poster) -Best poster prize

Time-resolved resonant soft X-ray microscopy of ultrafast spin current propagation

SXR-2019

Demonstration of THz-emission-based single shot temporal diagnostics at FELs

ESM-2019

THz emission from XUV pumped Spintronic emitter: A versatile tool for studying magnetization dynamics and parasitic timing diagnostics

UXSS-2018

(Beamtime proposal practice poster)

Probing Electron Transfer dynamics by Stimulated Resonant X-ray Raman Spectroscopy

Hercules-2018

Theoretical investigation of THz-driven dynamics in ferrimagnets

CFEL-Symposium-2017

Electric Field Effect on Skyrmion phase in Chiral Lattice Ferrimagnet Cu₂OSeO₃

PUBLICATIONS

[2022]

Ultrafast evolution of the exchange interactions and ferromagnetic domain nucleation during photo-induced phase transition in FeRh (N. Agarwal et al.)

Manuscript under preparation

[2022]

X-ray absorption spectroscopy of thermal effects in 3d transition metals (N. Agarwal et al.)

Manuscript under preparation

[2022]

Terahertz-wave decoding of femtosecond extreme-ultraviolet light pulses (I. Ilyakov, N. Agarwal et al.)

Manuscript accepted in Optica

[2022]

Nonequilibrium sub-10 nm spin-wave soliton formation in FePt nanoparticles (D. Turenne et al.)

<https://www.science.org/doi/full/10.1126/sciadv.abn0523>

[2021]

Megahertz-rate Ultrafast X-ray Scattering and Holographic Imaging at the European XFEL (N. Z. Hagström et al.)

<https://doi.org/10.48550/arXiv.2201.06350>

Manuscript submitted to Journal of Synchrotron Radiation

[2021]

Optical control of 4f orbital state in rare-earth metals (N. Thielemann-Kühn et al.)

<https://arxiv.org/abs/2106.09999v1>

[2020]

Optical laser delivery to the SCS instrument - first measurements of time arrival jitter (L. Mercadier et al.)

[2020]

Beam-splitting off-axis zone plate for time-resolved X-ray absorption spectroscopy at the SCS instrument (L. Le Guyader et al.)

[2016]

Electric field effect on skyrmion phase in chiral lattice ferrimagnet Cu₂OSeO₃ (N. Agarwal)

<https://infoscience.epfl.ch/record/261269>

[2015]

Spatial evolution of depolarization in homogeneous turbid media within the differential Mueller matrix formalism (N. Agarwal et al.), Optics Letters, Vol. 40, Issue 23, pp. 5634 -5637(2015)

<https://doi.org/10.1364/OL.40.005634>

